The magnetic properties of antiferromagnetic nanoparticles: NiO and Fe2O3

Bahl, Christian Robert Haffenden

Publication date:
2006

Document Version
Publisher's PDF, also known as Version of record

Risø-PhD-30(EN)

The Magnetic properties of antiferromagnetic nanoparticles: NiO and α-Fe_2O_3

Christian Robert Haffenden Bahl

Risø National Laboratory
Roskilde
Denmark
December 2006

Author: Christian Robert Haffenden Bahl
Title: The Magnetic properties of antiferromagnetic nanoparticles: NiO and α-Fe_2O_3
Department: Materials Research Department

This thesis is submitted in partial fulfilment of the requirements for the Ph.D. degree at Technical University of Denmark

Abstract (max. 2000 char.):
Nickel oxide (NiO) and hematite (α-Fe_2O_3), both antiferromagnets, have magnetic properties which at nanoscale differ from those of the bulk materials.
With emphasis on NiO nanoparticles and comparisons with α-Fe_2O_3 nanoparticles these magnetic properties are studied by a range of experimental techniques: elastic and inelastic neutron scattering, Mössbauer spectroscopy, x-ray diffraction, transmission electron microscopy and vibrating sample magnetometry.
Knowledge of the size and shape of the nanoparticles is an often neglected prerequisite for studies of their magnetic properties. The NiO nanoparticles are found to be plate shaped with the (111) planes as plate faces, a thickness of about 2.3 nm and a diameter of about 13 nm. The magnetic structure is similar to that of bulk NiO, with the spins confined in the (111) planes. Measurements of the spin dynamics reveal a value of the magnetic anisotropy aligning the spins along an easy axis within the planes significantly larger than the bulk value.
The agglomeration state of the particles has an important influence on the magnetic properties of the particles. In both materials exchange interactions between the particles strongly affect the spin dynamics, increasing the resonance energy of zero wave vector (**q** = 0) spin waves and suppressing the thermally activated relaxation of the spins, known as superparamagnetism. A significant reduction of this interaction is surprisingly achieved by simple mechanical treatments, such as grinding in a mortar by hand.
Nanoparticles of antiferromagnetic materials will have an uncompensated magnetic moment, arising at finite particle sizes because of a surplus of spins in one sublattice. This uncompensated moment is quantified in the NiO nanoparticles and found to be independent of the aggregation state.
Use of the recently implemented monochromatic imaging mode of the RITA-II triple axis neutron spectrometer to measure inelastic neutron scattering data from the NiO nanoparticle samples is described. The advantages of using such a multi-blade mode are demonstrated.

Risø-PhD-30(EN)
December 2006

ISBN 87-550-3572-8

Contract no.:

Group's own reg. no.:

Sponsorship:

Cover :

Pages: 244
Tables:
References:

Risø National Laboratory
Information Service Department
P.O.Box 49
DK-4000 Roskilde
Denmark
Telephone +45 46774004
bibl@risoe.dk
Fax +45 46774013
www.risoe.dk

The Magnetic properties of antiferromagnetic nanoparticles: NiO and α-Fe_2O_3

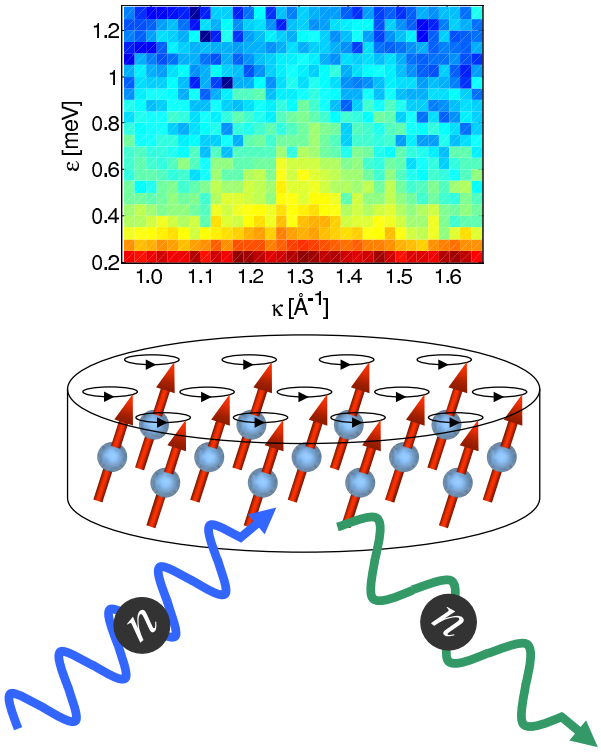

Christian Robert Haffenden Bahl

Materials Research Department
Risø National Laboratory

&

Department of Physics
Technical University of Denmark

Preface

This thesis and the papers appended to it are the result of a PhD project carried out partly at the Materials Research Department, Risø National Laboratory (Risø) and partly at the Department of Physics at the Technical University of Denmark (DTU). The project was supported by the Danish Technical Research Council through the Nanomagnetism programme.

Being jointly at Risø and DTU has been a rewarding experience and broadened the project. It has given me the opportunity to gain access to a broad range of different experimental techniques and experts within the different fields, which has been very fulfilling.

The intention of this thesis is to act as an introduction to the appended Papers I–XII. Papers IV–XI contain results of experiments conducted on both hematite (α-Fe_2O_3) and nickel oxide (NiO) nanoparticles. The emphasis of this thesis is on results obtained from NiO nanoparticles, with comparisons to the results from hematite nanoparticles. Many of the results pertaining to the hematite nanoparticles have previously been presented in PhD theses [1, 2].

Chapter 1 contains an introduction to some of the properties of nanomagnets and applications of these.

Chapter 2 gives a brief introduction to the various experimental techniques employed for the present work, with emphasis on measurements of nanoparticles.

Chapter 3 contains a presentation of the various nanoparticle samples presented in the papers. The structural, interaction and magnetic anisotropy properties of NiO and hematite are presented and compared.

Chapter 4 gives an overview of some of the results relating especially to the spin dynamics of NiO nanoparticles obtained by Mössbauer spectroscopy and inelastic neutron scattering.

Chapter 5 is an introduction to the multi-blade analyser modes of the RITA-II spectrometer, one of which was implemented during this project. Specifically the experimental choices during measurements of NiO nanoparticles are discussed.

Chapter 6 contains a brief conclusion and outlook of potential areas of further study for NiO nanoparticles.

Acknowledgements

First and foremost I would like to express my thanks to my two main supervisors, Kim Lefmann at Risø and Steen Mørup at DTU, for their guidance and always having the time to talk. Steen, also for sharing his encyclopedic knowledge of Mössbauer spectroscopy and Kim for sharing his experience of neutron

scattering, making the neutron scattering experiments productive.

Also, my co-supervisor Luise Theil Kuhn deserves thanks for her guidance, fruitful discussions and good company in the office.

At Risø, I thank Erik Johnson for translating my knowledge of electron microscopy into japanese and Bente Lebech for help with Rietveld refinement. Per-Anker Lindgård is thanked for helpful theoretical discussions.

At DTU I would like to thank Cathrine Frandsen, Britt R. Hansen and Daniel E. Madsen for fruitful discussion and enjoyable company. Also, I would like to thank Lis Lilleballe for help with the sample preparations and Helge K. Rasmussen for help with the high field Mössbauer measurements. Mikkel F. Hansen is thanked for introducing me to, and allowing me to use the often tempremental magnetometer.

The neutron scattering experiments and instrument development presented here were conducted at the Swiss spallation neutron source SINQ at the Paul Scherrer Institute, Villigen, Switzerland. I am gratefully to the Danish Neutron Scattering Centre DANSCATT for financially supporting the neutron scattering experiments in Switzerland.

At the PSI, I would like to thank Christof Niedermayer and Niels B. Christensen for their help with running the experiments. Also, everyone that I have spent long days (and nights) with during the experiments.

To my dear Michaela, thank you for your love and encouragement throughout this project.

Christian Robert Haffenden Bahl
Risø, July 1st 2006

Abstract

Nickel oxide (NiO) and hematite (α-Fe_2O_3), both antiferromagnets, have magnetic properties which at nanoscale differ from those of the bulk materials.

With emphasis on NiO nanoparticles and comparisons with α-Fe_2O_3 nanoparticles these magnetic properties are studied by a range of experimental techniques: elastic and inelastic neutron scattering, Mössbauer spectroscopy, x-ray diffraction, transmission electron microscopy and vibrating sample magnetometry.

Knowledge of the size and shape of the nanoparticles is an often neglected prerequisite for studies of their magnetic properties. The NiO nanoparticles are found to be plate shaped with the (111) planes as plate faces, a thickness of about 2.3 nm and a diameter of about 13 nm. The magnetic structure is similar to that of bulk NiO, with the spins confined in the (111) planes. Measurements of the spin dynamics reveal a value of the magnetic anisotropy aligning the spins along an easy axis within the planes significantly larger than the bulk value.

The agglomeration state of the particles has an important influence on the magnetic properties of the particles. In both materials exchange interactions between the particles strongly affect the spin dynamics, increasing the resonance energy of zero wave vector ($\mathbf{q} = 0$) spin waves and suppressing the thermally activated relaxation of the spins, known as superparamagnetism. A significant reduction of this interaction is surprisingly achieved by simple mechanical treatments, such as grinding in a mortar by hand.

Nanoparticles of antiferromagnetic materials will have an uncompensated magnetic moment, arising at finite particle sizes because of a surplus of spins in one sublattice. This uncompensated moment is quantified in the NiO nanoparticles and found to be independent of the aggregation state.

Use of the recently implemented monochromatic imaging mode of the RITA-II triple axis neutron spectrometer to measure inelastic neutron scattering data from the NiO nanoparticle samples is described. The advantages of using such a multi-blade mode are demonstrated.

Resumé

Nikkel oxid (NiO) og hematit (α-Fe_2O_3) er begge antiferromagneter med magnetiske egenskaber på nanoskala, som er forskellige fra dem i større krystaller.

Med hovedvægt på nanopartikler af NiO og sammenligninger med nanopartikler af hematit studeres disse magnetiske egenskaber med en række forskellige eksperimentelle teknikker: elastisk og uelastisk neutronspredning, Møssbauer spektroskopi, Røntgen diffraktion, transmissionselektron mikroskopi og vibrerende prøve magnetometri.

Kendskab til størrelsen og formen af partiklerne er en ofte overset forudsætning for studier af de magnetiske egenskaber. Nanopartiklerne af NiO vises at være pladeformede med (111) planer som flader, en tykkelse på omkring 2.3 nm og en diameter på omkring 13 nm. Den magnetiske struktur er magen til den i større krystaller, med spinnene holdt i (111) planerne. Målinger af spindynamikken afslører en værdi af den magnetiske anisotropi som retter spinnene ind efter en let retning i planerne, og som er væsentlig større end værdien i større krystaller.

Sammenkitningen af partiklerne har en vigtig indflydelse på partiklernes magnetiske egenskaber. I begge materialer påvirker exchange vekselvirkninger imellem partiklerne spindynamikken stærkt, resonans energien af spin bølger med nul bølge vektor ($\mathbf{q} = 0$) øges og den termisk drevne relaksation af spinnene, kendt som superparamagnetisme, undertrykkes. Denne vekselvirkning imellem partiklerne kan overraskende reduceres betydeligt ved simpel mekanisk behandling som knusning i en morter med hånden.

Nanopartikler af antiferromagnetiske materialer vil have et ukompenseret magnetisk moment, der opstår ved endelige partikelstørrelser på grund af overskydende spin på det ene undergitter. Dette ukompenserede moment kvantiseres i NiO nanopartiklerne og findes at være uafhængigt af sammenkitningen af partiklerne.

Den nyligt implementerede monokromatiske "billededannende mode" af RITA-II tre-akse neutronspektrometeret beskrives. Brugen af denne til at måle uelastisk neutronspredningsdata fra prøver af NiO nanopartikler og fordelene ved at bruge en sådan multiblads mode demonstreres.

Contents

Chapter 1

Introduction

Nanomagnetism is concerned with the study and exploitation of the magnetic properties of objects, where these are determined by the finite size of the objects. Such objects may include: a) thin films, where the film thickness is in the nanometer range while the other dimensions are macroscopical b) nano-rods or wires where the cross section is in the nanometer range but the length is larger c) nanoparticles where all the dimensions are in the nanometer range. Reviews of these three types of nanomagnetic objects are given in [3, 4].

In the present thesis only magnetic nanoparticles are considered. The dimensions of the particles are in the range 2–15 nm, and they are thus magnetically single domain [5].

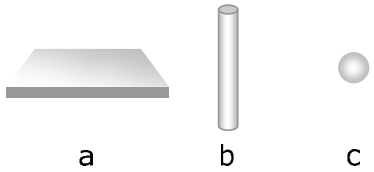

Figure 1.1: Three geometries of nanomagnetic objects. a) Thin film. b) Nano-rod or wire. c) Nanoparticle.

One of the early foundations of nanomagnetism was laid in 1899 when the Danish physicist Valdemar Poulsen pioneered magnetic recording by using an electromagnet to record sound on a steel wire wound on a cylinder [6]. Since the advent of computers in the 1950'ies, magnetic recording using magnetic particles on a rotating disc has remained the preferential way of storing data. As computers become ever more powerful, with a desire for storing increasing amounts of data, smaller and smaller magnetic particles are required.

At finite sizes magnetic nanoparticles will begin to exhibit properties differing from the bulk material. In a magnetic particle, the magnetic moment is held along a certain direction within the structure by the magnetic anisotropy, which will be discussed in Section 3.5. In the confined system of a finite sized particle, excitations are in discrete energy levels. The lowest level excitation of the spins is an infinite wavelength spin wave. Such coherent precession states of the spins, known as collective or uniform magnetic excitations, may be thermally excited. Classically the spins can be perceived to describe a cone around

the magnetisation direction defined by the anisotropy with some opening angle, just as a driven pendulum may swing around the energy minimum defined by gravity. Increasing the temperature will populate more infinite wavelength precession states at higher energies, i.e., larger opening angles of the cone.

Due to the finite size of the nanoparticles, the thermal energy may become comparable to the anisotropy energy at finite temperatures. This makes it possible to surmount the energy barrier between opposite magnetisation directions created by the anisotropy energy and thus reverse the magnetisation of the particle. This allows the magnetisation in nanoparticles to spontaneously flip with an Arrhenius like behaviour. The time between flips (relaxation time), τ_{r} is given by [7, 8]

$$\tau_{\mathrm{r}} = \tau_0 \exp\left(\frac{KV}{k_{\mathrm{B}}T}\right). \tag{1.1}$$

Here, k_{B} is Boltzmanns constant, K is the magnetic anisotropy density of the particle, as discussed in Section 3.5, V is the particle volume and τ_0 is a pre-factor depending on several parameters, such as the particle moment and anisotropy energy [8]. This flipping of the magnetisation is known as superparamagnetic relaxation.

As the magnetic particles used in the magnetic recording industry become ever smaller the particles will be near the superparamagnetic regime, with a loss of stored data as a result. To counteract this, materials with a high value of the anisotropy are sought. FePt alloys [9] and recently FeCo [10,11] have been found to be promising materials. These also offer a high sublattice magnetisation, M_{s}, which is desirable as the field the hard disc write unit must produce to change the magnetisation, $H_{\mathrm{w}} \approx K/M_{\mathrm{s}}$ [10], must not be too large for the unit to work efficiently.

1.1 Applications of magnetic nanoparticles

There are several applications of magnetic nanoparticles, apart from the important application in magnetic storage technology.

Magnetic nanoparticles of e.g. maghemite (γ-Fe_2O_3) and magnetite (Fe_3O_4) have recently found several useful applications in medicine. One of these is to separate certain cells from a liquid, e.g. blood, by affixing ferro- or ferrimagnetic nanoparticles to the particles and applying a strong magnetic field [12]. In the same way the nanoparticles may be bound to drugs in order to concentrate the drug in a certain part of the body using a magnetic field [12]. It has also been found that applying a magnetic field to ferromagnetic nanoparticles concentrated at a broken bone may accelerate bone growth [13].

Maybe the most promising application of nanomagnetism in medicine is the ability to concentrate nanoparticles near a cancer tumour and apply a fast oscillating magnetic field to induce a heating of the area, known as hyperthermia [12]. This allows destruction of the tumour without damaging other, healthy, areas of the body, contrary to other treatments available.

However, care should be taken when ingesting or injecting magnetic nanoparticles into the body. A significantly larger amount of magnetic nanoparticles have been observed within the brains of people with Huntingdon's, Alzheimer's and Parkinson's diseases than in healthy people [14]. This connection has yet to be explained.

Another potential application in nanomagnetism is to utilise knowledge of the magnetic properties of materials at the nanoscale to design and produce small but strong permanent magnets [15,16]. This would be important in many fields of technology, as it would reduce the weight of motors and generators potentially leading to significant savings in fuel.

1.2 Nanoscale antiferromagnetism

The above mentioned applications all utilise the external moment of ferro- or ferrimagnetic nanoparticles. The work presented in this thesis is concerned with nanoparticles of antiferromagnetic materials. These do not possess a significant external dipole moment and are therefore not interesting for such applications.

However, nanoscale antiferromagnets are still fundamentally and technologically important. The absence of an external moment means that magnetic interactions between particles will not be due to dipole attraction but rather to exchange interactions between the spins at the surface of the particles. Such exchange interactions are important for the understanding of agglomeration and crystal growth both in manufactured samples and in nature.

Nanoparticles of antiferromagnetic materials will exhibit both superparamagnetism and collective magnetic excitations just as the ferro- and ferrimagnetic nanoparticles. It has been shown that embedding ferromagnetic particles in an antiferromagnetic host will provide an extra source of anisotropy increasing the relaxation time at a given temperature [17]. The exchange coupling of nanoscale ferro- and antiferromagnets results in a pinning of the magnetisation in the ferromagnet, known as exchange bias [18]. In the emerging field of spintronics [19] this can be used to create spin-valve devices, where application of a magnetic field can alter the electrical resistance of the device. Importantly, this is utilised in read heads for hard discs. The antiferromagnet NiO in the shape of thin films is an important and useful material for such applications [20,21].

Indeed, the magnetic properties of plate shaped NiO nanoparticles is the main emphasis of this thesis. Apart from the applications in spintronics, nanoscale NiO has several other technologically important applications.

Nanoparticles of NiO are in use in the catalysis industry as a catalyst for CH_4/CO_2 reforming [22]. Also, various shapes of nanoparticles of NiO, especially ring shaped particles, have been found to catalyse CO oxidation [23]. Nanoparticles of NiO have also been shown to be promising as electrode materials in e.g. lithium ion batteries [24,25]. Although neither of these applications directly rely on the magnetic properties of the nanoparticles, these may still be important to study. Exchange interactions between the particles control the aggregation state. The aggregation state of the particles may be important [25,26] as it can alter the structural and surface properties of the particles. Also, an indirect connection between the magnetic and catalytic properties may be envisioned if the magnetic properties affect the band structure of NiO, thus changing the catalytic properties.

Another interesting aspect of nanoparticles of antiferromagnetic materials is that perfectly antiferromagnetic nanoparticles do not exist. Néel[1] proposed that the small size of an antiferromagnetic nanoparticle will inevitably result in an excess number of spins on one sublattice compared to the other [27,28].

[1] Recipient of the 1971 Nobel prize for his pioneering work in antiferromagnetism.

Three general cases of a cube shaped particle were considered [27, 29], as illustrated in Figure 1.2. In the first the missing spins were assumed to occur at random within a particle due to e.g. defects in the structure. This gives a number of uncompensated spins of $\delta \approx n_s^{1/2}$, where n_s is the total number of spins. If the cube surface has randomly distributed missing spins the number of uncompensated spins is $\delta \approx n_s^{1/3}$. In the final case the cube consists of an odd number of ferromagnetically ordered layers giving a number of uncompensated spins of $\delta \approx n_s^{2/3}$. In any of the three cases the excess moment from the uncompensated spins will give rise to an external moment, giving the particle weakly ferrimagnetic properties. Thus no perfect antiferromagnet is available at nanoscale.

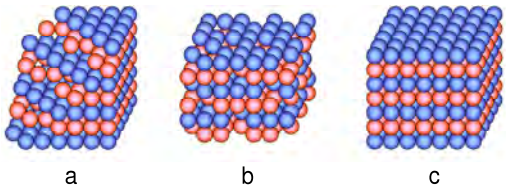

Figure 1.2: The three cases of uncompensated spins. a) Spins are missing at random within the particle. b) Spins are missing at random on the surface of the particle. c) Odd number of layers in a cube.

Chapter 2

Experimental methods

In the present work five different experimental techniques have been employed to study structure, morphology, magnetic properties and dynamics of antiferromagnetic nanoparticles. This chapter gives a brief introduction to each of the techniques with focus on antiferromagnetic nanoparticles. The main emphasis will be on neutron scattering and Mössbauer spectroscopy, as these are the main techniques of investigation. It is not the intention to give a complete and stringent presentation, as this can be found in numerous publications elsewhere. Rather, it is the intention to give a more phenomenological explanation of the techniques.

For neutron scattering a good introduction is given in Ref. [30] and more stringent presentations are given in Refs. [31,32]. An introduction to Mössbauer spectroscopy is given in Ref. [33] and further details especially with respect to nanoparticles may be found in Ref. [34]. For transmission electron microscopy a solid introduction is given in Ref. [35]. X-ray diffraction is described in Refs. [36, 37]. An introduction to vibrating sample magnetometry is given in Ref. [38].

2.1 Neutron Scattering

Much of the formalism concerning the interaction of neutrons with magnetic and non-magnetic matter had been worked out in the late 1930'ies [39, 40] following Chadwicks discovery of the neutron in 1932 [41] However, no sources strong enough to properly investigate neutron scattering were available until the first controlled fission experiments in 1942. Within ten years, neutron scattering had been developed as a powerful method for probing materials. Elastic and inelastic neutron scattering were pioneered by C. G. Shull and B. N. Brockhouse respectively. For this work they shared the 1994 Nobel prize in physics [42, 43].

The neutron is a chargeless particle with spin $\frac{1}{2}$, and mass m_{n}. The interaction of neutrons with matter is governed by the strong interaction, i.e., the interaction is with the nuclei of the sample. The magnetic moment associated with the spin of the neutron will also interact with a magnetic field within the sample, created by unpaired electrons. Both the structural and magnetic interactions are similar in strength. The interaction of neutrons with matter is very weak, so that neutrons may penetrate deep within samples. The energy of a

neutron with a velocity, v, is given by

$$E = \frac{1}{2} m_{\mathrm{n}} v^2. \tag{2.1}$$

With the de Broglie wavelength given by

$$\lambda = \frac{h}{m_{\mathrm{n}} v}, \tag{2.2}$$

where h is the Planck constant, a wave vector $\mathbf{k}$ with magnitude $|\mathbf{k}| = k = \frac{2\pi}{\lambda}$ may be defined. This allows the energy to be written as

$$E = \frac{\hbar^2 k^2}{2 m_{\mathrm{n}}}. \tag{2.3}$$

When scattering neutrons, the total momentum and energy are conserved, any energy or momentum lost by the neutron is gained by the sample and vice versa. A neutron with an initial momentum $\hbar\mathbf{k}_{\mathrm{i}}$ and a momentum $\hbar\mathbf{k}_{\mathrm{f}}$ after being scattered by the sample will transfer the momentum, $\hbar\boldsymbol{\kappa}$, and energy, $\hbar\omega$,

$$\hbar\boldsymbol{\kappa} = \hbar\mathbf{k}_{\mathrm{i}} - \hbar\mathbf{k}_{\mathrm{f}} \quad \text{and} \quad \hbar\omega = \frac{\hbar^2 k_{\mathrm{i}}^2}{2 m_{\mathrm{n}}} - \frac{\hbar^2 k_{\mathrm{f}}^2}{2 m_{\mathrm{n}}} \tag{2.4}$$

to the sample. Here, $\boldsymbol{\kappa}$ is known as the scattering vector. If the scattering is elastic there is no loss of energy so $\omega = 0$ and $|\mathbf{k}_{\mathrm{i}}| = |\mathbf{k}_{\mathrm{f}}|$. If however, $|\mathbf{k}_{\mathrm{i}}| \neq |\mathbf{k}_{\mathrm{f}}|$ the scattering is inelastic and energy is lost to or gained by the sample.

Neutron scattering is concerned with measuring the number of neutrons with the energy in the interval from E_{f} to $E_{\mathrm{f}} + dE_{\mathrm{f}}$ scattered by the sample into a small solid angle $d\Omega_{\mathrm{f}}$ from an incident beam of wave vector $\mathbf{k}_{\mathrm{i}}$. This is known as the differential cross section. Using Fermi's Golden Rule the differential cross section may be expressed as

$$\frac{d^2\sigma}{d\Omega_{\mathrm{f}} dE_{\mathrm{f}}} = \frac{k_{\mathrm{f}}}{k_{\mathrm{i}}} \Big(\frac{m_{\mathrm{n}}}{2\pi\hbar^2} \Big)^2 |\langle \mathbf{k}_{\mathrm{f}} \lambda_{\mathrm{f}} | V | \mathbf{k}_{\mathrm{i}} \lambda_{\mathrm{i}} \rangle|^2 \delta(\hbar\omega + E_{\mathrm{i}} - E_{\mathrm{f}}) \tag{2.5}$$

Here $\langle \lambda_{\mathrm{f}}|$ and $|\lambda_{\mathrm{i}}\rangle$ are the final and initial states of the sample, V is the interaction potential and δ is the Dirac delta function. Most of the following uses the notation and derivations of Shirane *et al.* [30].

2.1.1 Structural scattering

Initially, we shall be concerned with structural scattering from the sample nuclei, ignoring the magnetic contribution.

Due to the weakness of interaction with matter and the small size of a nucleus compared to the wavelength of the neutron, the initial and final neutron states may be considered as plane waves by the Born approximation, and the interaction potential may be considered as a delta function in real space. This leads to a cross section given by

$$\frac{d^2\sigma}{d\Omega_{\mathrm{f}} dE_{\mathrm{f}}} = N \frac{k_{\mathrm{f}}}{k_{\mathrm{i}}} b^2 \mathcal{S}(\boldsymbol{\kappa}, \omega) \tag{2.6}$$

where

$$\mathcal{S}(\boldsymbol{\kappa},\omega)=\frac{1}{2\pi\hbar N}\sum_{jk}\int_{-\infty}^{\infty}dt\langle e^{-\mathrm{i}\boldsymbol{\kappa}\cdot\mathbf{r}_k(0)}e^{-\mathrm{i}\boldsymbol{\kappa}\cdot\mathbf{r}_j(t)}\rangle e^{-\mathrm{i}\omega t} \tag{2.7}$$

b is known as the scattering length and is specific to a particular scattering nucleus, t is time, N is the number of nuclei in the sample and $\mathbf{r}_\mathrm{j}(t)$ and $\mathbf{r}_\mathrm{k}(t)$ are the positions of the scattering nuclei at the time t. $\langle\ldots\rangle$ means the average over initial states. $S(\boldsymbol{\kappa},\omega)$ is known as the scattering function. The integral over t is a convenient way of stating the delta function of energy conservation [44].

Only the elastic contribution to the structural scattering is considered here, as the inelastic structural scattering is associated with lattice dynamics such as phonons, which are not considered in the present work.

The scattering length b is strongly element- and isotope dependent. If the sample contains atoms with a random distribution of scattering lengths the mean of the square of the scattering length may be written $\overline{b^2}=\overline{b}^2+\overline{(b-\overline{b})^2}$, where the first term is the square of the mean scattering length and the second term is the mean of the square of the deviation of the scattering length from its mean value. This somewhat strange rewriting divides the scattering into two contributions: coherent and incoherent scattering, associated with the first and second terms respectively. The coherent and incoherent scattering lengths vary unsystematically from element to element, even the different isotopes of the same element may have widely different scattering lengths. Tables giving the coherent and incoherent scattering lengths are available for all isotopes of all the elements [45].

In the elastic case with a unit cell of volume v_0 containing one atom (Bravais lattice), the coherent term gives rise to an expression

$$\mathcal{S}(\boldsymbol{\kappa},\omega)_\mathrm{coh}=\delta(\hbar\omega)\frac{(2\pi)^3}{v_0}\sum_{\boldsymbol{\tau}}\delta(\boldsymbol{\kappa}-\boldsymbol{\tau})e^{-2W} \tag{2.8}$$

where $\boldsymbol{\tau}$ is a reciprocal lattice vector. Here e^{-2W} is the Debye-Waller factor due to thermal vibrations of the atoms around their equilibrium positions, $\mathbf{u}$. At small values of $\mathbf{u}$ it is given by

$$W=\frac{1}{2}\langle(\boldsymbol{\kappa}\cdot\mathbf{u})^2\rangle, \tag{2.9}$$

the brackets denoting the thermal average. Thus the coherent elastic cross section is

$$\frac{d\sigma}{d\Omega}_\mathrm{coh}=N(\overline{b})^2\frac{(2\pi)^3}{v_0}\sum_{\boldsymbol{\tau}}\delta(\boldsymbol{\kappa}-\boldsymbol{\tau})e^{-2W}. \tag{2.10}$$

There will be constructive interference whenever the scattering vector is a reciprocal lattice vector, $\boldsymbol{\kappa}=\boldsymbol{\tau}$. This condition is equivalent [46] to Braggs law, conventionally stated as

$$2d\sin\theta=n\lambda \tag{2.11}$$

where d is a lattice spacing in the sample, 2θ is the angle the neutrons are scattered from the incident beam, see Figure 2.1, and n is an integer.

For unit cells containing more than one atom, the structure factor must be included by replacing b^2 in Equation (2.6) with $|F_\mathrm{N}(\boldsymbol{\tau})|^2$, where

$$F_\mathrm{N}(\boldsymbol{\tau})=\sum_j\overline{b}_j e^{\mathrm{i}\boldsymbol{\tau}\cdot\mathbf{d}_j}. \tag{2.12}$$

Here $\mathbf{d}_j$ is the position of the j'th atom within the unit cell and $\overline{b}_\mathrm{j}$ is its mean scattering length. Also Debye-Waller factors for the individual atoms must be included by replacing e^{-2W} in Equation (2.8) with e^{-2W_j}.

In a similar way to the calculation of the coherent elastic cross section, the incoherent elastic cross section can be calculated for a Bravais lattice as

$$\frac{d\sigma}{d\Omega}_{\mathrm{incoh}} = N(\overline{b^2} - \overline{b}^2)e^{-2W}. \tag{2.13}$$

The coherent scattering can be considered as an interaction between the neutron wave and the whole sample, allowing interference between the coherently scattered neutron waves in some directions, giving Bragg reflections. Contrary the incoherent scattering may be considered as the neutron wave being scattered from each individual nucleus independently. This gives an isotropic scattering of the neutrons, and explains the lack of orientational dependence of Equation (2.13), except for the Debye-Waller term. Hydrogen is a strong incoherent scatterer and it will be shown later that water adsorbed on nanoparticle samples due to their large surface area will give rise to a strong and often annoying incoherent scattering signal at all scattering vectors.

Powder samples

The condition for elastic scattering, Equation (2.11), may be rewritten as $\kappa = 2k\sin\theta$, where 2θ is again the scatting angle. In a powder of randomly oriented particles, i.e., a sample of nanoparticles, neutrons will be Bragg scattered into cones around the incident beam, known as Debye-Scherrer cones, see Figure 2.1. The opening angle of the cones is given by the scattering angle, 2θ. The circumference of the cones and thus the solid angle which the neutrons are scattered into grows with θ, and the solid angle of the detector remains fixed. This, combined with the fact that in a powder of randomly oriented particles the number of particles fulfilling the Bragg condition varies with θ, means the scattered intensity must be corrected by the factor $(\sin\theta\sin 2\theta)^{-1}$, known as the Lorentz factor [47].

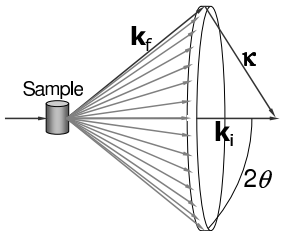

Figure 2.1: From a powder, the neutron scattered into cones with opening angles 2θ.

Finite-size broadening

The Bragg reflections are a product of constructive interference of spherical waves scattered from the sample. If the scattering crystal is infinitely large, the sum of these scattered waves is a delta function, giving reflections with essentially zero width. If however, the scattering crystal has some finite size, the

constructive interference will occur in a range of scattering angles, broadening the reflections [48]. This is formulated as the Scherrer equation

$$D_{hkl} = \frac{K\lambda}{B_{hkl}\cos\theta_{hkl}} \tag{2.14}$$

where D_{hkl} is the extent of the crystal perpendicular to the reflecting hkl-planes, B_{hkl} is the width of the reflection in radians and K is a constant with a value of about 0.9 [49], depending on the structure and shape of the crystal.

2.1.2 Magnetic scattering

In order to take the magnetic scattering into account the spin states of the incident, σ_i, and final, σ_f, neutrons must be considered in Equation (2.5). The magnetic moment of the neutron, $\mu_\mathrm{n} = -\gamma\mu_\mathrm{N}\sigma$, interacts with the field from the unpaired electrons in the sample. Here γ is the neutron gyromagnetic ratio equivalent to the $g = 2$ factor for electrons ($\gamma = 1.913$) and μ_N is the nuclear magneton, equivalent to the Bohr magneton for electrons ($\mu_\mathrm{N} = 5.05 \cdot 10^{27}$ JT^{-1}). Only scattering with initially unpolarised neutrons will be considered and no polarisation analysis is considered[1].

The cross section for magnetic scattering can be shown to be [30]

$$\frac{d^2\sigma}{d\Omega_\mathrm{f} dE_\mathrm{f}} = \left(\frac{\gamma r_0 g}{2}\right)^2 \frac{k_\mathrm{f}}{k_\mathrm{i}} N |f(\boldsymbol{\kappa})|^2 e^{-2W} \sum_{\alpha\beta} \left(\delta_{\alpha\beta} - \hat{\kappa}_\alpha \hat{\kappa}_\beta\right) \mathcal{S}^{\alpha\beta}(\boldsymbol{\kappa}, \omega) \tag{2.15}$$

where r_0 is the classic electron radius and $g = 2$ is the electron g-factor. $f(\boldsymbol{\kappa})$ is the magnetic form factor given by $f(\boldsymbol{\kappa}) = \int \rho_s(\mathbf{r}) e^{i\boldsymbol{\kappa}\cdot\mathbf{r}} d\mathbf{r}$, where $\rho_s(\mathbf{r})$ is the normalised density of unpaired spins on an atom. α and β are cartesian coordinates (x, y, z) and $\delta_{\alpha\beta}$ is the Kronecker delta. $\hat{\kappa}$ is the scattering unit vector and $\hat{\kappa}_\alpha$ is the α component of the magnetisation of the scattering ion along $\hat{\kappa}$. This leads to one of the central points in magnetic neutron scattering, namely that only components of the magnetisation perpendicular to the scattering vector give rise to scattering.

The form factor in Expression (2.15) is due to the electrons being distributed in shells around the nuclei, thus having spatial distributions. This is contrary to the structural scattering which has no form factor as the nuclei have negligible spatial size compared to the neutron wavelength.

As the present work only concerns the $3d$ transition metals, where the electron orbital moment is (almost) quenched, only the spin contribution to the magnetic moment will be considered. The magnetic scattering function is given by

$$\mathcal{S}^{\alpha\beta}(\boldsymbol{\kappa}, \omega) = \frac{1}{2\pi\hbar N} \int_{-\infty}^{\infty} dt\, e^{-\mathrm{i}\omega t} \sum_j e^{-\mathrm{i}\boldsymbol{\kappa}\cdot\mathbf{r}_j} \langle S_0^\alpha(0) S_j^\beta(t)\rangle \tag{2.16}$$

where the j sum is over nuclei and S^α is the α component of the spin of the scattering ion. Here, the brackets $\langle \ldots \rangle$ refer to the thermal average. The term contained in the brackets is known as the spin correlation function.

[1] Working with polarised neutrons and utilising polarisation analysis, can give valuable information when studying magnetic scattering [31, 32]

Elastic magnetic scattering

A simple ferromagnet can be defined by a Bravais lattice with one spin in each unit cell. Assume that all the spins are ordered along a certain direction as is the case at low temperatures. Here the ordering direction is defined as the z direction. The elastic coherent cross section in this situation may then be written as

$$\frac{d\sigma}{d\Omega}^{\text{mag}}_{\text{coh}} = \left(\frac{\gamma r_0 g}{2}\right)^2 \frac{(2\pi)^3}{v_\text{m}} N_\text{m} |f(\boldsymbol{\kappa})|^2 e^{-2W} \left(1-\hat{\kappa}_z^2\right) \langle S^z\rangle^2 \sum_{\boldsymbol{\tau}_\text{m}} \delta(\boldsymbol{\kappa}-\boldsymbol{\tau}_\text{m}) \quad (2.17)$$

where v_m and N_m are the volume of the magnetic unit cell and number of magnetic unit cells. $\boldsymbol{\tau}_\text{m}$ is a reciprocal unit vector in the magnetic unit cell and $\langle S^z\rangle$ is the thermal average magnitude of the spin along z.

It is seen that if the scattering vector is perpendicular to z, such that $\hat{\kappa}_z = 0$, the cross section is very similar to the one obtained in the structural case except for the magnetic form factor. In the ferromagnet the magnetic unit cell has the same volume as the structural and the magnetic reciprocal lattice will be the same as the structural. Thus the scattering will be observed as Bragg reflections at the same positions as the structural. If however every other spin along the z direction is oriented oppositely the sample is an antiferromagnet and the lattice becomes non Bravais. Now v_m is larger than in the ferromagnetic case and the magnetic reciprocal lattice will be different from the structural giving reflections at values of $\boldsymbol{\tau}_\text{m}$ that are different from the structural $\boldsymbol{\tau}$. The scattered intensity depends on $\langle S^z\rangle^2$ in both the ferromagnetic and antiferromagnetic cases.

A typical nanoscale effect in ferro- and antiferromagnetic nanoparticles is superparamagnetism. Here the spins are ordered along the z direction, but the magnetisation of a nanoparticle will flip between the two directions of the z axis. This happens with a flipping time τ_r. Thus the spin correlation is $\langle S^z(0)S^z(t)\rangle \propto S_z^2 e^{-|t|/\tau_\text{r}}$. The time integral of this gives a Lorenzian line shape in energy. This slightly broadened elastic peak is known as a quasielastic peak and has a HWHM of $\Gamma = \hbar/\tau_\text{r}$ [50].

Inelastic magnetic scattering

Most of the neutron scattering results presented here concern inelastic magnetic scattering from spin waves. Both the structural and magnetic signals contain both elastic and inelastic contributions. The discussion of spin waves is limited to dealing with the inelastic magnetic cross section in the case of elastic structural scattering.

The spins are again assumed ordered along z. In the case of inelastic magnetic scattering only the spin correlation functions $\langle S^\pm(0)S^\mp(t)\rangle$ do not vanish. Here as usual the raising and lowering operators are $\hat{S}^\pm = \hat{S}^x \pm \mathrm{i}\hat{S}^y$. The oscillations of the spins are in the x, y plane and as by definition $\hat{\kappa}_x^2 + \hat{\kappa}_y^2 + \hat{\kappa}_z^2 = 1$ the coordinate sum becomes

$$\sum_{\alpha\beta} \left(\delta_{\alpha\beta} - \hat{\kappa}_\alpha \hat{\kappa}_\beta\right) = \left(1-\hat{\kappa}_x^2\right) + \left(1-\hat{\kappa}_y^2\right) = \left(1+\hat{\kappa}_z^2\right). \quad (2.18)$$

The spin wave dispersion for a Heisenberg ferromagnet with nearest neighbour interactions is given at a small value of the spin wave vector $\mathbf{q}$ by $\hbar\omega_q^\text{FM} =$

$2JSa^2q^2$ where J is the exchange constant and a is the lattice constant. The scattering function of this may be derived as the sum of creation and annihilation of spin wave terms

$$\begin{aligned}\mathcal{S}^{\mathrm{FM}}(\boldsymbol{\kappa},\omega) &= S\sum_{\boldsymbol{\tau}_{\mathrm{m}}\mathbf{q}}\Big[\,(n(\omega)+1)\,\delta(\boldsymbol{\kappa}-\mathbf{q}-\boldsymbol{\tau}_{\mathrm{m}})\delta(\omega-\omega_q^{\mathrm{FM}})+\\ &\qquad n(\omega)\delta(\boldsymbol{\kappa}+\mathbf{q}-\boldsymbol{\tau}_{\mathrm{m}})\delta(\omega+\omega_q^{\mathrm{FM}})\Big].\end{aligned}\tag{2.19}$$

The Bose factor

$$n(\omega)=\frac{1}{e^{\hbar\omega/k_BT}-1}\tag{2.20}$$

is due to the different thermal population of the spin wave states.

The derivation of the scattering function for an antiferromagnet is similar to that of a ferromagnet but more complex. In the case of a simple Heisenberg antiferromagnet with no anisotropy, the spin wave energy at small values of $|\mathbf{q}|$, measured from a reciprocal vector in the antiferromagnetic lattice, is given by $\hbar\omega_q^{\mathrm{AFM}}=\hbar\mathcal{J}Saq$. Here $\mathcal{J}=\sum_l z_lJ_l$ is the effective exchange constant, where z_l is the number of l'th neighbours and J_l is the exchange constant to these. The scattering function may in this case be written as

$$\begin{aligned}\mathcal{S}^{\mathrm{AFM}}(\boldsymbol{\kappa},\omega) &= S\sum_{\boldsymbol{\tau}_{\mathrm{m}}\mathbf{q}}\frac{\mathcal{J}S}{\hbar\omega_q^{\mathrm{AFM}}}\Big[\,(n(\omega)+1)\,\delta(\boldsymbol{\kappa}-\mathbf{q}-\boldsymbol{\tau}_{\mathrm{m}})\delta(\omega-\omega_q^{\mathrm{AFM}})+\\ &\qquad n(\omega)\delta(\boldsymbol{\kappa}+\mathbf{q}-\boldsymbol{\tau}_{\mathrm{m}})\delta(\omega+\omega_q^{\mathrm{AFM}})\Big].\end{aligned}\tag{2.21}$$

The spin dynamics of nanoparticles will later be shown to be dominated by infinite wavelength ($\mathbf{q}=0$) spin waves. An antiferromagnet with a uniaxial anisotropy κ has the spin wave energy $\hbar\omega^{\mathrm{AFM}}\approx\sqrt{4\kappa\mathcal{J}S^2}$, see Section 3.7. Thus the scattering function at points on the antiferromagnetic reciprocal lattice may be written as

$$\begin{aligned}\mathcal{S}^{\mathrm{AFM}}(\boldsymbol{\kappa},\omega) &= S\sum_{\boldsymbol{\tau}_{\mathrm{m}}}\frac{\mathcal{J}S}{\hbar\omega^{\mathrm{AFM}}}\Big[\,(n(\omega)+1)\,\delta(\boldsymbol{\kappa}-\boldsymbol{\tau}_{\mathrm{m}})\delta(\omega-\omega^{\mathrm{AFM}})+\\ &\qquad n(\omega)\delta(\boldsymbol{\kappa}-\boldsymbol{\tau}_{\mathrm{m}})\delta(\omega+\omega^{\mathrm{AFM}})\Big].\end{aligned}\tag{2.22}$$

2.1.3 The Triple Axis Spectrometer

A powerful instrument in elastic and inelastic neutron scattering is the Triple Axis Spectrometer (TAS), pioneered by B. N. Brockhouse [43].

High energy neutrons are produced either by fission in a reactor or by spallation of heavy nuclei by a particle accelerator. The neutron energy may be reduced by allowing the neutrons to pass through liquid hydrogen or deuterium at 25 K, giving a Maxwell distribution of neutron energies. Guide tubes allow the neutrons to travel from here to the individual instruments.

In a TAS a monochromator crystal with a well defined lattice spacing and thus well defined reciprocal lattice vector $\boldsymbol{\tau}_{\mathrm{M}}$ is oriented at an angle θ_{M} to the incoming neutron beam, see Figure 2.2. From the Bragg condition $\boldsymbol{\tau}_{\mathrm{M}}=2\mathbf{k}\sin\theta_{\mathrm{M}}$ neutrons will leave the monochromator with a defined wave vector $\mathbf{k}_{\mathrm{i}}$ and thus energy E_{i} at the angle $2\theta_{\mathrm{M}}$ to the incoming neutron beam. After the

monochromator, a monitor measures the neutron flux onto a sample placed in the neutron path. Some neutrons are scattered by the sample. A second crystal with a well defined reciprocal lattice vector $\boldsymbol{\tau}_\mathrm{A}$ is placed at an angle 2θ from the direction of the neutrons incident on the sample. This analyser crystal again scatters neutrons according to $\boldsymbol{\tau}_\mathrm{A} = 2\mathbf{k}\sin\theta_\mathrm{A}$ making it possible to count the number of neutrons leaving the sample with wave vector $\mathbf{k}_\mathrm{f}$ and energy E_f in a detector at an angle $2\theta_\mathrm{A}$ to the direction of the neutron beam incident on the analyser. From momentum and energy conservation the sample scattering vector is $\boldsymbol{\kappa} = \mathbf{k}_\mathrm{i} - \mathbf{k}_\mathrm{f}$ and the energy loss in the sample is $\hbar\omega = E_\mathrm{i} - E_\mathrm{f}$. Rotating the sample appropriately, any combination of $\boldsymbol{\kappa}$ and ω allowed by the spectrometer geometry can be probed.

It is possible to scan energy transfer at a constant momentum transfer or to scan momentum transfer at a constant energy transfer. Normally, it is convenient to keep k_f fixed and vary k_i in order to scatter into the same solid angle Ω_f throughout the experiment. Also, the efficiency of the monitor will generally go as $1/k_\mathrm{i}$ so the counting time is proportional to k_i and the dependence of the cross section on $k_\mathrm{f}/k_\mathrm{i}$ as stated in Equation (2.5) is compensated.

The monochromator and analyser crystals are made with a mosaicity (often about 20'–80'). Introducing a mosaicity increases the integrated reflectivity of the crystals, allowing more neutrons to be reflected, but with a poorer resolution. Angular collimators can be placed on any of the three axes of the instruments to define the spread in wave vector allowed to pass. The resolution of the instrument is determined by the mosaicity, incoming energy and collimation scheme. Thus at a chosen incoming energy the resolution may be controlled by varying the collimation, keeping in mind that the tighter the collimation is, the less intensity is transmitted.

Due to the $n\lambda$ term in the Bragg equation (2.11) neutrons with wavelengths that are fractions ($\lambda/2$, $\lambda/3$, ...) of λ are also reflected. These have a higher energy and may contaminate the measured signal. A filter may be placed between the sample and the analyser to remove these higher order neutrons. The filter has a cutoff energy, efficiently transmitting neutrons with a lower energy and stopping neutrons with a higher energy. The filters used for the work presented here are Be and BeO that have cutoff energies of ≈ 5.2 meV and ≈ 3.8 meV respectively.

The drawback of the TAS is that only one point of $\boldsymbol{\kappa}$ and ω is measured at a time. In a neutron powder diffractometer the analyser is substituted by a large bank of detectors, sacrificing the energy resolution at the cost of being able to measure a large range of k_f simultaneously. An example of this kind of instrument is DMC at the Paul Scherrer Institute in Villigen, Switzerland [51].

A different approach is the Time Of Flight (TOF) spectrometer where short pulses of monochromatic neutrons are scattered by the sample to a large detector bank. Energy analysis is done by measuring the time of flight of the neutrons from the sample to the detector. The drawbacks of this type of spectrometer is lack of collimation and often a poor κ resolution but most importantly the requirement of short neutron pulses with a long delay between them, reducing the effective flux.

A way of enhancing the TAS with multiple detectors while maintaining the versatility was proposed in 1993 as the ReInvented Triple Axis (RITA) spectrometer [52]. Here multiple analysers and a large position sensitive detector make it possible to measure several points of $\boldsymbol{\kappa}$ and ω simultaneously with the

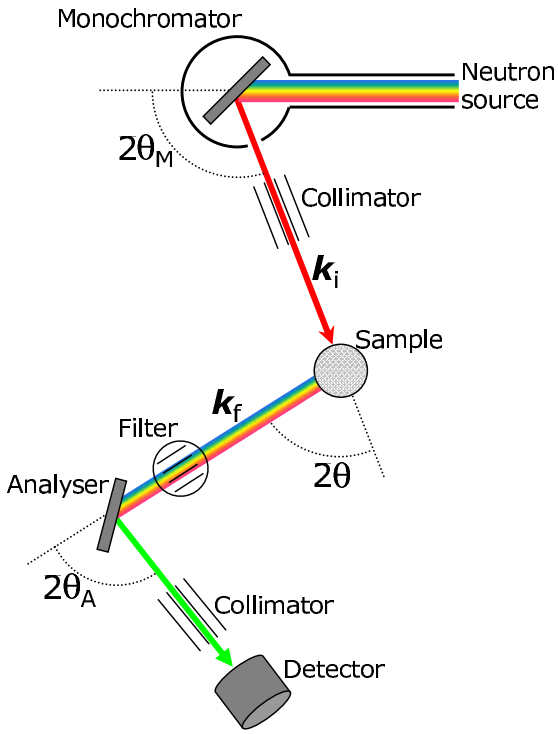

Figure 2.2: Traditional triple axis spectrometer showing the positions of the monochromator, sample, analyser and detector, as well as the three important scattering angles $2\theta_{\mathrm{M}}$, 2θ and $2\theta_{\mathrm{A}}$.

resolution control of TAS. This instrument (RITA-II) and the different configurations available will be presented in Chapter 5.

2.2 Mössbauer Spectroscopy

Mössbauer Spectroscopy relies on the recoil free resonant emission and absorbtion of γ-radiation. The effect was discovered in 1957 by R. L. Mössbauer [53] who received the Nobel prize for it in 1961 [54].

The Mössbauer effect has been demonstrated in more than 100 isotopes in many different elements since its discovery. In 1959 the Mössbauer effect was reported in ^{57}Fe [55,56] and this has remained the most frequently used isotope since then. The discussion is limited to this isotope as it is the only one used in the work presented here.

^{57}Co decays with a half life time of 270 days into an excited state of ^{57}Fe. The excited ^{57}Fe state with nuclear spin $I_{\mathrm{e}} = \frac{3}{2}$ will decay with a half-life time of $\tau_{\frac{1}{2}} = 98$ ns to the ground state with the spin $I_{\mathrm{g}} = \frac{1}{2}$, creating a γ-ray with an energy of 14.4 keV. This γ-ray may then be resonantly absorbed by another nucleus as illustrated in Figure 2.3. If the nuclei are isolated conservation of momentum will impart a recoil energy to the emitting nucleus reducing the energy of the γ-ray. Also, the absorbing nucleus will require a recoil energy in addition to the excitation energy, in order to be excited. In this way the

energy of a γ-ray emitted during a decay of an iron nucleus will not be enough to excite another iron nucleus. However, if the emitting and absorbing nuclei are in crystal lattices the entire lattice may absorb the recoil, making the recoil energy very small. The probability of this occurring is proportional to the f-factor given by

$$f = \exp\left(-\frac{E_\gamma^2}{\hbar^2 c^2}\langle u^2\rangle\right) \tag{2.23}$$

where E_γ is the γ-ray energy, c is the velocity of light. $\langle u^2\rangle$ is the mean square vibrational amplitude of atoms in the crystal, which increases as the temperature increases. The f-factor is equvalent to the Debye-Waller factor from the neutron scattering cross sections. The requirements for a large f-factor is a low E_γ and a small thermal vibration of the nuclei. ^{57}Fe in solid materials fulfills these conditions.

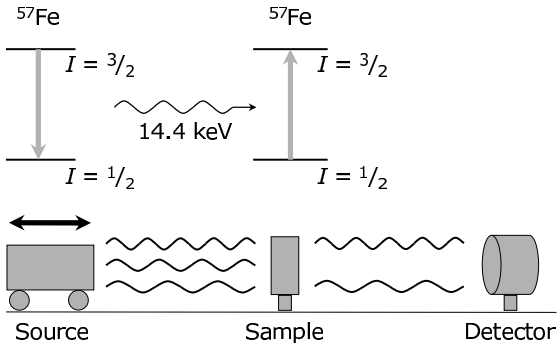

Figure 2.3: Experimental setup of a Mössbauer spectroscopy experiment.

If a source of emitting nuclei is moved at a velocity v compared to an absorber consisting of nuclei in environments identical to the emitting nuclei, the energy of the photons will be Doppler shifted to

$$E(v) = E_\gamma\left(1 + \frac{v}{c}\right). \tag{2.24}$$

Thus the resonance is destroyed everywhere except when $v = 0$. This is not entirely true as the emitted photons have a line width, $\Gamma = \frac{\hbar}{\tau_n}$, where $\tau_n = 141$ ns is the mean life time of the excited state, calculated by $\tau_{\frac{1}{2}} = \tau_n \ln 2$. Thus the velocity spectrum will display a Lorentzian of half width

$$v_{\frac{1}{2}} = 2c\frac{\Gamma}{E_\gamma} = 0.19 \text{ mm/s}. \tag{2.25}$$

The factor of 2 is due to the combined broadening from both the emitting and absorbing nuclei. Oscillating the source makes it possible to measure an energy spectrum.

Three major interactions affect the hyperfine energy levels of the nucleus: the electric monopole interaction, the magnetic dipole interaction and the electric quadrupole interaction. These are all extremely small compared to the energy levels of the nucleus (about 12 orders of magnitude), but the extremely high energy resolution of the Mössbauer effect enables observation of them.

2.2.1 The electric monopole interaction

Owing to the non-zero volume of the nucleus and non-zero density of s-electrons at the nucleus there will be an overlap between the two, giving a Coulomb interaction. The volume of the nucleus is different in its excited and its ground state and the density of s-electrons depends on the chemical environment of the atom. A difference in the electron density at the nucleus in the source, $|\psi_{\mathrm{s}}(0)|^2$ and the absorber, $|\psi_{\mathrm{a}}(0)|^2$ will give a shift in resonance energy of

$$\delta \propto (R_{\mathrm{e}}^2 - R_{\mathrm{g}}^2)\left(|\psi_{\mathrm{a}}(0)|^2 - |\psi_{\mathrm{s}}(0)|^2\right) \tag{2.26}$$

where R_{g} and R_{e} are nuclear radii of the ground and excited states, respectively. The interaction results in a shift in energy of the spectrum, known as the isomer shift, see Figure 2.4(a). As this shift is relative, it is generally calibrated at room temperature to zero with an iron foil absorber 12.5 μm thick.

The isomer shift is useful for studying the valence of iron as the different filling of the $3d$ shell in Fe^{2+} and Fe^{3+} will affect the s-electron density at the nucleus differently.

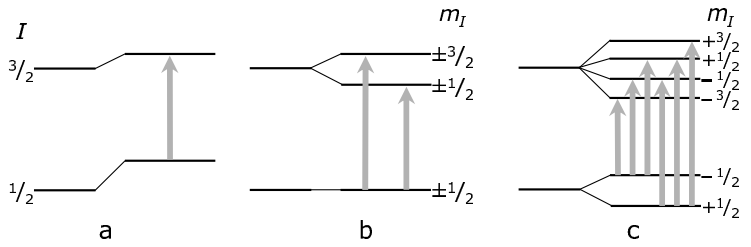

Figure 2.4: The three major interactions affecting the hyperfine energy levels of the nucleus. (a) The isomer shift. (b) The quadrupole splitting. (c) The magnetic hyperfine field splitting.

2.2.2 The electric quadrupole interaction

The ^{57}Fe nucleus in the excited state has a non spherical charge distribution. As this is only the case for nuclei with spin $I > \frac{1}{2}$ the charge distribution in the ground state will be spherical. The charges from other atoms in the structure will give rise to an electric field gradient at the nucleus. If there is an asymmetric charge distribution around the nucleus, this field gradient will be asymmetric. The interaction of the field gradient with the nuclear charge distribution is known as the quadrupole interaction. It will lift the degeneracy on the $I = \frac{3}{2}$ state splitting it into $m_I = \pm\frac{3}{2}$ and $m_I = \pm\frac{1}{2}$ states, where m_I is the magnetic spin quantum number, $m_I = I, I-1, ..., -I$. The resonance is split into a doublet, as illustrated in Figure 2.4(b). This splitting, known as the quadrupole splitting, has a magnitude of ΔE_{Q} depending on the size of the field gradient at the nucleus.

If the crystal structure is cubic, the field gradients from the surrounding atoms cancel out and there will be no splitting.

2.2.3 The magnetic dipole interaction

The interaction between the magnetic dipole moment of the nucleus and a magnetic field will give Zeeman splitting of the resonance energy, known as hyperfine field splitting. The energy levels in a magnetic field, B, are given by $E_{\mathrm{M}} = -g_{\mathrm{N}}\mu_{\mathrm{N}}Bm_I$. Here, g_{N} is the nuclear g-factor which is different for the ground and excited states ($g_{\mathrm{g}} = 0.181208$ and $g_{\mathrm{e}} = -0.10355$).

Thus the ground state with $I = \frac{1}{2}$ splits into two levels and the excited state splits into four levels, due to the four possible values of m_I. Of the eight combinations only six are allowed by the selection rules due to conservation of angular momentum, $|\Delta m_I| \leq 1$ as the photon has a spin of one. This is illustrated in Figure 2.4(c). Thus the resonance line of iron will split into a sextet in the presence of a magnetic field, with the splitting proportional to this field.

The field experienced by the nucleus, the hyperfine field, is composed of several terms, dominated in ^{57}Fe by the Fermi contact term. The Fermi contact term is due to the unpaired electrons in the d-shell that polarise s-electrons whose wave functions overlap the nucleus, thus polarising the nucleus. It should be kept in mind that the Fermi contact term is oriented opposite to the sublattice magnetisation. The hyperfine fields in both NiO and hematite are ~ 54 T at low temperature.

In the presence of an applied field, B_{appl}, the field the nucleus experiences is the vector sum of the hyperfine field and the applied field, $\mathbf{B}_{\mathrm{tot}} = \mathbf{B}_{\mathrm{hf}} + \mathbf{B}_{\mathrm{appl}}$. It can be shown that the relative intensity of the six resonance lines depends on the angle between the total field and the propagation direction of the γ-rays, θ, due to polarisation and conservation of angular momentum. The relative intensity ratios are [34]

$$3(1+\cos^2\theta) : 4\sin^2\theta : 1+\cos^2\theta : 1+\cos^2\theta : 4\sin^2\theta : 3(1+\cos^2\theta). \quad (2.27)$$

or

$$3 : p : 1 : 1 : p : 3 \quad \text{where} \quad p = \frac{4\sin^2\theta}{2-\sin^2\theta}. \quad (2.28)$$

This is a useful relation for determining the orientation of the hyperfine field and thus magnetisation within a sample, with respect to the radiation direction.

2.2.4 Relaxation

In order to measure the hyperfine field splitting, the hyperfine field at the nucleus must be constant for long enough time for the Zeeman splitting to occur. A characteristic time for this is the time of one Larmor precession, τ_{L}, of the magnetic moment of the nucleus in the presence of the hyperfine field. In a characteristic hyperfine field of 54 T the characteristic time is $\tau_{\mathrm{L}} \approx 10^{-9}$ s [57]. Note that $\tau_{\mathrm{L}} \ll \tau_{\mathrm{n}}$ such that there is ample time for the hyperfine splitting to occur during the lifetime of the excited state.

If there is a fluctuation of the hyperfine field with a time scale τ_{r} induced by a flipping or relaxation of the electron spins, three possible regimes are possible. When $\tau_{\mathrm{r}} \gg \tau_{\mathrm{L}}$ the hyperfine field is constant for long enough for Zeeman splitting to occur and the spectrum will display a hyperfine field splitting. If $\tau_{\mathrm{r}} \ll \tau_{\mathrm{L}}$ the field flips fast and only a time averaged hyperfine field is observed by the nucleus [58]. Thus, a spectrum will not display hyperfine field splitting,

but just a singlet or doublet depending on the quadrupole interaction. The case where $\tau_r \approx \tau_L$ is a complex regime, with spectra containing hyperfine field split spectra with broad line shapes.

In magnetic nanoparticles the main contribution to relaxation in magnetic nanoparticles is superparamagnetism, where the magnetisation spontaneously flips due to thermal agitation, as described by Equation (1.1). Here the relaxation time, τ_r, is strongly temperature and particle volume dependent.

2.2.5 Mössbauer Spectroscopy Instruments

The Mössbauer spectrometers used in the present work are situated at the Department of Physics at the Technical University of Denmark. The sources of ^{57}Co in a rhodium matrix can be oscillated sinusoidally in different velocity ranges. Most of the spectra presented in the papers were recorded with velocity range of ± 12.5 mms^{-1}. The sample is placed in a thin perspex container perpendicular to the beam. In the spectra recorded in an applied field, this was applied parallel to the radiation direction.

2.3 X-Ray diffraction

X-ray diffraction (XRD) was pioneered by W. and L. Bragg who were awarded the Nobel Prize in 1915 [59]. They formulated the Bragg condition in Equation (2.11), $2d \sin\theta = n\lambda$.

As x-rays interact mainly with electrons the scattering intensity will contain an angle dependent form factor equivalent to the one found for the magnetic scattering of neutrons. The scattered intensity may be written as

$$I(\theta) \propto z \left| \sum_j f_j e^{i\boldsymbol{\tau}\cdot\mathbf{d}_j} \right|^2 e^{-2W} \frac{1+\cos^2 2\theta}{\sin\theta \sin 2\theta}. \tag{2.29}$$

Here z is the multiplicity of the scattering planes given by the crystalline symmetry, f_j is the form factor of the j'th atom in the unit cell, located at $\mathbf{d}_j$, $\boldsymbol{\tau}$ is a reciprocal lattice vector and e^{-2W} is again the Debye-Waller factor discussed in Section 2.1.1. The denominator in the fraction is the factor introduced due to the sample being a powder of randomly oriented particles, as discussed in Section 2.1.1. The numerator, known as the polarisation factor, enters when the x-rays are unpolarised which is the case in the present work. The atomic form factor is proportional to the atomic number, Z, such that heavy elements scatter more than light elements.

2.3.1 Rietveld refinement

From knowledge of the crystal structure, a powder diffraction pattern may be calculated using Equation (2.29). The positions and relative intensities of the reflections in a measured diffraction pattern may be compared to such a simulated diffraction pattern to ensure that the crystal structure of the sample is what it is assumed to be. As in neutron diffraction the broadening of the reflections is due to the finite size broadening described by Equation (2.14). Also, lattice strain may contribute to the broadening. This contribution will be ignored in

this study due to the severe finite size broadening. Thus, measuring the width of each reflection allows an estimate of the particle size along the direction perpendicular to the scattering planes to be made. However, measuring the position, relative intensity and shape of each of the peaks can be tedious, as there may be many peaks. The Rietveld method [60, 61] allows the measured pattern to be fitted by a calculated pattern where the peak profile and crystallographical parameters are free. The method works by minimising [62]

$$\chi^2 = \sum_i w_i \left(Y_i^{\mathrm{o}} - Y_i^{\mathrm{c}}\right)^2 \tag{2.30}$$

where Y_i^{o} and Y_i^{c} are the observed and calculated intensities of the data point i in the pattern and w_i is the weight assigned to data point i, usually the square root of Y_i^{o}. The calculated intensity is given by

$$Y_i^{\mathrm{c}} = Y_i^{\mathrm{b}} + \sum_k G_{ik} I_k \tag{2.31}$$

where Y_i^{b} is the background value, G_{ik} is the peak profile and I_k is intensity of Bragg peak k, calculated by Equation (2.29). The calculated spectrum must be convoluted by the instrumental resolution before comparison. The simultaneous fitting of the peak profiles of all the reflections allows a determination of the shape of the particle from the estimated size of the particles in different directions. Several software packages are available for Rietveld refinement, the one used here was FullProf 2000 [62, 63].

2.3.2 XRD Instrument

All XRD patterns shown here were measured on a Philips PW 1820 diffractometer at the Department of Physics at the Technical University of Denmark. The patterns were measured using the $K\alpha$ radiation from a rotating Cu anode. The radiation consists of two lines, $K\alpha_1$ with a wavelength of 1.54056 Å and $K\alpha_2$ with a wavelength of 1.54439 Å and half the intensity. Both lines are included in the Rietveld refinement, but the finite size broadening of the nanoparticle Bragg reflections makes the contributions from them indistinguishable in diffraction patterns. The resolution of the instrument, measured as the broadening of a perfectly sharp Bragg reflection, is 0.14°.

2.4 Vibrating Sample Magnetometry

The vibrating sample magnetometer or Foner magnetometer was developed by S. Foner in the 1950'ies [38, 64, 65].

When a material is placed in a uniform magnetic field a magnetic moment will be induced in the material. The moment will be proportional to the product of the applied field and the susceptibility of the sample. From Faraday's law of induction, moving the sample will change the magnetic flux in a stationary coil close to the sample inducing a voltage, as illustrated in Figure 2.5. If the sample is oscillated sinusoidally the induced voltage will be proportional to the amplitude and frequency of the oscillation and also to the moment of the sample. In the sinusoidal oscillation the amplitude and frequency of the oscillation is kept constant in order to measure the moment.

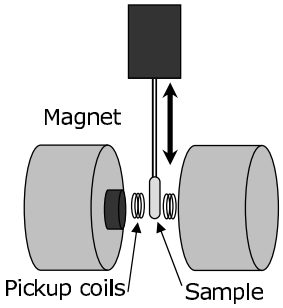

Figure 2.5: Principle of a Vibrating Sample Magnetometer.

2.4.1 VSM Instrument

The VSM used in the present work is a Lakeshore 7407 VSM, situated at the Department of Micro and Nanotechnology at the Technical University of Denmark. This is capable of a field of up to 1.6 T. To limit the noise and make measuring very small moments possible a lock-in amplifier is used, so that only signals with a periodicity the same as the sample oscillation of 85 Hz are measured.

2.5 Transmission Electron Microscopy

The pioneering work in developing a Transmission Electron Microscope (TEM) was carried out in the 1930'ies by E. Ruska and M. Knoll [66]. E. Ruska received the 1986 Nobel prize in physics for this work.

In optical transmission microscopy an image, created by transmitting light through a sample, is magnified by glass lenses. However, due to the Rayleigh criterion the maximum possible resolution in such a microscope is 0.6 times the wavelength of the light [67]. As visible light has a wavelength in the range 300-500 nm, this is a serious limitation in nanoscience.

A TEM is essentially analogous to the transmission light microscopy, except that it uses an accelerated electron beam instead of light. The motivation for the development of the TEM is the very short de Broglie wavelength of electrons. An electron accelerated to 300 keV has a wavelength of 1.97 pm, which is far below any lattice distances, and thus would promise an eminent resolution. However, due to inevitable imperfections in the magnifying lenses the resolution will be about a factor of 50 worse.

Whereas light microscopes rely on glass lenses that can be polished to near perfection in focusing the rays from all parts of the lens to a single point, electron microscopes use electromagnetic lenses where this is not the case. The two main imperfections present are the spherical and chromatic abberations. Spherical abberation covers the fact that electrons from the centre part of an imperfect lens will not be focused to the same point as electrons from the outer part of the lens, thus smearing the image. Chromatic abberation covers the fact that the focus point of a lens depends of the velocity of the electrons passing through it. Thus, any instability in the acceleration voltage will blur the image. Recently, there has been a drive to develop abberation correctors and monochromators for TEMs improving the resolution to about 0.7 Å [68]

2.5.1 Imaging in a TEM

When a parallel coherent electron beam interacts with a crystalline sample, the beam will be diffracted according to Braggs law. The diffraction angles will be very small as the lattice plane spacings are much larger than the electron wavelength. The direct and diffracted electron beams pass through a lens, known as the objective lens. The lens will create an image plane, imaging point to point from the sample to a magnified image of the sample as illustrated in Figure 2.6(a). There will also be a back-focal plane where all beams scattered to the same angle by the sample are focused to the same point, thus a diffraction pattern. Intermediate lenses determine whether the image or the diffraction pattern is focussed on a CCD camera at the bottom of the microscope. Inserting an aperture (objective aperture) in the back-focal plane, some of the diffracted beams can be removed from the magnified image. This creates so-called diffraction contrast in the image, as diffracting parts of the sample will appear dark, as shown in Figure 2.6(b). Alternatively, the aperture may be moved to let only the diffracted beams pass. This results in images where diffracting parts of the sample appear bright and non-diffracting parts appear dark, so called dark-field imaging, see Figure 2.6(c).

High resolution images of thin samples are created by phase contrast. The phase of electrons is changed be the potential of the atoms in the sample. After the sample, interference between the electron waves that have passed through different parts of the sample will create an image. Atomic resolution can routinely be obtained in this way. The resolution of such images is limited by the abberations described above.

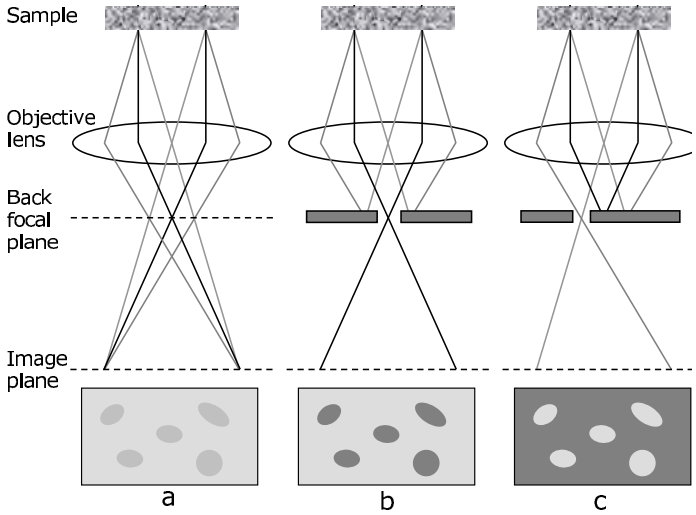

Figure 2.6: The principle of the main optics in a transmission electron microscope. Below the imaging plane there are a range of lenses used to create an image in the CCD camera. (a) Shows the optics. (b) Inserting an aperture in the back focal plane increases the image contrast. (c) Moving the aperture off-centre reverses the contrast, as indicated in the schematic images shown below.

2.5.2 TEM Instrument

The microscope used in the present work is a JEOL 3000F, situated at Risø National Laboratory. The microscope operates at an acceleration voltage of 300 keV and has a point resolution of 0.16 nm. The microscope is equipped with a 16 Mpix CCD camera recording images digitally, which is useful for post experiment image analysis. A fine copper grid coated with a thin carbon mesh is either dipped in a dry powder of nanoparticles, or the nanoparticles are suspended in water and a droplet is applied to the grid and dried.

2.6 Comparison of the experimental techniques

The five experimental techniques presented here are each useful for the study of antiferromagnetic nanoparticles in different ways. XRD is an excellent technique for determining the structure of the material in the sample and also for measuring the size and in some cases the shape of the particles. As the results obtained are volume averaged and a determination of the width of particle size distributions is not readily obtainable, TEM compliments the method well. TEM is the only one of the methods where single particles may be studied and measured. Thus the size, shape and crystal structure of individual particles can be determined and compared with the average values obtained by XRD. Another advantage is that XRD and often also TEM are available in most laboratories.

One of the clear advantages of neutron scattering over XRD is the magnetic moment of the neutron giving rise to magnetic scattering. This can be used to study magnetic ordering in nanoparticles, not possible by XRD. The other advantageous feature of neutron scattering is the possibility of studying inelastic properties of the sample. Neutrons with wavelengths of the order of magnitude of lattice spacings have energies in the range of spin waves and lattice vibrations, making it possible to probe these. Neutrons with a wavelength of $\lambda = 4$ Å have an energy of ~ 5 meV. The equivalent energy of a $\lambda = 4$ Å photon is ~ 3 keV, which is too high to study lattice vibrations, except at synchrotron sources with a very high energy resolution.

The main drawback of neutron scattering is that it is only available at a limited number of facilities around the world. With respect to nanoparticles a drawback of neutron scattering is the large incoherent scattering cross section from the hydrogen in water adsorbed to the surface of the particles giving rise to a large undesirable signal. In XRD the cross section depends on the atomic number, so hydrogen only scatters negligibly. Also, the weak interaction of the neutron with matter means that large amounts of sample are required, especially for inelastic scattering, where the scattering cross section is very small. In some cases however this may be an advantage as measurement of the entire sample and not just the surface is ensured.

As described above the timescale of relaxation probed by Mössbauer spectroscopy is $\sim 10^{-9}$ s. A very broad range of different neutron scattering instruments are available covering a range of energy resolutions of over 8 orders of magnitude. These allow dynamics to be studied with timescales from $\sim 10^{-8}$ s on spin echo instruments to $\sim 10^{-16}$ s on high energy instruments.

Inelastic neutron scattering can probe the energy and wave vector of spin waves. At low temperatures, due to small thermal populations of the excita-

tions, the signals from nanoparticles have a low intensity and may be difficult to fit reliably. Mössbauer spectroscopy, which is almost elastic, measures the reduction of the magnetisation due to excitation of spin waves. This can be done very accurately even at low temperatures.

Chapter 3

Antiferromagnetic nanoparticles

The aim of this chapter is to give a description of the nanoparticles studied in the appended papers. Nanoparticles of three different antiferromagnetic materials have been studied, hematite (α-Fe_2O_3), nickel oxide (NiO) and goethite (α-FeOOH). The main emphasis is on the nanoparticles of nickel oxide which are studied in papers VIII-XI. Nanoparticles of hematite with various sizes have been the main focus of the preceding studies of the nanomagnetism group. A description of the hematite particles used in the study of the interaction effects in Papers IV, VI and VII is presented. Although not yet published, some results of studies of goethite nanoparticles, with respect to the interparticle interactions, are given as these are interesting in the context of the other particles.

Also, the magnetic anisotropy energy of nanoparticles and bulk samples of NiO and hematite are discussed and compared.

3.1 Nickel oxide

Nickel oxide, NiO, also known as bunsenite after R. Bunsen, was discovered in 1858 and is only found pure in nature in a few locations around the world. The bulk mineral has a deep green colour while nanoparticles of NiO are black.

3.1.1 Bulk structure

Bulk NiO has a face centred cubic NaCl structure with the space group $Fm3m$, and a lattice parameter of $a = 4.177(6)$ Å [69]. This cubic structure is illustrated in Figure 3.1(a).

NiO is a type-II antiferromagnet with an antiferromagnetic ordering vector of $\left(\frac{1}{2}\frac{1}{2}\frac{1}{2}\right)$, i.e. along the space diagonal of the unit cube and the spins confined to the (111) plane. Below the Néel temperature of 523 K there is a slight contraction of the cubic structure along the [111] direction, known as exchange striction [70]. However, this contraction is less than 0.3% in bulk NiO and it will not be considered.

As it will be shown below, it is often useful to transform the cubic structure to a pseudo-hexagonal structure, with the space group $R\overline{3}m$ and $a_{\mathrm{h}} = a/\sqrt{2}$

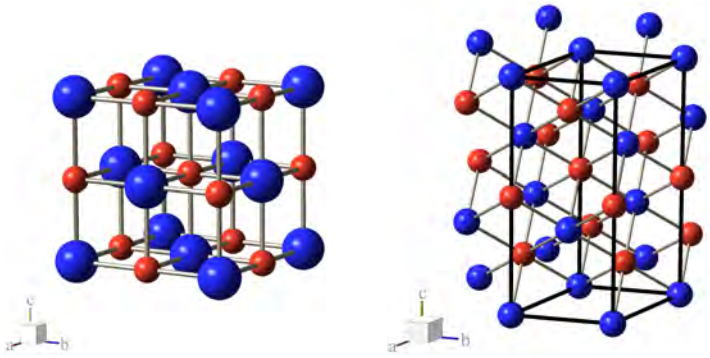

(a) (b)

Figure 3.1: The structure of NiO. Ni is shown as blue and oxygen as red. (a) Cubic crystal structure. (b) Pseudo-hexagonal crystal structure. The black wire frame indicates the unit cell.

and $c_h = a\sqrt{3}$ giving the structure illustrated in Figure 3.1(b). This was done in Ref. [71], where the lattice parameters $a_h = 2.9549(5)$ Å and $c_h = 7.2320(4)$ Å were measured. As a reference for the nanoparticle measurements, a sample of commercially obtained bulk NiO powder was measured. Rietveld refinement yielded lattice parameters of $a_h = 2.957$ Å and $c_h = 7.234$ Å, in reasonable correspondence with the literature values above. Although the pseudo-hexagonal structure is generally used for fitting XRD data in the following, the normal cubic indexing will be used throughout, to avoid confusion.

3.1.2 Structure and morphology of NiO nanoparticles

Preparation of the samples

Several methods of preparing nanoparticles of NiO are available such as microemulsion techniques [72], aqueous droplets in a flame reactor [73] or thermal decomposition of various precursors in solution [74,75]. The method chosen for preparation of the samples in the present work involves a thermal decomposition of nanoparticles of $Ni(OH)_2$ in atmospheric air [29,76–81]. The advantage of this method is that it is possible to reproducibly prepare large amounts of samples of fairly uniform particles. This is important for inelastic neutron scattering, where large amounts of sample are required. Also, the preparation method has been utilised in several publications, making comparison of results possible.

$Ni(OH)_2$ is precipitated chemically by mixing aqueous solutions of NaOH and $Ni(NO_3)_2{\cdot}6H_2O$. The resulting pale green slurry is washed and subsequently freeze dried, giving a fine pale green powder. Rietveld refinement of an x-ray diffraction pattern of this powder shows that it is $Ni(OH)_2$ with the trigonal space group $P\overline{3}m1$ and unit cell parameters $a = 3.129$ Å and $c = 4.778$ Å. As seen in Figure 3.2, no other phases are found in the XRD pattern, . It is observed that some of the Bragg reflections are broad and others are narrow. Using the Rietveld method described in Section 2.3.1 the particles have been determined to be plate shaped, with the [001] direction perpendicular to the plate face. The fit yields an estimated average diameter of 7.4 nm and an estimated average thickness of 1.5 nm.

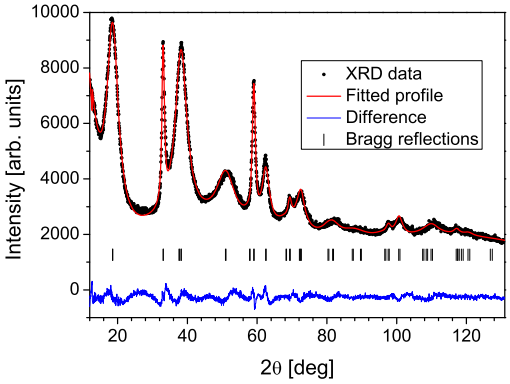

Figure 3.2: XRD pattern of $Ni(OH)_2$ showing broad and narrow peaks indicating non-spherical particles.

The $Ni(OH)_2$ is transformed to NiO by heating the powder in atmospheric air for 3 hours at various temperatures. At heating temperatures above 250°C the XRD patterns are found to contain only NiO and no other phases, as shown for particles heated at 300°C in Figure 3.3.

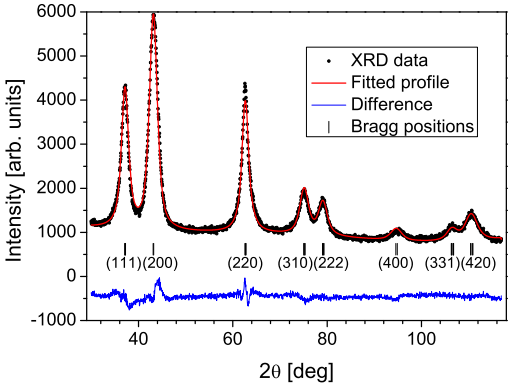

Figure 3.3: XRD pattern of NiO obtained by transforming $Ni(OH)_2$ at 300°C. Rietveld refined using the pseudo-hexagonal unit-cell.

TEM studies

The particles heated at 300°C were studied by TEM and found to be plate shaped. In the TEM images a projection of the particles is observed. When the particles are oriented with the plate normal along the electron beam direction (face-on), the projected thickness of the particles is small and thus the contrast in images is low, see Figure 3.4(a). If the particles are oriented with the electron beam parallel to the plate face (edge-on) the projected thickness and thus image contrast is much higher, see Figure 3.4(a). The plate shaped particles viewed edge-on are observed as dark rods with the length of the rods being the diameters of the particles and the thicknesses being the plate thicknesses. Measuring 66 particles gives an average thickness of 2.3±0.4 nm and an average diameter

of 13±3 nm, where the uncertainties are the standard deviations. The high resolution TEM image of one of the particles viewed edge-on shown in Figure 3.4(b) shows that the plate faces are {111} planes, by Fourier transformation of the image, as shown in the inset.

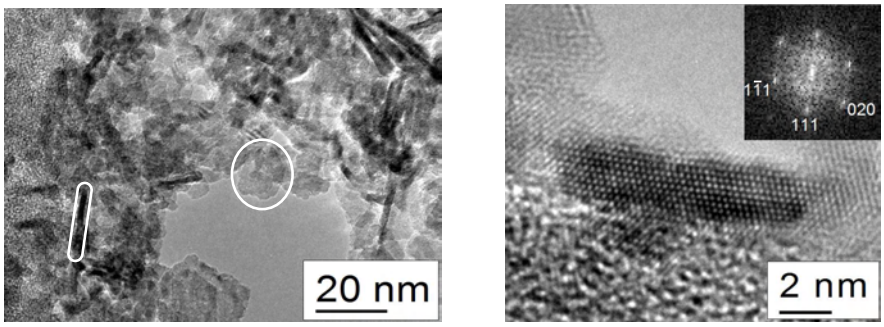

(a) (b)

Figure 3.4: TEM images of the NiO sample prepared at 300°. (a) Image showing a collection of NiO nanoparticles, the indicated particle to the left is viewed edge-on and the one to the right is viewed face-on. (b) High Resolution image of a plate-shaped NiO nanoparticle viewed edge-on. The inset is a Fourier transform of the image indicating that a {111} plane is parallel to the plate face.

XRD studies

To enable fitting of the XRD patterns with a plate shaped particle model by the Rietveld method, the pseudo-hexagonal structure must be used. In this way the (111) reflection from the planes parallel to the plate face becomes the $(003)_{\mathrm{h}}$ reflection which can be distinguished from the other three cubic {111} reflections that are not parallel to the plate face as these become $\{101\}_{\mathrm{h}}$ reflections. The structure of nanoscale NiO is the same as in bulk, albeit with an increase of the lattice parameters as the particle sizes decrease [69]. In the particles heated at 300°C, see Figure 3.3, lattice parameters of $a = 2.966$ Å and $c = 7.259$ Å were measured.

Table 3.1 gives the estimated dimensions of the particles prepared at different temperatures obtained from Rietveld refinement of the XRD patterns with the FullProf software [63] discussed in Section 2.3.1. No measure of the uncertainty is offered by the software. For comparison with other publications the particle diameters found by fitting assuming spherical particle shape are also given, as this is the conventional way of fitting found in the literature. It is seen that the particle volumes are significantly underestimated by the spherical fitting. Figure 3.5 shows an XRD pattern of the sample prepared at 300°C, fitted assuming spherical particles and a cubic unit-cell. The difference pattern is observed to vary more than in Figure 3.3.

The preparation of particles at a given temperature has been found to be fairly reproducible. The particle thickness is constant, but the the diameter may vary ∼10-15% from preparation to preparation. This may be due to differences in the crucibles used for heating or exact heating conditions such as temperature and position of the crucibles in oven.

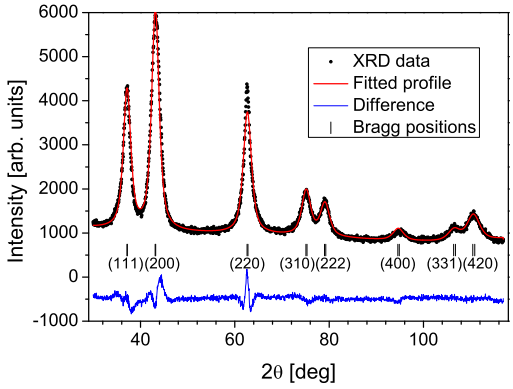

Figure 3.5: XRD pattern of NiO obtained by transforming $Ni(OH)_2$ at 300°C. Rietveld refined assuming a cubic unit-cell and spherical particles.

	Plate model			Spherical model	
Temperature	Thickness	Diameter	Volume	Diameter	Volume
[°C]	[nm]	[nm]	[nm^3]	[nm]	[nm^3]
250	1.6	7.2	65	2.6	9.2
300	2.3	7.9	113	3.6	24
350	3.7	11.0	352	5.4	82
600	12	38	13600	17	2572

Table 3.1: Sizes of the NiO nanoparticles obtained by heating $Ni(OH)_2$ at the indicated temperatures, estimated from a profile refinement of XRD patterns. Results from fitting with both a plate shaped model and a spherical particle model are given.

The dimensions of the particles transformed at the lowest temperature, where full transformation occurs, are similar to those of the $Ni(OH)_2$ precursor. When the heating temperature is increased, the particle sizes increase. This may be due to increased activity and surface diffusion of the atoms at elevated temperatures. The increase of the average particle size observed in the XRD data could be thought to be due to some of the particles melting together. However, measurements of the particle thicknesses in TEM do not indicate a broad size distribution as would be expected in this case.

The sample prepared at 300°C was chosen for further study. These particles will be the main focus of the NiO study throughout this work and are referred to as the as-prepared sample.

Good agreement is found for the plate thickness when comparing the particle dimensions obtained by XRD and TEM. Indeed, during the iterations of a Rietveld refinement the fitted value of the plate thickness is a stable parameter, not varying much. The plate diameter however, is very sensitive to the parameters in the Rietveld refinement, and poorer agreement is found between the two techniques. In Figure 3.3 the fit to the sharpest part of the peak from the {220} reflections (at $2\theta \approx 63°$) is not perfect. This peak is the sum of 6 reflections, 3 reflections from planes perpendicular to the plate face (-202), (-220) and (0-22) giving a correlation length of 7.9 nm and three reflections from planes at an angle of 35.3° to the plate face (202), (022) and (220) giving a correlation length of

2.7 nm. It may be difficult for the fitting routine to distinguish the contributions from these as the difference in correlation length is large, especially if there is a distribution of particle diameters giving a further smearing of the reflection. Thus, the plate diameters may be underestimated by XRD.

Neutron diffraction

Neutron diffraction was performed in 2002 at the DMC powder diffractometer at the Paul Scherrer Institute in Villigen, Switzerland by S.N. Klausen, L. Theil Kuhn and C. Frandsen. Diffraction data from the as-prepared NiO nanoparticle sample measured at 13 K is shown in Figure 3.6. Due to the long wavelength of the incoming neutrons ($\lambda = 2.54$ Å) only a small number of reflections are visible in the diffraction pattern, so a profile refinement was not performed. Instead the $\left(\frac{1}{2}\frac{1}{2}\frac{1}{2}\right)$ peak was fitted with a Gaussian line shape. Subtracting the instrumental broadening of the reflection the width is consistent with a magnetic correlation length of 3.1(4) nm.

As it will be discussed in Section 4.2.1 only the $\left(\frac{1}{2}\frac{1}{2}\frac{1}{2}\right)$ planes in which the spins are confined contribute intensity to the peak, as the other three $\{\frac{1}{2}\frac{1}{2}\frac{1}{2}\}$ planes have structure factors equal to zero. This is opposite to XRD where, as discussed above, all four reflections contribute to the peak. As the correlation length found by neutron diffraction is close to the plate thickness found by XRD, the {111} plane defining the plate surface must be the (111) plane in which the spins are confined. If the spins were confined in any of the three other {111} planes a correlation length about three times as large as the plate thickness would be expected. Thus, the spins are confined in planes parallel to the plate face, a result that may also be expected for symmetry reasons.

A similar measurement of the sample prepared at 250°C gave a correlation length of 1.7(1) nm in agreement with the plate thickness found by fitting the XRD data. Fitting the peaks with a Lorentzian line shape instead of a Gaussian resulted in similar parameters.

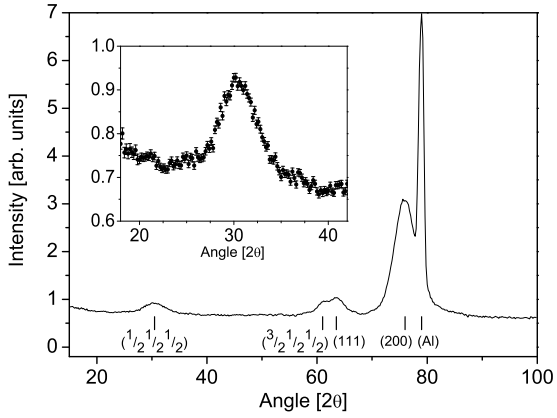

Figure 3.6: Neutron diffraction pattern of the as-prepared NiO sample prepared at 300°C. The inset shows a closeup of the $\left(\frac{1}{2}\frac{1}{2}\frac{1}{2}\right)$ reflection. The intense sharp peak is due to the aluminium sample container.

Mössbauer spectroscopy

The Mössbauer effect has been demonstrated in ^{61}Ni, which would be useful for studying NiO. However, the line width Γ is large and the f-factor is small necessitating cooling of the source and sample. In addition to this the half life of the parent isotope ^{61}Co is only 99 min, making it very unpractical for obtaining spectra. Thus ^{61}Ni Mössbauer spectroscopy is inferior to ^{57}Fe Mössbauer spectroscopy

In order to enable ^{57}Fe Mössbauer spectroscopy of the NiO nanoparticles it is necessary to dope them with iron. The amount of ^{57}Fe in natural iron is only 2.2%, so in order to get sufficient absorbtion from the sample without a high degree of doping, pure ^{57}Fe is used. To ensure a homogenous mixture of Fe and Ni, the iron is dissolved in acid and mixed with the $Ni(NO_3)_2{\cdot}6H_2O$ before precipitating $Ni(OH)_2$. Indeed as shown in Paper VIII the Fe is evenly mixed in the NiO, predominantly in the interior of the particles and primarily in cubic environments surrounded only by Ni.

Due to the price of ^{57}Fe the doped samples are only prepared in very small amounts (<200 mg). Thus different samples are used for Mössbauer spectroscopy, where only small amounts of sample are required, and inelastic neutron scattering, where several grams are needed. To ensure the equality of the samples, XRD patterns from a doped and an undoped sample of NiO prepared simultaneously by baking equal amounts in identical crucibles at 300°C have been Rietveld refined. The obtained estimated sizes were 2.2 nm (thickness) and 7.0 nm (diameter) for the doped sample and 2.3 nm (thickness) and 6.9 nm (diameter) for the undoped. The difference in diameter of this undoped sample and the one discussed in Table 3.1 may be due to the small amount of sample being baked compared to the size of the crucible.

3.2 Hematite

Hematite, α-Fe_2O_3, has been known since antiquity. Large samples of hematite have a metallic lustre. Crushing such a sample reveals a deep red powder, giving rise to the name hematite or blood-stone. Hematite is a common mineral, mined as a source of iron.

3.2.1 Bulk structure

The bulk crystal structure of hematite is hexagonal with the space group $R\overline{3}c$ and lattice parameters of $a = 5.038(2)$ Å and $c = 13.772(12)$ Å [82]. The iron and oxygen atoms are ordered in alternating planes (basal planes) along the [001] direction, as shown in Figure 3.7. An alternative representation of hematite mainly used in older literature is a rhombohedral unit cell where $[001]_{\mathrm{hex}}=[111]_{\mathrm{rhomb}}$, so care must be taken to avoid confusion. In the present work the hexagonal representation is used throughout. Hematite is antiferromagnetic with an ordering vector of (003) and a Néel temperature of about 950 K [83].

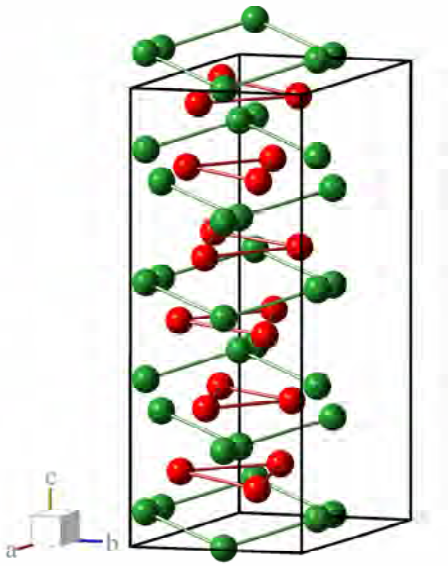

Figure 3.7: Hexagonal structure of hematite. Iron is shown as green and oxygen as red. The black wire frame indicates the unit cell.

3.2.2 Structure and morphology of hematite nanoparticles

Nanoparticles of hematite can be prepared by various methods. One of the main methods for preparing fairly monodisperse particles is the gel-sol method proposed by Sugimoto [84]. A modified version of this method has been used to prepare the particles in papers IV, VI and VII. Here, $FeCl_3$ is dissolved in water and precipitated with NaOH. This is repeated using the initial precipitate as a seed solution. An alternative method of preparing hematite nanoparticles is to heat $Fe(NO_3)_3{\cdot}9H_2O$ in atmospheric air at 90°C for 20 days. This method gives larger and not quite so spherical particles and was used to prepare the sample in Paper V.

The structure of nanoparticles of hematite is the same as in bulk, again with larger lattice parameters [85]. As $c > \sqrt{6}a$ the hexagonal unit cell of hematite may be considered to be "stretched" compared to the hexagonal unit cell of NiO. Thus the hexagonal {101} and (003) reflections have different plane spacings in hematite, whereas in NiO they are the same (except for the negligible exchange striction). This means that there is not a superposition of the two reflections and the XRD patterns become easier to fit.

Figure 3.8(a) shows a HRTEM image of a single hematite nanoparticle, that is seen to be crystalline and almost spherical in shape. The hematite particles have sizes of about 5-10 nm, as shown in Figure 3.8(b). In accordance with this Rietveld refinement of XRD spectra gives almost spherical particles with a size of 8 nm.

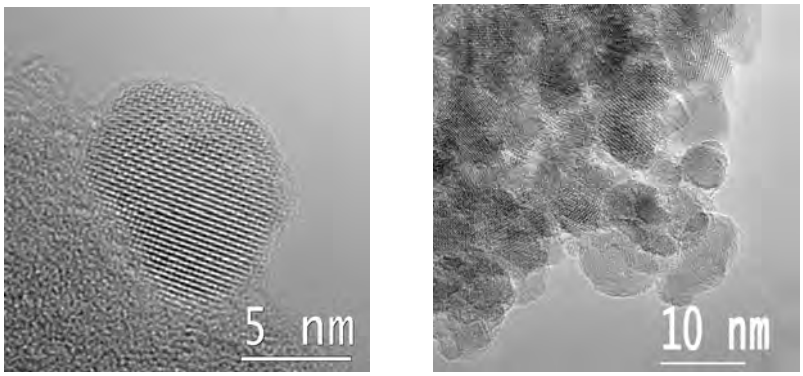

(a) (b)

Figure 3.8: TEM images of hematite nanoparticles. (a) A single nanoparticle of hematite, showing that this is crystalline and almost spherical (b) An area with many hematite nanoparticles, showing that the sizes are about 5-10 nm.

3.3 Goethite

Goethite, α-FeOOH, named after the writer J. von Goethe has been used as a pigment since antiquity. It has an ochre colour, with nanoparticles being darker, towards brown. Pure and well-crystalline goethite is only available at a few locations around the world, but non-perfect goethite is very common.

Goethite has an orthorhombic crystal structure with the space group $Pnma$ and lattice parameters $a = 9.949(1)$ Å, $b = 3.018(1)$ Å and $c = 4.600(1)$ Å [86]. Goethite is antiferromagnetic with the ordering vector (200) and Néel temperature of ≈ 400 K [87].

Nanoparticles of goethite can be precipitated by vigorously mixing $Fe(NO_3)_3$ dissolved in HNO_3 with NaOH, as described in [88]. TEM images of the resulting sample reveals rod-shaped particles found in bundles, see Figure 3.9. The size of each bundle is about 20 nm. From High resolution TEM images the long axis of the fibres is found to be the [010] direction, with rod lengths of about 50 nm. The dimensions of the rods in the [100] and [001] directions are about 5 nm.

3.4 Interparticle interactions

Previous measurements of hematite nanoparticles have shown how strong aggregation of the particles has a strong effect on the Mössbauer spectra of the samples [89, 90]. By studying the samples by Mössbauer spectroscopy it is possible to study the interactions between the particles and qualitatively determine the degree of aggregation. Such interparticle interaction effects are observed in all the three materials studied here.

All three materials are antiferromagnetic and the dipole interaction between surface atoms of different particles is negligible [91]. However, the surface atoms of neighbouring particles in very close proximity may exchange couple to each other. The energy E_i for particle i of such an interaction may be written

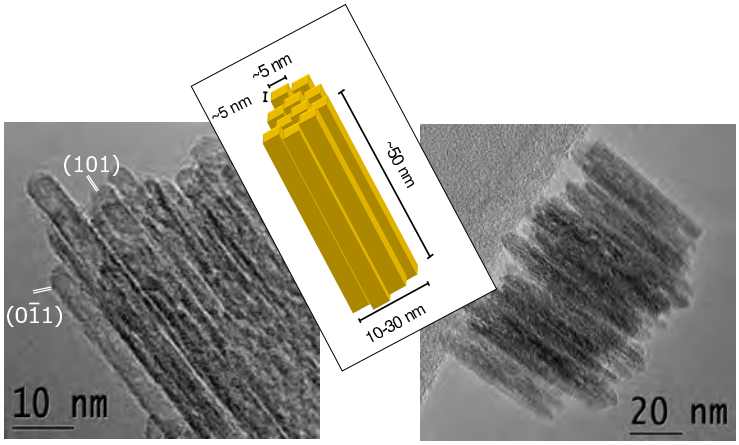

Figure 3.9: TEM images of bundles of goethite nanoparticles. The left figure shows a bundle of rod-shaped goethite particles at high resolution, as indicated by the sketch. The right figure shows an agglomerate of such bundles.

as [88–90]

$$E_i = -\mathbf{M}_i \cdot \sum_j K_{ij}\mathbf{M}_j \tag{3.1}$$

where $\mathbf{M}_i$ and $\mathbf{M}_j$ are the sublattice magnetisations of particles i and j and K_{ij} is an exchange coupling constant between the surface atoms in particles i and j. The equation may be written using a mean field model as

$$E_i = -\mathbf{M}_i \cdot K_{\mathrm{m}}\langle\mathbf{M}\rangle \tag{3.2}$$

with the effective exchange constant K_{m}. Exchange interactions are very strong, so just a few exchange bonds between particles will contribute a significant interaction energy. The interaction will dampen the superparamagnetic relaxation, maintaining a magnetic splitting of Mössbauer spectra in temperature regimes, where the spectra would otherwise display relaxation [89, 90]. This splitting of the spectra can be characterised by an ordering parameter due to the exchange interaction between the particles [88]. Variations in the interparticle interaction within the sample will give a distribution of this ordering parameter giving a broad and asymmetrical distribution of sextets in the Mössbauer spectra. A completely random orientation of the particles would result in a weak interaction as many of the contributions to the sum in Equation (3.1) would cancel each other out. Contrary, an oriented alignment of the particles in the sample would lead to a strong interaction between the particles [90].

It was found that a simple mechanical treatment can reduce these interparticle interactions. This was initially tested on hematite nanoparticles (Paper IV), but it was found that it could also be applied to nanoparticles of the two other materials (NiO in Paper IX). The treatment consisted of a hand grinding in a small agate mortar for periods of time in the range of 5 minutes to 60 minutes. Alternatively a low energy Retsch S100 centrifugal ball mill was used with an agate milling container. This gives a more reproducible grinding, but a large amount of sample is required, due to the size of the milling container. The use of nonmagnetic grinding media to further separate the particles was also studied.

3.4.1 Hematite

Mössbauer spectra of the sample of hematite nanoparticles from Paper IV, prepared as described above, are shown in the left part of Figure 3.10 at a selection of different temperatures. It is clearly seen how the lines in the Mössbauer spectra broaden asymmetrically as the temperature is increased, resulting in complex spectra. Each spectrum has been fitted with sextets with a distribution of different hyperfine fields. The distribution of hyperfine fields broadens asymmetrically until the distribution becomes very broad at room temperature. No collapsed signal due to fast relaxation from superparamagnetism is observed even at the highest temperature.

The hematite sample was ground by hand for 60 minutes as indicated in the top part of Figure 3.11. As shown in Paper IV the sizes of the particles are not changed significantly by this grinding. Mössbauer spectra of the ground sample are shown in the centre part of Figure 3.10. Here it is seen that the asymmetrical broadening progresses faster as the temperature increases than in the as-prepared sample. At about 180 K a doublet component due to fast superparamagnetism appears. This grows steadily and dominates the spectrum at room temperature. Again the spectra are fitted with a hyperfine field distribution. For clarity and comparison, the doublet component is fitted with sextets, having a very small hyperfine field. The hyperfine field distribution progresses in the same way as for the as-prepared sample, the dominance of the doublet becoming clear at the highest temperatures. To increase the effect of grinding, the hematite sample was mixed with nanoparticles of non-magnetic $\eta-Al_2O_3$ in the ratio 1:5. This mixture was also ground for 60 minutes as indicated in the bottom part of Figure 3.11 resulting in the spectra in the right part of Figure 3.10. As the temperature is increased an increasing amount of the particles display fast superparamagnetic relaxation, giving a doublet component in the Mössbauer spectra. There is only minor asymmetrical broadening of the sextets. This is the typical behaviour of isolated nanoparticles, suggesting very weak interparticle interactions.

A range of different non-magnetic nanoparticle materials have been tested as grinding media, $\eta-Al_2O_3$, amorphous SiO_2 and active carbon. Each of these three materials was found to reduce the interparticle interactions, when used as a grinding medium. However, it is difficult to remove the media from the sample after grinding. To solve this problem NaCl was high energy ball-milled to $\sim$20 nm particles and used as a grinding medium. The salt could subsequently be removed by repeatedly washing the sample in water.

Oriented attachment

In Paper VI several experimental techniques were employed to study the nature of the interactions between the hematite particles. An oriented attachment of the particles along the [001] direction was observed. This is convincingly seen in TEM studies. Figure 3.12(c) shows a TEM image obtained by cryo-TEM, where a thin film of an aqueous suspension of the hematite sample is instantly frozen and studied carefully by TEM [92,93]. The image shows hematite nanoparticles attached to each other in chains. When the sample is dried in-situ in the TEM the chains break apart into sections containing about 3 particles. These chain sections are also found in samples dried in air. HRTEM images of such sections

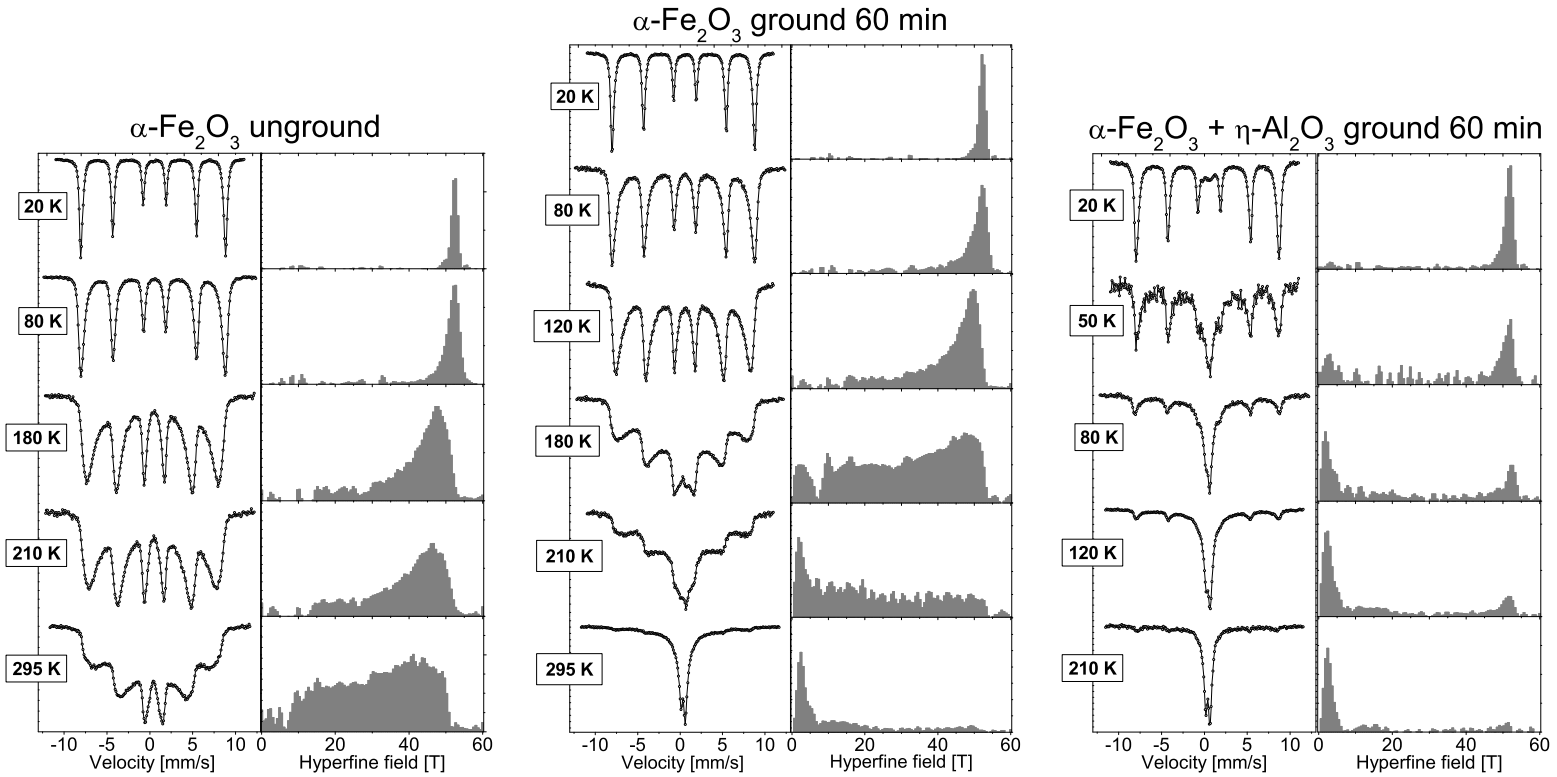

Figure 3.10: Mössbauer spectra of hematite samples subjected so various treatments, obtained at a range of temperatures. The figure shows spectra from the as-prepared (unground) sample, the sample ground by hand for 60 minutes and the sample ground for 60 minutes with $\eta-Al_2O_3$ in the ratio 1:5.

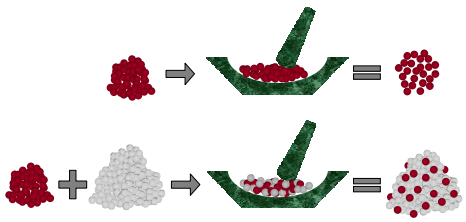

Figure 3.11: Schematic presentation of the grinding process.

are shown in Figures 3.12(a) and 3.12(b). By measuring the crystal lattice planes in the images, it was confirmed that the particles do indeed share a common [001] axis. Figure 3.12(d) shows the separated particles dispersed on a particle of amorphous SiO_2 after grinding a mixture of hematite and SiO_2.

The difference between the ground and unground samples are more clearly seen in Figure 3.13. Here, a sample of hematite mixed with $\eta-Al_2O_3$ ground by hand for 0 minutes and 60 minutes has been studied by dark-field TEM. In dark-field TEM only electrons that are diffracted are allowed to pass the objective aperture, see Section 2.5.1. Thus, well crystalline regions of the sample appear white in the images and amorphous or poorly crystalline regions appear dark. Before grinding the white spots from hematite nanoparticles are seen in aggregates, see Figure 3.13(a), whereas after the grinding these are found to be more isolated, see Figure 3.13(b), indicating a breaking apart of the aggregates.

Oriented attachment along the [001] direction has also been observed by neutron powder diffraction and synchrotron x-ray diffraction, see Paper VI. Here the magnetic (003) and structural (006) reflections are narrower than the other reflections in the as-prepared sample, indicating an extended correlation length. After grinding, the width of the two reflections increase to become comparable to the other reflections, as expected for spherical particles. The increased correlation length resulting in the narrowing of the peak must mean that the (003) plane spacing is constant over the length of several particles, so that the particles at the interface have the same spacing as the lattice spacing. This seems to confirm the possibility of strong exchange coupling between the particles.

3.4.2 Goethite

A strong interparticle interaction may be expected from the TEM images of goethite nanoparticles. Indeed this is also observed in Mössbauer spectra of the as-prepared sample displaying asymmetric broadening. An attempt to remove this interaction was done by grinding a goethite sample with salt nanoparticles in the ratio 1:5 in the Retsch ball mill operated at 40% intensity for 24 hours. The series of spectra before and after grinding are shown in Figure 3.14. The ground sample displays the same asymmetric broadening of the sextet contribution except as well as a doublet component that increases as the temperature is increased. A similar result could also be obtained by hand grinding.

The removal of interparticle interactions is not as complete as in hematite. An explanation of this may be that the bundles of goethite particles interact

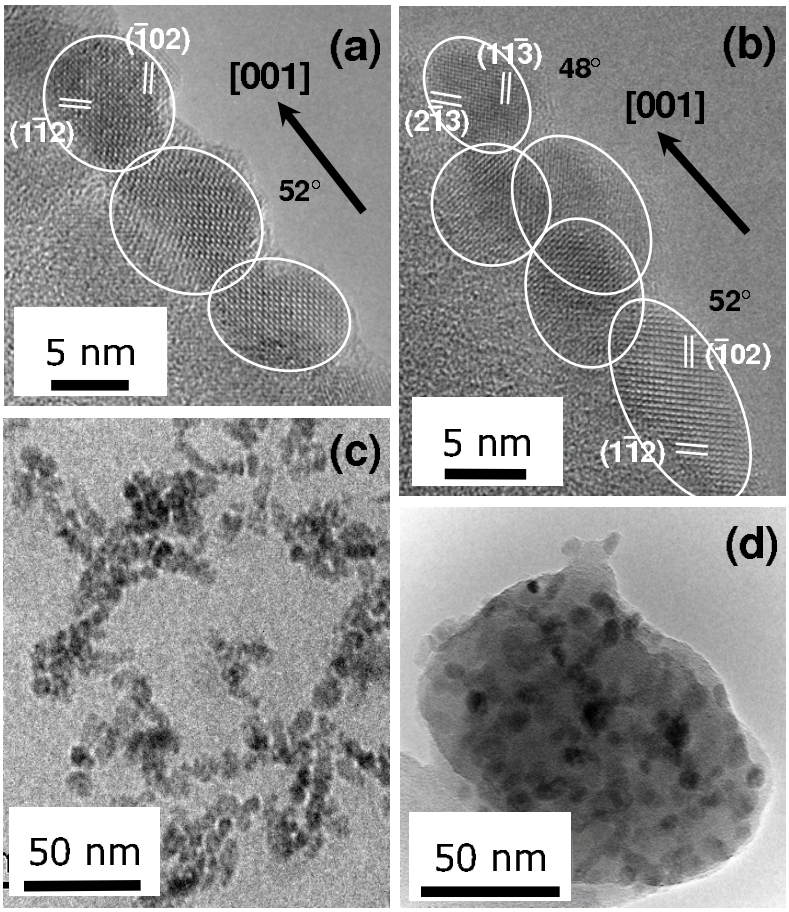

Figure 3.12: TEM images of hematite nanoparticles. (a) and (b) High resolution images of the attached particles. The outlines of the individual particles and lattice planes within these are indicated in white. The [001] directions and angles between these and the plane of the paper are indicated by black arrows and values. (c) Cryo-TEM image showing hematite chains embedded in a thin ice sheet. (d) An amorphous SiO_2 particle with dispersed hematite particles after grinding.

strongly. Grinding may chip particles (or parts of particles) from the bundles, leaving the bundles otherwise intact. Due to their small size these chipped off particles will display fast superparamagnetic relaxation giving doublets in the Mössbauer spectra. This chipping of the particles is confirmed by TEM where pieces of single rod like particles are found in the ground sample, see Figure 3.15. An indication of oriented attachment has been observed in neutron diffraction data as a narrowing of the diffraction lines from reflections perpendicular to the goethite rods [94].

3.4.3 NiO

TEM images of NiO nanoparticles do not reveal any systematic ordering of the particles as observed in hematite and goethite. However, Mössbauer spec-

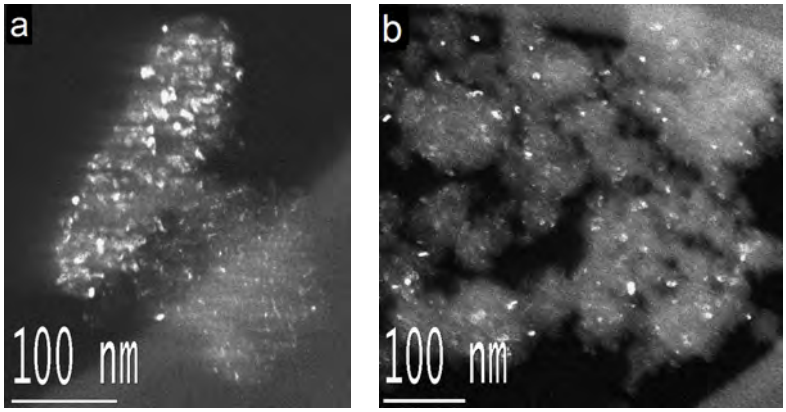

Figure 3.13: Dark-field TEM images of hematite nanoparticles mixed with $\eta-Al_2O_3$. (a) After grinding for 0 minutes. (b) After grinding for 60 minutes.

troscopy indicates some degree of interaction. Several grinding times with and without nanoparticles of salt were tested in order to find an efficient way of removing the interparticle interactions. The sample heated at 250°C was used to test the different treatments. Figure 3.16 shows Mössbauer spectra of the sample at 80 K after being subjected to a range of different treatments. Grinding for 45 minutes only results in a slightly larger superparamagnetic component than after 15 minutes of grinding. Surprisingly grinding with salt does not result in a significant reduction in the interactions.

In the study of the samples prepared at 300°C it was decided to use samples ground for 15 minutes without a grinding medium for the measurements. The samples, referred to as the ground samples in Papers VIII and IX, were thus prepared at 300°C and ground by hand for 15 minutes.

To ensure a further and permanent reduction of the interactions the ground sample was suspended in water and centrifuged as described in Ref. [76]. The smallest particles, i.e., those that are not aggregated, do not sediment, but stay in suspension. This suspension was mixed with H_3PO_4 giving a layer of phosphate coating around the particles. The particles, referred to as the coated sample in Papers X and XI were prepared in this way. Corresponding to the doped samples for Mössbauer spectroscopy, a set of ground and coated samples not doped with ^{57}Fe were prepared for XRD and neutron scattering by grinding in the Retsch ball mill operated at 30% for 3 hours. This was done because of the larger amount of sample. Rietveld refinement of the XRD pattern of the undoped coated sample again yields plate shaped particles with an estimated thickness of 2.1 nm and an estimated diameter of 7.9 nm, in correspondence with the dimensions for the particles in the as-prepared sample in Table 3.1

Mössbauer spectra of the as-prepared, the ground and the coated samples are shown in Figure 3.17 displaying a range of interparticle interactions. As it is seen, the phosphate layer contributes a small doublet component to the Mössbauer spectra. This is present at all temperatures, but it is insignificant at high temperatures due to the large singlet from particles with fast superparamagnetic relaxation.

The phosphate treatment described above was also applied to the hematite

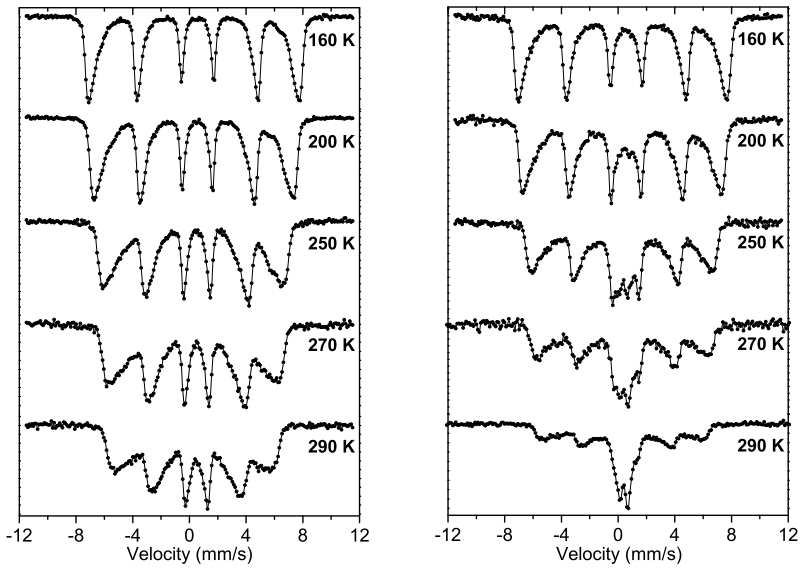

Figure 3.14: Mössbauer spectra of nanoparticles of goethite. (a) The as-prepared sample. (b) After grinding in the Retsch ball mill operated at 40% intensity for 24 hours with nanoparticles of salt in the ratio 1:5.

sample referred to as the coated sample in Paper VII.

Particle attachment

As discussed in Section 3.1.2 the magnetic correlation length perpendicular to the plate face in the as-prepared sample was found to be 3.1(4) nm. Fitting neutron powder diffraction data also obtained at 13 K from the coated sample in the same way gives a correlation length of 2.4(2) nm. Within the uncertainty these two correlation lengths are almost equal. The difference may suggest an attachment of the particles in the as-prepared sample along the [111] direction, as it was seen in hematite. But, as such an ordering is not observed in XRD data or clearly visible in TEM images the effect is expected to be weak.

3.4.4 Comparison of interaction strengths

The as-prepared samples of all three antiferromagnetic materials display interparticle interactions with different degrees of interaction. The goethite particles interact strongly in the bundles and are difficult to break apart even when using a grinding medium. Hematite also has strong coupling of particles often in chains with an oriented attachment. These can be broken apart efficiently using a grinding medium. Although no obvious oriented interaction in NiO is observed in the TEM images, neutron diffraction and Mössbauer spectroscopy suggests that there is some attachment of the particles and interaction between these. However, these can easily be broken apart by hand grinding even without a grinding medium, suggesting a weaker interaction. Indeed, as shown in

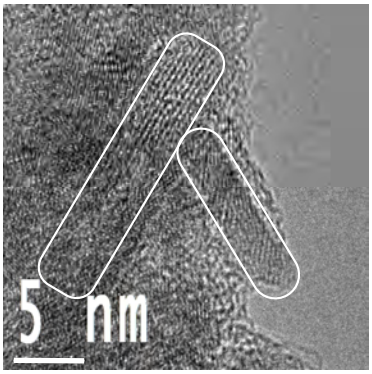

Figure 3.15: TEM images of Goethite particles after grinding in the Retsch ball mill operated at 40% intensity for 24 hours with nanoparticles of salt in the ratio 1:5.

Paper IX, the interaction between NiO nanoparticles can be removed by suspension in water or even storage in a moist atmosphere. No such effect was observed in the hematite samples.

As it did not seem possible to consistently separate the goethite particles from each other it would not be feasible to study interaction effects. Also, the large amount of hydrogen in the structure gives a large incoherent signal in neutron scattering. Inelastic neutron scattering was attempted, but due to the dominating incoherent signal no inelastic signal could be distinguished. So further studies of goethite were abandoned.

3.5 Magnetic anisotropy

The orientation of the spins and thus the magnetisation of a material will have some preferred directions in the crystalline lattice, known as easy axes. These are separated from each other by energy barriers. The magneto-crystalline anisotropy energy is the energy necessary to force the magnetisation across such a barrier.

The energy needed to change the orientation of one spin is the single ion anisotropy energy κ_a. A more useful parameter is the anisotropy energy density K related to the single ion anisotropy by $K = n\kappa_\mathrm{a}s^2$ (Paper V), where n is the density of magnetic ions and s is the spin of these. An anisotropy field, B_A, may be defined as [83, 95]

$$B_\mathrm{A} = \frac{|K|}{M_\mathrm{s}} = \frac{2\kappa_\mathrm{a}s}{g\mu_\mathrm{B}}, \tag{3.3}$$

where M_s is the sublattice magnetisation given by $M_\mathrm{s} = \frac{1}{2}g\mu_\mathrm{B}ns$.

The important terms contributing to the anisotropy of materials with transition metal magnetic ions, with unfilled $3d$ shells, are the magnetic dipolar interactions among the ions and a crystal field contribution from the surrounding ions. The former anisotropy is due to the anisotropic field experienced by one ion from the dipole moments of the neighbouring ions. In the case of oxide samples, the latter is due to the interaction of the incomplete electron orbitals of a magnetic ion with the electrons in the neighbouring oxygen anions [96]. This

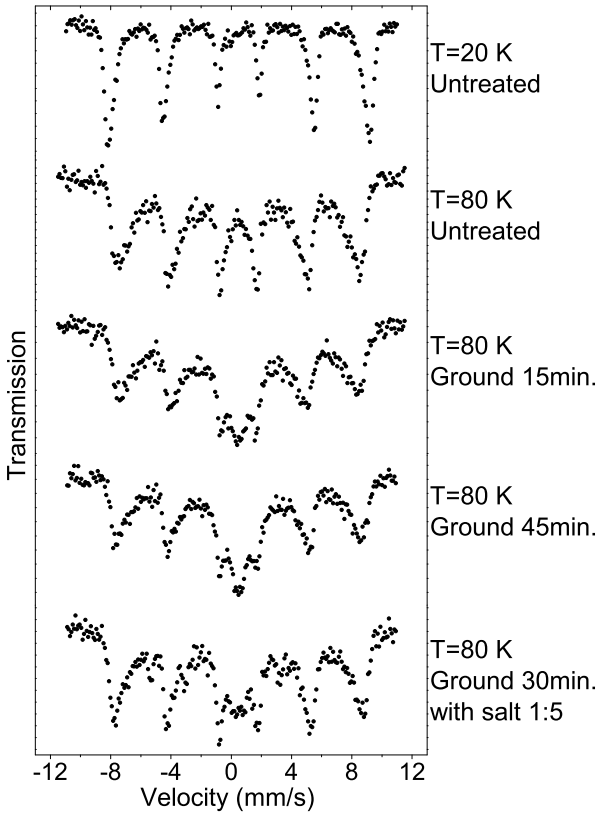

Figure 3.16: Mössbauer spectra of NiO particle prepared at 250°C. The labels indicate the treatment the sample has undergone. Grinding was done in the agate mortar by hand.

results in a coupling of the orbital moments to the lattice, with an anisotropy due to an asymmetry of the lattice[1]. If the lattice is strained, this coupling will change giving rise to a strain anisotropy.

An important anisotropy contribution in nanoparticles is the surface anisotropy arising from the very asymmetric crystal fields at the surface of particles due to missing neighbour ions. This contribution may be very large in nanoparticles, and increases as the particle size decreases due to the increasing surface area compared to volume [97].

In the following the theoretical and experimental values of the anisotropy for bulk and nanoparticles of NiO and hematite are discussed and compared.

3.5.1 Bulk NiO

In NiO where the structure is nearly cubic, the crystal field is expected to be nearly isotropic and will not contribute to the anisotropy energy. Calculating the classical dipole energy gives an expression for the anisotropy energy, which

[1] As Fe^{3+} has a spherically symmetric $L = 0$ ground state, the coupling is due to higher order terms [96].

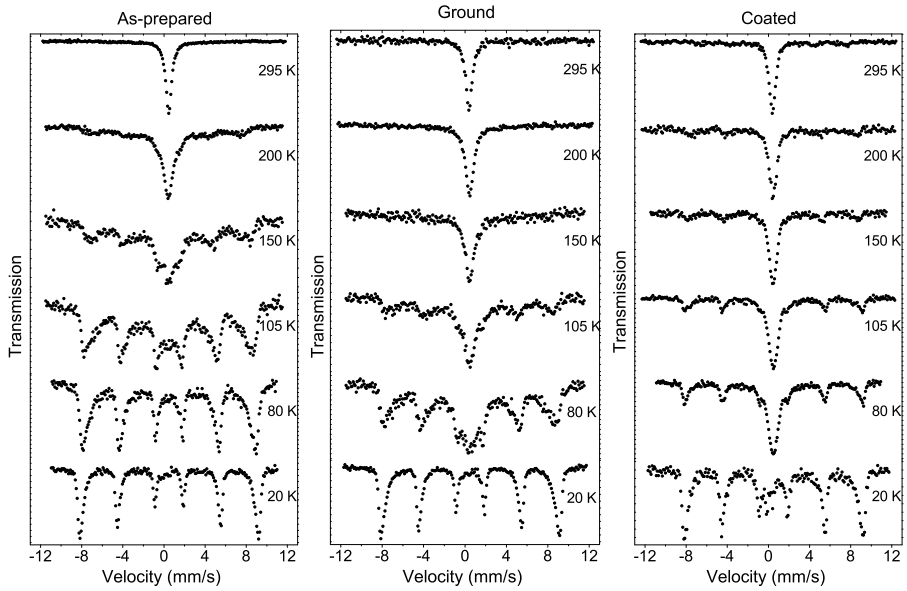

Figure 3.17: Mössbauer spectra obtained at various temperatures of NiO samples prepared at 300°C. (a) The as-prepared sample (b) The sample ground by hand for 15 minutes. (c) The sample ground for 15 minutes and coated with a phosphate layer.

may be approximated by

$$E_{\mathrm{dp}} \approx K_1 \cos^2 \theta \tag{3.4}$$

where θ is the angle from the spins to the [111] direction. The value of K is given by the expression [98]

$$K_1 = 86.12 \frac{(g\mu_{\mathrm{B}} s)^2}{a^6} \tag{3.5}$$

where a is the lattice constants of the material.

In bulk NiO the anisotropy constant has been calculated by this expression to be $K_1 = 7.0 \cdot 10^5\,\mathrm{Jm}^{-3}$ [99]. In fairly good accordance with this, the first experimentally measured value was found to be $K_1 = 4.96 \cdot 10^5\,\mathrm{Jm}^{-3}$ [99]. The positive value means that the spins are found somewhere within the (111) plane. The deviation of the structure from cubic due to the exchange striction will change K_1 by less than 1% [100].

Higher order contributions to the anisotropy will create an easy axis within the (111) plane. In bulk NiO, this direction has been found to be the $[11\overline{2}]$ axis [101, 102], thus giving a six-fold symmetry due to the symmetry of the crystal structure. Attempts at calculating the associated in-plane anisotropy energy theoretically arrive at a much smaller value $K_2 \approx 0.1\ \mathrm{Jm}^{-3}$ [102] than the measured value of $K_2 = 30\ \mathrm{Jm}^{-3}$ [103,104], obtained from a domain wall and strain free sample. The presence of domain walls may lead to an underestimate of the anisotropy [103]. If there is strain in the (111) plane of the samples, a two-fold symmetric in-plane strain anisotropy is created. This is often larger than the in-plane anisotropy and may be the origin of the large in-plane anisotropy

energy, $K_2 = 2.3(1.9) \cdot 10^4$ Jm^{-3}, value measured by Hutchings and Samuelsen in bulk NiO [105].

3.5.2 Bulk Hematite

Due to the non-cubic nature of the hematite crystal structure there is a strong crystal field anisotropy term. This has a positive value, thus seeking an alignment parallel to the c axis [001]. As in NiO there is also a dipole contribution seeking to align the spins perpendicular to the [001] axis, i.e., within the (001) plane. The two contributions are similar in size both being about 10^6 Jm^{-3} [106]. The sum of the two oppositely directed contributions has a value of $K_1 \approx -2 \cdot 10^4$ Jm^{-3} at low temperature where the crystal field term dominates [83,95]. The temperature dependence of the two contributions is not the same, so at some temperature there is a transition to a new regime where the dipole term dominates. This spin flop transition due to a change in sign of K_1 is known as the Morin transition. It occurs at ≈ 260 K in bulk hematite [106] giving a value of $K_1 \sim 1 \cdot 10^4$ Jm^{-3} at room temperature. Thus, below the transition the spins are aligned along the [001] axis and above the spins are confined to the basal plane (001). Above the Morin temperature a Dzialoshinski-Moriya interaction [107] gives a slight canting of the spins, resulting in a small moment within the basal plane given by the vector sum of the two spins.

Also in hematite higher order energy terms give rise to an in-plane anisotropy energy, K_2. This has a six-fold symmetry and values of $K_2 \approx 10$ Jm^{-3} have been measured [108]. Again, care must be taken as strain will introduce an in-plane strain anisotropy term. An example of this has been measured in a natural sample finding a value of $K_2 \approx 100$ Jm^{-3} [109].

Thus, both NiO and hematite, above the Morin transition, have large out-of-plane anisotropy energies confining the spins to the basal plane and in-plane anisotropy energies several orders of magnitude lower seeking to align the spins along an easy axis within the basal plane. The out-of-plane anisotropy in NiO is about 50 times larger than in hematite due to the large crystal field anisotropy in hematite counteracting the dipole term.

3.5.3 Nanoparticles of hematite

From the arguments above and previously published results [110], the anisotropy energy of hematite nanoparticles may be expressed as

$$E_{\mathrm{A}} = K_1 \cos^2\theta + K_2 \sin^2\theta \sin^2\phi, \tag{3.6}$$

where, as above, θ is the angle from the spins to the [111] direction and ϕ is the angle to the easy direction in the (111) plane.

The in-plane anisotropy of hematite nanoparticles has been measured by Mössbauer spectroscopy, revealing strongly size dependent values, significantly larger than bulk [97]. The values range from $K_2 = 1.7 \cdot 10^3$ Jm^{-3} for 27 nm particles to $K_2 = 2.4 \cdot 10^4$ Jm^{-3} for 5.9 nm particles. The strong increase is presumably due to surface anisotropy.

The increase in the lattice parameters of nanoparticles of hematite compared to bulk [85] changes the magnitudes of the the two contributions to the out-of-plane anisotropy discussed above [106]. The sum of the two contributions will

change significantly resulting in a reduction of the Morin transition temperature in nanoparticles [111,112]. The out-of-plane anisotropy energy has recently been measured by inelastic neutron scattering in 16 nm hematite particles, yielding a value of $K_1 \approx 5.0 \cdot 10^4$ Jm^{-3} at low temperatures increasing to $K_1 \approx 8.0 \cdot 10^4$ Jm^{-3} at room temperature, see Paper V. The dipole term dominates at all temperatures such that there is no change in sign of K_1, and thus no Morin transition.

3.5.4 Nanoparticles of NiO

In NiO nanoparticles the anisotropy may also be expressed by Equation (3.6). The in-plane anisotropy energy has been measured to be about $K_2 \approx 1 \cdot 10^4$ Jm^{-3}, see Paper XI and Sections 4.1.1 and 4.2.3. This value is observed to be significantly larger than the reported bulk values, except for the value in [105], which as discussed above seems overestimated.

The crystal structure of NiO nanoparticles is the same as that in bulk, albeit with a slightly enlarged unit cell [69]. The stretching of the unit-cell due to exchange striction is difficult to measure in nanoparticles because of the broad reflections in diffraction patterns. However, analysing XRD patterns would suggest that the exchange striction is not significantly larger than the bulk value. The increase of lattice parameters reported in Paper VIII gives rise to an increase of about 2% in the out-of-plane anisotropy energy in Equation (3.5). The bulk out-of-plane anisotropy energy is much larger than the value of the nanoparticle in-plane anisotropy energy which is presumably due to surface anisotropy. So the contribution to the nanoparticle out-of-plane anisotropy energy from surface anisotropy will be negligible. Thus no drastic change in the out-of-plane anisotropy of NiO is expected when entering the nanoparticles regime and a value of the same order of magnitude as the bulk value is expected. Indeed an experimental indication of this has recently been published [77].

Summarising, it was found that in both NiO and hematite nanoparticles the in-plane anisotropy energies are significantly larger than in the bulk material presumably due to an increase of the surface anisotropy because of the finite particle sizes. The out-of-plane anisotropy in hematite nanoparticles was found to be strongly size dependent, whereas in NiO nanoparticles such a size dependence is neither expected nor observed.

3.6 Exchange field of NiO

As the main emphasis of this thesis is the magnetic properties of NiO nanoparticles, only the exchange field of NiO is considered in the following. The exchange field of hematite may be calculated in the same way.

In the fcc structure of NiO each Ni atom has 12 nearest neighbours and 6 next nearest neighbours. Of the 12 nearest neighbours there are 6 with spins parallel to the spin of a given Ni atom, and 6 with spins antiparallel to it. Due to the exchange striction there is a slight difference between the exchange constants to the 6 parallel and 6 antiparallel spins, $J_1^{\uparrow\uparrow} = 16.1$ K and $J_1^{\uparrow\downarrow} = -15.7$ K respectively [105]. However, as all nearest neighbour superexchange paths through the O atoms involve approximately 90° angles all the exchange constants are small and the two pairs of 6 exchange constants can be considered

to cancel each other out. The 6 next nearest neighbours are all antiparallel with exchange paths of approximately 180° [81, 105]. This gives the large exchange constant of $J_2 = -221$ K [105]. Thus the effective exchange parameter of a Ni atom, including up to next nearest neighbour terms, is $\mathcal{J} = 6J_2 = -1326$ K. Similar values of the exchange constants have been found by several authors as listed in [113].

It is useful to introduce an exchange field defined as

$$B_{\mathrm{E}} = \frac{|\mathcal{J}|s}{g\mu_{\mathrm{B}}}. \tag{3.7}$$

The value of the g-factor of $g = 2.19$ found in Section 4.2.6 is in accordance with values measured in bulk [114,115]. With the spin of Ni $s = 1$ this gives an exchange field of $B_{\mathrm{E}} = 905$ T[2].

Applying high pressure to bulk NiO has been observed to reduce the cubic lattice parameter increasing the next nearest neighbour exchange constant, J_2 [116]. The lattice parameters of nanoparticles are generally increased compared to bulk, an effect that may be considered as a negative pressure [111]. Extrapolating the data from Ref. [116] may warrant a reduction of J_2 due to a larger lattice constant, but as it is only about 5% it will be ignored. A more important reduction of the exchange energy arises because of missing exchange bonds at the surface. Also, non-collinear alignment of some spins (spin canting) [117] may reduce the average effective exchange constant in nanoparticles.

3.7 Antiferromagnetic resonance in NiO

A perfect antiferromagnet will allow resonant absorbtion of radiation [118], known as antiferromagnetic resonance, at the energies calculated in Paper XII

$$\hbar\omega_\alpha \approx g\mu_{\mathrm{B}}\sqrt{2B_{\mathrm{A}2}B_{\mathrm{E}}} \tag{3.8}$$

$$\hbar\omega_\beta \approx g\mu_{\mathrm{B}}\sqrt{2(B_{\mathrm{A}2}+B_{\mathrm{A}1})B_{\mathrm{E}}} \approx g\mu_{\mathrm{B}}\sqrt{2B_{\mathrm{A}1}B_{\mathrm{E}}}. \tag{3.9}$$

Here $B_{\mathrm{A}i}$ are the anisotropy fields for K_i ($i = 1, 2$). The antiferromagnetic resonance is equivalent to an infinite wavelength ($\mathbf{q}$=0) spin wave. This antiferromagnetic resonance is an important method of measuring the magnetic anisotropy of materials, assuming knowledge of the exchange field [118].

Again, the following section will only be concerned with measurements of NiO. Several authors have measured the anisotropy of bulk NiO by far infra-red spectroscopy and Raman scattering. Kondoh [99] found the antiferromagnetic resonance of bulk NiO corresponding to $\hbar\omega_\beta$ by far-infrared spectroscopy at low temperature at 36.5 cm^{-1} equivalent to $\hbar\omega_\beta = 4.53$ meV, giving an out-of-plane anisotropy of $K_1 = 4.96 \cdot 10^5$ Jm^{-3}. Comparable resonance frequencies have been found by several others [119,120]. The temperature dependence has been found, as expected, to follow the sublattice magnetisation [121,122] towards zero at the Néel temperature. Also, an increase of the resonance frequency has been observed when pressure is applied [116]. A comparable value of $K_1 = 4.3(2) \cdot 10^5$ Jm^{-3} in bulk NiO has been measured by inelastic neutron scattering [105].

[2]This value differs from that of 987 T found in Paper VIII as a value of $g = 2$ was used there

A single study of the antiferromagnetic resonance due to the in-plane anisotropy by far infra-red spectroscopy has been reported [123]. The resonance was only observed when applying a magnetic field to Zeeman shift the energy of it, but the anisotropy energy could not be measured.

3.7.1 Uniform magnetic excitations in NiO nanoparticles

The $\mathbf{q}$=0 spin waves are coherent precessions of the spins around the easy axis defined by anisotropy, as discussed in Chapter 1. These are known as uniform or collective magnetic excitations. The energy gap between these precession states, at least for small opening angles, is given by the energy necessary to excite a $\mathbf{q}$=0 spin wave. Uniform magnetic excitations are the dominant excitations in nanoparticles [124]. These excitations have been observed by inelastic neutron scattering in ferromagnetic [125], ferrimagnetic [126] and antiferromagnetic [127] nanoparticles.

In bulk materials spin waves have continuous energy dispersions. At small wave vectors in NiO and hematite these have been found to be very steep, giving spin wave velocities of ~ 250 meVÅ for bulk NiO [105] and $140-200$ meV Å for bulk hematite [128]. However, due to the finite size, spin waves are quantised in nanoparticles, as there is a maximum extent of a spin wave, that may be contained by a particle. The maximum, non-infinite, wavelength allowed has been calculated to be $\lambda_{\max} \approx 1.4\,d$, where d is the size of the particles [129]. This gives energies of the first $\mathbf{q} \neq 0$ spin wave ranging from ≈35 meV for 3 nm particles to ≈10 meV for 10 nm NiO nanoparticles. This is far above the maximum employed energy transfer in the inelastic neutron measurements, so $\mathbf{q} \neq 0$ spin wave modes are not measured. The absence of a continuous dispersion has been confirmed by observation of a $\mathbf{q} = 0$ spin wave mode localised in $\mathbf{q}$ and energy in nanoparticles of both NiO (Paper X) and hematite (Paper V).

Only one investigation of the antiferromagnetic resonance in NiO nanoparticles has been reported [77]. Here the resonance energy of 43.5 nm particles was found to be close to the $\hbar\omega_\beta$ mode in bulk NiO. In a second sample of 5.7 nm particles[3], comparable to those presented in Paper VIII, two resonance signals were found, one at the same value as for bulk NiO and one slightly higher.

Assuming that the exchange field in nanoparticles of NiO is the same as in bulk, the out-of-plane anisotropy in NiO nanoparticles is comparable to the value found in bulk NiO. As discussed in Section 4.2.4 there may be a reduction of the exchange field in nanoparticles of up to 50% warranting an increase of the anisotropy by up to a factor of 2. However, the order of magnitude of the anisotropy is the same in bulk and nanoparticles of NiO and the strong size dependence found in hematite is not observed in NiO.

3.7.2 Uncompensated moments

As discussed in Chapter 1 nanoparticles of antiferromagnetic materials will possess an uncompensated moment due to their finite size. These uncompensated moments have been observed in different antiferromagnetic materials such as Cr_2O_3 [130, 131], CuO [132] and most notedly in the iron-storage protein ferritin [133–135]. Of relevance for the present work uncompensated moments

[3]The size of both samples in Ref. [77] was measured assuming a spherical particle shape.

have also been observed in NiO nanoparticles [29,136] as it will be discussed in Chapter 4, and in hematite as discussed in Paper VII. In all these materials the magnetic properties of the particles are significantly changed by the presence of an uncompensated moment.

The uncompensated moment is characterised by the ratio between the number of spins on the two sublattices $\xi = \frac{n_1}{n_2}$. It is shown in Paper XII that the spin wave energies are affected by the presence of an uncompensated moment, arriving at resonance energies

$$\hbar\omega_\alpha = \sqrt{a^2 - b^2 + ac(\xi+1) + \frac{1}{2}c^2(\xi-1)^2 - d} \tag{3.10}$$

$$\hbar\omega_\beta = \sqrt{a^2 - b^2 + ac(\xi+1) + \frac{1}{2}c^2(\xi-1)^2 + d} \tag{3.11}$$

where $a = g\mu_\mathrm{B}\left(B_{\mathrm{A}2} - \frac{1}{2}B_{\mathrm{A}1}\right)$, $b = g\mu_\mathrm{B}\left(\frac{1}{2}B_{\mathrm{A}1}\right)$, $c = g\mu_\mathrm{B}B_\mathrm{E}$ and

$$d = \sqrt{4a^2(\xi-1)^2 + c^2(\xi-1)^4 + 16b^2\xi + 4ac(\xi-1)^2(\xi+1)}.$$

In the simple case where the anisotropy is assumed to be uniaxial, i.e., $B_{\mathrm{A}1} = 0$ the resonance modes ω_α and ω_β are initially degenerate, splitting into two modes both with energies that are strongly dependent on ξ.

Such a uniaxial anisotropy was assumed for the initial calculations for NiO nanoparticles in Paper X. The shift of the resonance energy due to the uncompensated moment resulted in an increase of the calculated in-plane anisotropy value. However, the more detailed calculations presented in Paper XII show that the presence of a large out-of-plane anisotropy weakens the dependence of both spin wave modes on ξ. The resonance energy becomes almost independent of the uncompensated moment and thus the anisotropy calculated in Paper X will be erroneous.

The two anisotropy contributions for 8 nm hematite particles are assumed to be similar in size, (Paper VII). In this situation the resonance energy depends strongly on the uncompensated moment, see Paper XII, and the approximation of uniaxial anisotropy becomes valid. For simplicity this approximation was used for the calculations in Paper VII.

Chapter 4

Results and analysis

This chapter contains a summary of some of the results related to the spin dynamics of NiO nanoparticles obtained by Mössbauer spectroscopy and inelastic neutron scattering as found in Papers VIII and XI. Three samples with varying degrees of interparticle interactions have been studied. The samples are the as-prepared, the ground and the coated NiO samples presented and characterised in Chapter 3. As discussed there, the samples for Mössbauer spectroscopy were prepared by doping the NiO with ^{57}Fe, otherwise the samples have undergone the same treatments.

4.1 Low temperature Mössbauer spectroscopy

In Chapter 3 it was shown how interparticle interactions have a profound effect on the temperature dependence of Mössbauer spectra. In the following the interparticle interactions along with the in-plane anisotropy energy will be quantified. Also, the amounts of uncompensated moment are quantified by high-field Mössbauer spectroscopy.

4.1.1 The anisotropy and interaction energy

At low temperature the spins in NiO will all be very close to the in-plane easy axis. The anisotropy barrier is very high compared to the thermal energy, and thus the superparamagnetic flipping time is long. Collective magnetic excitations will be the dominant excitation [124]. In a classical picture, the spin can be imagined to precess around the easy axis with a certain opening angle. As the temperature is increased more precession levels with increasing opening angles will be populated, as illustrated in Figure 4.1. Increasing opening angles of the precessions will lead to a decrease of the thermal average of the spin, and thus magnetisation. The average of the magnetisation as a function of temperature in nanoparticles with various anisotropy configuration can be calculated by Boltzmann statistics [137].

For the anisotropy configuration of NiO the average magnetisation may be written at low temperature as [137]

$$\langle M(T)\rangle \approx M_0\left[1-\frac{k_BT}{2E_\mathrm{a}}\right] \tag{4.1}$$

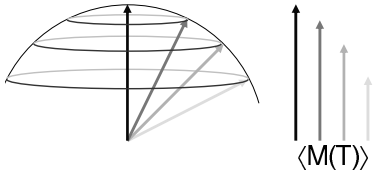

Figure 4.1: Illustration of the classical picture in which the thermal average of the magnetisation decreases as the temperature increases. The angles are greatly exaggerated.

where M_0 is the sublattice saturation magnetisation, V is the particle volume and

$$\frac{1}{E_\mathrm{a}} = \frac{1}{2K_2V} + \frac{1}{2K_1V}. \tag{4.2}$$

K_2 and K_1 are the in-plane and out-of-plane anisotropy energy densities, respectively, as discussed previously.

The reduction of the magnetisation gives rise to a reduction of the hyperfine field splitting. Measuring the average hyperfine splitting field by Mössbauer spectroscopy at low temperatures can thus give the anisotropy energy of the particle. The spectra obtained at each temperature are fitted with a distribution of sextets using the `bigfit` software [138]. The median hyperfine fields of these distributions are shown in Figure 4.2 including linear fits to the data.

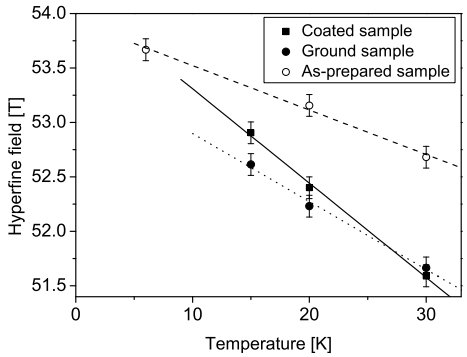

Figure 4.2: Linear fits to the average hyperfine field splittings in the three NiO samples, measured at low temperatures. The lines are linear fits to the data.

Due to the phosphate layer on the coated sample, there is a small doublet component in the Mössbauer spectra at low temperature. This is fitted separately, explaining the difference in the intersection of the lines in Figure 4.2. The phosphate component orders into a sextet at the lowest temperatures, so the data for the coated sample is only included above 15 K.

The data for the coated sample yields a value of $E_\mathrm{a}/k_\mathrm{B} = 310(30)$ K. Using the value of K_1 from bulk NiO, Equation (4.2) yields a value of $K_2V/k_\mathrm{B} = 155(15)$ K, equivalent to $K_2 = 8.2(8) \cdot 10^3$ Jm^{-3} or $B_{\mathrm{A}2} = 15(2)$ mT. As shown in Ref. [91] the exact value of K_1 is not important when $K_1/K_2 \gtrsim 20$, which is the case here and indeed the fit is found to be only very weakly dependent on K_1.

In the two other samples, there is a significant amount of exchange interaction between the particles. This may be included in the expression in the following way [137]

$$\frac{1}{E_{\mathrm{a}}} = \frac{1}{2K_2V + E_{\mathrm{int}}} + \frac{1}{2K_1V + E_{\mathrm{int}}}, \tag{4.3}$$

where E_{int} is a characteristic interaction energy. In the as-prepared sample a value of $E_{\mathrm{a}}/k_{\mathrm{B}} = 650(50)$ K was obtained by the linear fit and in the ground sample it was $E_{\mathrm{a}}/k_{\mathrm{B}} = 430(30)$ K. Assuming that the anisotropy energies of the three samples are the same, which is justified as the particles have the same size and shape in all three samples, the interaction energies can be calculated as $E_{\mathrm{int}}/k_{\mathrm{B}} = 360(60)$ K in the as-prepared sample and $E_{\mathrm{int}}/k_{\mathrm{B}} = 125(20)$ K in the ground sample. Thus, it is observed that the grinding treatment significantly reduces the interaction energy of the sample to a third of the value found in the as-prepared sample.

4.1.2 High-field measurements

When a ferrimagnetic sample is subjected to a large applied field, the spins in the sublattice with the largest moment will align with the field, while the spins in the other sublattice align antiparallel to the field. The alignment of the spins with the applied fields gives a field at a nucleus of $B_{\mathrm{tot}} = B_{\mathrm{hf}} + B_{\mathrm{appl}}$ in one sublattice and $B_{\mathrm{tot}} = B_{\mathrm{hf}} - B_{\mathrm{appl}}$ in the other sublattice. As the magnetic splitting of a sextet in a Mössbauer spectrum is an indication of the field experienced by the nuclei, the Mössbauer spectrum of a ferrimagnet would be expected to consist of two sextets with splitting larger and smaller than the single zero field sextet, according to the applied field. This splitting of the sextets in ferrimagnetic samples is the motivation for studying NiO nanoparticles in high applied fields, as the presence of an uncompensated moment will give the NiO a ferrimagnetic nature. However, if the amount of uncompensated moments is small, a complete alignment with the field will not be achieved due to the presence of magnetic anisotropy.

The as-prepared and the ground sample were measured in a helium cryostat at 6 K in zero applied field and a field of 6 T applied parallel to the γ-radiation. The reason for not measuring the coated sample was that, as discussed above, the phosphate doublet component in Mössbauer spectra orders magnetically at 6 K giving a sextet in the spectra. This extra sextet with a splitting comparable to NiO would create some confusion in a spectrum, making it difficult to fit, when a magnetic field is applied.

The obtained low temperature high-field spectra are shown in Figure 4.3. These could both be fitted with three sextets: a broad sextet centred at approximately the same hyperfine field as found in zero applied field, and a narrow sextet on either side of this. The splitting between the two narrow sextets is about 8 T which is less than the $2 \cdot 6$ T expected, indicating an incomplete alignment of the spins with the applied field.

Mössbauer spectra were simulated for a range of uncompensated moments in an applied field of 6 T, according to the procedure in Appendix A.2. Two anisotropy models were considered, a uniaxial ($K_1 = 0$) and planar ($K_1 = \infty$). The simulated spectra were fitted to obtain the magnetic splitting and line area ratio, p, from Equation (2.28). These parameters were compared to those found

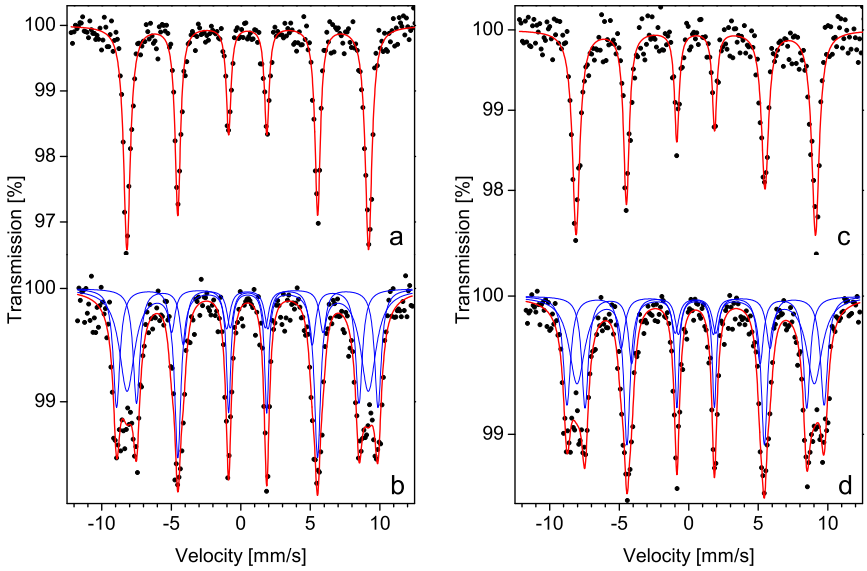

Figure 4.3: Mössbauer spectra of the as-prepared and ground NiO nanoparticles recorded at 6 K. (a-b) The as-prepared sample recorded in zero applied field and an applied field of 6 T, respectively. (c-d) The ground sample recorded in zero applied field and an applied field of 6 T, respectively. The small amount of iron in the samples is the reason for the poor statistics in the measured spectra. The thin blue lines are the individual sextets used to fit the data, and the broader red line is the sum of these.

by fitting the experimental spectra with sextets in order to find the amount of uncompensated moment in each of the samples.

As in Section 3.7.2 a measure of the uncompensated moment is ξ, defined as the ratio between the number of spins on the two sublattices. It was found that the spectra of both samples fitted well with a superposition between a broad sextet component equivalent to $\xi = 1$ and a component with $\xi = 0.993(1)$ or $\xi = 0.995(1)$ in the as-prepared and ground samples, respectively. This was found considering the planar anisotropy model, which is most realistic for NiO nanoparticles. However, in this region of uncompensated moments, both anisotropy models give approximately the same results.

Non-collinear spin orientations, known as spin canting, may occur in environments with a reduced coordination, such as the particle surface [139] or around vacancies [117]. Spin canting has been observed experimentally [140] and predicted to be present by numerical calculations [78]. The canting may be so strong that the field applied in an experiment cannot change the canting angle. In the Mössbauer spectra the broad sextet component equivalent to $\xi = 1$ is assumed to be due to such strongly canted spins. The large area of this sextet indicates a significant amount of canted spins in the particles.

4.2 Inelastic neutron scattering

Inelastic neutron scattering measurements were performed on the as-prepared and the coated samples. Each sample was measured at a range of temperatures

Sample	Instrument	Analyser mode	Measurement range	Final energy
As-prepared	TAS7	Single	T=10-330 K	5.0 meV
As-prepared	RITA-II	Focusing	B=0-8 T at T=300 K	3.6 meV
Coated	RITA-II	Imaging	T=2-300 K	5.0 meV
Coated	RITA-II	Imaging	B=0-13.5 T at T=200 K	5.0 meV

Table 4.1: Overview of the neutron scattering data recorded for the two samples.

in zero applied field and a range of fields at fixed temperatures. The measurements were done partly at the now decommissioned TAS7 spectrometer at Risø National Laboratory and partly at the RITA-II spectrometer at the Paul Scherrer Institute, Villigen, Switzerland. TAS7 was a triple axis spectrometer with a single analyser and detector. RITA-II, also a triple axis spectrometer, is equipped with a multi-blade analyser and position sensitive detector, that can be run in several different modes. The analyser modes of RITA-II are discussed in detail in Chapter 5. For clarity Table 4.1 gives an overview of the measurements of the NiO nanoparticles. The TAS7 data was recorded in 1998 by H. Vázquez, N. B. Christensen and K. Lefmann.

4.2.1 Neutron scattering from NiO nanoparticles

The aim of the neutron scattering study was to study the quantised infinite wavelength spin wave modes discussed in Section 3.7, in nanoparticles of NiO. These $\mathbf{q} = 0$ spin waves are observed as inelastic signals at the antiferromagnetic Bragg reflections. The antiferromagnetic ordering vector $\mathbf{Q}_{\mathrm{AFM}} = \{\frac{1}{2}\frac{1}{2}\frac{1}{2}\}$ was chosen as the scattering vector. As the samples are powders of randomly oriented particles, only the length of the scattering vector, κ, is measured. The antiferromagnetic ordering vector has a magnitude of $\kappa = Q_{\mathrm{AFM}} = 1.30$ Å^{-1}.

Due to the almost cubic nature of the NiO crystal structure, there will be 4 (almost) equivalent sets of {111} planes. One of these is the (111) plane in which the spins are confined and the other three are at angles of 70.5° to this, see Figure 4.4. However, calculating the magnetic structure factors of the three corresponding $\{\frac{1}{2}\frac{1}{2}\frac{1}{2}\}$ reflections shows that these are all zero. Thus, only the set of $\left(\frac{1}{2}\frac{1}{2}\frac{1}{2}\right)$ planes perpendicular to the antiferromagnetic ordering vector will contribute to the magnetic scattering cross section.

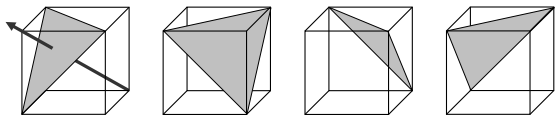

Figure 4.4: The four equivalent {111} planes in a cubic system. The arrow indicates the [111] direction perpendicular to the (111) plane.

A basic principle of magnetic neutron scattering states that only the components of a spin perpendicular to the scattering vector contribute to the scattering cross section, as expressed through the cartesian coordinate sum in Equation (2.18). In the superparamagnetic regime the spins flip between the two easy axes within the (111) plane, both perpendicular to the scattering vector along $\left(\frac{1}{2}\frac{1}{2}\frac{1}{2}\right)$, see Figure 4.5(a). Thus the full spin contributes to the scattering.

Also, due to the high out-of-plane anisotropy energy, the low energy resonance mode (ω_α from Section 3.7) is very elliptical. Thus, the spin wave amplitude is almost entirely within the (111) plane, again giving maximum contribution to the scattering, see Figure 4.5(b). The high energy resonance mode (ω_β from Section 3.7) is also elliptical, with the long axis perpendicular to the (111) plane, see Figure 4.5(c). This was shown experimentally in Paper V for hematite which, as discussed above, has the same anisotropy configuration as NiO. The spin wave amplitude is almost entirely along κ, such that the cartesian coordinate sum Equation (2.18) becomes small, predicting a negligible contribution to the scattering at $\kappa = (\frac{1}{2}\frac{1}{2}\frac{1}{2})$ from the high energy mode.

The ellipticity of this spin wave mode was also observed in bulk NiO by Hutchings and Samuelsen [105] using thermal neutrons. They observed the high energy resonance mode at the antiferromagnetic $\left(\frac{3}{2}\frac{1}{2}\frac{1}{2}\right)$ and $\left(\frac{3}{2}\frac{3}{2}\frac{1}{2}\right)$ scattering vectors, but it was absent at the $\left(\frac{1}{2}\frac{1}{2}\frac{1}{2}\right)$ scattering vector.

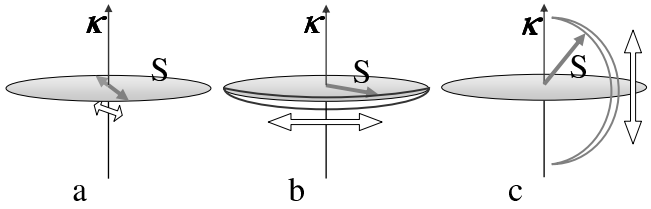

Figure 4.5: Dynamics of the spins in one of the sublattices. The spins in the other sublattice are antiparallel to these, but have been omitted for clarity. (a) Superparamagnetic relaxation. (b) The low energy resonance mode. (c) The high energy resonance mode. For clarity, the extent of the oscillation has been greatly exaggerated in the two resonance modes,

In the present experiments a signal from the high energy resonance mode was sought at the $\left(\frac{1}{2}\frac{1}{2}\frac{1}{2}\right)$ scattering vector as well as the $\left(\frac{3}{2}\frac{1}{2}\frac{1}{2}\right)$ scattering vector at $\kappa = 2.50$ Å^{-1}. No signal was observed at either scattering vector at energy transfers up to 5.2 meV, which was the maximum allowed by the geometry of the RITA-II spectrometer. As discussed in Section 3.5 and Ref. [77] the out-of-plane anisotropy in NiO nanoparticles is expected to be close to the value observed in bulk NiO. Thus the resonance signal should be found at about 4.5 meV. However, due to the reduction in the scattering cross section with energy transfer, from Equation (2.22), the scattered intensity at 4.5 meV is expected to be very low. If the signal is to be observed the high intensity of a thermal neutron instrument would be required.

As the high energy resonance mode is not observed in the neutron data, only the low energy resonance mode will be discussed in the following.

4.2.2 Fitting neutron data

In the following the procedure for fitting inelastic neutron data will be outlined. The acquirement and combining of data measured with the imaging or focusing modes of the RITA-II spectrometer was performed as described in Chapter 5.

The neutron scattering data consists of scans in energy recorded at the antiferromagnetic ordering vector, $\kappa = 1.30$ Å^{-1}, which is a purely magnetic reflection with no structural component. This magnetic signal consists of a Bragg

reflection, quasielastically broadened due to the superparamagnetic relaxation and inelastic signals either side of this from the excitation and de-excitation of energy levels of the $\mathbf{q} = 0$ spin waves.

The magnetic signals measured by inelastic neutron scattering on NiO nanoparticles are very weak, compared to the background. It is thus of utmost importance to ensure that any background signal not associated with the magnetic properties of the particles can be accounted for and subtracted. The most important contribution to this background is the strong incoherent signal due to water adsorbed on the particles [141]. As incoherent signals are isotropic, they can be fitted at other scattering vectors than the antiferromagnetic, to avoid confusion between the incoherent signal and the magnetic signal.

Background

In any neutron scattering experiment there will be a background, C, from fast neutrons and noise. This is small and constant in energy and thus straightforward to include in the fits.

In order to fit the inelastic neutron data, it is necessary first to establish the energy resolution function as any modelled signal must be convoluted by this before fitting to the experimental data. The resolution function, $R(\varepsilon)$, is determined by fitting data obtained at the lowest temperature, as this contains no excitations or broadening of the signal. It is found that the resolution function can be expressed as the sum of a narrow Gaussian line shape with a HWHM of 60 μeV to 80 μeV depending on the energy of the incoming neutrons and a Lorentzian line shape with an amplitude about 2% of the Gaussian and about twice the width. Due to the intensity in the long "tails" of a Lorentzian line shape, this will seem very broad in a logarithmic plot. The exact parameters of the resolution function depend on the incoming energy of the neutrons and the angular openings of the various collimators.

The next step is to determine the contribution from the water. Inelastic scans are recorded in the incoherent background either side of the antiferromagnetic reflection, $\kappa = 1.00$ Å^{-1} and $\kappa = 1.60$ Å^{-1}. In this region the incoherent background slopes linearly in κ, so averaging the data from the two background scans gives a reasonable background scan at $\kappa = 1.30$ Å^{-1}. As shown in Figures 5.5 and 5.10 even when using the multi-blade analyser modes of the RITA-II spectrometer, these background scans do not overlap the the magnetic reflection. The water bound to the surface of the nanoparticles will give rise to a combination of a Dirac delta function and a Lorentzian line shape due to dynamics in the water, which increase as the temperature is increased. Thus, the contribution from water may be expressed as

$$I(\varepsilon)_{\mathrm{Incoh}} = A_0\delta(\varepsilon) + D(\varepsilon)\frac{A_0'}{\pi}\frac{\Gamma_{\mathrm{w}}}{\varepsilon^2 + \Gamma_{\mathrm{w}}^2} \tag{4.4}$$

where $\varepsilon = \hbar\omega$, A_0 is the intensity from the bound water, A_0' is the intensity from the dynamic water and Γ_{w} is the width of the Lorentzian due to the dynamic water. $D(\varepsilon)$ is the detailed balance factor, describing the difference in the scattering function on the negative and positive side of the elastic signal. It

is given by

$$D(\varepsilon) = \frac{\varepsilon}{k_{\mathrm{B}}T}\left(\frac{1}{\exp\left(\frac{\varepsilon}{k_{\mathrm{B}}T}\right)-1}+1\right) = \frac{\varepsilon}{k_{\mathrm{B}}T}\left(n(\varepsilon)+1\right) \tag{4.5}$$

where $n(\varepsilon)$ is the Bose factor from Equation (2.20). This definition of the detailed balance factor differs from that stated in Refs. [91,127,142,143], where the expression was not normalised by $k_{\mathrm{B}}T$. However, the data in the previous publications was fitted using Equation (4.5).

Not normalising Equation (4.5) by $k_{\mathrm{B}}T$ results in a temperature dependent value of $D(\varepsilon)$ at $\varepsilon \approx 0$. Contrary, Equation (4.5) gives $D(\varepsilon) \approx 1$ at $\varepsilon \approx 0$ at all temperatures[1]. Both definitions fulfill the detailed balance criterion that

$$\mathcal{S}(-\boldsymbol{\kappa}, -\omega) = \exp\frac{-\varepsilon}{k_{\mathrm{B}}T}\,\mathcal{S}(\boldsymbol{\kappa}, \omega), \tag{4.6}$$

but Equation (4.5) is the most convenient when fitting data.

Due to the poor quality of the TAS7 data the water contribution was not fitted separately in this data set, but included as a broadening of the resolution function.

It is observed in the incoherent signal, that there is an asymmetry of the signal, with a broad feature on the negative side. This is due to contamination of the signal by higher order neutrons. The absence of this signal on the positive side is due the presence of a Be or BeO filter cutting off neutrons with energies higher than ≈ 5.1 meV and ≈ 3.8 meV respectively as described in Section 2.1.3. This asymmetry can be included in a fit by adding half a Lorentzian line shape to the background spectrum at $\varepsilon \lessapprox 0$, depending on the final energy used in the experiment. In the data obtained at RITA-II in the monochromatic imaging mode (see Chapter 5) there is a further asymmetry, due to inelastic cross-talk from one blade to the neighbouring counting window, as discussed in detail in Paper II. This cross-talk signal may be fitted by increasing the size of the half Lorentzian line shape.

Thus, including the contributions from water, the asymmetry parameters and a constant background, the incoherent spectrum obtained from an average of spectra recorded at $\kappa = 1.00$ Å^{-1} and $\kappa = 1.60$ Å^{-1} can be fitted. Fixing the parameters obtained in this way, the components associated with the magnetic properties of the particles may now be fitted.

Magnetic signal

The magnetic Bragg reflection may be fitted with a quasielastic Lorentzian line shape, as discussed in Section 2.1.2. When the flipping rate of the spins due to superparamagnetism increases, the width of the Lorentzian increases [127].

Collective magnetic excitations give rise to inelastic signals. Due to dampening of the spin waves the signals may be fitted with a damped harmonic oscillator model [30,91,127].

The total magnetic signal can thus be fitted by

$$I(\varepsilon)_{\mathrm{Magn}} = D(\varepsilon)\frac{A_1}{\pi}\frac{\Gamma}{\varepsilon^2+\Gamma^2} + D(\varepsilon)\frac{A_2}{\pi}\frac{2\gamma\varepsilon_0^2}{(\varepsilon^2-\varepsilon_0^2)^2+4\gamma^2\varepsilon^2} \tag{4.7}$$

[1]The expression is not valid at $\varepsilon = 0$, here a value of $D(0) = 1$ is defined in the fitting routine

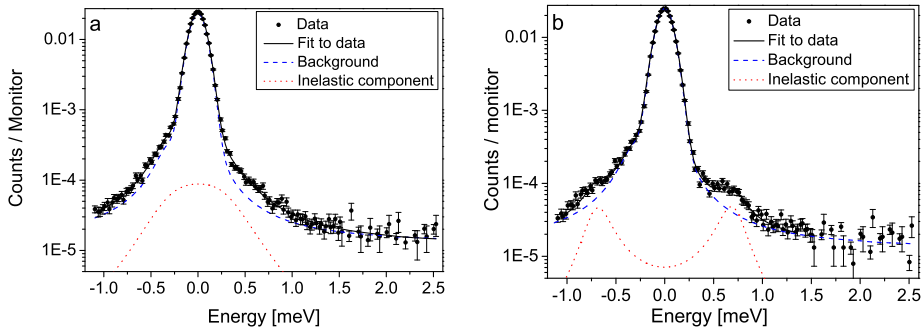

Figure 4.6: Fits to the raw data obtained from the coated sample at 200 K with $\kappa = 1.30$ Å^{-1}. The full black line is the total fit to the data. The dashed blue line is the fit to the incoherent signal and the dotted red line is the inelastic signal, convoluted with the resolution function. (a) Data obtained at zero applied field showing a broad inelastic signal. (b) Data obtained with an applied field of 4 T.

where A_1 is the area of the quasielastic peak with of width Γ, A_2 is the area of the inelastic peaks with widths γ and centre positions $\pm\varepsilon_0$.

Thus, the spectra obtained at the antiferromagnetic ordering vector may be described as a convolution between the resolution function and the sum of the incoherent and magnetic signals

$$I(\varepsilon) = \left[I(\varepsilon)_{\text{Incoh}} + I(\varepsilon)_{\text{Magn}} + C\right] \otimes R(\varepsilon). \tag{4.8}$$

When fitting data obtained at a series of temperatures, it is necessary to fit the incoherent background at each temperature, before fitting the magnetic parameters. In data obtained at a fixed temperature in a range of fields, it was found that it is sufficient to obtain just one incoherent background spectrum, at 0 T because, as expected the incoherent signals do not depend on the applied field.

An example of the raw data recorded at $\kappa = 1.30$ Å^{-1} from the coated sample at 200 K in zero applied field and an applied field of 4 T is shown in Figure 4.6. The spectra show the data from Figure 5.6, recorded using 7 blades in the monochromatic imaging mode. Here, the total fit to the data is shown by a black line in both figures, the incoherent background is shown as a dashed blue line and the inelastic component convoluted with the resolution function is shown by a dotted red line.

With the large number of parameters involved in fitting a spectrum, it is important to ensure a consistent method of fitting. Software was written using the Matlab `specnd` package [144] to automatically fit the resolution function, incoherent spectrum and magnetic signals as outlined above. In this way changes in the fitting routine, e.g., changing the order of fitting parameters can be carried out in a consistent way. During fitting, the parameters obtained at one temperature or field are used as the starting guess for the next temperature or field, as illustrated in Figure 4.7. There is an overlap of the data from the field series and the temperature series at zero applied and 200 K for the coated sample and zero applied and 300 K for the as-prepared sample. As it is seen in Figures 4.9 and 4.10 the fitted parameters from these data sets are consistent within the uncertainty.

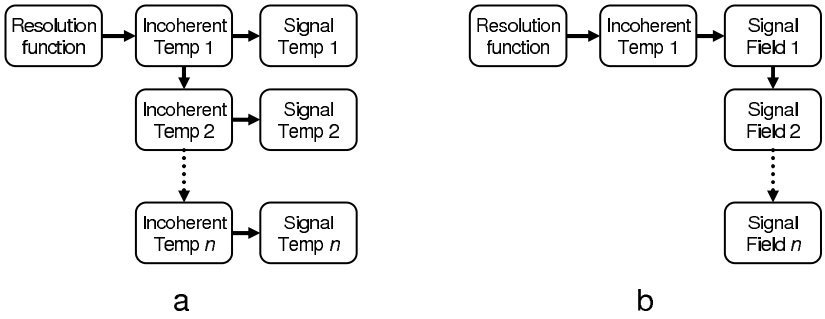

Figure 4.7: Outline of the method for automatic fitting of neutron data. (a) When fitting temperature data the incoherent signal must be fitted for each temperature. (b) In the field series just one incoherent signal is fitted at the temperature where the field series is obtained.

4.2.3 Determining K_2 by the area method

At the lowest temperatures in zero applied fields the spins will be almost static and aligned along the easy direction. The magnetic scattering intensity is predominantly in the quasielastic peak, comprising the Bragg reflection. As the temperature is increased more spin wave states, or oscillations of the spins, become excited and the areas of the inelastic scattering peaks grow, while the area of the quasielastic peak decreases. This is equivalent to the situation presented classically in Figure 4.1.

According to the polarisation argument above the spins are always perpendicular to the scattering vector and the full length of the spins contribute to the scattered intensity. As the number of spins is constant the sum of the quasielastic and inelastic areas contains the full magnetic scattering and should thus be proportional to $\langle S \rangle^2$. This is seen to be the case, at least for the as-prepared sample, in Figure 4.8. The full line is $\langle S \rangle^2$ data from Ref. [145], where the magnetisation of the as-prepared sample was measured, finding a Néel temperature of ≈ 460 K. This reduction in the Néel temperature and the fast decrease of the sublattice magnetisation observed in the coated sample is characteristic of nanoparticles [129]. The slower decrease of the sublattice magnetisation in the as-prepared sample may be due to interactions between the particles.

The temperature dependence of the fraction of the magnetic scattering intensity that is found in the quasielastic signal has been calculated by three dimensional Boltzmann statistics [91, 142].

$$\frac{A_1}{A_1 + A_2} = \frac{I_0(\frac{1}{2}\alpha_2) + I_1(\frac{1}{2}\alpha_2)}{2I_0(\frac{1}{2}\alpha_2)} \quad \frac{\alpha_1^{-\frac{1}{2}} e^{-\alpha_1} + \frac{1}{2}\sqrt{\pi}(2 - \alpha_1^{-1})\mathrm{erf}(\sqrt{\alpha_1})}{\sqrt{\pi}\mathrm{erf}(\sqrt{\alpha_1})} \tag{4.9}$$

where $\alpha_{1,2} = K_{1,2}V/k_\mathrm{B}T$, $I_n(x)$ is the modified Bessel function of the n'th order and $\mathrm{erf}(x)$ is the error function.

Assuming the value of K_1 reported for bulk NiO and the particle volume measured by TEM the measured data for the coated sample can be fitted with the expression in Equation (4.9) to give $K_2V/k_\mathrm{B} = 200(45)$ K equivalent to $K_2 = 11(2) \cdot 10^3$ Jm^{-3} or an anisotropy field of $B_{\mathrm{A}2} = 20(5)$ mT, see Figure 4.9(a). Again, as $K_1 \gg K_2$ the exact size of K_1 is not very important.

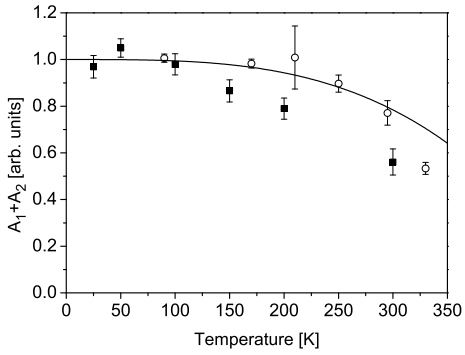

Figure 4.8: The sum of the contributions A_1 and A_2 for the two samples. ∘ is data from the as-prepared sample and ■ is data from the coated sample. The line is $\langle S \rangle^2$ data from the as-prepared sample obtained from Ref. [145].

At low temperatures $k_{\mathrm{B}}T \ll K_2V$ Equation (4.9) may be approximated by a linear expression equivalent to Equation (4.1)

$$\frac{A_1}{A_1 + A_2} \approx 1 - k_{\mathrm{B}}T \left(\frac{1}{2|K_1|V} + \frac{1}{2|K_2|V} \right). \tag{4.10}$$

Applying this to the measured data up to 150 K (the dotted line in Figure 4.9(a)) gives a value of $K_2V/k_{\mathrm{B}} = 206(10)$ K in accordance with the value obtained using Equation (4.9) above.

The value of $B_{\mathrm{A}2} = 20(5)$ mT obtained by Equation (4.9) is in agreement with the value of $B_{\mathrm{A}2} = 15(2)$ mT obtained by Mössbauer spectroscopy in Equation (4.1). The large uncertainty on the neutron result is due to the weakness of the inelastic signals giving large uncertainties in the fits to the data.

4.2.4 Determining K_2 by the resonance energy method

At low temperature the position of the inelastic signal has been determined to be $\varepsilon_0 = 0.47(1)$ meV. The expression

$$\varepsilon_0 = g\mu_{\mathrm{B}}\sqrt{2B_{\mathrm{A}2}B_{\mathrm{E}}} \tag{4.11}$$

from Section 3.7 gives $B_{\mathrm{A}2} = 7.6(3)$ mT equivalent to $K_2 = 4.2(2) \cdot 10^3$ Jm^{-3}, which is significantly lower than the values found above.

As discussed in Section 3.7.2 this difference was initially explained in Paper X by a decrease of the resonance energy as a result of uncompensated moments. However, the more detailed calculations in Paper XII showed that due to the large difference between K_1 and K_2, the presence of uncompensated moments in the nanoparticles will only shift the resonance energy slightly.

It is discussed in Paper XI how a lower exchange field may explain the underestimate of the in-plane anisotropy. Such a lowering of the exchange field may be explained by missing exchange bonds at the particle surface and spin canting in the particles [117], however a lowering of nearly 50% is required to account for the difference in the measured values of the anisotropy.

Thus, the conventional method for determining the anisotropy from the antiferromagnetic resonance, Equation (4.11), cannot directly be applied to

nanoparticles in the same way as for bulk materials, as the exchange field is not well-determined.

In the as-prepared sample at low temperature the resonance energy is larger than in the coated sample. This is due to the dampening of the dynamics by the interaction, giving larger energy gaps between the excitation states. This difference in resonance energy due to interactions decreases with temperature until the resonance energies in the two samples are similar at ∼250 K. This may be considered as the order of magnitude for the interaction energy. As discussed in Paper XI the temperature dependencies of ε_0 in both samples are empirically fitted with polynomial expressions.

The scattering intensities of the inelastic samples have been calculated within a proportionality constant for the two samples using the polynomial expressions for ε_0 and the scattering cross section in Equation (2.22). After dividing by the detailed balance factor the intensities may be fitted to the measured inelastic areas, A_2. The expressions quantitatively fit the measured data, except above 250 K.

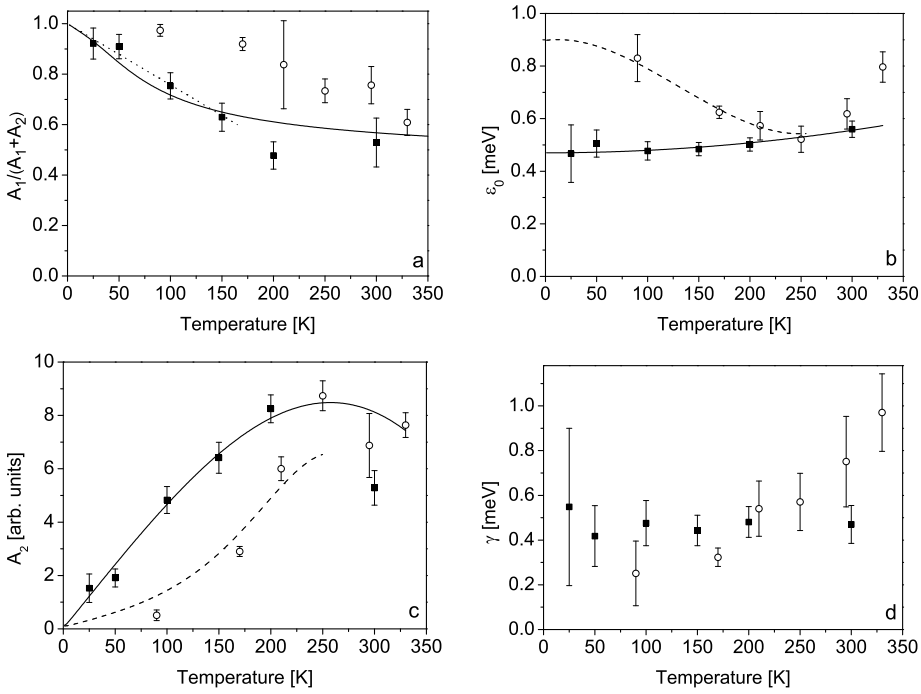

Figure 4.9: Fits to temperature series of data obtained in zero applied field. ∘ is data from the as-prepared sample and ■ is data from the coated sample. The full lines are fits to the data from the coated sample and the dashed lines are fits to the data from as-prepared sample. (a) The ratio of the quasielastic signal to the total inelastic signal. The full line is a fit using Equation (4.9) and the dotted line is from the approximation to this in Equation (4.10). (b) The position of the inelastic signals fitted empirically with polynomial expressions. (c) The area of the inelastic signal from the collective magnetic excitations. The lines are calculated from the polynomial expressions in (b). (d) The width of the inelastic signals from the collective magnetic excitations.

It was observed during the analysis of the monochromatic imaging mode

of the RITA-II spectrometer that the value of ε_0 depends on the number of blades used for the measurement, see Figure 5.7(d). It is shown there that the inner blades preferentially measure the largest particles, while the outer blades preferentially measure smaller particles. The value of ε_0 measured by the outer blades is larger than the value measured by the inner blades. Assuming the exchange field is similar in the different sized particles, this qualitatively indicates an increase of the anisotropy as the particle size decreases. This is in agreement with results obtained by measuring the size dependence of the in-plane anisotropy in hematite nanoparticles, where the anisotropy was found to increase with decreasing particle size [97].

4.2.5 Isotropic relaxation

In ferromagnetic particles with a uniaxial anisotropy a transition to a regime of isotropic relaxation is predicted to occur at temperatures $k_BT \gtrsim KV$ [146]. This is expected to result in a decrease of the resonance energy, ε_0, leading to a collapse of the inelastic signals to a broad signal around zero energy along with a sharp increase of the line width, γ [50, 146].

In the neutron data a value of $K_2V/k_\mathrm{B} \approx 200$ K is observed in the coated sample. The resonance energy is observed to increase in both samples above 250 K and a resulting decrease of scattering intensity is observed in both samples. The width of the inelastic signals in the coated sample is almost constant at all temperatures whereas it increases with temperature in the as-prepared sample, see Figure 4.9(d). This may be due to a change in the distribution in the interaction energies as the temperature increases resulting in a distribution of resonance energies, broadening the inelastic resonance signal.

Thus, the temperature dependence of the resonance energy is contrary to what is expected in a regime of isotropic relaxation. However, even at $k_BT \gg K_2V$ there will not be true isotropic relaxation as there is still a strong out-of-plane anisotropy energy and $k_BT \ll K_1V$.

4.2.6 Field dependence

Both sets of field data were measured at elevated temperatures, in order to ensure a high intensity of the inelastic signal. Due to a smaller amount of sample and shorter measuring times the data from the as-prepared sample at 300 K is of an inferior quality to that from the coated sample measured at 200 K, giving less well-defined parameters in the fits. Also, the as-prepared sample data is only available up to 8 T due to technical difficulties during the measurement. Therefore the main emphasis is on the data measured from the coated sample.

At large applied fields the moment of a particle will align with the applied field. As shown in Paper XI the field dependence of the resonance energy may be written

$$\varepsilon(B_\mathrm{appl}) = \sqrt{\varepsilon_0^2 + (g\mu_\mathrm{B}B_\mathrm{appl})^2}. \tag{4.12}$$

This expression is valid at zero applied field and at large applied fields, but not in moderate applied fields where the spin dynamics enter a complex regime. The expression in Equation (4.12) fits the field data obtained from the coated sample quite well except around 2 T, see Figure 4.10(a). The fit gives a value

of $\varepsilon_0 = 0.48(3)$ meV and a value of the g-factor of $g = 2.19(6)$ for the coated sample. Fitting the data for the as-prepared sample in the same way yields the values $\varepsilon_0 = 0.49(2)$ meV and $g = 2.34(14)$, see Figure 4.10(b). These values of the g-factor are in accordance with the reported observations of a non-quenched orbital momentum in NiO [114, 115].

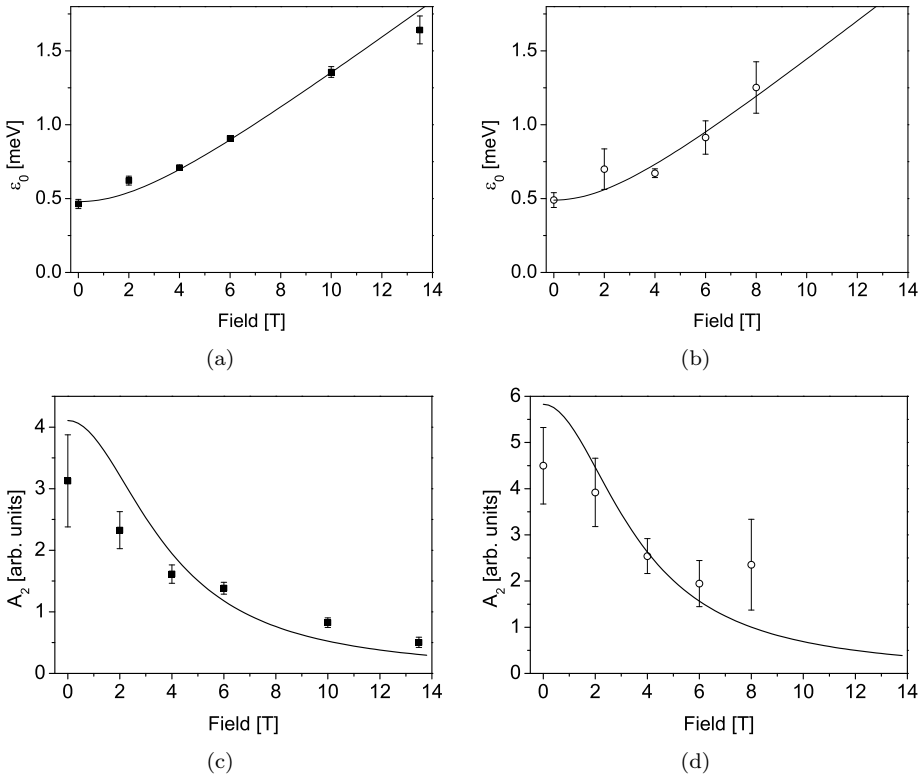

Figure 4.10: Fits to the field series. (a) The position of the inelastic signal in the coated sample. (b) The position of the inelastic signal in the as-prepared sample. The lines are fits to Equation (4.12). (c) The intensity of the inelastic signal from the coated sample. (d) The intensity of the inelastic signal from the as-prepared sample. The lines are calculated from the fits in (a) and (b).

Calculating the scattering intensity by Equation (2.22), gives the lines in Figures 4.10(c) and 4.10(d). The intensities are in qualitative agreement with the measured data.

In an alternative approach in order to understand the data at intermediate fields, the orientation of the spins are found by numerical energy minimisation calculations, see Appendix A. At modest applied fields the spins will be oriented close to the in-plane easy axis independent of the orientation of the applied field. Up to an applied field of $B_{\text{appl}} = 5$ T the maximum deviation is less than 30°. Thus, as in an antiferromagnet, the spin orientation will be dominated by the anisotropy field. An expression for the resonance frequency of an antiferromagnet with an applied magnetic field at an arbitrary direction to the easy axis is obtained by rewriting Equation (21) in [147]. This expression is valid at low temperatures and low applied fields, when the spins are close to the in-plane

anisotropy direction.

$$\hbar\omega = g\mu_B\left[\left(\frac{\varepsilon_0}{g\mu_B}\right)^2 + B_{\rm appl}^2\left(\cos^2\theta(1-y)^2 + \frac{1}{2}\sin^2\theta\right)\ldots \right.$$
$$\left. \pm\frac{1}{2}B_{\rm appl}\sqrt{B_{\rm appl}^2\sin^4\theta + 8\left(\frac{\varepsilon_0}{g\mu_B}\right)^2\cos^2\theta(2+y)(1-y)^2}\right]^{\frac{1}{2}} \quad (4.13)$$

where

$$y = \frac{B_{\rm appl}^2\sin^2\theta}{\left(\frac{\varepsilon_0}{g\mu_B}\right)^2}, \quad (4.14)$$

θ is the angle between the applied field and the easy axis and ε_0 is the resonance energy at zero applied field. Assuming an in-plane anisotropy field of $B_{\rm A2} = 20$ mT and a ratio between the number of spins in the two sublattices of $\xi = 0.994$ it is found that Equation (4.13) with a value of $\varepsilon_0 = 0.43$ meV gives a good description of the data from the coated sample up to a field of 5 T plotted as the dashed line in Figure 4.11(a). Above this field the system no longer resembles an antiferromagnet and the expression is no longer valid. At large values the applied field will dominate and the resonance frequency will tend towards $\hbar\omega \approx g\mu_B B_{\rm appl}$, where again $g = 2.19$. This is plotted as the solid line in Figure 4.11(a), and the resonance frequency is indeed seen to approach this at the highest fields.

Again, calculating the scattering intensity of the inelastic signal by Equation (2.22) gives the lines in Figure 4.11(b). The dashed and solid lines correspond to the low field and high field expressions respectively. Both lines are multiplied by a common proportionality factor and are seen to be quantitatively in accordance with the measured data, except at zero applied field.

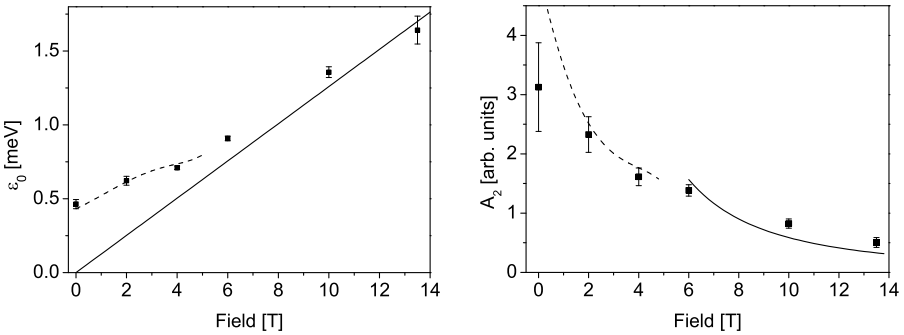

Figure 4.11: Fits to field data using the numerical model. (a) The position of the inelastic signal in the coated sample, (b) The intensity of the inelastic signal from the coated sample.

The two models of the field dependence of the resonance frequency are valid in different ranges of the applied field. The first model is only valid at zero applied fields and at high values of the applied field. This model can be used to obtain the value of the g-factor at high applied fields. The second model was considered due to the shortcomings of the first model in explaining the

data at moderate applied fields. In applied fields, below the estimated limit of validity of ~ 5 T, the calculated field dependence of the resonance energy is in accordance with measured resonance energy.

In both data sets the width of the inelastic signal has a characteristic minimum around 4 T, see Figure 4.12. This is not predicted by the calculations for either of the two models, and thus remains to be explained.

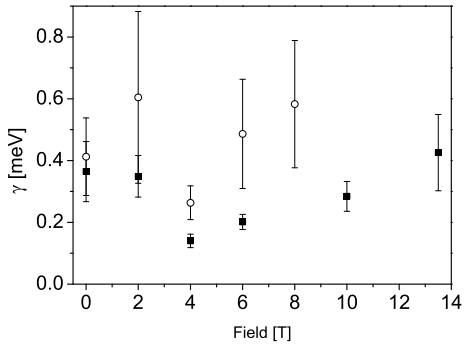

Figure 4.12: The widths of the inelastic signals as a function of applied fields. ○ is data from the as-prepared sample and ■ is data from the coated sample. A characteristic minimum is observed around 4 T, most notable in the data from the coated sample.

4.3 Comparison with literature

In the following section the results obtained above are discussed in relation to the published literature regarding NiO nanoparticles.

4.3.1 Size and shape

In Chapter 3 the NiO nanoparticles are well characterised with respect to the structure, size and shape of the particles. The purity of the NiO with respect to other phases was also ensured. The plate shape of NiO particles derived from $Ni(OH)_2$ particles has been noted in several publications [76, 79, 145, 148]. This particle shape is inherited from the precipitated precursor $Ni(OH)_2$ particles, which have been known to be plate shaped since 1949 [149], albeit for significantly larger particles than those studied here.

X-ray diffraction patterns of the plate shaped NiO particles have previously always been fitted assuming spherical particles [79, 145, 148]. As shown in Table 3.1, this gives an erroneous estimate of the particle volume. Also, most of the numerical modelling of NiO particles was done assuming spherical particles [79,150]. However, it is likely that the plate shape of the particles resulting in an increase of the surface area per volume by almost a factor of two is relevant for the magnetic properties of the particles.

4.3.2 Uncompensated moment

An abnormally high magnetic susceptibility was observed in NiO nanoparticles in 1956 by Richardson and Milligan [81]. Since then numerous papers have

been written on the subject of the magnetic properties of NiO nanoparticles. The susceptibility was found to increase linearly with the reciprocal particle size [29]. This has later been found to be applicable to NiO particles prepared by several different methods, such that the particle size may be estimated by measuring the susceptibility, which is useful in catalysis [151]. The increase in susceptibility was found to be due to superparamagnetism [29].

Associated with the increase in susceptibility Schuele and Deetscreek found a weak ferromagnetic moment observed as hystereses in magnetisation data from NiO nanoparticles. This was explained on the basis of the uncompensated moments in antiferromagnetic nanoparticles proposed by Néel [27, 28]. A weak ferromagnetic moment has been observed in many studies of NiO nanoparticles [29, 79, 80, 152, 153], but the corresponding fraction of uncompensated moments has not been quantified.

The suggestion that the observed moment is due to Ni^{3+} was disproved by placing NiO nanoparticles in a reducing hydrogen atmosphere, giving no change in the observed susceptibility [29].

The weak ferromagnetic moment is generally measured by magnetisation measurements. In the superparamagnetic state the spins of a particle flip coherently. Thus each particle in a sample will behave as a paramagnet with a moment of the size of the uncompensated moment [154]. The magnetisation of the sample can be described by a Langevin function,

$$L(x) = \coth x - \frac{1}{x} \qquad \text{where} \qquad x = \frac{\mu B_{\text{appl}}}{k_{\text{B}} T} \tag{4.15}$$

where μ is the particle magnetic moment and B_{appl} is the applied field.

Fitting Langevin functions to the measured magnetisation data has been used to measure the uncompensated moment [152, 155, 156]. But, as discussed by Silva *et al.* [157], the inevitable size distribution in samples of nanoparticles will give an overestimate of the average moment. Also, the presence of magnetic anisotropy will lead to non-Langevin magnetisation data [158, 159].

A more reliable approach is to fit the initial mass susceptibility at low applied fields [158]. This depends linearly on the average of the square of the particle moment, $\langle \mu^2 \rangle$, and is not sensitive to anisotropy or particle size distribution. In Paper VIII, this approach was taken, yielding uncompensated moments of 2%–3%. However, as discussed in the paper these values seem overestimated compared to the values of $\xi = 0.994$, equal to $\approx 0.6\%$ uncompensated moments in one sublattice, obtained by high field Mössbauer spectroscopy. This may be due to a difference in the sensitivity of the two techniques in the presence of a distribution of particle sizes, the Mössbauer spectroscopy signal being weighted by the volumes of the particles and the magnetometry signal by the moments of the particles. Also, the interparticle interactions in the as-prepared sample and the incomplete removal of these in the ground sample may increase the measured moment. Néel's model for a random occupation of uncompensated moments on the surface of a cubic particle ($\delta \approx n_{\text{s}}^{1/3}$) gives a value of $\approx 0.3\%$ uncompensated moments in one sublattice for particles with the volume measured here. However taking the plate shape of the particles into account gives $\approx 0.7\%$ uncompensated moments in one sublattice in accordance with the values measured by Mössbauer spectroscopy.

Recently, samples of NiO nanoparticles doped with up to 2% of iron were shown to have a ferromagnetic contribution at temperatures as high as room

temperature [24]. The samples were prepared in the same way as in the present work but at 600°C, resulting in particles about 40 nm large. The ferromagnetic contribution was determined to be due to clusters of iron within the NiO particles, and thus not associated with the NiO itself. This is not the case in the doped samples studied here by Mössbauer spectroscopy. As discussed in Paper VIII the absence of quadrupole splitting shows that the iron is evenly dispersed within the particles.

4.3.3 Modelling of NiO nanoparticles

Modelling of NiO nanoparticles has been done using micro-magnetic modelling [78, 79, 148] and a Monte Carlo method [150]. Both these modelling techniques result in multi-sublattice structures, with up to eight magnetic sublattices in the micro-magnetic model [79]. The micro-magnetic model was found to reproduce the large uncompensated moments and hysteresis behaviour of the magnetisation experimentally measured experimentally [79]. The model uses the bulk exchange and anisotropy parameters from Ref. [105]. As discussed in Section 3.5.1, the bulk in-plane anisotropy energy quoted there is several orders of magnitude larger than other published values. However, by serendipity the value given in Ref. [105] is close to the in-plane anisotropy energy measured in NiO nanoparticles in the present work, so it may be applicable to a nanoparticle model. The model also includes a surface anisotropy of 2 K per Ni atom, obtained from electron paramagnetic resonance measurements of isolated Ni^{2+} ions in Al_2O_3 [160]. This is equivalent to a volume anisotropy of $K \approx 8 \cdot 10^5$ Jm^{-3}, which is about 100 times larger than the values of K_2 measured in the present study by neutron scattering and Mössbauer spectroscopy. This value seems very high if the increase of K_2 compared to bulk is ascribed to a surface contribution, as a large fraction of the atoms in a particle are on the surface. But, such a high anisotropy for some of the surface spins may account for the large amount of canted spins observed in the high-field Mössbauer spectroscopy data.

The Monte Carlo modelling technique also yields a multi-sublattice structure, but without assuming a specific surface anisotropy [150]. However, the particles simulated by both methods are, in general, smaller than the particles studied experimentally here. Indeed the number of sublattices falls sharply with an increase of the particle size in the micro magnetic model [79].

The magnetic neutron scattering cross section from a multi-sublattice magnetic structure is not a simple matter. A thorough study by calculating the structure factors of different sublattice configurations would be necessary in order to determine the expected contributions to the reflections in the diffraction pattern, and the correlation lengths of these. In neutron diffraction of the NiO nanoparticle samples a temperature dependent, i.e. magnetic, signal was only observed in the purely magnetic reflections, not the structural. This, along with the similarity of the magnetic correlation length perpendicular to the plate faces and the structural one measured by XRD would seem to indicate a well ordered antiferromagnetic structure, that does not have multiple sublattices.

4.3.4 Interparticle interactions

Only a small part of the literature published on NiO nanoparticles has been concerned with the possible interactions between the particles. By Mössbauer

spectroscopy and magnetisation measurements, it was shown in Ref. [76] that separation and especially coating of NiO nanoparticles considerably reduces the blocking temperature, i.e., the temperature where superparamagnetism begins to dominate. Recently, a very strong decrease of the blocking temperature in rod shaped NiO particles was also found by ac susceptibility and electron magnetic resonance measurements of oleic acid coated particles compared to as-prepared particles [161,162]. As discussed in Section 3.1.2 many of the samples presented in the literature were prepared in the same way as the samples presented in the present work. Thus, interparticle interactions are likely to be present in these samples.

Non-interacting NiO nanoparticles dispersed in a SiO_2 matrix were found to have similar magnetic properties to interacting particles [80]. Indeed, the inverse size dependence of the mass susceptibility, discussed above, was observed to be valid for NiO nanoparticles prepared in a large range of different ways, ranging from pure as-prepared NiO to dispersion in different matrix materials [151]. This would suggest that the uncompensated moment of NiO nanoparticles does not depend on the interpaticle interactions. This result was confirmed in Paper VIII, where the difference in uncompensated moment between samples of weakly and strongly interacting particles was not found to be significant.

Chapter 5

The RITA-II triple axis spectrometer

As described above, a project was started at Risø National Laboratory in 1993 to enhance the rate of data recording of a triple axis spectrometer while still keeping a flexible control of the resolution function and maintaining a low background [52]. The way of achieving this was to construct a multi-bladed analyser that could direct the beams onto different parts of a large 2 dimensional position sensitive detector (PSD). Both the analyser and the detector were to be situated in a tank to eliminate background contributions.

Two instruments, RITA-I and RITA-II were constructed at Risø. After the closure of the DR3 reactor at Risø the RITA-II spectrometer was moved to the Paul Scherrer Institute in Villigen, Switzerland where it was commissioned largely due to D. F. McMorrow.

At the RITA-II instrument [163] the analyser consists, at present, of 7 blades mounted on a linear rack. Each blade can rotate about its centre and the entire rack can rotate about its centre, see Figure 5.1. A more detailed description of the analyser setup can be found in Papers I and II. With this analyser rack a range of different modes of operation can be envisioned. Many of these were conceptually presented in Ref. [164].

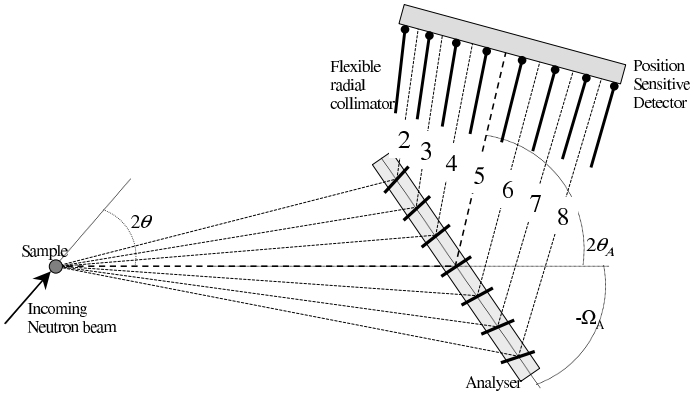

Figure 5.1: The geometry of the RITA-II spectrometer.

5.1 The monochromatic point-to-point focusing mode

Until recently the monochromatic point-to-point focusing mode was the only analyser mode in general use. Here, the scattering angle and thus final energy measured by each analyser blade is the same and all the analyser blades are set to scatter to a single point on the detector, as illustrated in Figure 5.2(a). This gives a coarse resolution in κ as the seven blades cover a large range of scattering angles. In return this allows a large intensity in a small area of the detector to be measured, giving less background signal. In general the resolution will be too bad if all seven blades are used and a practical maximum of three blades is used. An exception to this is inelastic experiments on nanoparticles, where the diffraction peak is very broad and the coarse κ resolution is unimportant, as discussed below.

5.2 The monochromatic imaging mode

A part of the present PhD project has been to develop and implement a monochromatic imaging mode. Here the analyser blades all scatter at the same angle, but to different parts of the detector, enabling a separation of the contributions from each of the seven blades. This is illustrated in Figure 5.2(b).

The derivation and implementation of the monochromatic imaging mode will not be discussed in detail here as this has been done in Paper I. Instead, the use of the mode for measuring nanoparticles will be presented.

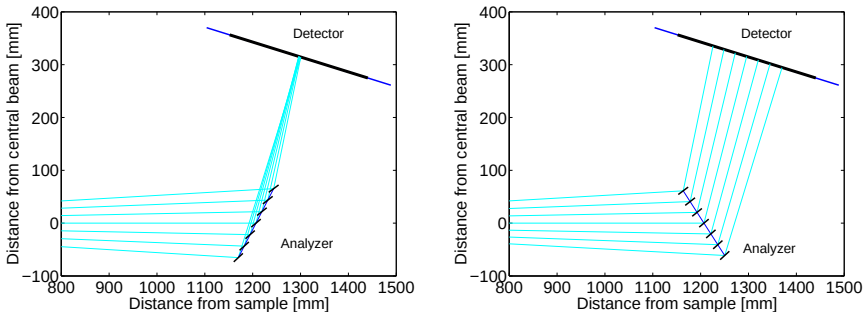

Figure 5.2: The geometry of the analyser in the two modes. (a) The monochromatic point-to-point focusing mode. (b) The monochromatic imaging mode.

The neutrons scattered from each analyser blade intersect the detector at different positions. It was found that a convenient distance between the interception points is the same as the distance between the analyser blades (25 mm). Windows can be software defined on the detector corresponding to each blade. As it is discussed in Papers I an II, some of the signal scattered from a given blade will inevitably be detected in the wrong window, so called cross-talk. As expected, the amount of this cross-talk depends on the width of the windows software defined on the detector. The height is not important as all the analyser blades are perpendicular to the scattering plane and the vertical extent of the

signal is defined by the spread of the beam and size of the sample. To reduce the cross-talk an adjustable radial collimator has been installed in front of the detector, as described in Paper II and illustrated in Figure 5.1.

The following sections will focus on examples of the use of the point-to-point focusing and imaging modes for studies of antiferromagnetic nanoparticles. It is not a complete and detailed comparison between the two modes, as most of the data has been obtained during test and development of the imaging mode and only seldom is data available from the same experiment in both modes. For a proper comparison data sets recorded from the same sample in the same sample environment and spectrometer geometry and collimation scheme would be necessary.

Only scattering from powders with random particle orientation will be considered. Thus, only the magnitude of the scattering vector, κ, is important and the orientation of $\boldsymbol{\kappa}$ within the sample need not be considered. For examples of inelastic experiments with single crystals see Papers II and III.

5.3 Elastic scattering experiments

As discussed in Chapter 2 there will often be a strong incoherent background and significant broadening of the reflections when conducting elastic neutron scattering experiments on nanoparticles. Also, the amount of sample available is often quite small, giving weak scattering. Thus, diffraction patterns from nanoparticles will often contain weak broad peaks above a strong background, requiring long experiments in order to obtain reasonable statistics. This is contrary to the case for larger bulk-like particles where the sharp reflections and much lower surface area per mass means that adsorbed water will not be a problem.

Often, it is more convenient to measure diffraction patterns using a powder diffractometer as described in Section 2.1.3, as this can simultaneously measure at a large number of scattering vectors albeit without the energy analysis of a TAS. However with the weak diffraction peaks in nanoparticles the energy analysis may be crucial, to remove inelastic contributions such as thermal diffuse scattering [165,166]. Also, inelastic signals in magnetic nanoparticles have been observed to broaden the diffraction peaks in data from a powder diffractometer leading to erroneous correlation length estimates [167].

5.3.1 The monochromatic point-to-point focusing mode

As an example of the use of the point-to-point focusing mode in elastic experiments a sample of nanoparticles of goethite, see Section 3.3, has been measured using just the middle analyser blade[1]. The data is shown in Figure 5.3(a). The sample was kept at 8 K and a diffraction pattern covering the magnetic (020) peak at $\kappa = 1.26$ Å^{-1} and partially magnetic partially structural (110) peak at $\kappa = 1.50$ Å^{-1} was measured in 2 hours. A large incoherent background of approximately the same intensity as the peak intensities is observed. In order to increase the statistics either each data point must be measured for longer time or more data points must be measured simultaneously. Keeping the same experimental conditions the three middle analyser blades of the analyser are set

[1] In this case the spectrometer performs as a conventional TAS.

in the point-to-point focusing mode, scattering to a single point of the detector. The experiment was repeated resulting in the data in Figure 5.3(b). As it is seen the count rate is about three times higher but at a cost to the resolution, giving a significant broadening of the peaks. Utilising a higher number of analyser blades would not be practical as the resolution would be too bad, making data analysis difficult.

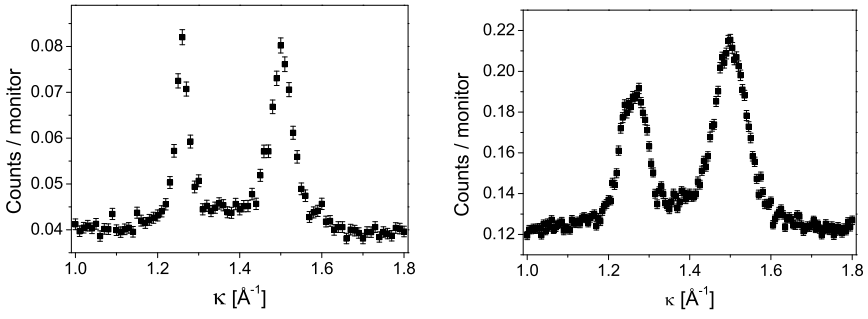

Figure 5.3: Diffraction patterns of goethite nanoparticles obtained at 8 K using the monochromatic point-to-point focusing mode. (a) Signal recorded using one analyser blade. (b) Signal recorded using three analyser blades. It is observed that both the integrated signal and the background increase by a factor of three.

5.3.2 The monochromatic imaging mode

In the monochromatic imaging mode the data from each analyser blade can be measured independently, effectively giving seven diffraction patterns each with the resolution of one analyser blade. The scattering vector of each of the analyser blades can be calculated geometrically at each point in the scan, making it possible to add the data from each blade to a single diffraction pattern. The advantage of this mode is illustrated by recording diffraction patterns of the coated NiO nanoparticles (discussed in Section 3.4.3) at 25 K. A diffraction pattern recorded around the magnetic $(\frac{1}{2}\frac{1}{2}\frac{1}{2})$ reflection in 30 minutes using just the central analyser blade of the analyser is plotted in Figure 5.4(a). Again an intense incoherent background is present and the weak reflection is only about 12% above the background. Adding the signals from all seven analyser blades reduces the error bars on the data points at no cost to the resolution, making it possible to more confidently fit the peak, as illustrated in Figure 5.4(b). The count per monitor in both scans is the same, as the signals from each of the seven blades are normalised by the monitor before being combined. To achieve the same statistics with just one analyser blade the experiment would have taken 3.5 hours. Due to the geometry of the analyser the solid angle subtended by each blade is different. This, along with a difference in distance from each blade to the detector and different scatting efficiencies of the blades, due to the blade quality, gives a difference in the signal from each of the blades of up to 20%. By normalising the signals from each of the analyser blades to be the same at an incoherent scattering vector this difference may be removed removed, as described in Paper I. The cross-talk from neighbouring blades of

0.2% (Paper I) is unimportant for the weak signals from nanoparticles. Thus, the monochromatic imaging mode is an efficient way of obtaining more diffraction data from a weak reflection without loss of resolution.

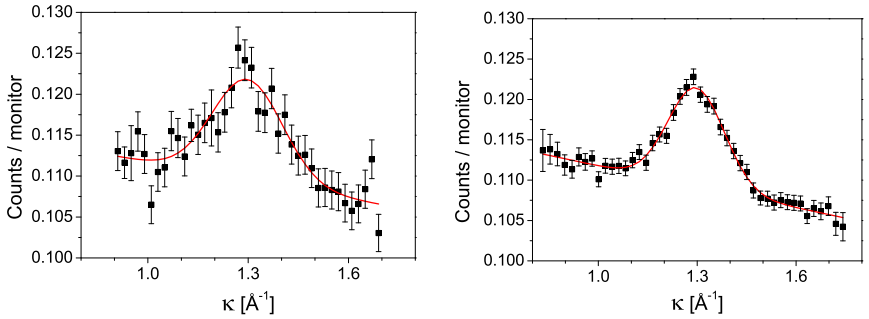

Figure 5.4: Diffraction patterns of coated NiO nanoparticles obtained at 25 K using the monochromatic imaging mode. (a) Signal recorded using one analyser blade. (b) Signal recorded by combining the contributions from all seven analyser blades.

5.4 Inelastic scattering

In an inelastic experiment the scattering vector of the central analyser blade is fixed to the desired value, and the incoming energy is scanned. The other six blades will measure energy spectra at slightly different values of κ depending on the spectrometer geometry.

In both the point-to-point and imaging modes the seven analyser blades will subtend an angle of about 7° at a final energy of $E_\mathrm{f} = 5.0$ meV. At a final energy of $E_\mathrm{f} = 3.6$ meV the subtended angle is about 5° in the imaging mode and 8° in the focusing mode. As the width of the magnetic $(\frac{1}{2}\frac{1}{2}\frac{1}{2})$ reflection in both samples of NiO nanoparticles is about 8° (FWHM), the poor angular resolution of the point-to-point focusing mode would not seem to be an issue.

In the imaging mode however, it is then possible to subsequently either add the signals giving a spectrum similar to the one obtained by the point-to-point focusing mode, or to consider the signal separately to create an energy-momentum map of the sample as shown for hematite and NiO nanoparticles in Papers V and X, respectively.

The advantage of the imaging mode is that this decision can be taken after the experiment. Indeed, the post-experiment analysis will allow a choice of the number of analyser blades to add, and also the size of the window in the PSD measuring the signal from each blade. Obviously the susceptibility to non sample dependent background, such as electronic noise or fast neutrons passing through the analyser housing will be higher due to the use of a larger counting area on the detector. However, the background at RITA-II has been measured to be just 8 counts/h in each of the detector windows associated with an analyser blade, so with a moderate signal the increase of detector area can in general be accepted.

5.5 Data acquisition

In the following section acquisition of inelastic data from NiO nanoparticles in the two modes will be described, along with examples of the potentials of post experiment decisions regarding the number of analyser blades used to measure data and the size of the software defined windows associated with each of these.

As described in Section 4.2.2 the procedure for studying the inelastic properties of antiferromagnetic nanoparticles is to determine background contributions from energy scans at scattering vectors in the incoherent background close to the antiferromagnetic ordering vector. Keeping these fixed the magnetic dynamics may be measured by fitting energy scans recorded with the scattering vector along the antiferromagnetic ordering vector. In NiO the two incoherent background scans are at $\kappa = 1.00$ Å^{-1} and $\kappa = 1.60$ Å^{-1} and the antiferromagnetic reflection is at $\kappa = 1.30$ Å^{-1}.

All fits presented here are merely for test and optimisation purposes. Results from a systematic data fitting are presented in Section 4.2 and Papers X and XI.

5.5.1 Monochromatic imaging mode data

In the imaging mode, the range of scattering vectors covered by each analyser blade is shown in Figure 5.5, calculated from the geometry of the spectrometer and the size of the blades.

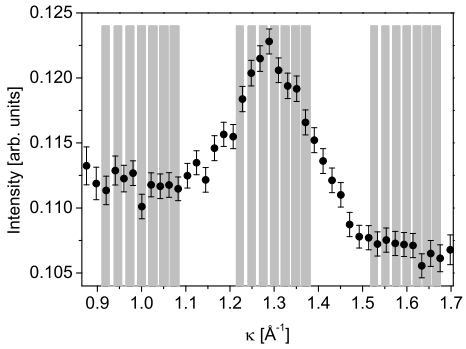

Figure 5.5: Footprints of the analyser blades in the imaging mode at at a final energy of 5.0 meV, during scans at $\kappa = 1.00$ Å^{-1}, $\kappa = 1.60$ Å^{-1} and $\kappa = 1.30$ Å^{-1}.

Signals from the desired number of analyser blades are added together to one data set. Due to slight misalignments of the blades, there will be a slight offset in energy of the signal from each blade, such that the elastic signal is not counted at $E = 0$. The offsets are all less than 0.03 meV and they are consistent in the two incoherent scans. These offsets are all much less than the energy resolution so the elastic signal is present in all blades in Figure 5.5. The offsets are compensated by shifting the signals by the energy offset measured for each analyser blade in the incoherent scans. Thus, all the signals that are added have the same energy centre making measurements of the broadening more reliable.

As an example, energy scans of the coated NiO nanoparticles at 200 K and an applied field of 4 T are analysed to find the preferential number of analyser

blades to measure data with and the optimal size of the software defined detector windows associated with each of these blades. This applied field was chosen as the inelastic signal is most clearly defined here.

Figure 5.6 shows the raw data obtained when adding the signal from seven analyser blades overlayed with data obtained from a single blade, both with detector windows 7 pixels (16 mm) wide. The hump around -0.3 meV is mainly due to the inelastic cross-talk from the neighbouring blade, as discussed in Paper II. This cross-talk is quite large (∼2%) but only observed on the negative side, due to the presence of a filter.

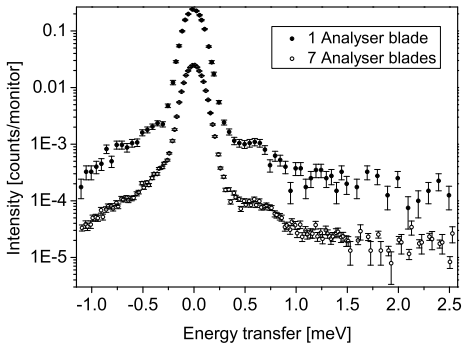

Figure 5.6: Raw inelastic data from the coated NiO particles at 200 K and an applied field of 4 T, recorded with $E_f = 5.0$ meV. The data was obtained in the imaging mode with scattering vector along the antiferromagnetic ordering vector, using the number of analyser blades indicated. For clarity the data obtained with one blade has been shifted 1 decade up.

Initially, an inelastic scan measured in the incoherent background with seven blades has been fitted as described in Section 4.2.2. Using different sizes of the detector windows the intensity of the Gaussian line shape from the elastic signal, the inelastic background and the intensity of the cross-talk signal have been found. As expected, these intensities all increase as the size of the detector window is increased. However, as seen in Figure 5.7(a) the intensity of the elastic signal will flatten out when a detector window reaches a size where it contains the full elastic signal scattered from the associated analyser blade. The background and cross-talk signals will continue to grow as the window size is increased. From the plot in Figure 5.7(a) an optimal window size of 9 pixels (21 mm) was chosen in order to maximise the scattering signal without having to much background and cross-talk contribution.

Using windows 9 pixels wide to record the signal from each analyser blade, the intensity, A_2, width, γ, and the position, ε_0 of the inelastic signal were fitted from the data recorded at the antiferromagnetic reflection. Each fit was done by adding the signals from a number of analyser blades. The signals were added from 1, 3, 5 or 7 blades centred around the middle blade. Also the signal measured by the four outer blades (two on either side) was fitted. The variation of the fitted parameters as a function of the number of blades used for fitting is shown in Figures 5.7(b-d).

The reason for the increase of ε_0 is that each blade measures a different part of the diffraction peak. In a diffraction pattern from a sample of particles with a distribution of sizes, the central part of a reflection will come mostly from the

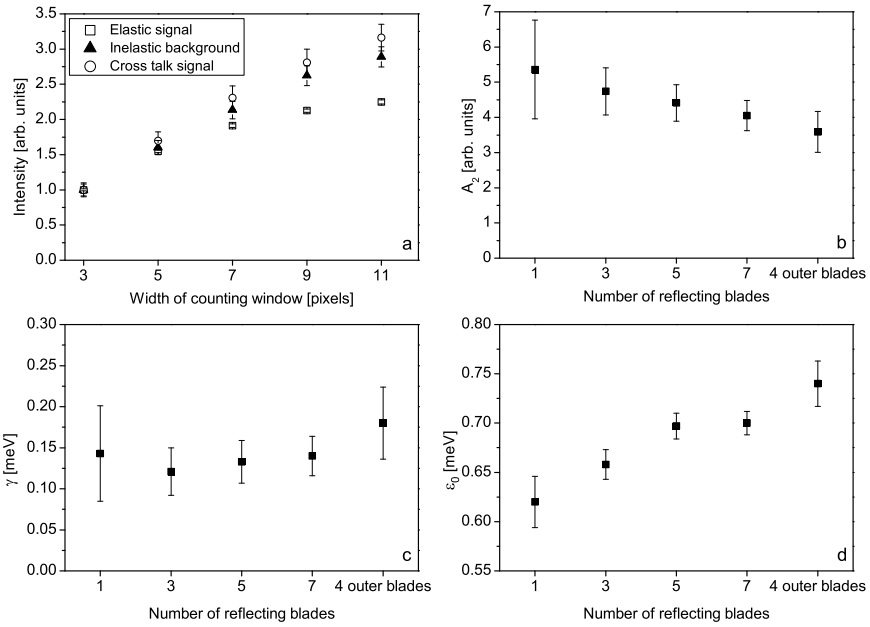

Figure 5.7: Results of fits to the data obtained from the coated NiO sample at 200 K and an applied field of 4 T at $E_f = 5.0$ meV. (a) The effect of changing the window size on the elastic intensity, the inelastic background and cross-talk signals of data recorded at scattering vectors in the incoherent background. For comparison, all signals are normalised to 1 at the 3 pixel window width, as the ratio between the elastic signal and the background is about 2000. (b-d) The intensity, width and position of the inelastic signal, respectively. The parameters are from fits to data recorded with the scattering vector along the antiferromagnetic ordering vector.

largest particles, that contribute with a narrow intense diffraction peak, while the outer parts are mostly due to broad peaks from the smallest particles [142], see Figure 5.8.

In the NiO nanoparticle data it was decided to include all seven analyser blades as this takes account of the whole sample, and not just one size partition of the particles. Thus, all the data presented in Section 4.2 is measured with seven blades and detector windows 9 pixels wide.

Generally it is preferential to add the data from all the blades when working with nanoparticles, as the diffraction peaks are broad in κ. If the sample consists of larger particles or a single crystal the option of choosing just one blade may useful. An example of this is given in Figure 5.9(a), where the spin wave gap of bulk hematite has been measured at 150 K. The dispersion is known to be very steep, about 140 meV Å along the [001] direction [128]. The gap is about 1 meV in the data from the middle blade, around 3.5 meV in the data from the two neighbouring blades and about 6 meV in the data from the next blades. As shown in Figure 5.9(b) this is in correspondence with the published spin wave velocity [128] and spin wave gap [83] below the Morin temperature. Adding the data sets presented would result in a significantly smearing of the signal and higher background.

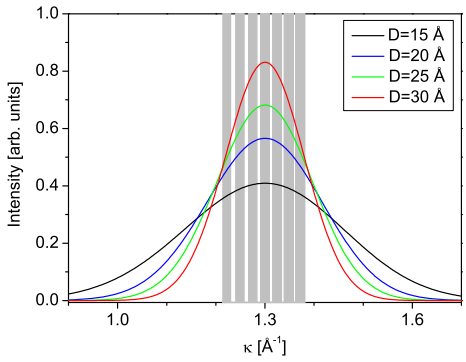

Figure 5.8: Simulated diffraction reflections for particles with various correlation lengths. It is observed that the inner blades are most sensitive to the largest particles and the outer blades are most sensitive to the smallest particles.

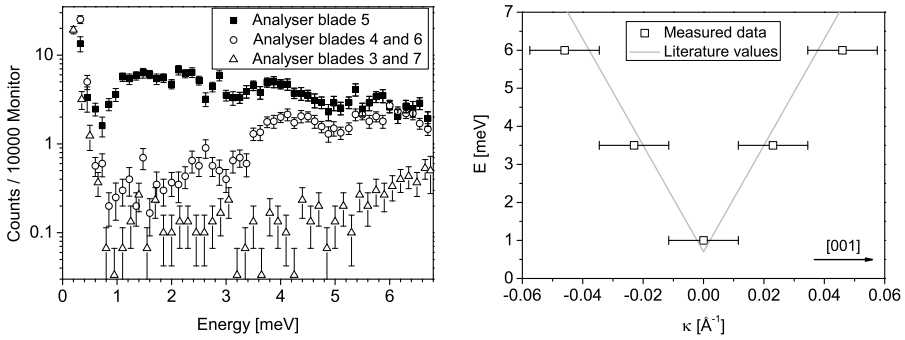

Figure 5.9: Data recorded from a single crystal of hematite (∼2 cm^3) at 150 K. The scattering vector probed by the central analyser blade is the antiferromagnetic (003) reflection, the separation between the blades is 0.023 Å^{-1} along the [001] direction. (a) The data measured by the blades. For numbering of the blades, see Figure 5.1. (b) The dispersion data derived from the spin wave gaps overlaid by the published dispersion relation. The dispersion is measured along the [001] direction from the (003) reflection.

5.5.2 Monochromatic point-to-point focusing mode data

In the point-to-point focusing mode, the range of scattering vectors covered by each blade is shown in Figure 5.10, calculated from the geometry of the spectrometer and the size of the analyser blades. The signals from the blades are instrumentally added, so it is not possible to correct for the scattering efficiency of the individual blades, as in the imaging mode. The energy offsets of the individual signals cannot either be corrected, resulting in some broadening of the absolute signals. However, as the offsets are constant throughout an experiment a relative broadening may still be measured.

As an example, energy scans of the as-prepared NiO nanoparticles measured at 300 K in zero applied field are analysed to find the preferential width of the detector window. This is a different sample to the one used to analyse the imaging mode. The data was measured in the focusing mode at an energy of

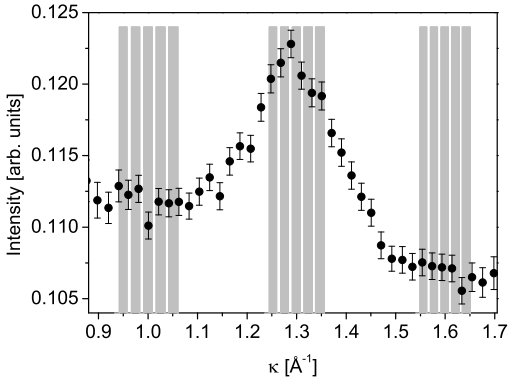

Figure 5.10: Footprints of the 5 analyser blades in the focusing mode at a final energy of 3.6 meV. The footprints have been superimposed on the data from the coated NiO sample measured using the high resolution of the imaging mode.

E_f=3.6 meV using only 5 analyser blades, due to alignment problems with the outer blades.

As for the imaging mode data the elastic intensity and background measured at scattering vectors in the incoherent background have been fitted using different detector window sizes, normalising both at a window width of 7 pixels (16 mm), see Figure 5.11. Again the background signal grows as the window width is increased, while the elastic signal flattens out. As described in Paper I the focusing mode is not perfect, as there is a spread of about 2 pixels in the intersection points of the signals from the blades on the detector. It was decided to use a window size of 15 pixels (35 mm) to ensure that the full signal from all the blades is measured, as a smaller window may cut off some of the signal from the outer blades. This is the window size used for the data in Section 4.2. In general a large window will normally be preferable when measuring nanoparticles.

An example of a situation where the window size is important is given in Paper III, where the spin wave gap of (Tl,K)$CuCl_3$ was measured using the focusing mode. The signal to noise ratio of the spin wave gap was significantly changed when changing the size of the detector window.

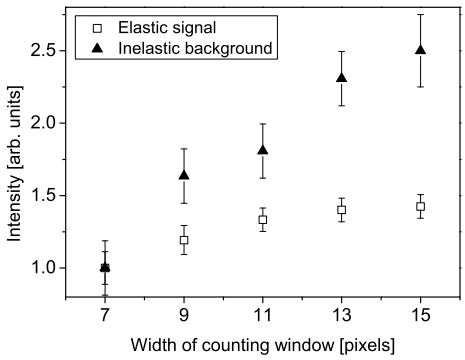

Figure 5.11: The relative increase of the elastic intensity and inelastic background signals measured from the as-prepared NiO sample in zero applied field at 300 K and $E_{\mathrm{f}} = 3.6$ meV. The data is recorded at scattering vectors in the incoherent background using the indicated size of the counting window on the detector. For comparison the two signals have been normalised to one at the 7 pixel window width, as the ratio between the elastic and the background intensity is about 2000.

Chapter 6

Conclusion and Outlook

6.1 Conclusion

The magnetic properties of nanoparticles of the antiferromagnets nickel oxide (NiO) and hematite (α-Fe_2O_3) have been studied using a range of experimental techniques. This use of different techniques allows a comparison of results and an assessment the validity of results from the individual techniques to be made.

The particles have been well characterised with respect to size and morphology using x-ray diffraction and transmission electron microscopy. Whereas the hematite particles are almost spherical, and thus simple to characterise, the NiO particles, which have been the main emphasis of this thesis, are plate shaped. This non-spherical shape makes an accurate characterisation important, as a wrong model will lead to an erroneous estimate of the volume and surface area of the particles, altering estimates of the measured properties. The particle size depends on the preparation conditions, with the particles in the present study having a diameter of about 13 nm and a thickness of about 2.3 nm.

Strong interparticle interactions, due to exchange interactions between the particles, were observed in both the hematite and NiO samples. In hematite oriented attachment of the particles in chains resulted in a strong interaction. The interactions between the NiO particles were weaker and no preferred attachment orientation was observed. It was found that it was possible to significantly reduce these exchange interactions by simple mechanical treatments, such as grinding by hand. Samples of weakly interacting particles were prepared in this way, further reducing the interactions by coating with a layer of phosphate.

In both materials, the interparticle interactions were observed by inelastic neutron scattering to increase the resonance energy of $\mathbf{q} = 0$ spin waves, reducing the scattering intensity accordingly. A suppression of the superparamagnetic relaxation and the spin waves was also observed by Mössbauer spectroscopy.

The presence of an uncompensated moment, due to the finite particle size, has been calculated theoretically to alter the resonance energy of the $\mathbf{q} = 0$ spin waves. In hematite a significant reduction is predicted, whereas in NiO the reduction is predicted to be much less, due to the difference in the ratio between the in-plane and out-of-plane anisotropy energies in the two materials.

In NiO nanoparticles, the amount of uncompensated moment has been estimated by comparing high-field Mössbauer spectroscopy measurements and nu-

merical simulations. A value of $\approx 0.6\%$ of the spins in one sublattice was found, in agreement with a model assuming a random distribution of uncompensated spins on the surface.

The magnetic structure of NiO nanoparticles was found to be similar to that of bulk, with the spins held in the (111) planes parallel to the plate faces. From literature, a value of the large out-of-plane anisotropy, K_1, was found to be similar to that of bulk NiO. The in-plane magnetic anisotropy, defining an easy direction within the plane, was measured to be about $K_2 \approx 1 \cdot 10^4$ Jm^{-3}. This is more than two orders of magnitude larger than the value in bulk NiO, a result that may be due to significant surface anisotropy. Measurements also indicate a decrease of the effective exchange coupling between the spins, which may be explained by missing bonds at the particles surface and canting of the spins within the particles.

A monochromatic imaging mode has been implemented at the RITA-II spectrometer. This has been compared to the already existing focusing mode, with respect to conducting inelastic neutron scattering experiments on NiO nanoparticles.

Due to the broad reflections from nanoparticles the full extent of the analyser is needed to cover the reflections in both modes. This would initially suggest that there is no advantage in using the imaging mode, as this would only contribute more background. However, it was found that the background contribution was not a problem. The powerful potentials of post experiment decision making with regards to the data make the imaging mode attractive.

6.2 Outlook

The study of the magnetic properties of NiO nanoparticles is far from exhausted, as several aspects of the magnetic properties of NiO nanoparticles remain to be studied.

High energy mode

The main focus of the present work has been the low energy resonance mode ω_α, associated with the in-plane anisotropy. Studying the high energy mode ω_β was not possible due to limitations of the RITA-II spectrometer. It would be interesting to use the higher intensity and larger κ range of a thermal TAS to study this mode. Knowledge of the energy of ω_β is important not only to gain fundamental insight into the size dependence of the out-of-plane anisotropy, but also to calculate the dependence of the ω_α mode on the uncompensated moment.

The high energy mode may also be measured by far infra-red spectroscopy as in Ref. [77]. A more systematic study of the high-energy mode in a range of samples may be undertaken in this way.

Size dependence of parameters

Only NiO particles heated at 300° are presented here. Plate shaped NiO nanoparticles can fairly reproducibly be prepared with a range of particle sizes depending on the heating temperature. Thus a study of the size dependence of the measured parameters could be undertaken. This may lead to interesting

results as a significant difference between 8 nm and 16 nm particles of hematite has been observed, see Paper VII and Ref. [142].

When undertaking a study of the size dependence of parameters it would seem preferential to first separate and coat the particles, as the effects of interaction are not trivial to understand especially not in neutron scattering results.

Morphology dependence of parameters

Ball milling of both the NiO and the precursor particles has unsuccessfully been attempted in order to break apart the plates and change the particle morphology. At high energy the particles "melted" together into larger particles, and at low energy the particle morphology was not changed.

NiO nanoparticles can be prepared by a range of techniques, of which only one has been used in the present work. As the morphology in the particles presented here is inherited from the precursor, it may be possible to achieve a different morphology of the particles using the other preparation techniques and precursors. Thus, the effect of the plate shape of the particles on the magnetic properties may be analysed.

Varying the uncompensated moment

It would be interesting to be able to vary the uncompensated moment of particles identical in size. Magnetic separation has been attempted by submersion of a strong permanent magnet into a suspension of NiO nanoparticles in water. But the moment of the particles was not large enough to be attracted to the magnet, maybe due to thermal movement of the water. However, this may be attempted using a stronger magnet and thin tubes with a laminar flow of liquid.

Exchange striction

The slight deformation of the unit cell, known as exchange striction, is difficult to measure in nanoparticles due to the broad diffraction lines. Measuring the size dependence of this deformation may yield important results regarding the magnetic structure of the nanoparticles. Using high intensity synchrotron XRD and subsequent profile refinement, it may be possible to measure this deformation. The peaks will still be broadened due to the the finite size broadening, but the high intensity may make a more confident fitting of the peak profile an positions possible.

Appendix A

Numerical calculations of spin orientation

A.1 Spin orientation in an antiferromagnet

In a classical mean-field model, the energy of an antiferromagnet with uniaxial anisotropy and an uncompensated magnetic moment may be written as (assuming low temperature, thus neglecting thermal effects) [168, 169]

$$E = S_{\mathrm{a}} g \mu_{\mathrm{B}} \big[B_{\mathrm{E}} \xi \cos(\theta_{\mathrm{a}} - \theta_{\mathrm{b}}) - \frac{1}{2} B_{\mathrm{A}} \cos^2(\theta_{\mathrm{a}} - t) - \frac{1}{2} B_{\mathrm{A}} \xi^2 \cos^2(\theta_{\mathrm{b}} - t) - B_{\mathrm{appl}} (\cos\theta_{\mathrm{a}} + \xi \cos\theta_{\mathrm{b}}) \big]. \quad \text{(A.1)}$$

Here S_{a} and S_{b} are the total spins of the two sublattices, where $S_{\mathrm{b}} = \xi S_{\mathrm{a}}$ ($\xi \leq 1$). B_{E} and B_{A} are the exchange and anisotropy fields as defined in Sections 3.6 and 3.5, respectively. B_{appl} is the applied field. It is assumed that all three fields are constant everywhere within the antiferromagnet. $\theta_{\mathrm{a}}, \theta_{\mathrm{b}}$ are the angles between the two sublattice magnetisation directions and the applied field, and t is the angle between the anisotropy field of the particle (the easy axis) and the applied field. The angles are defined in Figure A.1.

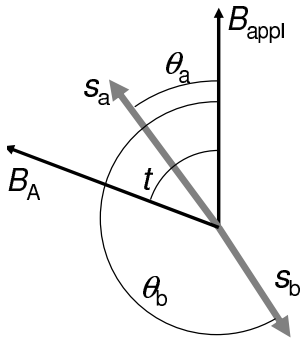

Figure A.1: Definition of the angles θ_{a}, θ_{b} and t in relation to the applied field, B_{appl} and the anisotropy field B_{A}.

Equation (A.1) can be used to study the two extremes of the anisotropy energy presented in Paper XII. The uniaxial case, with out-of-plane anisotropy $B_{A1} = 0$, can be modelled by choosing $B_A = B_{A2}$ and allowing the orientation of the spins to be in any direction. Alternatively, the strongly planar case $B_{A1} \approx \infty$ can be modelled by again choosing $B_A = B_{A2}$ but confining the spins to only move in a plane. For both cases the orientations of the spins (θ_a and θ_b) may be found at a given orientation of t by minimising Equation (A.1).

Spin flop

As a test of the simulation routine and to demonstrate the sensitivity to a small uncompensated moment, the spin flop field has been considered in the case of uniaxial anisotropy in NiO nanoparticles. At moderate applied fields parallel to the anisotropy field, the spins on the two sublattices of an antiferromagnet will be parallel and antiparallel to the applied field. At the spin flop field $B_{sf} = \sqrt{2B_A B_E}$ the spins will flop to the more energetically favourable orientation perpendicular to the field. From here, the spins will be forced towards the field direction, with the angle between them decreasing as the field increases.

An exchange field of $B_E = 987$ T was taken from Paper XI[1] and an anisotropy field of $B_A = 0.015$ T was used in accordance with the low temperature Mössbauer spectroscopy measurements in Section 4.1.1. The spin flop field in the perfect antiferromagnet with the anisotropy and exchange fields as given above is $B_{sf} = 5.4$ T. Figure A.2(a) shows the orientation of the spins on one sublattice, θ_a, as a function of applied fields for various easy axis orientations, t. It is seen that even as slight deviation of the easy axis from the direction of the applied field will smear out the spin flop transition. This is in complete accordance with the results obtained in Ref. [170]. Figure A.2(b) shows that, as intuitively expected, the presence of uncompensated moments will increase the spin flop field at $t = 0$. It is noteworthy how large the effect is even at a small uncompensated moment.

A.2 Simulation of Mössbauer spectra

Equation (A.1) has been used to simulate Mössbauer spectra of NiO nanoparticles in an applied field of 6 T. Again, values of $B_E = 987$ T and $B_A = 0.015$ T are chosen.

Two parameters of a sextet component in a Mössbauer spectrum are sensitive to an applied field. Firstly, the splitting of the sextet depends on the field experienced by the nuclei, B_{tot}, which may be expressed as

$$B_{hf}^2 = B_{tot}^2 + B_{appl}^2 - 2B_{tot}B_{appl}\cos\theta. \tag{A.2}$$

where B_{hf} is the hyperfine field and θ is the angle between the total field and the radiation direction, which in the present experiment was along B_{appl}, as shown in Figure A.3.

[1] This value differs from the value of 905 T found in Section 3.6 due to a difference in the value of the g-factor. As the exchange field is substantially larger than the anisotropy and applied fields, this difference is insignificant.

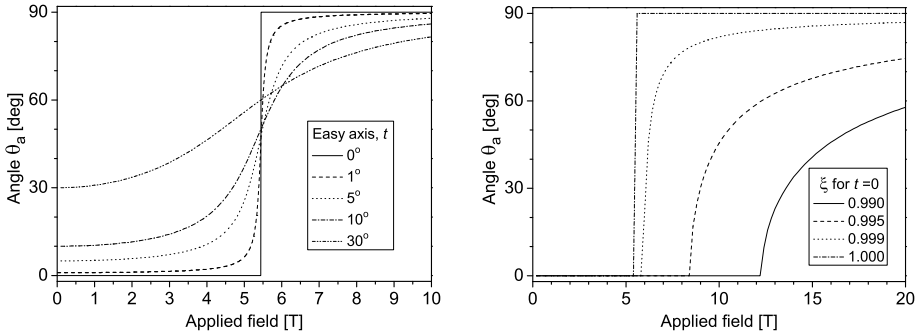

(a) (b)

Figure A.2: The angle between the spins in one sublattice and the applied field direction as a function of applied field. (a) Perfect antiferromagnet with various orientations of the easy axis compared to the applied field. (b) Various amounts of uncompensated moments with the easy axis parallel to the applied field.

Secondly, the areas of the the six lines (assuming a thin absorber) will scale as $3 : p : 1 : 1 : p : 3$, with

$$p = \frac{4\sin^2\theta}{2 - \sin^2\theta}. \tag{A.3}$$

Thus a Mössbauer spectrum may be simulated from a knowledge of θ. To simulate the spectrum for a powder of randomly oriented particles, spectra for all orientation of t are calculated and added, weighted by $\sin t$ [168,169]. In this way Mössbauer spectra can be simulated for any applied field and amount of uncompensated spins.

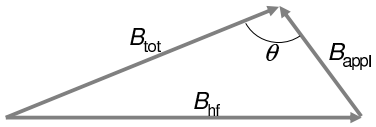

Figure A.3: Relationship between the fields $B_{\rm tot}$, $B_{\rm appl}$ and $B_{\rm hf}$ and the angle θ.

Due to the size of the exchange field, this will dominate, such that the spins will be almost antiparallel at all conceivable applied fields. The equilibrium orientation of the spins is the result of a struggle between the anisotropy field and the applied field acting on the uncompensated moment. In the regime where $B_{\rm A} \approx B_{\rm appl}(1-\xi)$, i.e., when $\xi \approx 0.99$, both the applied field and the anisotropy field will strongly influence the spin directions.

As discussed in Paper VIII and Section 4.1.2 the measured high-field Mössbauer spectra are best described by simulated spectra with a value of $\xi \approx 0.994$. At this value the two anisotropy models, uniaxial and planar give almost the same values of p and the hyperfine splitting.

Bibliography

[1] S. N. Klausen, *Magnetic dynamics of hematite nanoparticles*. PhD thesis, Technical University of Denmark (2003).

[2] C. Frandsen, *An experimental study of nanomagnets and their interactions*. PhD thesis, Technical University of Denmark (2004).

[3] R. Skomski, "Nanomagnetics" *J. Phys.: Condens. Matter* **15**, R841 (2003).

[4] A. Fert and L. Piraux, "Magnetic nanowires" *J. Magn. Magn. Mater.* **200**, 338 (1999).

[5] R. H. Kodama, "Magnetic nanoparticles" *J. Magn. Magn. Mater.* **200**, 359 (1999).

[6] V. Poulsen, "Das Telegraphon" *Ann. der Physik* **308**, 754 (1900).

[7] W. F. Brown, Jr., "Relaxational Behavior of Fine Magnetic Particles" *J. Appl. Phys.* **30**, S130 (1959).

[8] W. F. Brown, Jr., "Thermal Fluctuations of a Single-Domain Particle" *Phys. Rev.* **130**, 1677 (1963).

[9] S. Sun, C. B. Murray, D. Weller, L. Folks, and A. Moser, "Monodisperse FePt Nanoparticles and Ferromagnetic FePt Nanocrystal Superlattices" *Science* **287**, 1989 (2000).

[10] T. Burkert, L. Nordström, O. Eriksson, and O. Heinonen, "Giant Magnetic Anisotropy in Tetragonal FeCo Alloys" *Phys. Rev. Lett.* **93**, 27203 (2004).

[11] G. Andersson, T. Burkert, P. Warnicke, M. Björck, B. Sanyal, C. Chacon, C. Zlotea, L. Nordström, P. Nordblad, and O. Eriksson, "Perpendicular Magnetocrystalline Anisotropy in Tetragonally Distorted Fe-Co Alloys" *Phys. Rev. Lett.* **96**, 37205 (2006).

[12] Q. A. Pankhurst, J. Connolly, S. K. Jones, and J. Dobson, "Applications of magnetic nanoparticles in biomedicine" *J. Phys. D: Appl. Phys.* **36**, R167 (2003).

[13] S. H. Cartmell, A. Keramane, G. R. Kirkham, S. B. Verschueren, J. L. Magnay, A. J. E. Haj, and J. Dobson, "Use of magnetic particles to apply mechanical forces for bone tissue engineering purposes" *J. Phys.: Conf. Series* **17**, 77 (2005).

[14] J. F. Collingwood, A. Mikhaylova, M. R. Davidson, C. Batich, W. J. Streit, T. Eskin, J. Terry, R. Barrea, R. S. Underhill, and J. Dobson, "High-resolution X-ray absorption spectroscopy studies of metal compounds in neurodegenerative brain tissue" *J. Phys.: Conf. Series* **17**, 54 (2005).

[15] S. D. Bader, "Colloquium: Opportunities in nanomagnetism" *Rev. Mod. Phys.* **78**, 1 (2006).

[16] D. Goll and H. Kronmüller, "High-performance permanent magnets" *Naturwissenschaften* **87**, 423 (2000).

[17] V. Skumryev, S. Stoyanov, Y. Zhang, G. Hadjipanayis, D. Givord, and J. Nogués, "Beating the superparamagnetic limit with exchange bias" *Nature* **423**, 850 (2003).

[18] J. Nogués and I. K. Schuller, "Exchange bias" *J. Magn. Magn. Mater.* **192**, 203 (1999).

[19] S. A. Wolf, D. D. Awschalom, R. A. Buhrman, J. M. Daughton, S. von Molnár, M. L. Roukes, A. Y. Chtchelkanova, and D. M. Treger, "Spintronics: A Spin-Based Electronics Vision for the Future" *Science* **294**, 1488 (2001).

[20] N. J. Oliveira, S. X. Li, and P. P. Freitas, "Performance of NiO spin-valve tape heads for high recording densities" *J. Appl. Phys.* **85**, 5849 (1999).

[21] J. F. Bobo, L. Gabillet, and M. Bibes, "Recent advances in nanomagnetism and spin electronics" *J. Phys.: Condens. Matter* **16**, S471 (2004).

[22] Z. Xu, Y. Li, J. Zhang, L. Chang, R. Zhou, and Z. Duan, "Ultrafine NiO-La_2O_3-Al_2O_3 aerogel: a promising catalyst for CH_4/CO_2 reforming" *Appl. Catalysis A* **213**, 65 (2001).

[23] D. Wang, R. Xu, X. Wang, and Y. Li, "NiO nanorings and their unexpected catalytic property for CO oxidation" *Nanotechnology* **17**, 979 (2006).

[24] J. Wang, J. Cai, Y. Lin, and C. Nan, "Room-temperature ferromagnetism observed in Fe-doped NiO" *Appl. Phys. Lett.* **87**, 202501 (2005).

[25] P. Poizot, S. Laruelle, S. Grugeon, L. Dupont, and J. M. Tarascon, "Nano-sized transition-metal oxides as negative-electrode materials for lithium-ion batteries" *Nature* **407**, 496 (2000).

[26] F. Huang, B. Gilbert, H. Zhang, and J. F. Banfield, "Reversible, Surface-Controlled Structure Transformation in Nanoparticles Induced by an Aggregation State" *Phys. Rev. Lett.* **92**, 155501 (2004).

[27] L. Néel, "Superparamagnétisme des grains très fins antiferromagnétiques" *C. R. Hebd. Seances Acad. Sci.* **252**, 4075 (1961).

[28] L. Néel, *Low Temperature Physics*, Gordon & Breach (1962).

[29] J. T. Richardson, D. I. Yiagas, B. Turk, K. Forster, and M. V. Twigg, "Origin of superparamagnetism in nickel oxide" *J. Appl. Phys.* **70**, 6977 (1991).

[30] G. Shirane, S. M. Shapiro, and J. M. Tranquada, *Neutron Scattering with a Triple-Axis Spectrometer*, Cambridge University Press (2002).

[31] G. L. Squires, *Thermal neutron scattering*, Cambidge University Press (1978).

[32] W. Marshall and S. W. Lovesey, *Theory of Thermal Neutron Scattering*, Oxford University Press (1971).

[33] M. Kopcewicz, *Mössbauer Effect in Encyclopedia of Applied Physics*, VCH Publishers, Inc. (1994).

[34] S. Mørup, *Mössbauer spectroscopy and its applications in materials science*, Technical University of Denmark (2004).

[35] D. B. Williams and C. B. Carter, *Transmission electron microscopy: a textbook for materials science*, Plenum Press, New York (1996).

[36] H. P. Klug and L. E. Alexander, *X-ray diffraction procedures*, John Wiley & Sons, Inc. (1970).

[37] B. E. Warren, *X-ray diffraction*, Addison-Wesley (1969).

[38] S. Foner, "Versatile and Sensitive Vibrating-Sample Magnetometer" *Rev. Sci. Instrum.* **30**, 548 (1959).

[39] J. S. Schwinger, "On the Magnetic Scattering of Neutrons" *Phys. Rev.* **51**, 544 (1937).

[40] O. Halpern, M. Hamermesh, and M. H. Johnson, "The Passage of Neutrons Through Crystals and Polycrystals" *Phys. Rev.* **59**, 981 (1941).

[41] J. Chadwick, "Possible Existence of a Neutron" *Nature* **129**, 312 (1932).

[42] C. G. Shull, *Early Development of Neutron Scattering*, Nobel Lecture (1994). `http://nobelprize.org`.

[43] B. N. Brockhouse, *Slow Neutron Spectroscopy and the Grand Atlas of the Physical World*, Nobel Lecture (1994). `http://nobelprize.org`.

[44] L. van Hove, "Correlations in Space and Time and Born Approximation Scattering in Systems of Interacting Particles" *Phys. Rev.* **95**, 249 (1954).

[45] A. Dianoux and G. Lander, eds., *Neutron Data Booklet*, Old City Publishing (2003).

[46] C. Kittel, *Introduction to solid state physics*, John Wiley & Sons, Inc. (1996).

[47] F. C. Blake, "On the Factors Affecting the Reflection Intensities by the Several Methods of X-Ray Analysis of Crystal Structures" *Rev. Mod. Phys.* **5**, 169 (1933).

[48] P. Scherrer, "Bestimmung der Grösse und der inneren Struktur von Kolloidteilchen mittels Röntgenstrahlen" *Nachr. Ges. Wiss. Göttingen* **7**, 98 (1918).

[49] J. I. Langford and A. J. C. Wilson, "Scherrer after sixty years: A survey and some new results in the determination of crystallite size" *J. Appl. Cryst.* **11**, 102 (1978).

[50] M. F. Hansen, F. Bødker, S. Mørup, K. Lefmann, K. N. Clausen, and P.-A. Lindgård, "Magnetic dynamics of fine particles studied by inelastic neutron scattering" *J. Magn. Magn. Mater.* **221**, 10 (2000).

[51] The DMC powder spectrometer homepage can be found at `http://sinq.web.psi.ch/sinq/instr/dmc/`.

[52] K. N. Clausen, D. F. McMorrow, K. Lefmann, G. Aeppli, T. E. Mason, A. Schröder, M. Issikii, M. Noharae, and H. Takagi, "The RITA spectrometer at Risø design considerations and recent results" *Physica B* **241-243**, 50 (1997).

[53] R. L. Mössbauer, "Kernresonzfluoreszenz von Gammastrahlung in Ir^{191}" *Z. Physik.* **151**, 124 (1958).

[54] R. L. Mössbauer, *Recoilless Nuclear Resonance Absorption of Gamma Radiation*, Nobel Lecture (1961). `http://nobelprize.org`.

[55] R. V. Pound and G. A. Rebka, Jr., "Resonant absorption of the 14.4-keV γ ray from 0.10-μsec Fe^{57}" *Phys. Rev. Lett.* **3**, 554 (1959).

[56] J. P. Schiffer and W. Marshall, "Recoilless resonance absorption of gamma rays in Fe^{57}" *Phys. Rev. Lett.* **3**, 556 (1959).

[57] S. Mørup, *Paramagnetic and Superparamagnetic Relaxation Phenomena studied by Mössbauer Spectroscopy*, Polyteknisk forlag (1981).

[58] M. Blume and J. A. Tjon, "Mössbauer Spectra in a Fluctuating Environment" *Phys. Rev.* **165**, 446 (1968).

[59] L. Bragg, *The Diffraction of X-Rays by Crystals*, Nobel Lecture (1922). `http://nobelprize.org`.

[60] H. M. Rietveld, "Line profiles of neutron powder-diffraction peaks for structure refinement" *Acta Cryst.* **22**, 151 (1967).

[61] H. M. Rietveld, "A profile refinement method for nuclear and magnetic structures" *J. Appl. Cryst.* **2**, 65 (1969).

[62] J. Rodríguez-Carvajal, *An introduction to the program FullProf 2000* (July 2001). `http://www-llb.cea.fr/fullweb/`.

[63] The FullProf software can be found at `http://www-llb.cea.fr/fullweb/`.

[64] S. Foner, "Vibrating Sample Magnetometer" *Rev. Sci. Instrum.* **27**, 548 (1956).

[65] S. Foner, "The vibrating sample magnetometer: Experiences of a volunteer" *J. Appl. Phys.* **79**, 4740 (1996).

[66] E. Ruska, *The Development of the Electron Microscope and of Electron Microscopy*, Nobel Lecture (1986). `http://nobelprize.org`.

[67] L. Rayleigh, "Investigation in Optics with special reference to the Spectroscope" *Phil. Mag.* **8**, 261 (1879).

[68] B. Freitag, S. Kujawa, P. M. Mul, J. Ringnalda, and P. C. Tiemeijer, "Breaking the spherical and chromatic aberration barrier in transmission electron microscopy" *Ultramicroscopy* **102**, 209 (2005).

[69] F. Fiévet, P. Germi, F. de Bergevin, and M. Figlarz, "Lattice parameter, microstrains and non-stoichiometry in NiO. Comparison between mosaic microcrystals and quasi-perfect single microcrystals" *J. Appl. Cryst.* **12**, 387 (1979).

[70] L. C. Bartel and B. Morosin, "Exchange Striction in NiO" *Phys. Rev. B* **3**, 1039 (1971).

[71] D. Rodic, V. Spasojevic, V. Kusigerski, R. Tellgren, and H. Rundlof, "Magnetic Ordering in Polycrystalline $Ni_xZn_{1-x}O$ Solid Solutions" *Phys. Stat. Sol. (b)* **218**, 527 (2000).

[72] D. Y. Han, H. Y. Yang, C. B. Shen, X. Zhou, and F. H. Wang, "Synthesis and size control of NiO nanoparticles by water-in-oil microemulsion" *Powder Technology* **147**, 113 (2004).

[73] D. J. Seo, S. B. Park, and Y. C. K. K. L. Choy, "Formation of ZnO, MgO and NiO nanoparticles from aqueous droplets in flame reactor" *J. Nanopart. Res.* **5**, 199 (2003).

[74] M. Ghosh, K. Biswas, A. Sundaresan, and C. N. R. Rao, "MnO and NiO nanoparticles: synthesis and magnetic properties" *J. Mater. Chem.* **16**, 106 (2006).

[75] J. Park, E. Kang, S. U. Son, H. M. Park, M. K. Lee, J. Kim, K. W. K. KW, H. J. Noh, J. H. Park, C. J. Bae, J. G. Park, and T. Hyeon, "Monodisperse nanoparticles of Ni and NiO: Synthesis, characterization, self-assembled superlattices, and catalytic applications in the Suzuki coupling reaction" *Advanced Materials* **17**, 429 (2005).

[76] F. Bødker, M. F. Hansen, C. B. Koch, and S. Mørup, "Particle interaction effects in antiferromagnetic NiO nanoparticles" *J. Magn. Magn. Mater.* **221**, 32 (2000).

[77] V. V. Pishko, S. L. Gnatcheko, V. V. Tsapenko, R. H. Kodama, and S. Makhlouf, "Temperature dependence of magnetic resonance in NiO nanoparticles" *J. Appl. Phys.* **93**, 7382 (2003).

[78] A. E. Berkowitz, R. H. Kodama, S. A. Makhlouf, F. T. Parker, F. E. Spada, E. J. McNiff, and S. Foner, "Anomalous properties of magnetic nanoparticles" *J. Magn. Magn. Mater.* **196-197**, 591 (1999).

[79] R. H. Kodama, S. A. Makhlouf, and A. E. Berkowitz, "Finite size effects in antiferromagnetic NiO nanoparticles" *Phys. Rev. Lett.* **79**, 1393 (1997).

[80] Y. Ichiyanagi, N. Wakabayashi, J. Yamazaki, S. Yamada, Y. Kimishima, E. Komatsu, and H. Tajima, "Magnetic properties of NiO nanoparticles" *Physica B* **329**, 862 (2003).

[81] J. T. Richardson and W. O. Milligan, "Magnetic Properties of Colloidal Nickelous Oxide" *Phys. Rev* **102**, 1289 (1956).

[82] L. W. Finger and R. M. Hazen, "Crystal structure and isothermal compression of Fe_2O_3, Cr_2O_3, and V_2O_3 to 50 kbars" *J. Appl. Phys.* **51**, 5362 (1980).

[83] A. H. Morrish, *Canted antiferromagnetism: Hematite*, World Scientific Publishing Co. Pte. Ltd. (1994).

[84] T. Sugimoto, Y. Wang, H. Itoh, and A. Muramatsu, "Systematic control of size, shape and internal structure of monodisperse α-Fe_2O_3 particles" *Colloid. Surf. A* **134**, 265 (1998).

[85] L. Lu, L. Li, X. Wang, and G. Li, "Understanding of the Finite Size Effects on Lattice Vibrations and Electronic Transitions of Nano α-Fe_2O_3" *J. Phys. Chem.* **109**, 17151 (2005).

[86] J. M. D. Coey, A. Barry, J. Brotto, H. Rakoto, S. Brennan, W. N. Mussel, A. Collomb, and D. Fruchart, "Spin flop in goethite" *J. Phys.: Condens. Matter* **7**, 759 (1995).

[87] J. B. Forsyth, I. G. Hedley, and C. E. Johnson, "The magnetic structure and hyperfine field of goethite (α-FeOOH)" *J. Phys. C* **1**, 179 (1968).

[88] S. Mørup, M. B. Madsen, J. Franck, J. Villadsen, and C. J. W. Koch, "A new interpretation of Mössbauer spectra of microcrystalline goethite: Super-ferromagnetism or super-spin-glass behaviour?" *J. Magn. Magn. Mater.* **40**, 163 (1983).

[89] M. F. Hansen, C. B. Koch, and S. Mørup, "Magnetic dynamics of weakly and strongly interacting hematite nanoparticles" *Phys. Rev. B* **62**, 1124 (2000).

[90] S. Mørup, C. Frandsen, F. Bødker, S. N. Klausen, K. Lefmann, P.-A. Lindgård, and M. F. Hansen, "Magnetic Properties of Nanoparticles of Antiferromagentic Materials" *Hyperfine Interact.* **144-145**, 347 (2002).

[91] M. F. Hansen, *Magnetic properties of systems of magnetic particles.* PhD thesis, Technical University of Denmark (1998).

[92] J. R. Bellare, H. T. Davis, L. E. Scriven, and Y. Talmon, "Controlled Environment Vitrification System: An improved Sample Preparation Technique" *J. Electron Microsc. Tech.* **10**, 87 (1988).

[93] M. Adrian, J. Dubochet, J. Lepault, and A. W. McDowall, "Cryo Electron Microscopy of Viruses" *Nature* **308**, 32 (1984).

[94] C. R. H. Bahl, C. Frandsen, S. N. Klausen, L. Theil Kuhn, and L. Keller, "Interparticle Correlation in Nanocrystalline Goethite" *PSI Experimental Reports* , I/04 S–68(2) (2004).

[95] J. O. Artman, J. C. Murphy, and S. Foner, "Magnetic Anisotropy in Antiferromagnetic Corundum-Type Sesquioxides" *Phys. Rev.* **138**, A912 (1965).

[96] K. Yosida, *Theory of Magnetism*, Springer-Verlag (1998).

[97] F. Bødker and S. Mørup, "Size dependence of the properties of hematite nanoparticles" *Europhys. Lett.* **52**, 217 (2000).

[98] J. I. Kaplan, "Magnetic Dipolar Interactions in MnO and in Ferrites" *J. Chem. Phys* **22**, 1709 (1954).

[99] H. Kondoh, "Antiferromagnetic Resonance in NiO in Far-infrared Region" *J. Phys. Soc. Japan* **15**, 1970 (1960).

[100] F. Keffer and W. O'Sullivan, "Problem of Spin Arrangements in MnO and Similar Antiferromagnets" *Phys. Rev.* **108**, 637 (1957).

[101] W. Roth, "Magnetic Structures of MnO, FeO, CoO, and NiO" *Phys. Rev.* **110**, 1333 (1958).

[102] T. Yamada, "Spin Configuration in Antiferromagnetic Domain Walls of the NiO-Type Crystals" *J. Phys. Soc. Japan* **21**, 650 (1966).

[103] K. Kurosawa, M. Miura, and S. Saito, "Magnetic torque measurements on NiO (111) platelets" *J. Phys. C: Solid St. Phys.* **13**, 1521 (1980).

[104] S. Saito, M. Miura, and K. Kurosawa, "Optical observations of antiferromagnetic S domains in NiO (111) platelets" *J. Phys. C: Solid St. Phys.* **13**, 1513 (1980).

[105] M. T. Hutchings and E. J. Samuelsen, "Measurement of Spin-Wave Dispersion in NiO by Inelastic Neutron Scattering and Its Relation to Magnetic Properties" *Phys. Rev. B* **6**, 3447 (1972).

[106] P. J. Besser, H. Morrish, and C. W. Searle, "Magnetocrystalline Anisotropy of Pure and Doped Hematite" *Phys. Rev.* **153**, 632 (1967).

[107] T. Moriya, "Anisotropic Superexchange Interaction and Weak Ferromagnetism" *Phys. Rev.* **120**, 91 (1960).

[108] P. J. Flanders and W. J. Schuele, "Anisotropy in the Basal Plane of Hematite Single Crystals" *Phil. Mag.* **8**, 485 (1964).

[109] K. Mizushima and S. Iida, "Effective In-Plane Anisotropy Field in α-Fe_2O_3" *J. Phys. Soc. Japan* **21**, 1521 (1966).

[110] F. Bødker, M. F. Hansen, C. B. Koch, K. Lefmann, and S. Mørup, "Magnetic properties of hematite nanoparticles" *Phys. Rev. B* **61**, 6826 (2000).

[111] D. Schroeer and R. C. Nininger, Jr., "Morin transition in α-Fe_2O_3 microcrystals" *Phys. Rev. Lett.* **19**, 632 (1967).

[112] R. D. Zysler, D. Fiorani, A. M. Testa, L. Suber, E. Agostinelli, and M. Godinho, "Size dependence of the spin-flop transition in hematite nanoparticles" *Phys. Rev. B* **68**, 212408 (2003).

[113] R. Shanker and R. A. Singh, "Analysis of the exchange Parameters and Magnetic Properties of NiO" *Phys. Rev. B* **7**, 5000 (1973).

[114] W. Low, "Paramagnetic and Optical Spectra of Divalent Nickel in Cubic Crystalline Fields" *Phys. Rev.* **109**, 247 (1958).

[115] V. Fernandez, C. Vettier, F. de Bergevin, C. Giles, and W. Neubeck, "Observation of orbital moment in NiO" *Phys. Rev. B* **57**, 7870 (1998).

[116] Y. Mita, Y. Ishida, M. Kobayashi, and S. Endo, "Pressure effect on first-order magnetic Raman scattering in NiO" *J. Phys.: Condens. Matter* **14**, 11173 (2002).

[117] S. Mørup, "Spin-canting and transverse relaxation at surfaces and in the interior of ferrimagnetic particles" *J. Magn. Magn. Mater.* **266**, 110 (2003).

[118] L. R. Maxwell and T. R. McGuire, "Antiferromagnetic Resonance" *Rev. Mod. Phys.* **25**, 279 (1953).

[119] D. J. Lockwood, M. G. Cottam, and J. H. Baskey, "One- and two-magnon excitaions in NiO" *J. Magn. Magn. Mater.* **104-107**, 1053 (1992).

[120] J. Milano, L. B. Steren, and M. Grimsditch, "Effect of Dipolar Interaction on the Antiferromagnetic Resonance Spectra of NiO" *Phys. Rev. Lett.* **93**, 077601 (2004).

[121] A. J. Sievers and M. Tinkham, "Far Infrared Antiferromagnetic Resonance in MnO and NiO" *Phys. Rev.* **129**, 1566 (1963).

[122] M. Grimsditch, L. E. McNeil, and D. J. Lockwood, "Unexpected behaviour of the antiferromagnetic mode of NiO" *Phys. Rev. B* **58**, 14462 (1998).

[123] V. S. Mandel, M. M. Lebedev, V. D. Voronkov, and V. V. Lyukshin, "Low-Frequency Branch of Magnetic-Resonance in NiO-type Antiferromagnets" *Izvestiya Akademii Nauk SSSR Seriya Fizicheskaya* **36**, 1564 (1972).

[124] S. Mørup and B. R. Hansen, "Uniform magnetic excitations in nanoparticles" *Phys. Rev. B* **72**, 024418 (2005).

[125] M. Hennion, C. Bellouard, I. Mirebeau, J. L. Dormann, and R. Ober, "Dynamics of fine particles observed in zero-field neutron scattering" *J. Appl. Phys.* **75**, 5900 (1994).

[126] K. Lefmann, F. Bødker, S. N. Klausen, M. F. Hansen, K. N. Clausen, P.-A. Lindgård, and S. Mørup, "A neutron scattering study of spin precession in ferrimagnetic maghemite nanoparticles" *Europhys. Lett.* **54**, 526 (2001).

[127] M. F. Hansen, F. Bødker, S. Mørup, K. Lefmann, K. N. Clausen, and P.-A. Lindgård, "Dynamics of Magnetic Nanoparticles Studied by Neutron Scattering" *Phys. Rev. Lett.* **79**, 4910 (1997).

[128] E. J. Samuelsen and G. Shirane, "Inelastic neutron scattering investigation of spin waves and magnetic interactions in α-Fe_2O_3" *Phys. Stat. Sol. (b)* **42**, 241 (1970).

[129] P. V. Hendriksen, S. Linderoth, and P.-A. Lindgård, "Finite-size modification of the magnetic properties of clusters" *Phys. Rev. B* **48**, 7259 (1993).

[130] C. Vázquez-Vázquez, M. Bañobre-López, M. A. López-Quintela, L. E. Hueso, and J. J. Rivas, "Evidence of weak ferromagnetism in chromium(III) oxide particles" *J. Magn. Magn. Mater.* **272-276**, 1547 (2004).

[131] W. S. Zhang, E. Brück, Z. D. Zhang, O. Tegus, W. F. Li, P. Z. Si, D. Y. Geng, and K. H. J. Buschow, "Structure and magnetic properties of Cr nanoparticles and Cr_2O_3 nanoparticles" *Physica B* **358**, 332 (2005).

[132] A. Punnoose, H. Magnone, M. S. Seehra, and J. Bonevich, "Bulk to nanoscale magnetism and exchange bias in CuO nanoparticles" *Phys. Rev. B* **64**, 174420 (2001).

[133] J. G. E. Harris, J. E. Grimaldi, D. D. Awschalom, A. Chiolero, and D. Loss, "Excess spin and the dynamics of antiferromagnetic ferritin" *Phys. Rev. B* **60**, 3453 (1999).

[134] S. H. Kilcoyne and R. Cywinski, "Ferritin: a model superparamagnet" *J. Magn. Magn. Mater.* **140-144**, 1466 (1995).

[135] S. A. Makhlouf and F. T. Parker, "Magnetic hysteresis anomalies in ferritin" *Phys. Rev. B* **55**, R14717 (1997).

[136] W. J. Schuele and V. D. Deetscreek, "Appearance of a Weak Ferromagnetism in Fine Particles of Antiferromagnetic Materials" *J. Appl. Phys.* **33**, 1136 (1962).

[137] S. Mørup, "Magnetic hyerfine splitting in Mössbauer spectra of microcrystals" *J. Magn. Magn. Mater.* **37**, 39 (1983).

[138] C. Wivel and S. Mørup, "Improved computational procedure for evaluation of overlapping hyperfine parameter distributions in Mössbauer spectra" *J. Phys. E.: Sci. Instrum.* **14**, 605 (1981).

[139] R. H. Kodama, A. E. Berkowitz, E. J. McNiff, Jr., and S. Foner, "Surface Spin Disorder in $NiFe_2O_4$ Nanoparticles" *Phys. Rev. Lett.* **77**, 394 (1996).

[140] T. A. Anhøj, B. Bilenberg, B. Thomsen, C. D. Damsgaard, H. K. Rasmussen, C. S. Jacobsen, J. Mygind, and S. Mørup, "Spin canting and magnetic relaxation phenomena in $Mn_{0.25}Zn_{0.75}Fe_2O_4$" *J. Magn. Magn. Mater.* **260**, 115 (2003).

[141] L. Theil Kuhn, K. Lefmann, S. N. Klausen, H. M. Rønnow, A. Murani, and R. Stewart, "Dynamics in γ-Fe_2O_3 nanoparticles studied by time-of-flight polarized neutron scattering" *Physica B* **350**, E217 (2004).

[142] S. N. Klausen, K. Lefmann, P.-A. Lindgård, K. N. Clausen, M. F. Hansen, F. Bødker, S. Mørup, and M. Telling, "An inelastic neutron scattering study of hematite nanoparticles" *J. Magn. Magn. Mater.* **226**, 68 (2003).

[143] S. N. Klausen, K. Lefmann, P.-A. Lindgård, L. Theil Kuhn, C. R. H. Bahl, C. Frandsen, S. Mørup, B. Roessli, N. Cavadini, and C. Niedermayer, "Magnetic anisotropy and quantized spin waves in hematite nanoparticles" *Phys. Rev. B* **70**, 214411 (2004).

[144] `specnd` is an extension to the `spec1d` package available at `http://www.ill.fr/tas/matlab/`.

[145] S. N. Klausen, P.-A. Lindgård, K. Lefmann, F. Bødker, and S. Mørup, "Temperature Dependence of the Magnetization of Disc Shaped NiO Nanoparticles" *Phys. Stat. Sol. (a)* **189**, 1039 (2002).

[146] A. Würger, "Thermal fluctuations of fine magnetic particles" *Europhys. Lett.* **44(1)**, 103 (1998).

[147] F. Keffer and C. Kittel, "Theory of Antiferromagnetic Resonance" *Phys. Rev.* **85**, 329 (1952).

[148] R. H. Kodama and A. E. Berkowitz, "Atomic-scale magnetic modeling of oxide nanoparticles" *Phys. Rev. B* **59**, 6321 (1999).

[149] W. Feitknecht and H. Studer, "Elektronenmikroskopische Untersuchungen über die Größe und Form der Teilchen kolloider Metallhydroxyde" *Kolloid Zeitschrift* **115**, 13 (1949).

[150] P.-A. Lindgård, "Theory and simulation of antiferromagnetic nanoparticles" *J. Magn. Magn. Mater.* **266**, 88 (2003).

[151] J. T. Richardson and M. V. Twigg, "A Simple Method for Determining the Size of Nickel Oxide Crystallites in Catalysis" *J. Catal.* **188**, 226 (1999).

[152] M. A. Khadar, V. Biju, and A. Inoue, "Effect of finite size on the magnetization behaviour of nanostructured nickel oxide" *Mat. Res. Bull.* **38**, 1341 (2003).

[153] H. Bi, S. Li, Y. Zhang, and Y. Du, "Ferromagnetic-like behaviour of ultrafine NiO nanocrystals" *J. Magn. Magn. Mater.* **277**, 363 (2004).

[154] C. P. Bean and J. D. Livingston, "Superparamagnetism" *J. Appl. Phys.* **30**, 120S (1959).

[155] S. A. Makhlouf, F. T. Parker, F. E. Spada, and A. E. Berkowitz, "Magnetic anomalies in NiO nanoparticles" *J. Appl. Phys* **81**, 5561 (1997).

[156] M. S. Seehra, P. Dutta, H. Shim, and A. Manivannan, "Temperature dependence of electron magnetic resonance and magnetization in NiO nanorods" *Solid State Commun.* **129**, 721 (2004).

[157] N. J. O. Silva, V. S. Amaral, and L. D. Carlos, "Relevance of magnetic moment distribution and scaling law methods to study the magnetic behavior of antiferromagnetic nanoparticles: Application to ferritin" *Phys. Rev. B* **71**, 184408 (2005).

[158] D. E. Madsen, S. Mørup, and M. F. Hansen, "On the interpretation of magnetization data for antiferromagnetic nanoparticles" *J. Magn. Magn. Mater.* **305**, 95 (2006).

[159] M. Hanson, C. Johansson, and S. Mørup, "The influence of magnetic anisotropy on the magnetization of small ferromagnetic particles" *J. Phys.: Condens. Matter* **5**, 725 (1993).

[160] A. K. Petrosyan and A. A. Mirzakhanyan, "Zero-field splitting and g-values of d^8 ions in a trigonal crystal field" *Phys. Stat. Sol. (b)* **133**, 315 (1986).

[161] M. S. Seehra, H. Shim, P. Dutta, A. Manivannan, and J. Bonevich, "Interparticle interaction effects in the magnetic properties of NiO nanorods" *J. Appl. Phys.* **97**, 10J509 (2005).

[162] H. Shim, A. Manivannan, M. S. Seehra, K. M. Reddy, and A. Punnoose, "Effect of interparticle interaction on the magnetic relaxation in NiO nanorods" *J. Appl. Phys.* **99**, 08Q503 (2006).

[163] The RITA-II homepage can be found at `http://sinq.web.psi.ch/sinq/instr/rita2/`.

[164] K. Lefmann, D. F. McMorrow, H. M. Rønnow, K. Nielsen, K. N. Clausen, B. Lake, and G. Aeppli, "Added flexibility in triple axis spectrometers: the two RITAs at Risø" *Physica B* **283**, 343 (2000).

[165] B. T. M. Willis, "The correction of measured neutron structure factors for thermal diffuse scattering" *Acta Cryst. A* **26**, 396 (1970).

[166] M. J. Cooper, "The evaluation of thermal diffuse scattering of neutrons for a one-velocity model" *Acta Cryst. A* **27**, 148 (1971).

[167] C. Frandsen, K. Lefmann, C. R. H. Bahl, B. R. Hansen, B. Lebech, and L. Keller, "Line Width Increase in Magnetic Reflections of α-Fe_2O_3 Nanoparticles Obtained from Neutron Powder Diffraction Measurements on DMC" *PSI Experimental Reports* , I/04–S68 (2004).

[168] Q. A. Pankhurst, "Measurement of magnetic anisotropy in ferrimagnetic powders by applied field Mössbauer spectroscopy" *J. Magn. Magn. Mater.* **101**, 291 (1991).

[169] Q. A. Pankhurst and R. J. Pollard, "Mössbauer spectra of antiferromagnetic powders in applied fields" *J. Phys.: Condens. Matter* **2**, 7329 (1990).

[170] S. Foner, "High-Field Antiferromagnetic Resonance in Cr_2O_3" *Phys. Rev.* **130**, 183 (1963).

List of Papers

Instrumentation

Paper I The monochromatic imaging mode of a RITA-type neutron spectrometer
C.R.H. Bahl, P. Andersen, S.N. Klausen and K. Lefmann
Nuclear Instruments and Methods B **226** 667 (2004)

Paper II Inelastic neutron scattering experiments with the monochromatic imaging mode of the RITA-II spectrometer
C.R.H. Bahl, K. Lefmann, A.B. Abrahamsen, H.M. Rønnow, F. Saxild, T.B.S. Jensen, L. Udby, N.H. Andersen, N.B. Christensen, H.S. Jakobsen, T. Larsen, P.S. Häfliger, S. Streule and Ch. Niedermayer
Nuclear Instruments and Methods B **246** 452 (2006)

Paper III Realizing the full potential of a RITA spectrometer
K. Lefmann, Ch. Niedermayer, A.B. Abrahamsen, C.R.H. Bahl, N.B. Christensen, H.S. Jacobsen, T.L. Larsen, P.S. Häfliger, U. Filges and H.M. Rønnow
Physica B **385-386** 1083 (2006)

Hematite nanopatrticles

Paper IV Inter-particle interactions in agglomerates of α-Fe_2O_3 nanoparticles: Influence of grinding
M. Xu, C.R.H. Bahl, C. Frandsen and S. Mørup
Journal of Colloid and Interface Science **279** 132 (2004)

Paper V Magnetic anisotropy and quantized spin waves in hematite nanoparticles
S.N. Klausen, K. Lefmann, P.-A. Lindgård, L. Theil Kuhn, C.R.H. Bahl, C. Frandsen, S. Mørup, B. Rössli, N. Cavadini and C. Niedermayer
Physical Review B. **70** 214411 (2004)

Paper VI Oriented attachment and exchange coupling of α-Fe_2O_3 nanoparticles
C. Frandsen, C.R.H. Bahl, B. Lebech, K. Lefmann, L. Theil Kuhn, L. Keller, N.H. Andersen, M. v. Zimmermann, E. Johnson, S.N. Klausen and S. Mørup
Physical Review B **72** 214406 (2005)

Paper VII A neutron study of magnetic excitations in 8 nm α-Fe_2O_3 nanoparticles
L. Theil Kuhn, K. Lefmann, C.R.H. Bahl, S.N. Ancona, P.-A. Lindgård, C. Frandsen, D. E. Madsen and S. Mørup
Physical Review B **74** 184406 (2006)

NiO nanoparticles

Paper VIII The magnetic moment of NiO nanoparticles determined by Mössbauer spectroscopy
C.R.H. Bahl, M.F. Hansen, T. Pedersen, S. Saadi, K.H. Nielsen, B. Lebech and S. Mørup
Journal of Physics: Condensed Matter **18** 4161 (2006)

Paper IX Controlling exchange interaction between NiO nanoparticles
C.R.H. Bahl and S. Mørup
Nanotechnology **17** 2835 (2006)

Paper X Uniform Magnetic Excitations in NiO nanoparticles
C.R.H. Bahl, L. Theil Kuhn, K. Lefmann, P.-A. Lindgård and S. Mørup
Physica B **385-386** 398 (2006)

Paper XI Spin dynamics in interacting and non-interacting NiO nanoparticles
C.R.H. Bahl, K. Lefmann, L. Theil Kuhn, N.B. Christensen, H. Vázquez and S. Mørup
Journal of Physics: Condensed Matter **18** 11203 (2006)

Theory

Paper XII Uniform spin wave modes in antiferromagnetic nanoparticles with uncompensated moments
C.R.H. Bahl, K. Lefmann, T. B. S. Jensen, P.-A. Lindgård, D.E. Madsen and S. Mørup
To be published

Paper I

Available online at www.sciencedirect.com
SCIENCE DIRECT®
Nuclear Instruments and Methods in Physics Research B 226 (2004) 667–681
NIM B Beam Interactions with Materials & Atoms
www.elsevier.com/locate/nimb

The monochromatic imaging mode of a RITA-type neutron spectrometer

C.R.H. Bahl [a,b,*], P. Andersen [a,c], S.N. Klausen [a], K. Lefmann [a]

[a] Department of Materials Research, Risø National Laboratory, Building 227, Frederiksborgvej 399, DK-4000 Roskilde, Denmark
[b] Department of Physics, Technical University of Denmark, DK-2800 Lyngby, Denmark
[c] Niels Bohr Institute for Astronomy, Physics and Geophysics, University of Copenhagen, DK-2100 Copenhagen, Denmark

Received 13 April 2004; received in revised form 6 July 2004

Abstract

The imaging monochromatic mode of a neutron spectrometer with a multi-bladed RITA analyser system is so far unexplored. We present analytical calculations that define the mode. It is shown that the mode can be realised for PG (002) analyser crystals, from incident energies of about 3.2 meV and up, allowing the important cases of 3.7, 5.0 and 13.7 meV. Due to beam divergence, the neutron rays from neighbouring analyser blades are found to overlap slightly. Hence, the optimal use of the monochromatic imaging mode would be found by employing an adjustable radial collimator to limit the spread of the ray from each analyser blade.

PACS: 29.30.H; 25.40.D
Keywords: Neutron spectrometers; Multiple analyser

1. Introduction

The triple-axis spectrometer has since the 1960s been the work-horse of neutron scattering science, despite the limitations of data taking on a point-by-point basis [1] Developments in instrumentation have shown multiple data acquisition both in diffraction (powder diffractometers, small angle instruments, image plate Laue cameras [2], and time-of-flight diffractometers) and in spectroscopy (chopper and backscattering time-of-flight spectrometers). However, the triple-axis spectrometer is still a competitive instrument for various types of experiments, in particular due to its flexibility in e.g. defining the resolution function. An obvious way of improving the triple-axis design is to

* Corresponding author. Address: Department of Materials Research, Risø National Laboratory, Building 227, Frederiksborgvej 399, DK-4000 Roskilde, Denmark. Tel.: +45 4677 5491; fax: +45 4677 5758.
E-mail address: christian.bahl@risoe.dk (C.R.H. Bahl).

0168-583X/$ - see front matter
doi:10.1016/j.nimb.2004.07.005

combine the flexibility of this spectrometer type with a multiple data collection mode. This was the cornerstone in the "Re-Invented Triple Axis" (RITA) project started at Risø National Laboratory in 1993, and implemented at the RITA-II [4] spectrometer at SINQ (PSI). The key features in the RITA concept are [3]

- Super-mirror beam optics to maximize flux at the sample position.
- An analyser–detector tank to minimize background, while having a flexible analyser geometry.
- A multi-bladed analyser and a position-sensitive detector to enable multiple data acquisition.
- User-friendly software control of all elements.

Most of these features are already in use at many spectrometers worldwide. However, the multiple data taking option has only been utilized at a few instruments, presumably due to the complexity and the intrinsic difficulties in constructing and running these modes.

A design similar to the one described in this paper is implemented at SPINS [5] at NCNR (NIST) and one will soon be implemented at PUMA [6] at the recently opened FRM-II. The spectrometers E2 [7] at BENSC (HMI) and IN3 (the MULTI [8] option) at ILL both have multi-blade analyser systems for monochromatic multiple data taking. E2 uses flatcone geometry to reflect out of plane to remove the inelastic part of the signal in diffraction. IN3 MULTI has 31 (with a potential for 61) analysers and detectors in plane, each collecting data at a different scattering angle. There are long collimator blades from the analysers to the detectors, creating one channel for each detector. This is the optimal configuration of the imaging mode described here, as the problems of cross-talk addressed later are avoided. Both E2 and IN3 are thermal instruments, relying on the smaller scattering angles of thermal neutrons compared with cold neutrons.

RITA-II has a very large range of possible analyser scattering angles, making an imaging mode possible with cold neutrons. It also has the versatility of easily being able to change between the various different modes, in which it can be run. In [9], we presented a selection of these modes for running a RITA-type multi-analyser system. So far only the monochromatic point-to-point focusing mode has been utilized [10], with one exception where an energy-dispersive mode was used [11]. The present paper will delve deeper into the details of the monochromatic imaging mode, which is shown to be a generalization of the point-to-point focusing mode, and present implementations, Monte Carlo simulations, and actual data taken in this mode, RITA-II.

2. Derivation of the monochromatic analyser settings

We first give a brief description of the essentials of the imaging monochromatic analyser mode. The neutrons scattered from the sample are allowed to diverge by a radial collimator into the large opening of the analyser–detector tank. The analyser blades are positioned on a linear support. A number of the available analyser blades are positioned to cover different scattering angles. These blades are set to reflect neutrons of the same energy (hence the name "monochromatic"). The rays from the blades are directed towards different parts of the PSD. For each spectrometer setting, this allows for one data collection area on the PSD per active analyser blade (see Fig. 1).

The mathematics of the mode is in-principle simple but rather tedious, and we leave the details for Appendix A. Our results for the monochromatic focusing mode were presented earlier [9], but appear here as a special case of the more general imaging mode.

The analyser support is rotated by the angle Ω_A from the incoming beam direction. We need to find an equation for Ω_A given by the geometry of the spectrometer. We arrive at the equation

$$\cos\Omega_A = \frac{r\sin 2\theta_A \pm (\cos 2\theta_A + R)\sqrt{1 - r^2 + R^2 + 2R\cos 2\theta_A}}{1 + R^2 + 2R\cos 2\theta_A}, \quad (1)$$

where $2\theta_A$ is the neutron scattering angle, r is the ratio between the distance between the intercep-

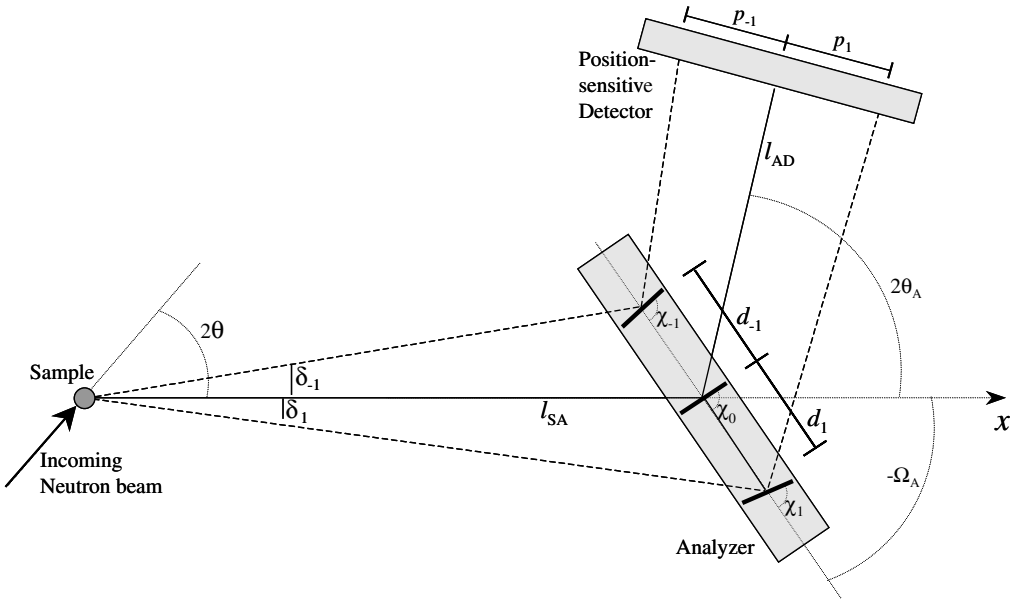

Fig. 1. The geometry of the monochromatic imaging mode set-up showing the position of the analyser blades in the scattering plane seen from above.

tion points on the detector and the distance between the analyser blades and R is the ratio between the analyser–detector and the sample–analyser distances. A derivation of this equation can be found in Appendix A.

3. Monochromatic analyser modes at RITA-II

We now investigate how to implement the mode of Eq. (1) to the RITA-II spectrometer at SINQ. Typical spectrometer settings are $l_{AD} = 0.328$ m, $l_{SA} = 1.207$ m and $d_i = 25$ mm, whereas p_i can be chosen freely by setting software windows on the PSD. The seven central blades of the analyser are presently installed. Useful values for the final energy, E_f, would include 3.7, 5.0 and 13.7 meV, corresponding to the use of BeO, Be and PG filters, respectively.

In general, (1) will define two solutions for $\cos\Omega_A$, in turn giving four solutions of $\Omega_A(r)$ (see Fig. 2). Some of these will be unphysical, as they give values of the p_i's, that differ from the initial values specified. To determine which of the four solutions of (1) to use as Ω_A the values given above were inserted in (A.9), and each of the four solutions was checked and visualized graphically, as seen in Fig. 3(a). The figure shows the path of the neutron beams from the sample the analyser and from here to the detector, looking down from above. Fig. 4 shows the position on the detector for the neutron beam from each of the seven blades as a function of the angle Ω_A in the $E_f = 5.0$ meV case. The four solutions with $r = 1$ are indicated by vertical pale

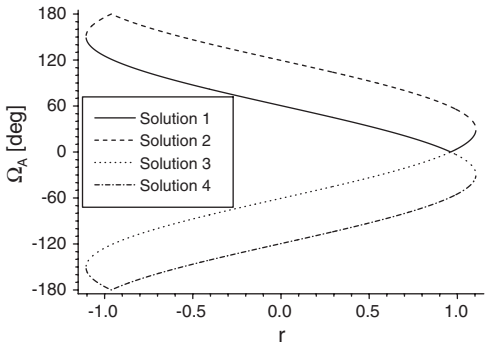

Fig. 2. The four solutions to Eq. (1), giving Ω_A as a function of r at 5.0 meV, with $R = 0.2718$. Solution 4 is found to give the best values.

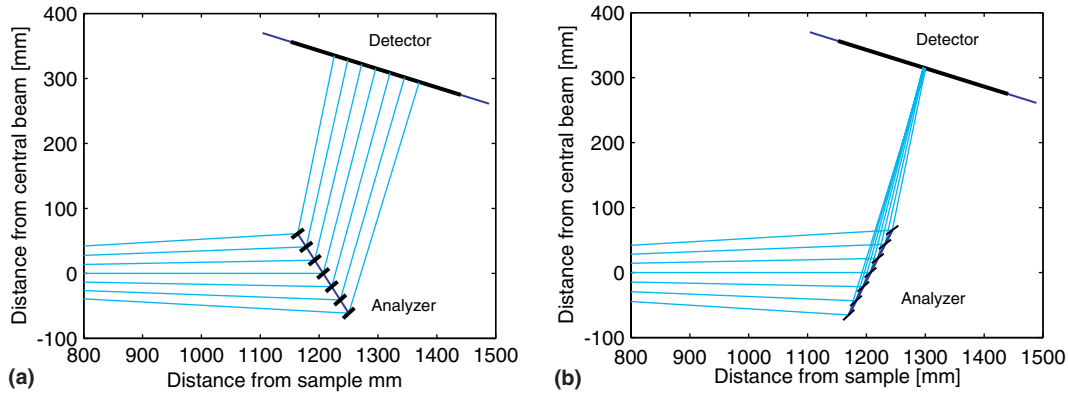

Fig. 3. Graphical visualization of the analyser setup in the monochromatic imaging mode and the point-to-point focusing mode at $E_f = 5$ meV, as seen from above. The active area of the detector is indicated by a broader line. (a) The monochromatic imaging mode and (b) The point-to-point focusing mode.

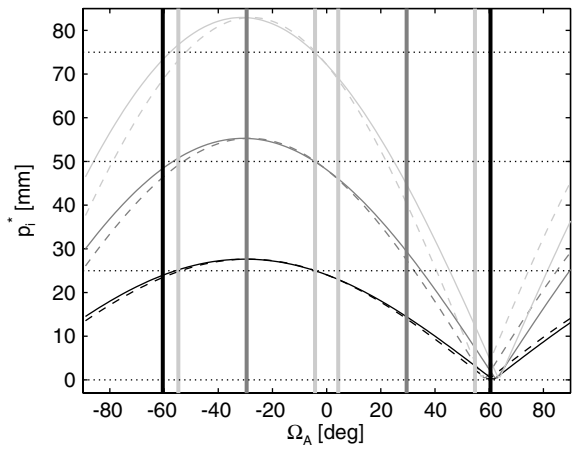

Fig. 4. The position of the intersections of the centres of the beams from each blade on the detector as a function of the angle Ω_A, for $E_f = 5$ meV. The curves show the calculated intersection points p_i^* from the seven blades. Solid lines indicate a positive value of the blade number i and dashed lines indicate a negative value of i. The pale grey curves are from $i = \pm 3$, the dark grey are from $i = \pm 2$ and the black are from $i = \pm 1$. $i = 0$ is always zero. The four possible solutions for $r = 1$ are indicated by vertical pale grey lines (see discussion in the text). The vertical dark grey lines are the solutions for $r = r_{max}$, and the black ones are the solutions for $r = 0$, i.e. the point-to-point focusing mode. The horizontal dotted lines indicate the positions on the detector corresponding to a spacing between the intersection points of 25 mm. These show the intended intersection points p_i.

grey lines. The value $\Omega_A = -54.74°$ was found to be the best solution. The values of χ_i are found according to the calculations in Appendix A. Table 1 gives the best solutions for Ω_A for a number of different energies. The solution is determined as the one with the least asymmetry, as described below, but also taking into account that the angle Ω_A should not be so small, that the blades overlap seen from the sample. At some of the analyser settings, including the energy values 2.5 and 3.7 meV and the range between these, some amount of overlapping of the blades cannot be avoided. But this is in most cases not a significant amount.

The square root in (1) constrains the maximum possible value of r, thus giving a limit to the separation of the intersection points of the beams from the different analyser blades on the detector. With an energy E_f of 5.0 meV, the maximum value of $p_i = 1.11 \cdot d_i$ (or 27.6 mm) is found. Throughout this paper we will use the value $p_i/d_i = r = 1$, which must be considered to be the smallest reasonable value due to beam divergence, as will be discussed later. r is kept constant in order to be able to build a radial collimator, with one channel for each blade, in IN3 MULTI style, as discussed later. Having the blades at fixed positions means requiring that r is the same for all energies. The smallest energy, that allows $r = 1$ is found to be 3.21 meV, as seen in Fig. 5. We find that the minimum energy allowed is 2.0 meV giving maximum of $r = 0.793$. This minimum energy is due to the physical limitations of the spectrometer, as a value of $2\theta_A$ larger

Table 1
Properties of the monochromatic imaging mode for a selection of final neutron energies, using the experimental settings at RITA-II with PG (002) analysers ($\tau = 1.8733$ Å^{-1})

E_f	$2\theta_A$	r_{max}	Ω_A ($r = 1$)	a_3^δ (%)	a_3^p (mm)	a_{-3}^p (mm)
2.0	144.88°	0.79	48.73°	−4.1	0.26	0.24
2.5	117.03°	0.91	19.80°	−5.8	0.20	0.22
3.7	89.01°	1.04	−32.22°	5.3	0.68	0.76
5.0	74.17°	1.11	−54.74°	3.6	1.71	1.88
8.0	56.94°	1.17	−75.60°	1.5	2.67	2.82
13.7	42.72°	1.21	−21.49°	5.8	−1.11	−1.24

The values of Ω_A for $E_f = 2.0$ and 2.5 meV are found with values of $r = 0.79$ and 0.90, respectively, as $r_{max} < 1$, the others are found with $r = 1$.

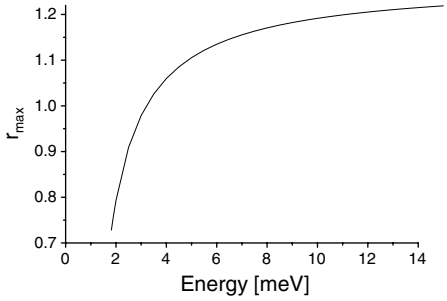

Fig. 5. Calculated maximum value of the parameter $r = p_i/d_i$ as a function of final energy E_f. The value is limited by the square root in Eq. (1).

than the 144.88° found for the 2.0 meV case would place the detector in the incoming beam.

In the imaging mode the signal from each blade should be analysed separately. The blades are 25 mm wide, and seen under an angle of $2\theta_A$. Therefore for a 10 mm wide sample, the distance collimation over the 1.207 m from the sample to the analyser gives an angular resolution of 0.69–0.71° FWHM for each blade.

As mentioned above the monochromatic point-to-point focusing mode is a special case of Eq. (1), with all $p_i = 0$. In the graphical visualization this is indeed seen to be the case, as all the beams are focused on the detector for $\Omega_A = 60.49°$, see Fig. 3(b). As the difference in δ_i between two blades is about 1.0°, the PSD will detect a number of 2θ values simultaneously, giving very coarse angular resolution in the focusing mode ($\Delta 2\theta \sim 7°$). The capability to use between 1 and 7 blades to control this angular resolution is a part of the flexibility of the RITA spectrometer.

The use of horizontally focusing analysers to concentrate more signal onto a smaller area of the detector is well established. The analyser is oriented in the conventional way at half the scattering angle ($\Omega_A = \theta_A$), but it is slightly curved instead of being flat. This enhances the signal on the detector at the expense of angular resolution. This way of focusing needs identical sample–analyser and analyser–detector distances to be point-to-point focusing. The mode described here will be point-to-point focusing at any sample–analyser and analyser–detector distances, thus making a short analyser–detector distance possible, without spreading out the signal.

Because of the asymmetry of the analyser as seen from the sample, there will be an asymmetry in the δ_i values. This asymmetry is defined as

$$a_i^\delta = \frac{\delta_i + \delta_{-i}}{|\delta_i| + |\delta_{-i}|}, \tag{2}$$

where the δ_i's are given by Eq. (A.4).

Since l_{SA} is very large compared to the d_i's, a_i^δ only amounts to 1.2% for the blades with $i = \pm 1$ rising to 3.6% for the blades with $i = \pm 3$, in the 5.0 meV case. In a monochromatic mode the scattering angle of the analyser blades is constant. The asymmetry in the δ_i's will then give an offset in the values for the p_i's, which can be expressed as

$$a_i^p = p_i^* - rd_i, \tag{3}$$

where p_i^* is the actual intersection point of the beam on the detector opposed to $rd_i = p_i$ which is the intended intersection point.

As the distance to the detector from each blade is different, an extra asymmetry is introduced, so

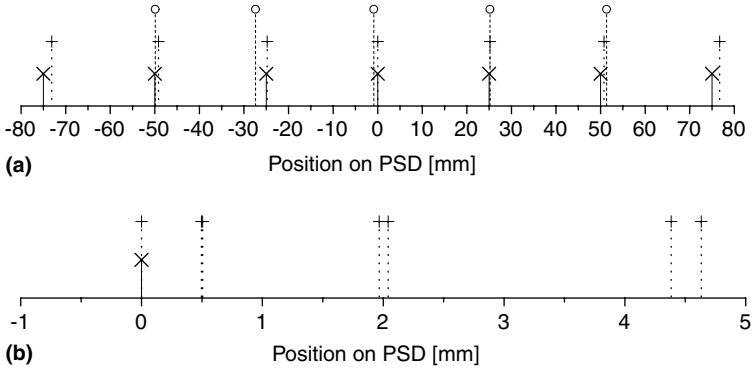

Fig. 6. The actual intersection points on the PSD compared to the intended ones. (a) is the multi-blade monochromatic imaging mode and (b) is the point-to-point focusing mode. (×) indicates the intended equidistant positions, (+) indicates the positions calculated by the equations in Appendix A and (○) indicates the actual measured positions. It is seen that the offset a_i^p is always in the same direction, and that it grows as the distance to the central blade grows.

that the value of p_3 is 1.71 mm higher than the intended value, whereas the value of p_{-3} is 1.88 mm higher. The offsets for p_1 and p_{-1} are both as low as 0.20 mm. All the intersections with the detector are shifted, in the direction of positive x in Fig. 1, compared to the intended values. This shifting is also seen in the point-to-point focusing mode. Thus it is not truly a point-to-point mode, as there is some spread out of the intersection points on the PSD. The shifts in both modes are shown in Fig. 6 for the case with $E_f = 5.0$ meV. The figure shows the actual intersection points of the neutron beams on the PSD compared with the intended intersection points.

In Fig. 4 it is seen that the offset a_i^p vanishes using one of the solutions of (1) at $r = r_{max}$. At $r = 0$ and $r = r_{max}$ the four solutions of (A.17) combine to two. One that is correct and one that is not a physical solution. Going to solutions with r smaller than r_{max} increases the number of solutions to four, and introduces an offset in a_i^p. The figure also shows how there will always be an offset at $r = 0$, whatever the value of Ω_A, as there is nowhere where the signal from all the blades intersect the zero point on the detector at the same time.

To ensure that the multi-blade imaging mode is indeed monochromatic, energy scans have been performed on the (1 0 2) powder peak in Al_2O_3, using only blades $i = -2$, 0 and 2. The spectra from all three blades are centred within 0.02 meV of the elastic peak. Inelastic aspects of the imaging mode will be presented and analysed in a later publication [12].

4. Powder diffraction experiments

4.1. Selection of the counting windows

For calibration and benchmarking, we used a standard sample of polycrystalline α-Al_2O_3. Data collection was performed using the analyser setup described above. An 80′ collimator was used to define the beam after the vertically focusing PG (0 0 2) monochromator. The initial and final neutron energies were 5.0 meV. Slits were set to reduce the background, but the slit after the sample was set rather open in the horizontal direction to allow line-of-sight from the sample to all of the analyser blades. A Beryllium filter with radial collimation was used between the sample and analyser to reduce background and second order contamination.

Figs. 7(a) and (b) show the sum of the PSD images taken during a 2θ scan of α-Al_2O_3. In this way the contribution from each blade is clearly seen. Fig. 7(b) has the five central blades of the analyser reflecting, whereas Fig. 7(a) only has the blades with $i = -2$, 0 and 2 reflecting. In the TASCOM spectrometer control software [13], the 9 possible blades of the analyser are numbered 1–9. These numbers will be used in the following, with

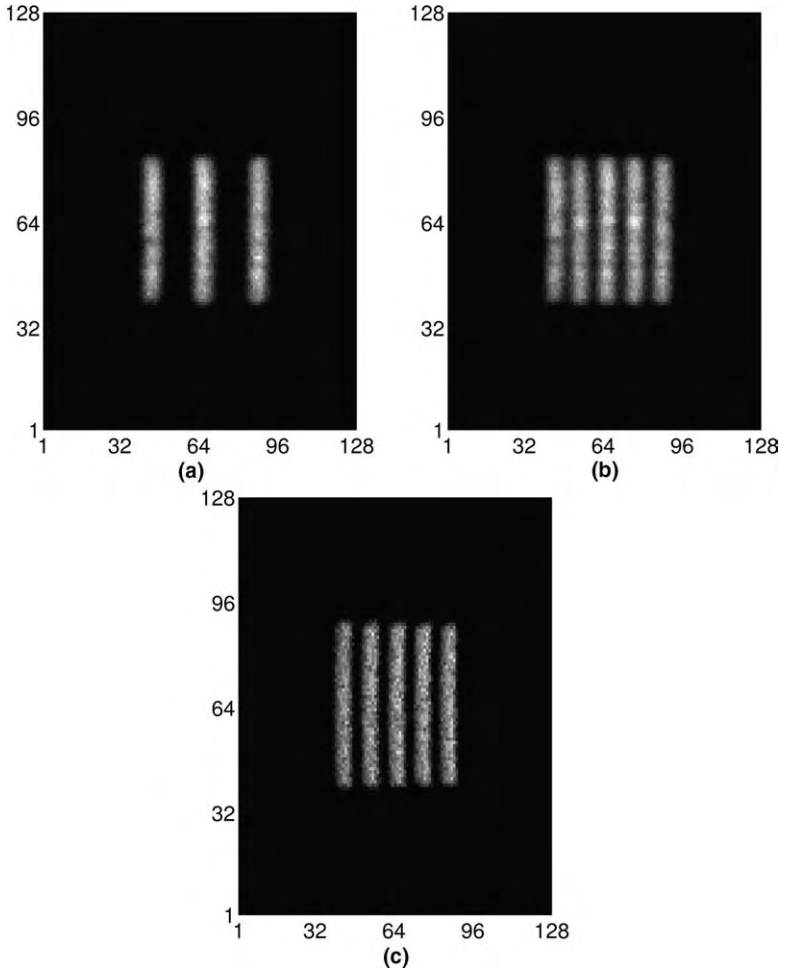

Fig. 7. Sum of all PSD images recorded during a scan of the (1 0 2) peak of α-Al_2O_3. (a) has blades 3, 5 and 7 reflecting and (b) has blades 3, 4, 5, 6 and 7 reflecting. The remaining blades are in a non-reflecting orientation in both cases. (c) is a simulated PSD image calculated using the McStas software package. The calculation is done for the 5-blade mode, using a virtual isotropically scattering Vanadium sample. All the images have a linear intensity scale from black to white, white being the most intense.

$i = -2$, 0 and 2 corresponding to blades 3, 5 and 7, respectively.

The initial and somewhat naive method of signal collection would be to divide the PSD into slices, cutting halfway between the signals from the different blades. This would give 2θ scans collected by the central blade as shown in Figs. 8(a) and (d) for the 3-blade and 5-blade modes, respectively. These scans have considerable cross-talk from the other blades, certainly in the 5-blade mode, seen as extra peaks centred at 2θ values $\sim 1^\circ$ of from the nominal -71.0°. It is clear that defining smaller counting windows around the signals on the PSD is necessary.

Windows of equal area were software defined on the PSD, corresponding to the blades. The whole PSD is 128×128 pixels, corresponding to an active area 300 mm wide and 500 mm high. In the 3-blade mode each window was 15 pixels (35 mm) wide and 48 pixels (113 mm) high, with a spacing of 6–8 pixels between them. (The difference is due to the slight asymmetry of the p_i's discussed above.) In the 5-blade mode each window was 6×47 pixels (14×110 mm), with a spacing

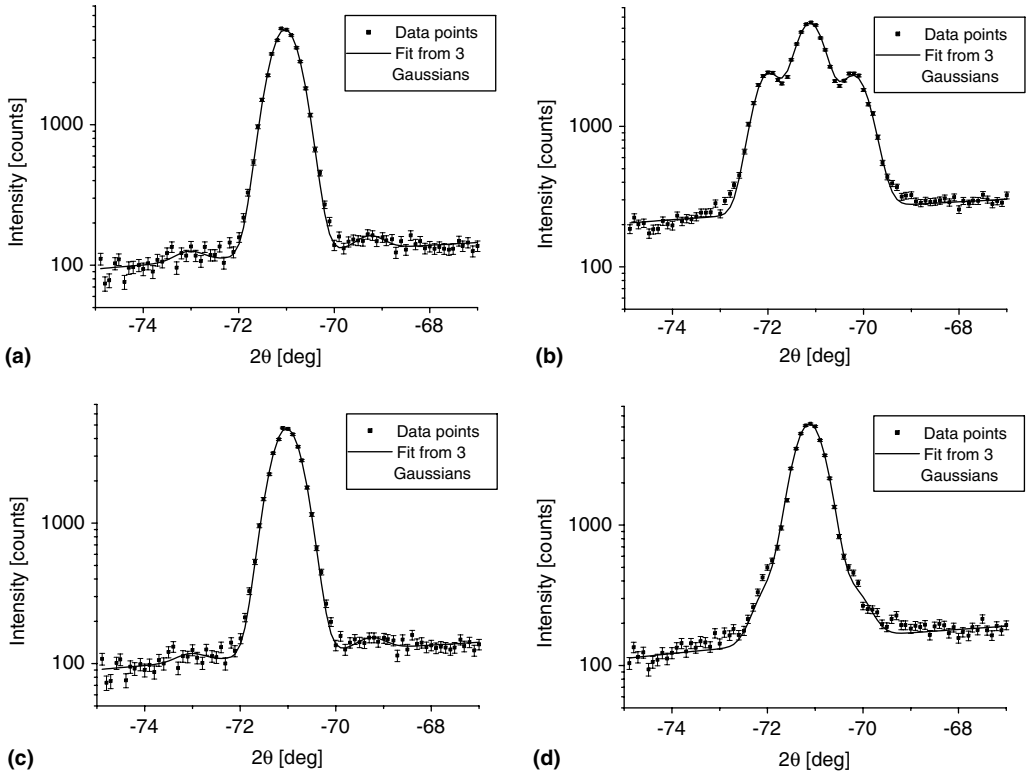

Fig. 8. Data from different sizes of the counting window in the 3- and 5-blade modes shown on logarithmic scales. (a) Data from a window ranging 10 pixels each side of the middle of the central blade in the 3-blade mode. (b) Data from a range 10 pixels each side of the middle of the central blade in the 5-blade mode. (c,d) Data ranging six pixels each side of the middle of the central blade, in the 3- and 5-blade modes, respectively. All the data is fitted with three Gaussian distributions. The centres and widths of these are fixed and the amplitudes are fitted from the data.

of 4–5 pixels between them. Counting was done in the defined windows independently of each other, for each scan point.

Even with the narrow software-defined windows there is a possibility of cross-talk between the signals from the blades, especially in the 5-blade mode. Therefore this cross-talk has been quantified for each of the two modes. A measurement of the cross-talk may be found by using a 2θ scan of one powder line and analysing these data with different sizes of the counting window on the PSD, as seen in Fig. 8. Starting with a window centred around the middle of the peak from the central blade, large enough to include signals from the neighbouring blades, the intensities of the three peaks in the counting window are found by fitting with Gaussian distributions. Fixing the position and widths of the three peaks, the size of the counting window is reduced in steps until it only encompasses the centre of the peak from the central blade. In each step the amplitudes of the three peaks are recorded. Fig. 9 shows the amplitudes of the peaks versus the size of the window for the 3-blade and the 5-blade modes. The vertical lines indicate the edge of the previously defined counting windows. Within the counting window of the 3-blade mode, as defined above, the signal from the central blade is at its maximum, and the intensities from the neighbouring blades are about 0.2% of this. In the 5-blade mode it is more difficult to find a window size where the central blade has maximum intensity and the neighbouring blades have minimum. The chosen window size also gives a cross-talk of about 0.2%, but a slight

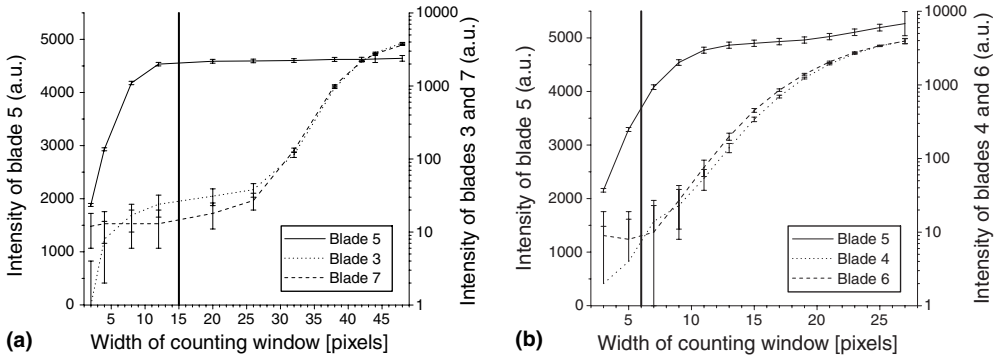

Fig. 9. Plot of the intensities of the signals from the blades, as a function of the size of the counting window in pixels. The intensities are the amplitudes of Gaussian fits to the data, keeping the centre and widths of the these fixed. The vertical line is the edge of the software-defined window chosen for future measurement. In (a) the blades 3, 5 and 7 have been used (3-blade mode) and in (b) the blades 4, 5 and 6 have been used (5-blade mode). Note the plots are on different scales.

misalignment may easily increase this. This minute remaining signal of 0.2% may be due to incoherent scattering from the α-Al_2O_3 reflected from the neighbouring blades or it may be due to a point spread function in the detector.

Using small six pixel windows in order to minimize cross-talk gives a 10–15% reduction in the detected signal, slightly reducing the gain in intensity of the multi-blade modes. An obvious way to avoid the cross-talk is to use an adjustable coarse radial collimator before the detector defining one vane for each analyser blade, as on IN3 MULTI. This would make it possible to use larger windows in the 5-blade mode. Such a collimator has recently been built, and will be presented in a later publication [12].

4.2. Calibration sample: α-Al_2O_3

In order to minimize the problem of cross-talk, we decided to use every other blade (3, 5 and 7), for the remaining experiments, leaving the others at non-reflecting angles. Fig. 10 shows a 2θ scan of the α-Al_2O_3 (1 0 2) peak ($q = 1.8049$ Å^{-1}), with the counting windows set to 15×48 pixels as described above. Actually this is the very same data set as used to investigate the counting windows in Section 4.1. The recorded intensity from each of the windows is given as a function of scattering angle. It is seen that each of the windows on the PSD records the (1 0 2) peak, but as expected the peak is found at different values of 2θ in the different windows. The angular spacings between the peaks are discussed below. Having found these spacings the three spectra can be shifted, resulting in one combined spectrum with three times the intensity of a scan with just one blade, but with no loss of resolution.

The proper angular shifts of the signals from blades 3 and 7 have been found from the data to be +1.999° and −1.770°, respectively. These angles should be equal to the differences of the δ_i's for the blades. The calculated amounts are +1.985° and −1.892°, respectively, from Eq. (A.4), giving deviations 0.014° and 0.122°, respectively. The positions, amplitudes and FWHM of the peaks are given in Table 2, along with the integrated areas and background intensities.

An explanation of the observed error in the offset of the δ_i angles, may be a wrong calibration of the spectrometer. If the distance l_{SA} was 1.242 m instead of 1.207 m, the errors would be 0.08° and 0.07° for blades 3 and 7, respectively. Measurement of the offsets of the angles in the 5-blade mode also supports this explanation. This shows the importance of correct calibration of the spectrometer, as the precise measurement of a distance that is generally not very significant here becomes important.

The considerations above suggest that the monochromatic imaging mode would be ideal for powder diffraction experiments to study very weak

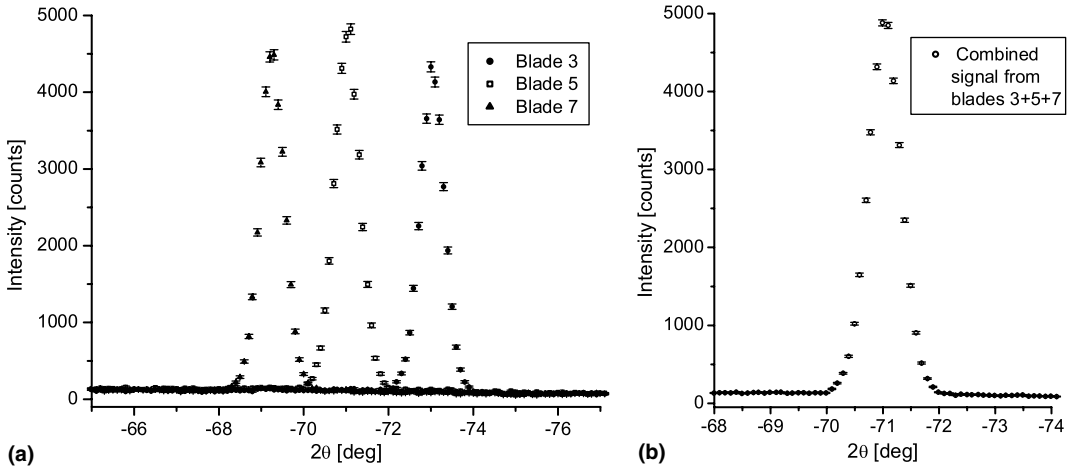

Fig. 10. 2θ scan of α-Al_2O_3 in the 3-blade mode as described in the text. The offsets in angles between the blades are clearly seen. The right figure is data combined from all three blades.

Table 2
Parameters from Gaussian fits to the data in Fig. 10

Blade	3	5	7	Combined
Position [deg]	−73.025(2)	−71.026(2)	−69.256(2)	−71.025(1)
Amplitude [counts]	4094(43)	4590(47)	4341(45)	4699(33)
FWHM [deg]	0.691(2)	0.719(2)	0.697(2)	0.705(1)
Background [counts]	93(3)	120(3)	105(2)	114(2)
Integrated area	3013(32)	3516(37)	3222(35)	3529(25)

The signal from each blade is fitted separately. The combined data is found by averaging the data from the data sets from blades 3, 5 and 7 point by point, after transposing the data from blades 3 and 7.

peaks, that are difficult to distinguish from the background. We use a triple-axis setup for reducing the background, by removing inelastic signals such as thermal diffuse scattering. By combining the signals from the three blades, the statistics of the spectra are improved. This is indeed seen in Table 2. The Gaussian fit to the combined data from three blades has almost identical parameters as the one for data from blade 5 alone, it just has three times the statistics. This makes identification and quantification of weak peaks easier, as will be shown in the next section.

It was observed that the three blades do not contribute with the same signal. The ratios of the integrated areas of the (1 0 2) peak in α-Al_2O_3 from the three blades are 0.857(19):1.000(14):0.916(17) for blades 3, 5 and 7, respectively, and from the background around the peak the signal ratios are 0.775(32):1.000(25):0.875(28). So blade 5 gives a signal that is about 10–20% above the others. We have considered two possible reasons for this. (1) Blade 5 could just reflect better than the others. This would not be seen in the conventional point-to-point focusing mode, as the signals from the blades overlap. (2) The neutron beams to or from the outer blades may be partly blocked either by the sample slits, the detector tank opening or the detector shielding. This may also explain why blade 7 has a higher signal than blade 3, as it is further away from the tank entrance, and the right slit would cut off less of the signal. Opening up the right and left sample slits from 18 to 40 mm each did not change the signal ratios however. By varying the software windows, we checked that the effect cannot be explained by using a wrong definition of these. A ray-tracing simulation of the spectrometer

has been done using the McStas software package [14,15]. A simulated PSD image in 5-blade mode is shown in Fig. 7(c). Summing the data in this figure in the vertical direction gives the intensity ratios 0.89(6):0.98(6):1.00(6):0.98 (6):0.95(6). It is seen that most of the difference in blade intensity can be reproduced by simulation, and is thus explained by the geometry of the problem.

Another contribution to the difference in the integrated signal ratios is that each analyser blade is made from two pieces of pyrolytic graphite, mounted above each other in the vertical direction. Analysis of the PSD images during alignment, has shown that there is a slight misalignment of between 0.01° and 0.09° between the top and bottom pieces, of each of the blades. This misalignment leads to a reduction of the reflected intensity, as both parts of the blades cannot be perfectly Bragg reflecting at the same time.

The higher ratios in the background signal may be explained by the more "open" geometry of the middle blade making it more susceptible to noise from the surroundings than the other blades.

The difference in signal intensity from the three blades must be taken into account when combining data. The three contributions should be normalized, to be combined properly. This can be done using the integrated signal ratios, of the different blades. Indeed this has been done for the combined signal in Table 2. The reason why the amplitude of the combined signal is slightly higher than any of the individual amplitudes is that the normalization has been done using the ratios of the integrated areas of the peaks and not the amplitudes.

4.3. Test experiment: $YBa_2Cu_3O_{6+x}$

The monochromatic imaging mode of RITA-II has been utilized in the measurement of the $(\frac{1}{2}\,\frac{1}{2}\,1)$ magnetic peak in $YBa_2Cu_3O_{6+x}$ nanoparticles. The particles are disk-shaped with a diameter of ~50 nm and a thickness of about ~3 nm in the *c*-axis direction. The particles were prepared by a citrate gel modification of the sol–gel technique as described in [16,17]. This experiment used a set-up with the 3-blade monochromatic analyser mode as described above, but with 40′ collimation between monochromator and sample, to match the distance collimation after the sample. The sample temperature was 9 K. The $(\frac{1}{2}\,\frac{1}{2}\,1)$ peak is on the shoulder of the stronger, broad (201) peak from $Y_2Cu_2O_5$ impurities.

For calibration, a scan of the strong (003) structural peak of $YBa_2Cu_3O_{6+x}$ was taken. This peak is more well defined than the $(\frac{1}{2}\,\frac{1}{2}\,1)$ peak, so it is better suited for measuring the offsets in the angles and signals from the different blades [18].

For the $YBa_2Cu_3O_{6+x}$ sample the shifts in the angles between the peaks in the 3-blade mode are +2.006° and −1.734° for the (003) peak. These are in accordance with the shifts found for α-Al_2O_3 above.

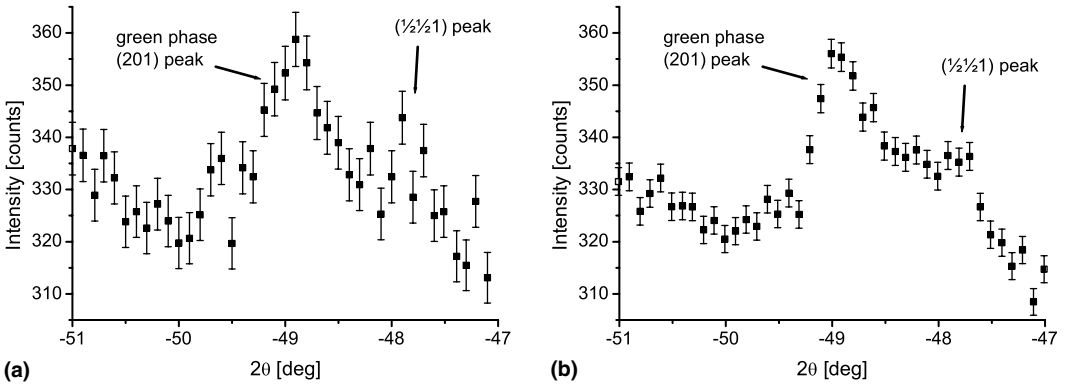

Fig. 11. 2θ scan of the magnetic $(\frac{1}{2}\,\frac{1}{2}\,1)$ peak in $YBa_2Cu_3O_{6+x}$ on the shoulder of the (201) peak from the $Y_2Cu_2O_5$ (green phase) impurity. (a) Data from one blade and (b) data from the same scan, combining three blades 3, 5 and 7.

Surprisingly we find that the intensity ratios in the structural (0 0 3) peaks of the $YBa_2Cu_3O_{6+x}$ nanoparticles is different from that found in the α-Al_2O_3. At 9 K the ratio is 0.776(54):1.000(71): 0.768(50). This could be because of a slightly different alignment of the analyser blades leading to a reduction in the signal from one of the two halves of the blades. Thus it is always important to measure the intensity ratio in a reference peak in the same alignment the experiment in order to be able to correctly analyse and normalize data.

Figs. 11(a) and (b) show two scans of the $(\frac{1}{2}\,\frac{1}{2}\,1)$ peak in $YBa_2Cu_3O_{6+x}$ at 9 K. In Fig. 11(a) only data from blade 5 is used, while Fig. 11(b) shows combined data from blades 3, 5 and 7. The data has been transposed and normalized using the offsets and ratios found above. It is clearly seen that the smaller errorbars and better statistics in the 3-blade figure makes the peak easier to identify and quantify, while the peak and background intensities are unaltered.

2θ scans of 8° were performed across the peaks. However, because of the offset of the blades only an area of 4° has triple statistics. The area with double and single statistics can of course still be used in the data analysis.

5. Summary and conclusion

The multi-blade analyser of the RITA type can be run in a number of modes, some q-dispersive and some energy dispersive. However, the only well explored mode has been the monochromatic point-to-point focusing mode at RITA-II [10] and the flat analyser mode at SPINS.

Here we have presented a derivation and analysis of the imaging monochromatic mode, a generalization of the previously used point-to-point focusing mode and similar to the IN3 MULTI backend. From the analysis, computer simulations and experiments, we conclude that the mode is feasible to use for final neutron energies ranging from approximately 3.2 meV and up, although there is some overlapping of the line of sight to the individual blades below energies of about 3.7 meV. We have performed experiments at $E_f = 5.0$ meV. The use of consecutive analyser blades gives some cross-talk between the signals from the different blades. Using the imaging monochromatic mode with every second blade is found to be a large improvement for triple-axis powder diffraction, where a factor of almost 3 in data acquisition is achieved, with no loss in resolution and only small complications in data analysis.

An obvious way of avoiding the cross-talk due to spreading of the beams is a coarse radial collimator placed in front of the PSD. This would minimize the cross-talk from one channel to the neighbouring one. Such a device for RITA-II has recently been built. The performance of the collimator, along with test results for both elastic and inelastic experiments, will be published later [12].

It has been observed, that the scattering intensity from each of the analyser blades is not the same. This has been shown to be due partly to the geometry of the analyser tank, and partly to the positioning and scattering efficiency of the pyrolytic graphite on the analyser blades. The latter is intrinsic to these blades, thus it will be present in all configurations of the RITA-II spectrometer. Both contributions should generally be taken into account, when analysing data.

Neither the cross-talk nor the difference in scattering intensity from the analyser blades have previously been considered, as these are not important when using the spectrometer in the point-to-point focusing mode. But when employing the described imaging mode they become significant. For future elastic and inelastic work the difference in scattering intensity of the blades must be normalized using elastic or inelastic scans of vanadium with each blade separately, to account for the different resolution functions from the blades.

In conclusion we have shown that an imaging mode can be realised on RITA type spectrometers, extending the flexibility. Multiple data taking in an imaging mode configuration has already been implemented at IN3 MULTI, using a more optimal design than presented here. The advantage of the RITA concept is the flexibility in allowing many different analyser–detector configurations, making a whole range of data taking modes possible. More of these modes will be explored in the future.

Acknowledgements

We thank the RITA-II responsible scientists, Christof Niedermayer and Asger B. Abrahamsen for keeping the instrument in a shape to allow for this work. We also thank Luise Theil Kuhn and Petrina Paturi for preparing the $YBa_2Cu_3O_{6+x}$ nanoparticles and Henrik M. Rønnow for valuable discussions.

The project has been supported by the EU through the programs Cool Neutrons, TECHNI and SCANS, and by the Danish Natural Science Council through the Dnish Neutron Scattering Centre DANSCATT. CHRB is supported by the Danish Technical Research Council, through the Nanomagnetism framework program.

Appendix A. Derivation of the monochromatic mode

This appendix gives the calculations required in order to find the relationship between the angle of the analyser support, Ω_A and the geometry of the spectrometer as given in Eq. (1) and shown in Fig. 1.

We approximate the sample by a point at its centre-of-mass, and we assume a coordinate system with origin at the sample centre and x-axis along the nominal sample–analyser direction (towards the central analyser blade), see Fig. 1. The analyser blades are labelled by positive or negative integers, i, where $i = 0$ corresponds to the central blade. The blades are positioned on a linear support, which is rotated by the angle Ω_A from the x-axis. The position of each blade relative to the support is denoted d_i, and the rotation χ_i. The nominal neutron scattering angle at each blade is denoted $2\theta_{A,i}$. The position where the nominal scattering direction intersects the position-sensitive detector is given by the distance, p_i, between the intersection and the beam from the central blade, see Fig. 1. The nominal sample–analyser distance is l_{SA}, and the nominal analyser–detector distance is l_{AD}.

For the calculation we treat l_{SA}, l_{AD} and d_i as constants. The nominal analyser scattering angle $2\theta_A \equiv 2\theta_{A,0}$ is given by the final neutron energy, $E_f = \hbar^2 k_f^2/(2m_N)$, via the Bragg law:

$$\tau_A = 2k_f \sin\theta_A, \tag{A.1}$$

where τ_A is the scattering vector of the analyser (higher order contamination is neglected). We assume monochromatic scattering from all the blades:

$$2\theta_{A,i} = 2\theta_A. \tag{A.2}$$

What remains now is to find the relation between Ω_A and the p_i's, in particular to find the value(s) of Ω_A for a particular choice of the p_i's.

We assume $|p_i|, |d_i| \ll l_{SA}, l_{AD}$, and linearize the equations in d_i to find that p_i/d_i becomes a constant which defines Ω_A. Below follow the details.

The position of the analyser blades are given by

$$\vec{R}_{A,i} = \vec{R}_A + d_i \begin{pmatrix} \cos\Omega_A \\ \sin\Omega_A \end{pmatrix} \quad \text{where } \vec{R}_A = l_{SA}\begin{pmatrix} 1 \\ 0 \end{pmatrix}. \tag{A.3}$$

It is seen that $\vec{R}_A \equiv \vec{R}_{A,0}$ is the position of the central blade. The difference in scattering angle (2θ) between neutrons hitting the central blade and neutrons hitting blade i can be found directly from the equations above:

$$\tan\delta_i = \frac{d_i \sin\Omega_A}{l_{SA} + d_i \cos\Omega_A}, \tag{A.4}$$

as also found in [9]. The linearized version of this reads

$$\delta_i = d_i \frac{\sin\Omega_A}{l_{SA}}. \tag{A.5}$$

The individual rotation of each blade is found from δ_i and from the condition of monochromatic scattering:

$$\delta_i + \Omega_A + \chi_i = \theta_{A,i} = \theta_A. \tag{A.6}$$

Neutrons scattered from the midpoint of the central blade will intersect the detector at

$$\vec{R}_D = \vec{R}_A + l_{AD}\begin{pmatrix} \cos 2\theta_A \\ \sin 2\theta_A \end{pmatrix}, \tag{A.7}$$

whereas neutrons from a general blade will (by the definition of p_i) intersect the detector at

$$\vec{R}_{D,i} = \vec{R}_D + p_i \begin{pmatrix} \sin 2\theta_A \\ -\cos 2\theta_A \end{pmatrix}. \tag{A.8}$$

Following the neutron ray from blade i using the monochromatic condition (A.2), the neutron ray is represented by the parameterized expression

$$\vec{R}'_{\mathrm{D},i} = \vec{R}_{\mathrm{A},i} + l_i \begin{pmatrix} \cos(2\theta_\mathrm{A} + \delta_i) \\ \sin(2\theta_\mathrm{A} + \delta_i) \end{pmatrix}, \tag{A.9}$$

where the parameter l_i represents the distance from blade i to the detector. This parameter is determined by the intersection of the ray with the detector surface:

$$(\vec{R}_\mathrm{D} - \vec{R}'_{\mathrm{D},i}) \cdot (\vec{R}_\mathrm{D} - \vec{R}_\mathrm{A}) = 0, \tag{A.10}$$

which reduces to

$$l_\mathrm{AD}^2 = (\vec{R}'_{\mathrm{D},i} - \vec{R}_\mathrm{A}) \cdot (\vec{R}_\mathrm{D} - \vec{R}_\mathrm{A}) \tag{A.11}$$

or

$$l_\mathrm{AD} = \begin{pmatrix} \cos 2\theta_\mathrm{A} \\ \sin 2\theta_\mathrm{A} \end{pmatrix} \cdot \begin{pmatrix} d_i \cos\Omega_\mathrm{A} + l_i \cos(2\theta_\mathrm{A} + \delta_i) \\ d_i \sin\Omega_\mathrm{A} + l_i \sin(2\theta_\mathrm{A} + \delta_i) \end{pmatrix}. \tag{A.12}$$

Linearizing in d_i, (A.12) readily reduces to

$$l_i = l_\mathrm{AD} - d_i \cos(2\theta_\mathrm{A} - \Omega_\mathrm{A}), \tag{A.13}$$

which is to be inserted in (A.9). We now require that (A.8) and (A.9) are equal. This gives two equations; the x component reads

$$\begin{aligned} l_\mathrm{AD}\cos 2\theta_\mathrm{A} + p_i \sin 2\theta_\mathrm{A} &= d_i \cos\Omega_\mathrm{A} \\ &+ \cos(2\theta_\mathrm{A} + \delta_i)[l_\mathrm{AD} - d_i(\cos(\Omega_\mathrm{A} - 2\theta_\mathrm{A}))], \end{aligned} \tag{A.14}$$

whereas the y component becomes

$$\begin{aligned} l_\mathrm{AD}\sin 2\theta_\mathrm{A} - p_i \cos 2\theta_\mathrm{A} &= d_i \sin\Omega_\mathrm{A} \\ &+ \sin(2\theta_\mathrm{A} + \delta_i)[l_\mathrm{AD} - d_i(\cos(\Omega_\mathrm{A} - 2\theta_\mathrm{A}))]. \end{aligned} \tag{A.15}$$

Linearizing either of these two expressions in d_i gives the following equation to determine Ω_A:

$$\frac{p_i}{d_i} = -\sin\Omega_\mathrm{A}\left(\cos 2\theta_\mathrm{A} + \frac{l_\mathrm{AD}}{l_\mathrm{SA}}\right) + \cos\Omega_\mathrm{A}\sin 2\theta_\mathrm{A}. \tag{A.16}$$

The latter equation is of the form $A\cos x + B\sin x = C$, where the solution is $\cos x(A^2 + B^2) = CA \pm B\sqrt{A^2 + B^2 - C^2}$. Solving (A.16) for Ω_A gives us the answer

$$\begin{aligned} &\cos\Omega_\mathrm{A} \\ &= \frac{r\sin 2\theta_\mathrm{A} \pm (\cos 2\theta_\mathrm{A} + R)\sqrt{1 - r^2 + R^2 + 2R\cos 2\theta_\mathrm{A}}}{1 + R^2 + 2R\cos 2\theta_\mathrm{A}}, \end{aligned} \tag{A.17}$$

where we have introduced the ratios $r = p_i/d_i$ and $R = l_\mathrm{AD}/l_\mathrm{SA}$.

A special case of (A.17) is the monochromatic point-to-point focusing mode, where all rays intersect the detector at the same point, i.e. $r = 0$. In this case, (A.17) reduces to

$$\cos\Omega_\mathrm{A} = \frac{\pm(\cos 2\theta_\mathrm{A} + R)}{\sqrt{1 + R^2 + 2R\cos 2\theta_\mathrm{A}}}. \tag{A.18}$$

Using $\cot^2 x = \cos^2 x/(1 - \cos^2 x)$ we reach

$$\cot\Omega_\mathrm{A} = \pm\frac{R + \cos 2\theta_\mathrm{A}}{\sin 2\theta_\mathrm{A}}. \tag{A.19}$$

This, however, only serves as a consistency check, as it is calculated more directly from (A.16), and is also presented in [9] (mode "B" therein).

References

[1] G. Shirane, S.M. Shapiro, J.M. Tranquada, Neutron Scattering with a Triple-Axis Spectrometer, Cambridge University Press, 2002.

[2] D.A.A. Myles, C. Bon, P. Langan, F. Cipriani, J.C. Castagna, M.S. Lehmann, C. Wilkinson, Physica B 241–243 (1997) 1122.

[3] K.N. Clausen, D.F. McMorrow, K. Lefmann, G. Aeppli, T.E. Mason, A. Schröder, M. Issikii, M. Nohara, H. Takagi, Physica B 241–243 (1998) 50.

[4] http://rita2.psi.ch.

[5] http://www.ncnr.nist.gov/instruments/spins/.

[6] http://www.frm2.tu-muenchen.de/puma/.

[7] http://www.hmi.de/bensc/instrumentation/instrumente/e2/e2.html.

[8] F. Demmel, A. Fleischmann, W. Gläser, Nucl. Instr. and Meth. A 416 (1998) 115. http://www.ill.fr/YellowBook/IN3/.

[9] K. Lefmann, D.F. McMorrow, H.M. Rønnow, K. Nielsen, K.N. Clausen, B. Lake, G. Aeppli, Physica B 283 (2000) 343.

[10] S.N. Klausen, K. Lefmann, P.-A. Lindgård, L.T. Kuhn, C.R.H. Bahl, C. Frandsen, S. Mørup, B. Roessli, N. Cavadini, C. Niedermayer, Phys. Rev. B, submitted for publication.

[11] P. Zetterström, A. Chahid, R.L. McGreevy, Physica B 266 (1999) 115.

[12] C.R.H. Bahl et al., in preparation.
[13] J. Bundgaard, P. Skaarup, TASCOM User Manual v.3.12, Risø National Laboratory, Denmark, 2002.
[14] K. Lefmann, K. Nielsen, Neutron News 10 (1999) 20.
[15] http://mcstas.risoe.dk.
[16] E. Blinov, V.G. Fleisher, H. Huhtinen, R. Laiho, E. Lähderanta, P. Paturi, Yu.P. Stepanov, L. Vlasenko, Supercond. Sci. Technol. 10 (1997) 818.
[17] J.J. Raittila, H. Huhtinen, P. Paturi, Yu.P. Stepanov, Physica C 371 (2002) 90.
[18] P. Andersen et al., in preparation.

Paper II

Available online at www.sciencedirect.com
SCIENCE DIRECT®
Nuclear Instruments and Methods in Physics Research B 246 (2006) 452–462
NIM B
Beam Interactions with Materials & Atoms
www.elsevier.com/locate/nimb

Inelastic neutron scattering experiments with the monochromatic imaging mode of the RITA-II spectrometer

C.R.H. Bahl [a,b], K. Lefmann [a,*], A.B. Abrahamsen [a], H.M. Rønnow [c], F. Saxild [a], T.B.S. Jensen [a], L. Udby [a], N.H. Andersen [a], N.B. Christensen [a,c], H.S. Jakobsen [d], T. Larsen [d], P.S. Häfliger [c], S. Streule [c], Ch. Niedermayer [c]

[a] *Department of Materials Research, Risø National Laboratory, Building 227, Frederiksborgvej 399, DK-4000 Roskilde, Denmark*
[b] *Department of Physics, Technical University of Denmark, DK-2800 Lyngby, Denmark*
[c] *Laboratory for Neutron Scattering, Paul Scherrer Institute, CH-5232 Villigen, Switzerland*
[d] *Niels Bohr Institute for Astronomy, Physics and Geophysics, University of Copenhagen, DK-2100 Copenhagen, Denmark*

Received 4 November 2005; received in revised form 13 January 2006
Available online 9 March 2006

Abstract

Recently a monochromatic multiple data taking mode has been demonstrated for diffraction experiments using a RITA type cold neutron spectrometer with a multi-bladed analyser and a position-sensitive detector. Here, we show how this mode can be used in combination with a flexible radial collimator to perform real inelastic neutron scattering experiments. We present the results from inelastic powder, single crystal dispersion and single crystal constant energy mapping experiments. The advantages and complications of performing these experiments are discussed along with a comparison between the imaging mode and the traditional monochromatic focussing mode.

PACS: 29.30.−h; 25.40.Fq

Keywords: Neutron spectrometers; Multiple analyser; Inelastic neutron scattering

1. Introduction

In inelastic neutron scattering, the limited neutron flux is often the main restricting factor in conducting experiments in a reasonable time. This has lead to much ingenuity in the strive to utilise the available neutrons. Two main types of spectrometers have evolved. The time-of-flight spectrometer (TOF) [1] and the triple axis spectrometer (TAS) [2]. The TOF may simultaneously measure a wide range of points in $(\mathbf{q},\omega)$ space, but pulsed neutron sources have at present a low intensity. The new high flux spallation sources under construction (SNS and J-PARC) as well as the proposed ESS are set to significantly increase the intensity and thus reduce measuring times for TOF experiments. The TAS has a high intensity from a continuous source but only measures one point in $(\mathbf{q},\omega)$ space at a time. Also the TAS offers more flexibility in controlling the resolution in momentum and energy. Combining these two, i.e. simultaneously detecting many points in $(\mathbf{q},\omega)$ space while keeping the high signal to noise ratio and resolution, was a corner stone in the "Reinvented triple axis" (RITA) concept started at Risø National Laboratory in 1993 [3].

Multiple data taking has been implemented at a handful of TAS instruments around the world, most notably the SPINS spectrometer at NIST [4] the flat-cone instrument E2 at HMI [5] and the MAD option of IN3 at ILL [6]. In preparation are the RITA like IN12 at ILL and PUMA at FRM-2, and also EIGER at SINQ, PSI, the MACS

* Corresponding author. Tel.: +45 4677 4726; fax: +45 4677 5758.
E-mail addresses: christian.bahl@risoe.dk (C.R.H. Bahl), kim.lefmann@risoe.dk (K. Lefmann).

0168-583X/$ - see front matter © 2006 Elsevier B.V. All rights reserved.
doi:10.1016/j.nimb.2006.01.023

instrument at NIST as well as IN8 and IN20 at ILL. A comparative study between the IN3 (MAD) at ILL and the TOF spectrometer MARI at ISIS using real experiments on the 2D dispersion manifold in $CuGeO_3$ is given in [7]. Good agreement was found between the results from the two experiments.

In a recent paper [8], we showed how multiple data taking has been implemented at the RITA-II spectrometer at SINQ, PSI [9]. In the present paper we present the implementation of the monochromatic imaging mode for real inelastic experiments and the considerations necessary for planning and analysing these experiments. Whereas IN3 operates at thermal final energies E_f giving limited analyser scattering angles $2\theta_A$, we show that RITA-II can sample values of E_f down to 3.0 meV giving analyser scattering angles in excess of 90°.

We particularly consider the potential problem of "cross-talk" between the different data taking channels, and show that in the inelastic regime cross-talk may occur both due to insufficient collimation and detection errors. The elastic cross-talk is found to be about 0.2% and the inelastic is found to be about 2%. Cross-talk must always be considered when building instruments capable of taking multiple data.

2. The monochromatic imaging mode

The monochromatic imaging mode of a RITA type triple axis spectrometer has been described in [8], see an illustration in Fig. 1. The analyser of the RITA-II spectrometer at SINQ consists of seven PG-blades, that can be rotated independently of each other on a mount that can rotate around its centre. All the blades are set to scatter neutrons of the same energy, hence the term monochromatic. The angle of the mount, Ω_A, where each blade Bragg reflects the neutrons is determined geometrically, from a requirement that there is a certain spacing between where the neutrons reflected from the analyser intersect the detector, see Fig. 1. The signal from each blade intersects a particular predefined area on a position-sensitive detector. Counting is done in software defined windows on the detector. However, as the full detector image is saved at each scan point, the exact position of these windows can be defined as a part of the post-experiment analysis. Previously, the RITA-II spectrometer has mainly been used in a mode where the reflections from all blades are directed onto the same part of the detector, the so-called monochromatic focussing mode as also described in [8].

2.1. The adjustable radial collimator

An adjustable radial collimator has been installed fixed to the front of the detector. It has cadmium covered vanes, each 15 cm long and 30 cm high, see Fig. 2. The vanes define separate channels for the neutrons from each analyser blade, to intersect the detector in predefined regions, thus giving a 1:1 correspondence between collimator channels and analyser blades. The collimator blades are hinged with a fixed distance of 25 mm closest to the detector with the possibility of changing the distance at the opening according to the projected distance between the analyser blades, seen from the detector. The five left blades are moved by a motor, and are geared 9:7:5:3:1. The five right blades are geared similarly and moved by a second motor.

The fixed distance of 25 mm is equivalent to the distance between the analyser blades, and was chosen as it was previously found to be a very convenient distance between the channels at a wide range of incoming energies ($r = 1$ in [8]).

2.2. Use of the inelastic mode

In the case of purely elastic scattering experiments, i.e. diffraction, the monochromatic imaging mode is straight forward to understand. Each analyser blade receives

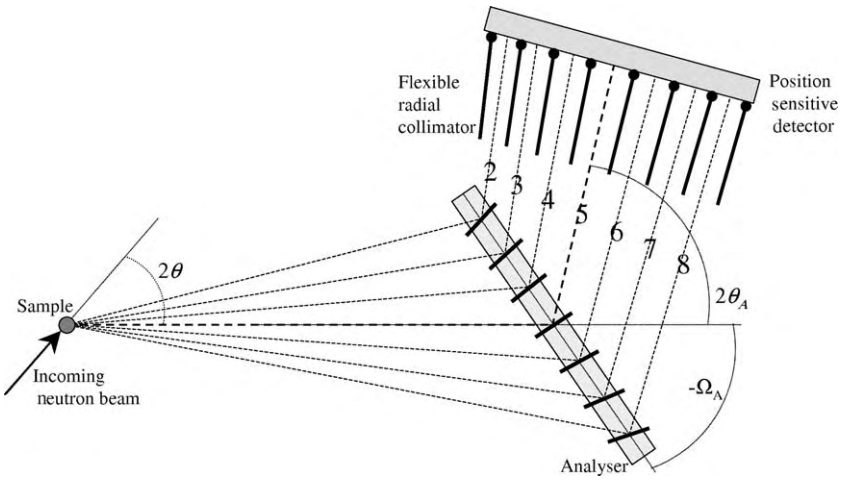

Fig. 1. The geometry of the secondary spectrometer at RITA-II including the analyser and radial collimator. Ω_A indicates the rotation of the analyser mount and 2θ is the scattering angle. The numbers indicate the blade/channel numbers. The dimensions are exaggerated, as the sample–analyser distance is 1.208 m and the analyzer–detector distance is 0.328 m. The numbering of channels from 2 to 8 is in anticipation of the installation of a nine-blade analyser.

Fig. 2. Picture of the flexible radial collimator for RITA-II. The five left blades are here moved inwards and the five right blades are all set straight.

neutrons scattered at a different angle, 2θ, from the sample. The difference in angle is given by the distance between the individual analyser blades, typically 1.0° at 5.0 meV and 0.7° at 3.7 meV. This can be utilised when scanning, as the data sets collected from each individual blade can be added (with correction) to give one data set with better statistics. The usefulness of this type of multi-analyser data for powder diffraction in 3-axis mode was presented in [8].

Inelastic scattering presents more complications both for powder and single crystal work, as the momentum transfer at a given scattering angle depends on the energy. The scattering geometry is more conveniently described by the scattering vector $\mathbf{q} = \mathbf{k}_\mathrm{i} - \mathbf{k}_\mathrm{f}$, where $\mathbf{k}_\mathrm{i}$ and $\mathbf{k}_\mathrm{f}$ are the initial and final wave vectors of the neutrons, respectively. All blades scatter at the same energy but different blades measure at slightly different positions in reciprocal space. When scanning, the blades will thus cover a two-dimensional region in reciprocal space instead of just a line.

2.3. Calculating q, ω and hkl maps

The positions of the blades during a scan can be calculated geometrically prior to performing the scan. It is important to do so, as only the path in reciprocal space of the central blade is controlled by a scan, the positions in reciprocal space of the others follow geometrically from the requirements of the monochromatic imaging mode [8]. The distance between the blades $|\Delta\mathbf{q}|$ remains constant during an experiment. Often, mapping out a two-dimensional region (*hkl*) space along one crystallographic direction will be preferential to mapping along another as the span of the blades will differ.

As an introduction, consider the difference in $\mathbf{q}$ between one blade and the central blade given by $\Delta\mathbf{q}_j = \mathbf{q}_j - \mathbf{q}_0 = \mathbf{k}_{\mathrm{f},0} - \mathbf{k}_{\mathrm{f},j}$, see Fig. 3. In the frame of reference of the analyser, this is constant as long as E_f does not change. However, $\Delta\mathbf{q}_j$ rotates in the more relevant frame of reference, i.e. that of the sample, during a scan.

During energy scans for measuring, e.g. dispersions along a particular direction in reciprocal space, it will, in general, be desirable that $\Delta\mathbf{q}_j$ should be as parallel to the scan direction as possible. This ensures that the scattering vectors, $\mathbf{q}_j$, of the blades do not stray too far from the desired scan path. To first approximation, $\Delta\mathbf{q}_j$ is perpendicular to the final wave vector $\mathbf{k}_{\mathrm{f},0}$, so by considering the scattering triangle, see Fig. 3, the angle α is found to be given by

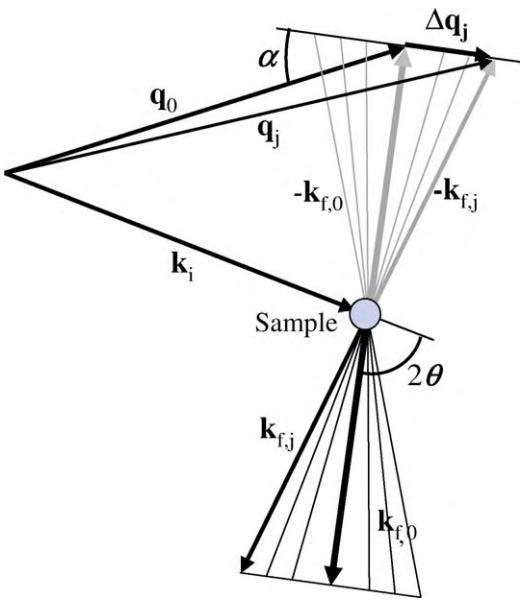

Fig. 3. Geometrical calculation of the angle α between the trajectory of the blades and the scattering vector $\mathbf{q}$. $\mathbf{k}_\mathrm{i}$ and $\mathbf{k}_\mathrm{f}$ are the initial and final wave vectors of the neutrons, and the blade numbers are denoted by j, where 0 is the central blade. See Eq. (1) and the discussion in the text.

$$\sin\alpha = \frac{k_\mathrm{i}^2 - k_\mathrm{f}^2 - q^2}{-2k_\mathrm{f}q}. \tag{1}$$

The angle α is zero when $k_\mathrm{i}^2 = k_\mathrm{f}^2 + q^2$, so this is the optimal situation for a longitudinal trajectory of the blades ($\Delta\mathbf{q} \| \mathbf{q}_0$). Another way of stating this is by writing q^2 in terms of an energy

$$E_q \equiv \frac{\hbar^2 q^2}{2m} = \frac{\hbar^2 k_\mathrm{i}^2}{2m} - \frac{\hbar^2 k_\mathrm{f}^2}{2m} = \hbar\omega. \tag{2}$$

This energy is found to be identical to the energy transfer in the experiment. $\Delta\mathbf{q}_j$ may be written as the sum of a component parallel to $\mathbf{q}_0$ and one perpendicular.

$$\Delta\mathbf{q}_j = \Delta q\cos\alpha\hat{\mathbf{e}}_{q\|} + \Delta q\sin\alpha\hat{\mathbf{e}}_{q\perp}. \tag{3}$$

Here $\hat{\mathbf{e}}_{q\|}$ is a unit vector parallel to $\mathbf{q}_0$ and $\hat{\mathbf{e}}_{q\perp}$ is a perpendicular unit vector. The transverse component is the interesting one as it describes the straying of the blades from the direction of the scattering vector, again assuming a longitudinal scan. Using Eq. (1), the component can be calculated as

$$\Delta\mathbf{q}_{j\perp} = \Delta q\left(\frac{-mE}{\hbar^2 k_{\mathrm{f},0} q_0} + \frac{q_0}{2k_{\mathrm{f},0}}\right)\hat{\mathbf{e}}_{q\perp}, \tag{4}$$

where E is the energy transfer of the experiment.

Thus it is seen that in constant-q_0 scans, the straying of the blades will be linear in energy, whereas in constant energy scans, the blades will follow more complicated hyperbolic paths.

At each point of a constant-q_0 scan the detected intensity from each blade is recorded, making one scan giving a two-dimensional $(\mathbf{q}, \omega)$ map. Alternatively for constant energy scans the detected intensity can be displayed for each position of the blades along two directions in reciprocal space, also giving a two-dimensional map. Combining several adjacent scans provides mapping out of large areas. When presenting the data from such a collection of scans a fine masked regular grid is constructed around the measured grid data. In this paper, we have chosen the grid size so that there is at least one data point in each grid square. Optimally there should be exactly one data point in each grid square. However, due to the curved path of the blades in reciprocal space, this is generally not feasible. If there are two data points in a grid square, the average value is used. Careful considerations must be made before analysing and fitting data as the above procedure is effectively a rebinning of the data.

2.4. Comparison of imaging and focussing mode

To compare the resolution of the spectrometer in imaging mode and focussing mode, a nuclear Bragg reflection (the (0 0 2) of $Cu_2Te_2O_5Cl_2$) has been mapped by constant-E scans around the Bragg reflection and constant-q_0 scans at the Bragg reflection. Fig. 4 shows that the energy resolution of the two modes is almost identical, whereas the resolution in q-space is significantly better in the imaging mode, see Fig. 5. The top and bottom part of Fig. 5 show the intensity in one channel at the centre of the detector in the imaging and focussing modes, respectively. In the middle panel the sum of the seven signals in seven blade imaging is shown. The separation of the seven peaks in the focussing mode data is due to the contribution from each of the seven blades, but unlike in the imaging mode, the individual contributions cannot be separated. The q-resolution in focussing mode is dominated by the width of the whole analyser, while in imaging mode it is given by the width of the individual blades. So, in conclusion, the imaging mode has a much better q-resolution, but the same integrated intensity. The use of focussing and imaging mode is discussed further in Section 6.2.

3. Cross-talk

In the experiments we have performed at the RITA-II spectrometer the neutron beam was linearly collimated (by 40′ or 80′) after the monochromator. A radial collimation of the scattered neutrons takes place inside the Be or BeO filter, placed between the sample and analyser [10]. In the open RITA geometry without collimation between analyser and PSD, we showed in [8] that about 0.2% of cross-talk was present in elastic experiments, i.e. some neutrons from one analyser blade hitting another part of the detector. In order to utilise the monochromatic imaging mode it is important that the amount of cross-talk is minimal.

Elastic scattering experiments often operate over several orders of magnitude between signal and background, making cross-talk an important consideration, but in inelastic experiments the ratio between signal and background is usually significantly less, so that cross-talk becomes less

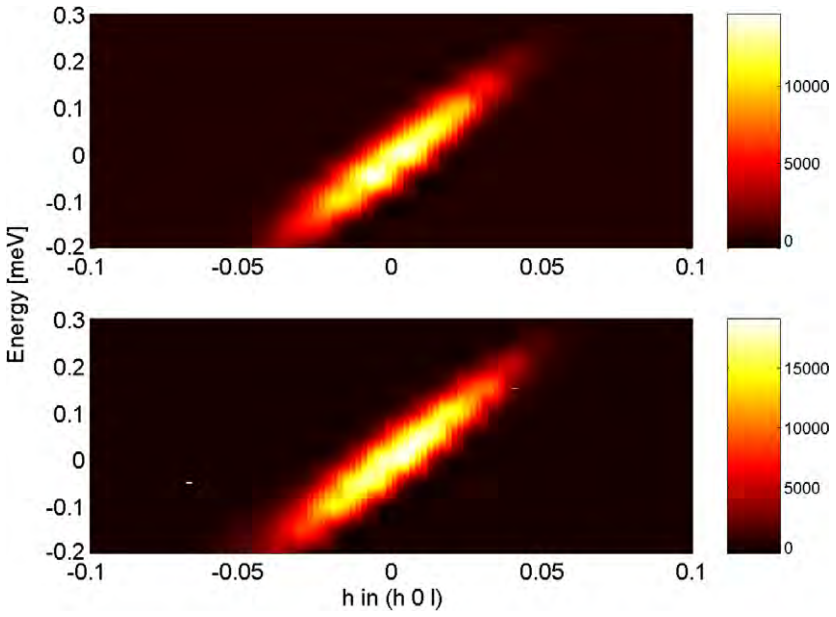

Fig. 4. Map made from scanning the energy at different (h02) values around the nuclear (0 0 2) Bragg peak of $Cu_2Te_2O_5Cl_2$. The energy resolution is seen to be comparable in the imaging mode (top) and the focussing mode (bottom).

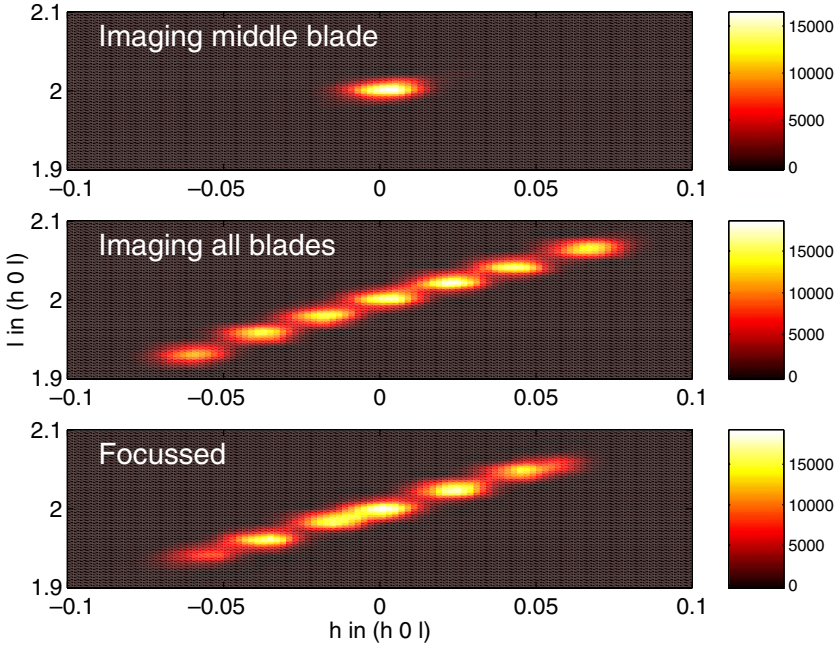

Fig. 5. Map of the nuclear (0 0 2) Bragg peak of $Cu_2Te_2O_5Cl_2$ in the (*h*0*l*) plane. The resolution of the imaging mode using both a single blade and seven blades is compared to the focussing mode. The difference in resolution for the two modes is seen by a comparison of the top and bottom panels.

important. In inelastic experiments a cross-talk of $\leqslant 5\%$ will, in general, be acceptable. If one channel contains an elastic signal, this will not be true, as even 5% of an elastic signal will often be large compared to an inelastic signal. But, as the mode is monochromatic all the blades scatter at the same energy. It will be shown that inelastic cross-talk from an elastic signal only occurs at small negative energy transfers, strongest on the negative side.

3.1. Cross-talk experiments

As presented in Section 2.1 a flexible radial collimator defines separate channels for the neutrons from each analyser blade, to intersect the detector in predefined regions. In each of the channels a counting window is software defined on the detector. These are set according to the experiment, to be performed. A size of 6 pixels (14 mm) corresponding to the footprint of an analyser blade (15 mm) is used in this paper for a final energy of $E_f = 5.0$ meV as found in [8].

To quantify the amount of elastic cross-talk with the collimator installed, the analyser was adjusted so that only the middle blade reflected the neutrons. The slits in front of the analyser were set tightly around this blade. A strip of boron-plastic with a profile of 5×5 mm^2 was stuck to the front of the collimator blade between channels 5 and 6 on the side facing channel 6. With this configuration neutrons with an incoming energy of 5 meV were scattered elastically from an α-Al_2O_3 sample around the Bragg reflection at $q = 1.805$ Å, and the neutrons in each of the collimator channels were counted. The experiment was repeated with a block of boron-plastic placed inside channel 5. Both setups are illustrated in Fig. 6.

Fitting Gaussians to the measured peaks, the elastic experiment on α-Al_2O_3 gave peak amplitudes of 4556 counts (in 200 s) in channel 5 and 11.6 counts and 6.5 counts in channels 4 and 6, respectively, equivalent to cross-talk values of 0.14% and 0.25%, respectively. With the boron-plastic block in place the same experiment gave less than one count in any of the channels on average, hence the elastic cross-talk is almost eliminated. This is collaborated by an inelastic scan of an incoherently scattering perspex sample, where the slits were opened slightly and all the blades were set to reflect, with the boron-plastic block in place. Here, the signals were 9312 counts and 7554 counts in channels 4 and 6, respectively, and 33 counts in channel 5 at zero energy transfer, giving a cross-talk of 0.2%.

From the elastic experiments it can be concluded that the elastic cross-talk happens behind the collimator, since neutrons are prevented by the absorber to pass through the channel. This can be explained by the point spread function (PSF) of the detector. Affixing a cadmium plate with a 1 mm diameter hole in it to the detector and reflecting a strong Bragg peak onto the hole makes it possible to quantify the PSF. This was found to be approximately gaussian with a FWHM of 7.4 mm both vertically and horizontally, although the pixel size is different in the two directions. With this magnitude of PSF it is reasonable that a small amount of neutrons in one channel is perceived by the detector as belonging to the neighbouring channel, see Fig. 6(a).

In the inelastic scan of the plastic sample mentioned above, there is a side peak at an energy transfer of -0.35 meV in channel 4, see Fig. 7. This side peak is due to neutrons with an energy of $E_f = E_i = 4.65$ meV

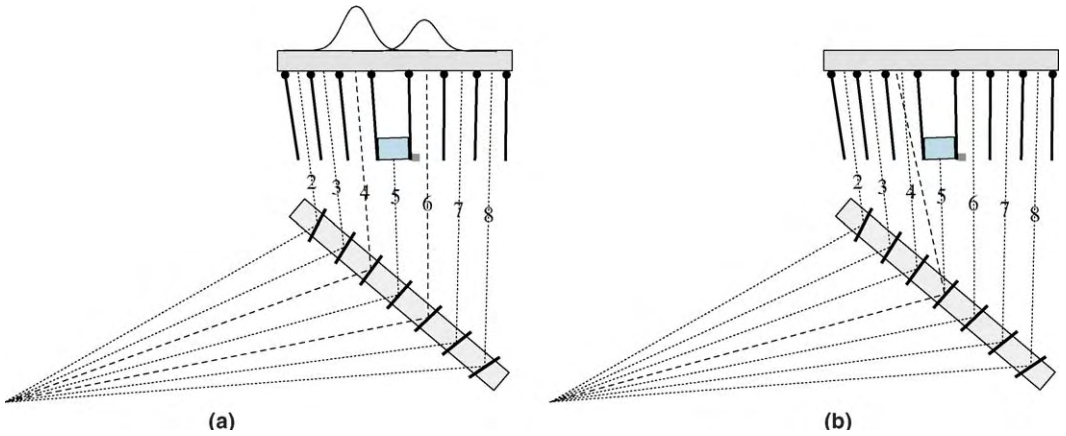

Fig. 6. Schematic representation of the two types of cross-talk between the signals from the analyser blades. The block in channel 5 and the small square on the blade between channels 5 and 6 represent the boron-plastic block and strip, respectively, as described in Section 3.1. (a) Elastic cross-talk comes from the point spread function of the detector. The point spread functions of channels 4 and 6 are indicated by exaggerated Gaussians in the figure. These give some signal in the neighbouring channels, notably in channel 5. (b) The inelastic cross-talk comes from neutrons passing in front of the collimator, here in channel 4 from blade 5. The dimensions in the figure are exaggerated for clarity.

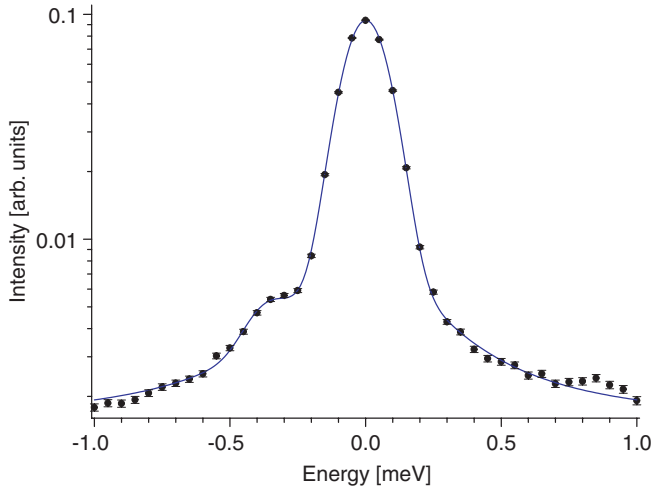

Fig. 7. Scan of the incoming energy using an incoherent scatterer (perspex) detected in channel 4 in the setup of channel 5. The data are plotted on semilog scale and show a side peak at −0.36 meV. The central peak is fitted with the sum of a Gaussian and a Lorentzian as the resolution function. The side peak is fitted with a Gaussian of the same width and has an intensity of 1.75% of the central Gaussian.

scattering off blade 5. Neutrons with this energy have a different Bragg angle from the PG(0 0 2) analyser, $\Delta\theta = 1.6°$ compared to at 5.0 meV. This enables the neutrons to enter the neighbouring channel, as seen in Fig. 6(b). The 40′ mosaicity of the analyser blades and thermal diffuse scattering accounts for the finite reflectivity in the PG crystal at this angle.

Using the same configuration of the instrument, several experiments were performed with an energy transfer of −0.35 meV. These are summarised in Table 1. The signal in channel 4 is ~60% larger when all the blades are reflecting than it is when only blade 4 is reflecting, but reduced below 1% when all blades are turned away. Hence there is considerable cross-talk, coming mostly from blade 5.

Table 1
Counts in 180 s in the three central channels at an energy transfer of −0.35 meV, during experiments with an incoherently scattering perspex sample and a boron-plastic block in channel 5, using software windows that are 6 pixels wide

Reflecting blades	Channel 4	Channel 5	Channel 6
All blades	524	7	338
Only blade 5	143	0	3
Only blade 4	328	3	2
No blades	2	2	2

In the corresponding elastic case the intensities in channels 4 and 6 are 9312 and 7554, respectively, with all the blades scattering.

The intensity of the side peak in Fig. 7 is 1.75% of the central peak. This is approximately the level of inelastic cross-talk. Since channel 5 is blocked, the cross-talk cannot be explained by the PSF of the detector proving our assumption on inelastic cross-talk before the collimator, see Fig. 6(b).

3.2. Reduction of cross-talk

The elastic cross-talk, due to the PSF, can be minimised by masking the detector, so that only the areas actually used for counting are visible to the neutrons. Cadmium plates with rectangular holes have been tested for the central channel. The results of the test using the setup described for the elastic experiments are seen in Table 2. As the slit width decreased, so did the elastic cross-talk, but also the relative intensity in channel 5. Thus there is a tradeoff between signal and cross-talk. The fact that a 15 mm opening reduces the signal in the 14 mm counting window by 12% is an effect of the PSF of the detector. An acceptable level would be a slit width of 15–20 mm, corresponding to slightly more than the size of a counting window. Such a cadmium mask with 20 mm wide holes for each channel has recently been installed.

Table 2
Table giving the average elastic cross-talk in the neighbouring channels and the relative intensity in channel 5 as a function of the width of a cadmium slit stuck to the detector

Slit width (mm)	Cross-talk (%)	Intensity in channel 5
30	0.19	1.00
20	0.18	0.96
15	0.12	0.88
10	0.12	0.65

In the inelastic experiment it was seen that fixing a boron-plastic strip to the blade between channels 4 and 5 reduces the counts in channel 4 from 143 to 38, in the case where only blade 5 is reflecting. The cross-talk is not seen in channel 6 as this would require blade 5 to scatter neutrons with an energy higher than 5.0 meV and the Be filter cuts off neutrons with this energy. Hence, the side peak at this energy is absent, as seen in Fig. 7. Thus there is only cross-talk at negative energy transfer, when a filter is used.

In conclusion, the elastic cross-talk is about 0.2% and the inelastic is about 10 times larger. They can be reduced to 0.1% and 0.5%, respectively, using relatively simple methods. However, in the inelastic case a strong optimisation is not always desirable as it decreases the signal, and 2% of cross-talk will often be acceptable.

4. Data correction

The seven blades do not scatter equally well. This is partially due to the crystal quality of the blades, and partially to slight misalignments of the individual blades. Also, the blades are constructed from two pieces of PG, that are not perfectly co-aligned, thus effectively broadening the mosaicity of some blades. Lastly, it has been seen in simulations performed using the McStas software package [11] that the slight difference in distance between the different blades and the detector will change the size and shape of the illuminated area on the detector.

When making a grid-map from data collected from the seven blades, it is important to correct for the scattering efficiency of the blades. This may be done by normalising each blade with the scattering intensity of the signal from an incoherent scatterer, e.g. vanadium or preferably the sample itself. In elastic experiments the blades are normalised by the incoherent elastic signal measured in each channel as described previously [8]. For inelastic experiments the intensity of an energy scan of incoherent scattering in each detector channel is integrated. The integrated intensities are proportional to the scattering efficiency multiplied with the resolution volume. These integrated intensities vary slightly from experiment to experiment, depending on the exact alignment of the instrument and sample size and shape. At RITA-II they are typically found to be around: 0.97, 0.92, 0.93, 1.00, 0.88, 0.77, 0.95 for channels 2–8, respectively. The detected signal should be normalised in each channel by the integrated intensities measured in the same configuration.

5. Examples of inelasic experiments

Demonstrating the usefulness of the monochromatic imaging mode in inelastic experiments is best done by considering real experiments. We therefore present three different examples of measurements using this mode.

5.1. Phonons in Pb

The dispersion relation of phonons in lead (Pb) has been well known since the early days of neutron scattering [12,13]. In addition, samples of single-crystal Pb can be made very large. This makes Pb a good model system with which to test the monochromatic imaging mode. The spectrometer was set up with 40′ collimation after the monochromator, a radially collimating Be filter after the sample and the adjustable radial collimator before the detector described in Section 2.1. A final energy of $E_f = 5.0$ meV was chosen with (hk0) as the scattering plane. Constant energy maps were made from a number of scans where the central blade traversed the (0 1 0) direction, starting from different positions in the (hk0) plane. The six other blades also remain in the (hk0) plane having trajectories almost parallel to the central blade, certainly at the small energy transfers used. The trajectories of the seven blades during one of the scans are shown for both 2.0 meV and 4.0 meV energy transfers in Fig. 8.

The mapping was done at two different energies (2.0 meV and 4.0 meV), resulting in the constant energy maps seen in Fig. 9, normalised according to the procedure described in Section 4. The crystal is $5 \times 2 \times 10$ cm^3, but the slits before it are set 8 cm high and 4 cm wide to improve resolution and the signal to background ratio. The grid-map at 2.0 meV consists of 11 scans with a total of 721 analyser settings at ~45 s/point giving $7 \times 721 = 5040$ data points. The data set was taken in 9 h. The grid-map at 4.0 meV consists of a total of 6748 data points

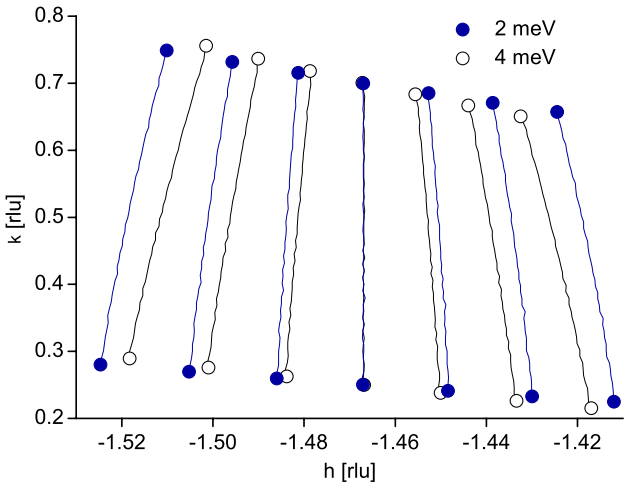

Fig. 8. The trajectory of the seven blades in one of the scans making up Fig. 9(a) and (b). It is seen how the traces of the blades at 4 meV energy transfer twist more than at 2.0 meV during the scan.

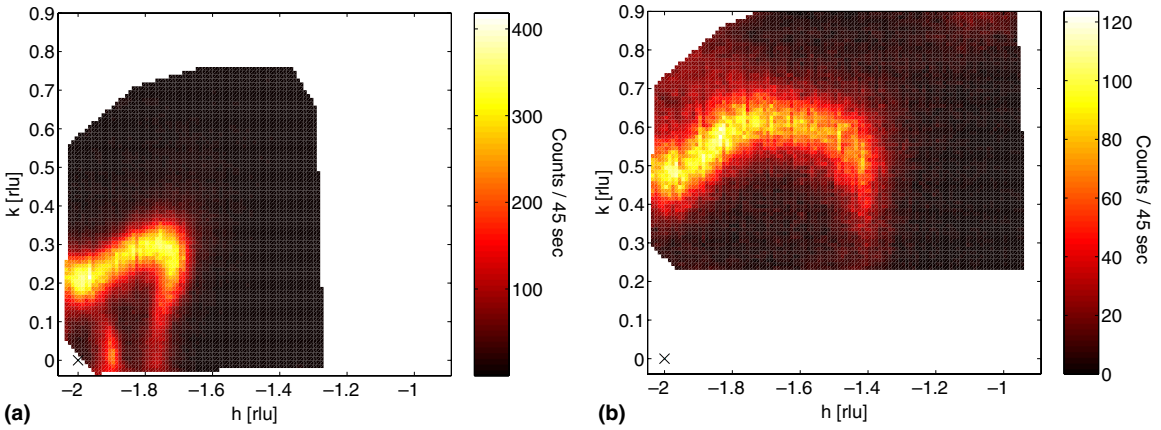

Fig. 9. Constant energy grid-maps of a phonon branch in lead around the Bragg point (−200), indicated in both figures by ×. The maps are made from parallel scans in the k direction, as sketched in Fig. 8. (a) Grid-map at a fixed energy transfer of 2.0 meV and (b) grid-map at a fixed energy transfer of 4.0 meV. (For the colour figure, the reader is referred to the web version of this article.)

at ~45 s/point and took 12 h. The phonon branch is seen clearly, having an intensity of around 500 counts/min at 2.0 meV and around 150 counts/min at 4.0 meV compared to a background of around 2–4 counts/min in both scans. This experiment was a demonstration of the monochromatic imaging mode in mapping out a large part of the Brillouin zone at high resolution in a relatively short time. The phonon branch could easily have been measured using shorter counting times and fewer points.

5.2. Quantised spin waves in hematite nanoparticles

A powder sample of 16 nm hematite (α-Fe_2O_3) particles has previously been studied by neutron scattering [14,15]. Much of the work has concerned collective magnetic excitations, which are infinite wavelength spin waves quantised due to the finite size of the particles. Such an excitation has recently been found at $\hbar\omega = 1.1$ meV and $q = 1.51$ Å^{-1} [16]. The excitation has been seen in both constant energy scans and constant-q scans, and it was presumed to be localised, i.e. non-dispersive. To prove this, we scanned a (q,ω) map around the excitation. The monochromatic imaging mode is ideal for this. Further, low energy transfer implies that the analyser blades follow approximately straight lines in (q,ω) space during constant-q scans.

The experiment was carried out by setting the central blade to a certain value of q and scanning the energy transfer from 0.7 meV to 1.8 meV with a final energy of $E_f = 5.0$ meV while keeping q_0 fixed. The collimation before the sample was 80′. A series of nine of such scans were taken. To ensure smoothness at the interface between two scans, the scans overlap each other. Fig. 10 shows the data from these scans after normalisation by the method described in Section 4. The 9 scans cover the region $q =$ 1.12–1.88 Å^{-1}. Each scan had 29 points in energy at ~14 min/point, so the grid-map consists of a total of 1827 data points, taking a total of 60 h to complete, with a sample mass of ~5 g. It is also seen in Fig. 10 that the difference in the spreading out of the seven blades in q-space

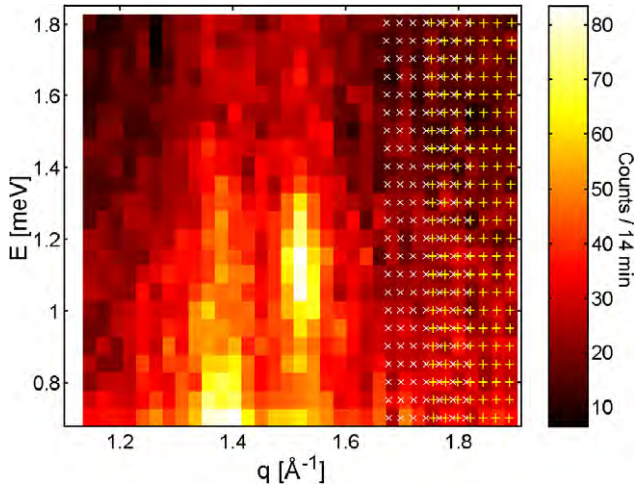

Fig. 10. Colour map of the excitation in hematite nanoparticles at $E = 1.1$ meV and $q = 1.51$ Å^{-1}, showing that it is localised. The map is made from 9 energy scans. The data points in the two first scans are shown as + and ×, respectively. For clarity only the part of the scan above $E = 0.7$ meV is shown. (For the colour figure, the reader is referred to the web version of this article.)

does not change much from the smallest to the largest energy transfers.

The grid-map shows that the excitation is indeed localised at $q = 1.51$ Å^{-1} and $E = 1.1$ meV. The signal at $q = 1.37$ Å^{-1} is the Lorentzian tail of a stronger (also localised) signal centred at 0.26 meV [16].

5.3. Spin waves in α-$MnMoO_4$

The magnon dispersion in the tetramer-based antiferromagnetic compound α-$MnMoO_4$ has been measured at 1.8 K [17]. The sample is a large single crystal (sample mass 10.8 g). It was aligned with the h-axis perpendicular to the scattering plane and a dispersion was sought along the $(0k\frac{k}{2})$ direction in a longitudinal scan. A part of the magnon branch is shown in Fig. 11(a), normalised according

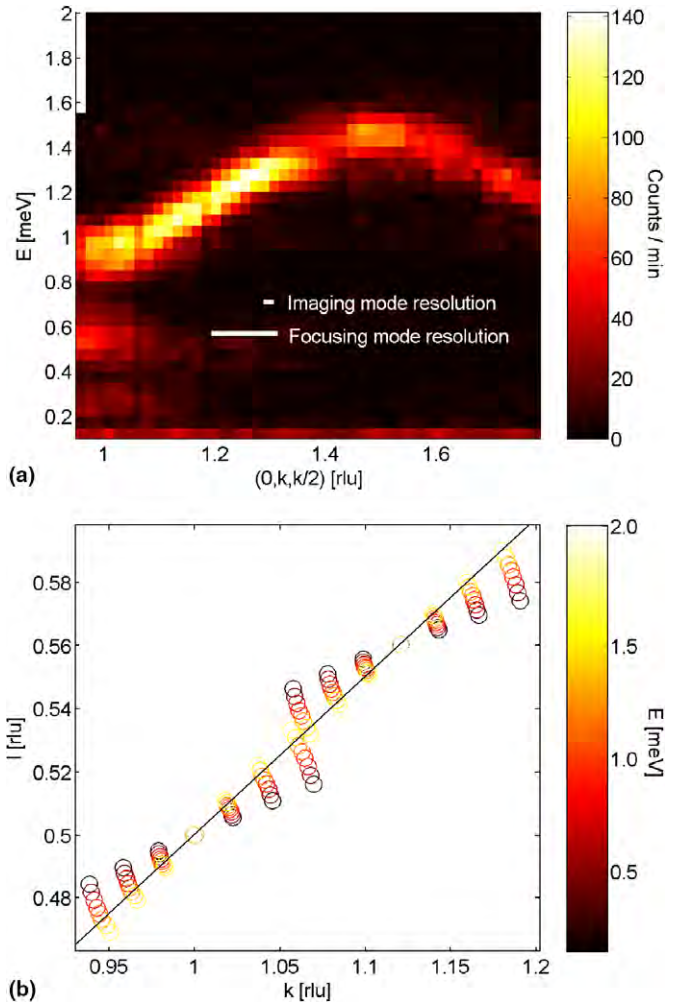

Fig. 11. Part of a magnon branch in α-$MnMoO_4$ along $(0k\frac{k}{2})$. (a) Grid-map consisting of 7 scans showing the magnon signal. The data were recorded in about 5 h. (b) The positions of the blades are plotted for 9 of the 39 points in energy for the two first scans. The 9 points are approximately equally spaced. The diagonal line shows the $(0k\frac{k}{2})$ direction. It is seen that the blades follow slightly helical paths in (k,l,ω) space. (For the colour figure, the reader is referred to the web version of this article.)

to Section 4. The collimation before the sample was 40′. The map consists of seven energy scans at a final energy of $E_f = 3.7$ meV, keeping the central blade at a fixed $(0k\frac{k}{2})$. Each scan was 39 points in energy, taking a total of about 5 h.

In contrast to working with powders, where only the size of q is important, in a single crystal the direction of q in (hkl) is important. When scanning the central blade through energy at a fixed $(0k\frac{k}{2})$, the other blades will inevitably stray from the direction of the scan, because of the geometrical constraints explained earlier. The trajectory of the blades will be helical in (k,l,ω) space, as sketched in Fig. 11(b). The trajectories in the first scan, centred at $(0\,1\,\frac{1}{2})$, are seen to have the least straying at about $E = 1.3$ meV, consistent with the value of 1.3 meV found from Eq. (2). The energy is quite close to that of the magnon, so the dispersion can be measured with very little straying of the blades.

6. Discussion

6.1. The monochromatic imaging mode

As presented above the monochromatic imaging mode has been utilised in different experiments. Mapping the $(hk0)$ plane in a lead single crystal at constant energy transfers can be done efficiently while keeping the scattering vectors from all the blades in the $(hk0)$ plane. The trajectories of the blades do begin to deviate from being parallel, but as shown in Fig. 8, this deviation is fairly limited. When scattering from a powder, only the magnitude of q is important, thus simplifying the use of imaging mode. Scans of energy transfer at a fixed value of q have been performed on a sample of hematite nanoparticles. These could be used to build a (q,ω) map of the sample, with almost equidistant points. The small change in distance between the blades in q-space as a function of energy transfer was not a problem in practice. Finally, energy scans at a fixed scattering vector were performed on a single crystal of α-$MnMoO_4$. Here, the blades were found to stray from the scan direction in reciprocal space due to geometrical constraints. This straying was small and unimportant in the present experiment. However, the experiment was only conducted below an energy transfer of 2.0 meV, and as the straying increases as a function of energy transfer, some experiments may be difficult to perform. This is the major drawback of the monochromatic imaging mode for performing $(\mathbf{q},\omega)$ mapping for single crystals.

In all the test experiments the signal to noise ratio was large enough to justify using the imaging mode without having to consider the extra background counts from the larger active detector area. No effects due to cross-talk have been observed in the test experiments.

To aid visualisation and data manipulation, software has been written to display data and normalise this in accordance with the geometry and scattering efficiency of the blades. Software has also been written to visualise the sometimes complicated trajectories of the blades in reciprocal space, thus aiding the planning of experiments.

Data from experiments carried out at a final energies of $E_f = 5.0$ meV and 3.7 meV have been presented here. The monochromatic imaging mode has been tested with the flexible collimator in place in the final energy range of 3.7–13.7 meV. It was found to function well in this range, making it possible to use the imaging mode in conjunction with BeO, Be and PG filters.

6.2. The imaging mode versus the focussing mode

The described experiments show how the imaging mode can be utilised to perform real experiments with a high data output. But it is important to realise that when sampling data using a large area of the detector, the background will

inevitably be higher. This is a problem, that is avoided with the traditional focussing mode, as all the neutrons are directed onto the same small area of the detector, no matter how many blades are used.

The actual count rate on the detector is determined by the active solid angle of the analyser, which is the same for the two modes, as long as the same number of blades and the same collimation scheme is used. Thus even if the background is negligible, there is no intensity argument for using the imaging mode. However, focussing mode will give a very coarse q-resolution, as shown in Section 2.4. If the resolution obtained by using all available blades in focussing mode is acceptable, this is often the favourable mode, although as shown in [8] the focussing of the neutrons from the different blades will never be perfect with a linear analyser mount. However, there are often situations where such a coarse resolution renders the measurement impossible. For dispersive modes it is most often the case that a maximum of $N_f = 3$ blades are employed. In focussing mode any further blades will merely add to the tail and in constant-q scans create an asymmetric line-shape towards higher energies. In contrast, the same scan performed in imaging mode will produce sharp peaks also in the outer channels, but at slightly different energies, as exemplified in Fig. 11. In these cases, the choice is between using a limited number of blades in focussing mode or all blades in imaging mode.

To quantify the break-even point between focussing and imaging modes, we consider a situation, were the signal reflected by one blade is S and the sample independent background in one window of the detector is B. We consider a ''worst case'' scenario where there is the same amount of signal in each blade. Recently, the beam blocked background on RITA-II was measured to be 8 counts/h in a counting window as described above (half of that from fast neutrons and the other half from electronic noise). Because the background B is sample independent, its mean value can be determined very accurately, but it will contribute to the statistical error in the background subtracted signal S. Hence, in focussing mode, the N_f blades will collect a total signal of $y_f = N_f S + B$. The counting error is $e_f = \sqrt{N_f S + B}$. In imaging mode, the total collected signal is $y_i = N_i S + N_i B$, giving an error of $e_i = \sqrt{N_i(S + B)}$. The goal in a measurement is to minimise the relative error e/y, and break even between the two configurations therefore occurs when the ratio

$$\frac{e_f/y_f}{e_i/y_i} = 1. \tag{5}$$

Lifting the square roots, the break-even condition becomes

$$N_f(S + B) = N_i\left(S + \frac{B}{N_f}\right)$$
$$\Rightarrow N_f(\beta + 1) = N_i\left(\beta + \frac{1}{N_f}\right), \tag{6}$$

where $\beta = S/B$ is the signal to noise ratio in each window.

We now analyse this relation for different situations. Firstly, regardless of signal to noise ratio, imaging mode always wins if $N_i \geqslant N_f^2$. For a nine-blade setup this means that three-blade focussing is never favourable. If the signal to noise ratio is $\beta = 1$ or better, imaging mode is favourable as long as

$$N_i \geqslant \frac{2N_f}{1 + 1/N_f} \simeq 2N_f - 2. \tag{7}$$

In the particular case of RITA-II where three blades are a reasonable limit for focussing in the case of dispersive modes and there are a total of seven blades available for imaging (nine channels will be available in the near future), this means that imaging is better than focussing as long as the signal to noise is better than 1/6. For $B = 8$ counts/h, this corresponds to $S > 1.3$ counts/h. Below this, it would in any case take unreasonably long to perform the experiment. In general, one will not obtain the same signal in all the blades, as assumed in this calculation. This will further favour the imaging mode, as a sharp signal will be resolved much better using the imaging mode. We therefore conclude that for RITA-II, imaging mode is always favourable under the conditions described above.

Increasing the number of analyser blades clearly makes the imaging mode even more favourable. The MAD option of IN3 at ILL has 31 analyser blades, but with the large analyser scattering angles required for a cold neutron spectrometer, the geometry would be very involved with this number of blades. The planned 9 analyser blades would seem to be close to the maximum reasonable with the present geometry of the RITA-II spectrometer. A higher number of analyser channels would require a different approach, such as the flat-cone geometry.

7. Conclusion

Implementation of the monochromatic imaging mode in conjuncture with a flexible radial collimator, has allowed multi-blade data taking on a RITA type cold neutron triple axis spectrometer in real inelastic experiments. Cross-talk has been analysed and quantified and it was found that this could be reduced to an acceptable level by use of software masking and an adjustable radial collimator before the detector.

It has been demonstrated how the monochromatic imaging mode of the seven-blade analyser at RITA-II can be used for both constant E mapping, for (q, ω) maps for powders, and for mapping out dispersion relations in single crystals. Analysis has shown that the imaging mode will be superior to the previously used focussing mode in almost any experiment with a practically conceivable signal to noise ratio.

The implementation of the monochromatic imaging modes has improved the RITA-II spectrometer and unleashed some of its potential. The combination of this mode, the recently acquired 15 T cryo-magnet, the low background, the proposed improvement of the beam guide [18] and a large increase of neutron intensity [19] at SINQ com-

bined with the planned implementation of 9 analyser blades will make RITA-II a very powerful instrument indeed.

Acknowledgements

This work was performed at SINQ at the Paul Scherrer Institute, Villigen, Switzerland. We gratefully acknowledge the Danish Neutron Scattering Centre DANSCATT for financial support during neutron scattering experiments. The development of the flexible radial collimator has been supported by the EU through the TECHNI program. CHRB is supported by the Danish Technical Research Council through the Nanomagnetism programme. We acknowledge K.N. Clausen, D.F. McMorrow, G. Aeppli and T.E. Mason for the original RITA design. From the Risø Technical staff we thank K. Theodor, O. Rasmussen, S. Bang, C.G. Sørensen, B. Breiting, P. Skårup and J.H. Hansen for the design and construction work. For help with measurements and supplying samples we are grateful to S.N. Klausen, P. Andersen and F. Bødker. At PSI we thank F. Altorfer and the technical staff for assistance in the installation of RITA-II.

References

[1] C.G. Windsor, Pulsed Neutron Scattering, Taylor & Francis, London, 1981.
[2] G. Shirane, S.M. Shapiro, J.M. Tranquada, Neutron Scattering with a Triple-Axis Spectrometer, Cambridge University Press, 2002.
[3] K.N. Clausen, D.F. McMorrow, K. Lefmann, G. Aeppli, T.E. Mason, A. Schröder, M. Issikii, M. Nohara, H. Takagi, Physica B 241–243 (1998) 50.
[4] http://www.ncnr.nist.gov/instruments/spins/.
[5] http://www.hmi.de/bensc/instrumentation/instrumente/e2/e2_en.htm.
[6] F. Demmel, A. Fleischmann, W. Gläser, Nucl. Instr. and Meth. A 416 (1998) 115.
[7] F. Demmel, N. Grach, H.M. Rønnow, Nucl. Instr. and Meth. A 530 (2004) 404.
[8] C.R.H. Bahl, P. Andersen, S.N. Klausen, K. Lefmann, Nucl. Instr. and Meth. B 226 (2004) 667.
[9] http://rita2.psi.ch.
[10] K. Lefmann, D.F. McMorrow, H.M. Rønnow, K. Nielsen, K.N. Clausen, B. Lake, G. Aeppli, Physica B 283 (2000) 343.
[11] http//www.mcstas.org.
[12] B.N. Brockhouse, T. Arase, G. Caglioti, K.R. Rao, A.D.B. Woods, Phys. Rev. 128 (1962) 1099.
[13] R. Stedman, L. Almqvist, G. Nilsson, G. Raunio, Phys. Rev. 162 (1967) 545.
[14] M.F. Hansen, F. Bødker, S. Mørup, K. Lefmann, K.N. Clausen, P.-A. Lindgård, Phys. Rev. Lett. 79 (1997) 4910.
[15] S.N. Klausen, K. Lefmann, P.-A. Lindgård, K.N. Clausen, M.F. Hansen, F. Bødker, S. Mørup, M. Telling, J. Magn. Magn. Mater. 266 (2003) 68.
[16] S.N. Klausen, K. Lefmann, P.-A. Lindgård, L. Theil Kuhn, C.R.H. Bahl, C. Frandsen, S. Mørup, B. Roessli, N. Cavadini, C. Niedermayer, Phys. Rev. B 70 (2004) 214411.
[17] P.S. Häfliger et al. (in preparation).
[18] C. Schanzer, P. Böni, U. Filges, T. Hils, Nucl. Instr. and Meth. A 529 (2004) 63;
J.K. Hansen, K.S. Hansen, B.P. Kristensen, Student's Report, Roskilde University, 2004.
[19] K.N. Clausen, personal communication.

Paper III

Available online at www.sciencedirect.com
ScienceDirect
Physica B 385–386 (2006) 1083–1085
PHYSICA B
www.elsevier.com/locate/physb

Realizing the full potential of a RITA spectrometer ☆

K. Lefmann[a,*], Ch. Niedermayer[b], A.B. Abrahamsen[a], C.R.H. Bahl[a], N.B. Christensen[a,b], H.S. Jacobsen[c], T.L. Larsen[c], P. Häfliger[b], U. Filges[b], H.M. Rønnow[b]

[a]*Risø National Laboratory, Frederiksborgvej 399, DK-4000 Roskilde, Denmark*
[b]*Laboratory for Neutron Scattering, ETH-Zürich and Paul Scherrer Institut, CH-5232 Villilgen, Switzerland*
[c]*Niels Bohr Institute, University of Copenhagen, DK-2100 Copenhagen Ø, Denmark*

Abstract

The "re-invented triple-axis spectrometer (RITA) concept has existed for a decade. Recent developments at RITA-2 at PSI, have revealed more of the potential of this instrument class. We demonstrate the performance of the multi-blade imaging mode, which has been applied e.g. to studies of dispersion relations and emphasize the power of this mode in combination with the low background of RITA-2. In addition, we present other ways of utilizing the position sensitive detector in a RITA instrument. Simulations of a planned upgrade of the guide-monochromator system at RITA-2 have shown a potential to increase the flux at the sample position by a factor 5.

PACS: 78.70.Nx

Keywords: Triple-axis spectrometer; Multi-analyzer system; Position sensitive detector

1. Introduction

In the "re-invented triple-axis spectrometer" (RITA), the conventional triple-axis design is optimized in a number of ways. Most notably, the data taking rate is increased by employing a multi-blade crystal analyzer and a position-sensitive detector (PSD) within a shielded analyzer tank [1]. Besides RITA-2 at PSI [2], the only other existing cold-neutron RITA-type spectrometer is SPINS at NIST [3], while a RITA-like option is being prepared for IN8 and IN12 at ILL [4]. The MACS spectrometer under construction at NIST will have a fixed final energy common for each of its many analyzer–detector channels [3]. Multiplexing thermal neutron triple-axis spectrometers all use a set-up with fixed final energy, this includes the MULTI option at IN3, ILL [4], and the flat-cone instrument E2, HMI [5], and the recent flat-cone options at the ILL instruments IN8, IN14, and IN20 [4]. The plans for the new EIGER at PSI represent an improvement of the flat-cone idea. Also the PUMA instrument at FRM-2 is prepared for a RITA multi-analyzer option [6].

We here present the progress in instrument development at the RITA-2 spectrometer at PSI, especially the commissioning of the new "monochromatic imaging" analyzer mode, and other uses of the PSD.

2. Analyzer modes of RITA-2

In a RITA spectrometer, the combination of the flexible analyzer and the PSD opens for a multitude of different focusing and "imaging" analyzer modes [7]. By imaging mode we here understand a setting of the analyzer system where several different data points are measured simultaneously.

The monochromatic focusing mode (similar to a conventional focusing analyzer) and the trivial flat mode has long been of regular use at RITA-2. Recently, we have defined and commissioned the monochromatic imaging mode, where all analyzer blades scatter neutrons at the same energy, directing the rays to different points at the

☆This work was supported by the Danish Natural Sciences Council through DANSCATT and by the EU FP5 program TECHNI. The work was performed at the SINQ neutron source, Paul Scherrer Institut, Switzerland.
*Corresponding author. Tel.: +45 4677 4726; fax: +45 4677 5758.
E-mail address: kim.lefmann@risoe.dk (K. Lefmann).

0921-4526/$ - see front matter © 2006 Elsevier B.V. All rights reserved.
doi:10.1016/j.physb.2006.05.372

PSD [8]. At RITA-2, the 7 PG (0 0 2) analyzer blades are spaced 25 mm apart at the analyzer mount. We have chosen the same distance for the intended spacing between the signals at the PSD, since this value is suitable for the most commonly used E_f values: 3.7 and 5.0 meV [8]. The analyzer blades lie very close in scattering angle, 0.7°–1.0° at the two typical final energies, respectively. To eliminate "cross-talk" between different signals, we use Be and BeO filters with built-in radial collimation between sample and analyzers. Further, we have constructed a coarse adjustable collimator, which defines one channel from each analyzer blade to its corresponding image at the PSD. The blades of this collimator are hinged close to the detector. The analyzer and colimator are seen in Fig. 1.

Due to difference in geometry and crystal quality, the scattering efficiency varies by $\approx 20\%$ from blade to blade, whence the imaging mode needs calibration for normalization in each setting. This is managed by an elastic incoherent scatterer like a thin plastic rod, V, or (preferably) the sample itself. For elastic experiments, we use one single PSD picture in a background region. For inelastic experiments, a scan of the incoming neutron energy is needed in order to take into account the full volume of the resolution function for each blade.

The use of the monochromatic imaging mode is exemplified in Fig. 2, showing an intensity map of the magnetic excitations in α-$MnMoO_4$. The data consists of 4802 data points which were collected during 20 h. Compared the SINQ flux, the data quality is impressive and many fine details are visible.

3. Use of the position-sensitive detector

The PSD at RITA-2 is a crossed-wire ^{3}He counter with an efficiency of 75% in the energy range 3.0–14 meV, calibrated against a standard ^{3}He tube detector. The detector has an active area of $500 \times 300\,mm^2$ and is divided into 128×128 pixels. The spatial resolution of the PSD is Gaussian with 7.4 mm FWHM [8].

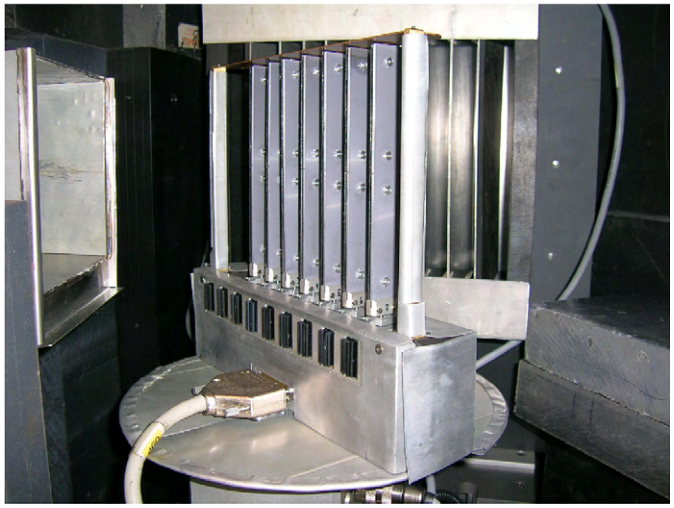

Fig. 1. A view inside the RITA-2 tank showing the multi-blade analyzer (picture centre) and the movable radial collimator (behind, right). The neutrons enter the tank from the left and scatter from the analyzer blades into the PSD through the collimator.

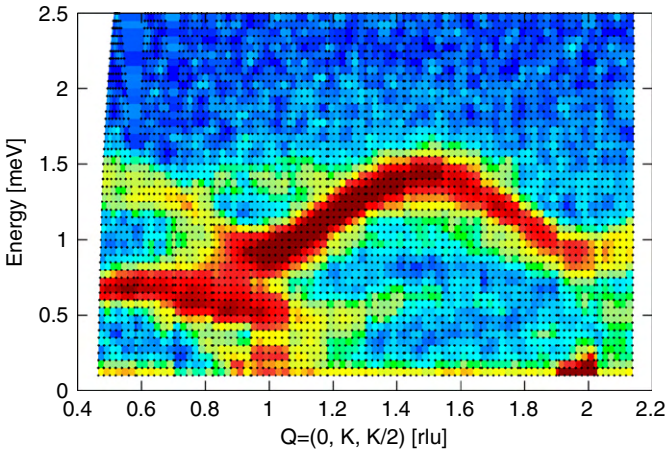

Fig. 2. A colormap of the magnetic excitations in α-$MnMoO_4$ taken at 1.5 K. The data covers the $(q_{01(1/2)}, \hbar\omega)$ plane and are taken in the RITA-2 monochromatic imaging mode at $E_f = 3.7$ meV, using a total of 14 constant-q scans with approx. 100 s per point. Each black dot represents one data point.

Having a PSD is an advantage over a single detector for many purposes. Above all, it is crucial for the imaging modes to distinguish signals from different analyzer blades.

We here focus on the possibility to use the stored PSD images for post-experiment analyses. At the RITA-2 spectrometer, this is performed by the MATLAB-based program `specND`. One advantage of adjusting the effective analyzer area is the possibility to remove spurious background signals, as was presented earlier [7]. The method also serves as a way to change the resolution of the measurements by reducing the detector size in (particularly) the horizontal direction. An example of this effect was seen in a recent measurement of the spin gap in (Tl, K)$CuCl_3$. The experiment was performed in monochromatic focusing mode with a small, unintended misalignment of the analyzer mount, resulting in defocusing of the beam spot, which induces tails around the elastic line. In the integrated data, these tails completely obscure the spin gap, as shown in Fig. 3. However, tails are reduced by narrowing the integration window at the PSD, opening for the determination of the spin gap. This effect, although less pronounced, is also present in experiments with no misalignments.

Another significant advantage of PSD data analysis is the resolution of the vertical component of the scattering vector. By un-focusing the monochromator (possibly inserting vertical collimation before the sample), a good vertical resolution can be obtained. This has proven very useful during crystal alignment, but can also be of use in real experiments, e.g. studies of critical scattering, where the vertical resolution is an issue. However, the latter option has not yet been used.

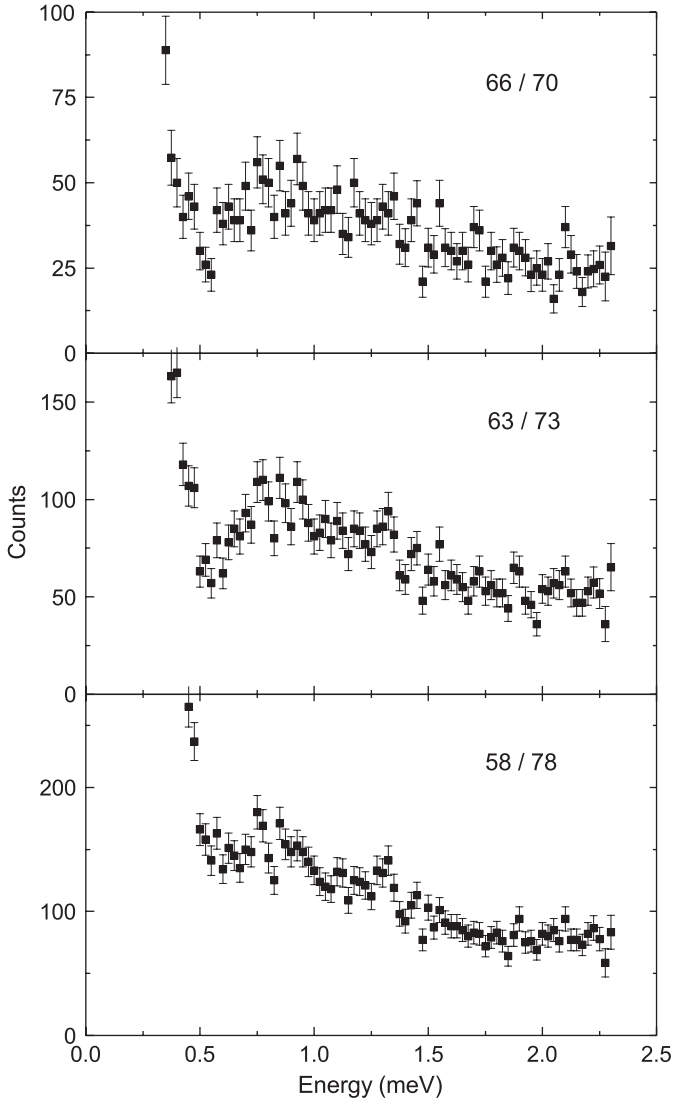

Fig. 3. A post-experiment analysis of a constant-q scan on the magnetic compound (Tl,K)$CuCl_3$. The three different panels illustrate the effect of changing the integration area of the PSD. The signal-noise ratio is clearly best using a window width of 11 pixels (middle).

The third advantage of the PSD is that of signal-to-background adjustment. By decreasing the detector windows from "full size" 60×13 pixels to 48×8 pixels ($188 \times 19\,mm^2$), the inelastic background value has been reduced by a factor of 2 due to smaller detector area, while the signal was reduced by only 5%. Recently, the fast-neutron background has been further lowered due to improved shielding around the SINQ guide system and inside the RITA-2 tank. The background level in a reduced window is now 0.25/min, hereof 0.10/min being electronic background.

4. Simulated RITA-2 upgrade

The current flux at the RITA-2 sample position is at maximum (7–10 meV): $5.0 \times 10^6/cm^2/s/mA$, where the SINQ current is presently 1.3 mA [9]. This places the instrument about an order of magnitude below the best cold-neutron triple-axis spectrometers IN14 (ILL) and PANDA (FRM-2).

There are current plans to upgrade the $120 \times 30\,mm^2$ $m = 2$ guide to gain additional flux. One idea is to install a guide with elliptical focusing in both vertical and horizontal directions. Recent simulations have shown that it is then possible to obtain gain factors between 4 and 5 when also increasing m to 3 or 3.5 [10]. Another simulation has investigated the gains from installing a conventional curved guide with $m = 3$ and the measures $150 \times 50\,mm^2$. In this scenario, the existing vertically focusing monochromator is replaced by a doubly focusing one. The overall gain in this second set of simulations is also a factor between 4 and 5 [11]. Both sets of simulations were performed using the McStas simulation package [12]. Simulations combining the two scenarios are in progress.

Further, it is under consideration to increase the SINQ current by a factor ~1.5. Together with a new guide system, this will give RITA-2 a flux gain of a factor 8, reaching a total flux of $5 \times 10^7/cm^2/s$.

5. Summary

We have shown that the monochromatic imaging mode of the RITA-2 spectrometer is a very powerful tool for creating maps in reciprocal space. The position-sensitive detector at RITA-2 provides additional flexibility, e.g. the possibility of post-experiment optimization of signal-to-noise ratio by adjustments of the effective detector area corresponding to each blade. Simulations show that there is large potential for upgrade of the spectrometer, where a new guide and monochromator can give RITA-2 a flux comparable to IN 14 at ILL. Combining these advantages, RITA-2 has the potential to become a very powerful instrument.

References

[1] K.N. Clausen, D.F. McMorrow, K. Lefmann, G. Aeppli, T.E. Mason, A. Schröder, M. Issikii, M. Nohara, H. Takagi, Physica B 241–243 (1998) 50.
[2] RITA-2: ⟨rita2.psi.ch⟩.
[3] NIST spectrometers: ⟨www.ncnr.nist.goc/instruments/⟩.
[4] ILL spectrometers: ⟨www.ill.fr/YellowBook/INxx/⟩.
[5] E2: ⟨www.hmi.de/bensc/instrumentation/instrumente/e2/e2.html⟩.
[6] PUMA: ⟨www.frm2.tum.de/puma/⟩.
[7] K. Lefmann, D.F. McMorrow, H.M. Rønnow, K. Nielsen, K.N. Clausen, B. Lake, G. Aeppli, Physica B 283 (2000) 343.
[8] C.H.R. Bahl, K. Lefmann, A.B. Abrahamsen, H.M. Rønnow, F. Saxild, T.B.S. Jensen, L. Udby, N.H. Andersen, N.B. Christensen, H.S. Jakobsen, T. Larsen, P.S. Haefliger, S. Streule, Ch. Niedermayer, Nucl. Instr. and Meth B 246 (2006) 452.
[9] S.N. Klausen, K. Lefmann, D.F. McMorrow, F. Altorfer, S. Janssen, M. Lüthy, Appl. Phys. A 74 (2002) S1508.
[10] U. Filges, An eliptic guide for RITA-2, Paul Scherrer Institut, 2004.
[11] B.P. Christensen, J.K. Hansen, K.S. Hansen, K. Lefmann, Simulations of a new guide for RITA-2, Risø National Laboratory, 2004.
[12] K. Lefmann, K. Nielsen, Neutron News 10/3 (1999) 20 see also the home page: ⟨www.mcstas.org⟩.

Paper IV

Available online at www.sciencedirect.com
SCIENCE DIRECT®
Journal of Colloid and Interface Science 279 (2004) 132–136
JOURNAL OF Colloid and Interface Science
www.elsevier.com/locate/jcis

Interparticle interactions in agglomerates of α-Fe_2O_3 nanoparticles: influence of grinding

Min Xu [a,1], Christian R.H. Bahl [a,b], Cathrine Frandsen [a], Steen Mørup [a,*]

[a] *Department of Physics, Bldg. 307, Technical University of Denmark, DK-2800 Kgs. Lyngby, Denmark*
[b] *Department of Materials Research, Risø National Laboratory, DK-4000 Roskilde, Denmark*

Received 5 November 2003; accepted 16 June 2004

Available online 3 August 2004

Abstract

We have chemically prepared a sample of antiferromagnetic α-Fe_2O_3 nanoparticles by a gel–sol technique. Mössbauer spectra of the as-prepared sample showed that superparamagnetic relaxation was suppressed due to strong magnetic interparticle interactions even at room temperature. However, subsequent grinding of the sample by hand in a mortar for some minutes resulted in fast superparamagnetic relaxation of some of the particles. The effect was even more dramatic if the α-Fe_2O_3 powder was ground for a longer time or together with nonmagnetic η-Al_2O_3 nanoparticles. Similar effects were found after low-energy ball milling. Thus it is found that the agglomeration of the nanoparticles during preparation under wet conditions results in strong magnetic interparticle interaction, but a relatively gentle mechanical treatment is sufficient to break up the agglomerates, resulting in much weaker interactions. We show that these effects can also be seen when a soil sample containing magnetic nanoparticles is ground.

Keywords: Nanoparticles; Hematite; Mössbauer spectroscopy; Grinding; Agglomeration; Superparamagnetism; Soil

1. Introduction

Many studies have shown that interparticle interactions between magnetic nanoparticles can significantly influence the magnetic properties, in particular the superparamagnetic relaxation, of the particles [1–15]. In samples of ferro- or ferrimagnetic particles, long-range dipole interactions can have a significant effect, even if the particles are coated with nonmagnetic molecules so that they are well separated [1–6]. For antiferromagnetic nanoparticles the magnetic dipole interactions are negligible, but it has been reported [7–15] that the superparamagnetic relaxation can be suppressed by interactions to a large extent if the particles are allowed to agglomerate. This can be explained by the exchange coupling between surface atoms of particles in close proximity [8,10,12].

The influence of interactions between iron-containing nanoparticles on the superparamagnetic relaxation can conveniently be studied by Mössbauer spectroscopy. This has been discussed in detail in earlier publications [10,12]. Typically, the spectrum of noninteracting magnetic nanoparticles is a six-line spectrum (a sextet) at low temperatures, while at higher temperatures a one- or two-line component (a singlet or a doublet) is formed at the expense of the sextet because of fast superparamagnetic relaxation. In spectra of samples of interacting nanoparticles, the sextet does not readily collapse with increasing temperature, but the lines become asymmetrically broadened and the average hyperfine splitting decreases. Usually, the spectral change from a sextet into a doublet or a sextet with asymmetrically broadened lines takes place over a temperature range, typically of some tens to hundreds of Kelvin, due to a distribution of particle size and interaction strength.

* Corresponding author. Fax: +45-45-93-23-99.
E-mail address: morup@fysik.dtu.dk (S. Mørup).
[1] Present address: School of Materials and Metallurgy, Northeastern University, Shenyang 110004, China.

0021-9797/$ – see front matter
doi:10.1016/j.jcis.2004.06.039

During studies of interaction effects in samples containing antiferromagnetic α-Fe_2O_3 nanoparticles, we found accidentally that grinding the samples by hand in a small mortar apparently reduced the interparticle interactions. We have therefore carried out a systematic study of the effects of grinding a sample of 11-nm α-Fe_2O_3 particles. We have found that grinding the sample even for a short time can drastically increase the relaxation because the strength of the interparticle interaction is decreased. Similar effects were found in samples exposed to low-energy ball milling.

Mössbauer spectroscopy has been extensively used for studies of soils, which often contain magnetic nanoparticles. Commonly, the samples are ground in a mortar before the Mössbauer absorber is prepared. In this connection, it is important to know if the grinding of such soil samples can have an effect on the magnetic properties. We have tested the grinding effect on a natural soil sample, too, and the result of this study shows consistency with the effect of grinding the synthetic samples.

2. Materials and methods

α-Fe_2O_3 (hematite) nanoparticles were prepared by means of a gel–sol method similar to that developed by Sugimoto et al. [16]. The sample studied here was prepared by freeze-drying particles precipitated during centrifugation of an aqueous suspension of the so-called D-preparation [16]. η-Al_2O_3 nanoparticles with an average diameter of 4 nm were obtained by calcining commercially obtained pseudoboehmite powder at 500 °C.

Grinding was carried out by hand in an agate mortar with a diameter of 60 mm, moving the pestle in a circular motion, applying a pressure of about 2 kg to it. Two series of samples were prepared. In the first, 50 mg of α-Fe_2O_3 nanoparticles were ground for various periods of time (0, 5, 20, and 60 min). In the second, mixtures of 50 mg of α-Fe_2O_3 and 250 mg of η-Al_2O_3 nanoparticles were ground for different periods of time (0, 2, 5, 10, 20, and 60 min).

A mixture of 200 mg of α-Fe_2O_3 and 1 g of η-Al_2O_3 was ball-milled for different periods of time (0, 5, 20, and 60 min). Ball milling was performed using a Retsch reversible mill with agate vial and balls. A ball-to-powder weight ratio of about 30:1 was used. The dry milling was performed at low energy with a rotation speed of 80 rpm. Both grinding and ball milling were performed in air.

A magnetic soil sample from a site called the Salten Forest in Jutland, Denmark was also studied in this investigation. A sample of 100 mg of this soil was ground by hand for 60 min by the same method as used for the α-Fe_2O_3 nanoparticles.

All three samples, α-Fe_2O_3, η-Al_2O_3, and Salten Forest, were loose, dry powders with little visible indication of agglomeration.

The structure and the particle size of pure α-Fe_2O_3 samples, both before and after grinding for 60 min, were examined by X-ray diffractometry (XRD). The XRD spectra were recorded using Cu$K\alpha$ radiation in a Philips PW 1820 diffractometer.

The samples containing mixtures of α-Fe_2O_3 and η-Al_2O_3 were studied by high-resolution transmission electron microscopy (HRTEM) and dark-field TEM (DF-TEM) in a JEOL 3000F electron microscope operated at 300 keV. The samples were prepared by dipping grids in the dry mixtures of α-Fe_2O_3 and η-Al_2O_3 particles.

The samples were studied at room temperature and at 80 K by ^{57}Fe Mössbauer spectroscopy using constant-acceleration spectrometers with sources of ^{57}Co in rhodium. The spectra were obtained using a temperature-controlled liquid nitrogen cryostat. The spectrometers were calibrated with a 12.5-μm-thick α-Fe foil at room temperature.

3. Results and discussion

The XRD spectra of the as-prepared α-Fe_2O_3 sample (Fig. 1a) showed only the presence of diffraction lines characteristic of hematite. From the linewidth of the diffraction peaks we estimated an average crystallite size of 11 nm. In α-Fe_2O_3 nanoparticles, prepared by the gel–sol technique used here, the line broadening due to lattice strain is negligible [17].

The HRTEM images of α-Fe_2O_3 mixed with η-Al_2O_3 nanoparticles showed well-crystallized hematite particles with sizes in accordance with the XRD data, both before and after grinding for 60 min. In both samples, the α-Fe_2O_3 and η-Al_2O_3 nanoparticle mixture was found to consist of ∼0.1–1 μm sized agglomerates. No lattice planes of the η-Al_2O_3 were observed. This is probably due to the small crystallite size of the η-Al_2O_3 or possibly a destruction of the crystal structure of this phase by the electron beam. Using DF-TEM it can be seen that the α-Fe_2O_3 particles, seen as bright spots, stick together in agglomerates in the as-prepared sample (Fig. 2a); i.e., the α-Fe_2O_3 particles are in close contact.

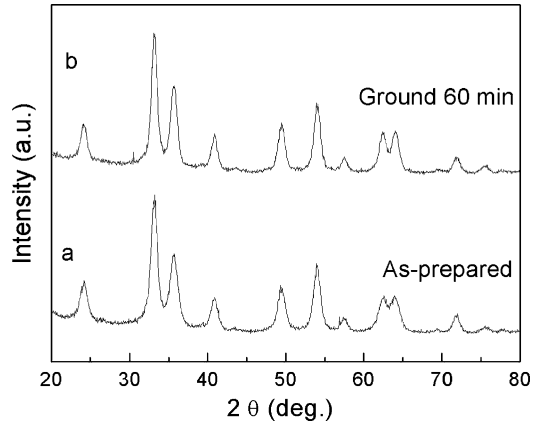

Fig. 1. XRD spectra of α-Fe_2O_3 samples, as prepared and ground for 60 min in a mortar.

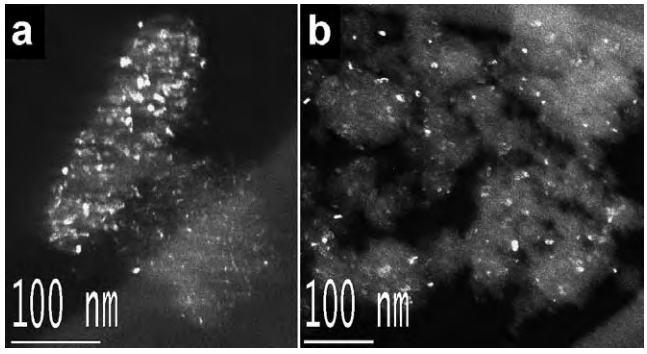

Fig. 2. Dark-field TEM images of the mixed α-Fe_2O_3/η-Al_2O_3 sample. The bright spots are the α-Fe_2O_3 nanoparticles. (a) Image obtained from the sample before grinding. (b) Image obtained after grinding for 60 min.

The image obtained after grinding (Fig. 2b) shows that the particles are distributed more evenly.

Fig. 3 shows room-temperature and 80-K Mössbauer spectra of the pure α-Fe_2O_3 nanoparticles after grinding in the mortar for up to 60 min. The room-temperature spectra show a clear evolution with grinding time. The spectrum of the as-prepared sample has the typical features of nanoparticles with strong interparticle interactions [10,12,14], i.e., a sextet with very broad and asymmetric lines, but no doublet component due to particles with fast superparamagnetic relaxation. However, after 5 min of grinding, there is already an indication of a doublet with a relative intensity that increases with further increased grinding time. After 60 min the doublet is predominant in the spectrum. These results show that an increasing fraction of the particles perform superparamagnetic relaxation when the sample has been ground because the interparticle interactions are reduced. All the spectra obtained at 80 K consist of sextets, but the linewidth and the line asymmetry also increase with grinding time. This is also in accordance with weakened interparticle interaction [10,14].

It might be argued that the evolution of the Mössbauer spectra with grinding time could be explained by a decrease of the particle size during grinding, and this would result in faster superparamagnetic relaxation. To check this possibility we have obtained XRD spectra of the samples after grinding for 60 min (Fig. 1b). A decrease of the size of the individual crystallites should result in a broadening of the diffraction lines. However, the data in Fig. 1 show the opposite effect, namely a slight line narrowing indicating an ∼10% growth of the crystallites during grinding. This is clearly visible by considering, for example, the peaks between 60° and 65°. The increase of the crystallite size may at first glance seem surprising. However, it has previously been shown that mechanical treatment of nanoparticles by ball milling can result in an increase of the crystallite size [18]. It is likely that a similar process takes place during grinding in a mortar. One might expect increased lattice strain after grinding. This should result in line broadening, but this was not observed. The XRD data show clearly that the change in relaxation behavior upon grinding is not due to a reduction of the crystallite size. This supports our interpretation in terms of diminished magnetic interaction between the particles after grinding.

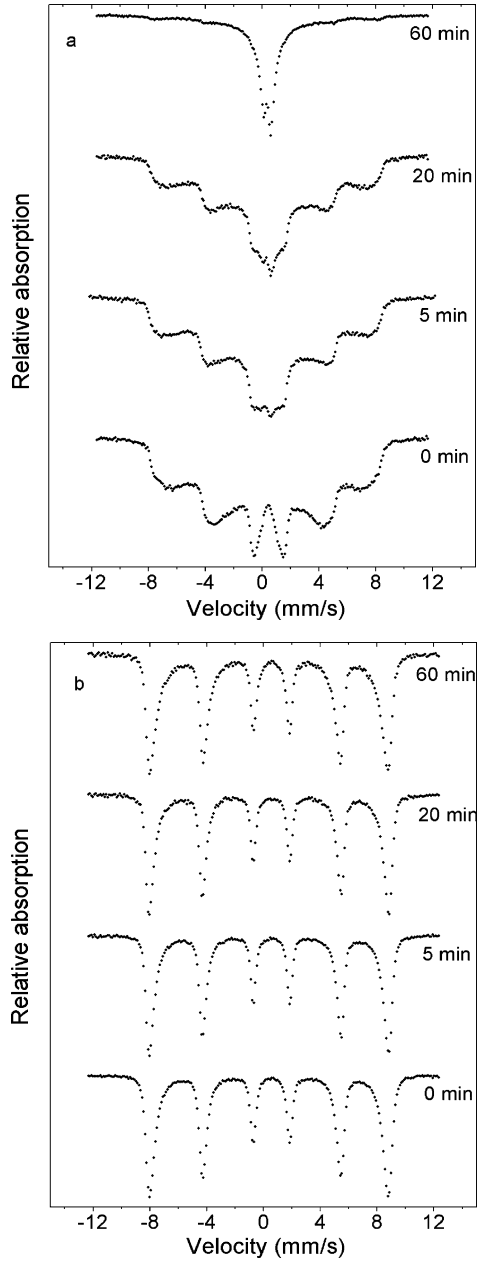

Fig. 3. Mössbauer spectra of α-Fe_2O_3 nanoparticles ground in a mortar for the indicated periods of time. (a) Spectra obtained at room temperature. (b) Spectra obtained at 80 K.

In order to further study the influence of grinding, we repeated the grinding experiments with a mixture of α-Fe_2O_3 and η-Al_2O_3 nanoparticles. The Mössbauer data are shown in Fig. 4. In this case, the evolution of the spectra is much faster than that seen in the sample of pure α-Fe_2O_3 nanoparticles. In the room-temperature spectra there is a clearly visible doublet already after 2 min and after only 10 min the spectrum consists of an intense doublet and a sextet with almost negligible intensity. After longer grinding times the

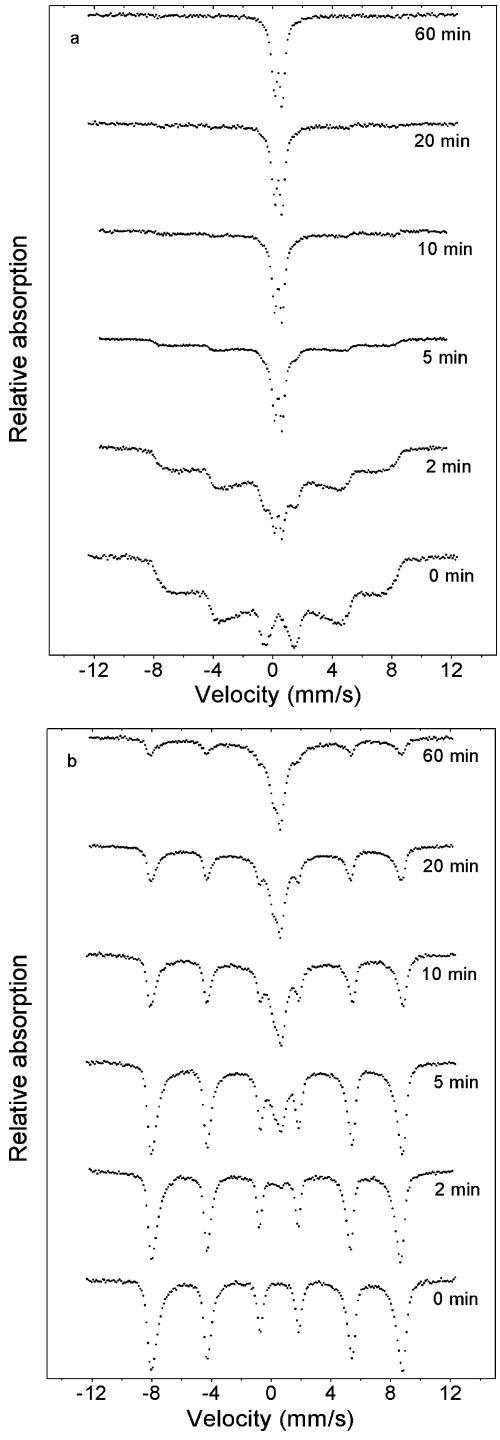

Fig. 4. Mössbauer spectra of α-Fe_2O_3 nanoparticles ground in a mortar with η-Al_2O_3 nanoparticles for the indicated periods of time. (a) Spectra obtained at room temperature. (b) Spectra obtained at 80 K.

spectra essentially consist of a doublet. In the spectra obtained at 80 K, a doublet gradually appears and grows to a significant intensity after 60 min. These spectra consist of superpositions of doublets and sextets with relatively narrow lines. This is characteristic for particles for which the relaxation is governed by the anisotropy energy barrier of

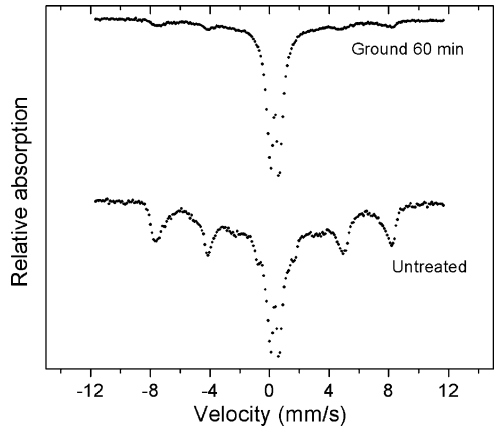

Fig. 5. Mössbauer spectra of a soil sample from the Salten Forest in Denmark. The spectra are from an untreated sample and one that has been ground for 60 min.

the individual particles rather than by interparticle interactions [10,12,14]. In fact, the spectrum obtained at 80 K after grinding for 60 min is similar to those of coated (noninteracting) α-Fe_2O_3 particles with similar size obtained at the same temperature [12,17].

Some of the grinding experiments were repeated in order to check the reproducibility. It was found that the spectra were qualitatively similar to those of the first series although there were small differences in the relative areas of the sextets and the doublets. We also found that if the amount of powder in the mortar was increased, the evolution of the spectra with grinding time was correspondingly slower.

The evolution of the Mössbauer spectra of the ball-milled sample of a mixture of α-Fe_2O_3 and η-Al_2O_3 nanoparticles as a function of milling time is similar to the evolution of the spectra of the corresponding hand-ground samples (Fig. 4). However, the transformation to a doublet took longer in the ball-milling experiment. This can be explained by the significantly increased amount of sample and the low energy of the ball mill.

The results of these experiments show that the as-prepared α-Fe_2O_3 nanoparticles are attached to each other in a way which gives rise to a strong magnetic interparticle interaction. During grinding, these agglomerates are broken up so that the magnetic interaction between the particles is considerably reduced. Although new agglomerates may be formed during grinding under dry conditions, the interparticle interactions in these agglomerates are much weaker. If the α-Fe_2O_3 nanoparticles are mixed with an excess of nonmagnetic η-Al_2O_3 nanoparticles, the grinding results in an almost negligible magnetic interparticle interaction.

In order to investigate if similar phenomena can be encountered in natural samples, we have studied a magnetic soil sample from the location Salten Forest in Jutland, Denmark. Soils from this location, which have a saturation magnetization, $\sigma_s > 1\ \mathrm{A\,m^2/kg}$, have recently been characterized by Mössbauer spectroscopy [19]. Room-temperature Mössbauer spectra of a sample from Salten Forest before and

after grinding in a mortar for 60 min are shown in Fig. 5. As in the synthetic samples, there is a clear effect of the grinding: the relative area of the doublet increases at the expense of the sextet. Thus, it is found that the spectrum of a natural sample can change considerably if the material is ground. Although it is unlikely that one would normally grind a natural sample for 60 min before making an absorber for Mössbauer spectroscopy, changes may also take place after shorter grinding times. In fact, it has been reported that even a gentle smearing of a soil sample that had been heated at 225 °C can have a significant effect on the Mössbauer spectra [19], which is similar to our results for synthetic samples that have been ground for several minutes.

4. Summary

The present study has shown that the magnetic properties of the α-Fe_2O_3 nanoparticles formed by the gel–sol technique are strongly influenced by interparticle interactions. However, grinding by hand in a mortar or ball milling at very low energy can result in a dramatic reduction of the strength of these magnetic interactions. Thus a relatively gentle macroscopic mechanical treatment affects the agglomeration on the nanometer scale. Especially when the magnetic nanoparticles are ground together with an excess of nonmagnetic alumina nanoparticles, there is a very significant effect of grinding. It is also shown that the magnetic properties of natural soil samples can be strongly changed by a gentle mechanical treatment. Thus the results show that the as-prepared sample consists of agglomerates with a strong magnetic interparticle interaction, but after mechanical treatment under dry conditions, the contact between the nanoparticles is reduced so that the magnetic interaction is much weaker.

Acknowledgments

This work was supported by the Danish Technical Research Council and the Danish Natural Science Research Council. We thank Franz Bødker and Lis Lilleballe for preparation of the synthetic α-Fe_2O_3 samples and H.P. Gunnlaugsson for providing the Salten Forest sample.

References

[1] W. Luo, S.R. Nagel, T.F. Rosenbaum, R.E. Rosensweig, Phys. Rev. Lett. 67 (1991) 2721.
[2] S. Mørup, E. Tronc, Phys. Rev. Lett. 72 (1994) 3278.
[3] C. Djurberg, P. Svedlindh, P. Nordblad, M.F. Hansen, F. Bødker, S. Mørup, Phys. Rev. Lett. 79 (1997) 5154.
[4] H. Mamiya, I. Nakatani, T. Furubayashi, Phys. Rev. Lett. 80 (1998) 177.
[5] T. Jonsson, P. Svedlindh, M.F. Hansen, Phys. Rev. Lett. 81 (1998) 3976.
[6] D. Fiorani, J.L. Dormann, R. Cherkaoui, E. Tronc, F. Lucari, F. D'-Orazio, L. Spinu, M. Nogués, A. Garcia, A.M. Testa, J. Magn. Magn. Mater. 196–197 (1999) 143.
[7] S. Mørup, M.B. Madsen, J. Franck, J. Villadsen, C.J.W. Koch, J. Magn. Magn. Mater. 40 (1983) 163.
[8] C.J.W. Koch, M.B. Madsen, S. Mørup, G. Christiansen, L. Gerward, Clays Clay Miner. 34 (1986) 17.
[9] R.A. Borzi, S.J. Stewart, G. Punte, R.C. Mercader, M. Vasquez-Mansilla, R.D. Zysler, E.D. Cabanillas, J. Magn. Magn. Mater. 205 (1999) 234.
[10] M.F. Hansen, C.B. Koch, S. Mørup, Phys. Rev. B 62 (2000) 1124.
[11] C.W. Ostenfeld, S. Mørup, Hyperfine Interact. C 5 (2002) 83.
[12] C. Frandsen, S. Mørup, J. Magn. Magn. Mater. 266 (2003) 36.
[13] F. Bødker, M.F. Hansen, C.B. Koch, S. Mørup, J. Magn. Magn. Mater. 221 (2000) 32.
[14] S. Mørup, C. Frandsen, F. Bødker, S.N. Klausen, K. Lefmann, P.-A. Lindgård, M.F. Hansen, Hyperfine Interact. 144–145 (2002) 347.
[15] M.A. Polykarpov, I.V. Trushin, S.S. Yakimov, J. Magn. Magn. Mater. 116 (1992) 372.
[16] T. Sugimoto, Y. Wang, H. Itoh, A. Muramatsu, Colloids Surf. A 134 (1998) 265.
[17] F. Bødker, S. Mørup, Europhys. Lett. 52 (2000) 217.
[18] S. Mørup, J.Z. Jiang, F. Bødker, A. Horsewell, Europhys. Lett. 56 (2001) 441.
[19] H.P. Gunnlaugsson, J.P. Merrison, L.A. Mossin, P. Nørnberg, J. Sanden, E. Uggerhøj, G. Weyer, Hyperfine Interact. 144–145 (2002) 365.

Paper V

Magnetic anisotropy and quantized spin waves in hematite nanoparticles

S. N. Klausen,* K. Lefmann,† P.-A. Lindgård, L. Theil Kuhn, and C. R. H. Bahl
Materials Research Department, Risø National Laboratory, DK-4000 Roskilde, Denmark

C. Frandsen and S. Mørup
Department of Physics, Technical University of Denmark, DK-2800 Kgs. Lyngby, Denmark

B. Roessli, N. Cavadini, and C. Niedermayer
Laboratory for Neutron Scattering, Paul Scherrer Institute, CH-5232 Villigen PSI, Switzerland
(Received 7 July 2004; published 9 December 2004)

We report on the observation of high-frequency collective magnetic excitations, $\hbar\omega \approx 1.1$ meV, in hematite (α-Fe_2O_3) nanoparticles. The neutron scattering experiments include measurements at temperatures in the range 6–300 K and applied fields up to 7.5 T as well as polarization analysis. We give an explanation for the field- and temperature dependence of the excitations, which are found to have strongly elliptical out-of-plane precession. The frequency of the excitations gives information on the magnetic anisotropy constants in the system. We have in this way determined the temperature dependence of the magnetic anisotropy, which is strongly related to the suppression of the Morin transition in nanoparticles of hematite. Further, the localization of the signal in both energy and momentum transfer brings evidence for finite-size quantization of spin waves in the system.

DOI: 10.1103/PhysRevB.70.214411 PACS number(s): 75.75.+a, 25.40.Fq, 75.30.Ds

I. INTRODUCTION

The magnetic dynamics of nanoparticles is an interesting field both technologically and scientifically. As the size of a particle decreases and enters the nanometer scale, the magnetic properties change and new phenomena appear. One example is superparamagnetic relaxation, in which the direction of the total magnetic moment of the particle performs a spontaneous reversal. A related example is collective magnetic excitations, which can be described as a spin wave with wave vector $q=0$: the individual magnetic moments move coherently and the total (sublattice) spin performs a precession in an effective crystal anisotropy field. This corresponds to the lowest magnetic excitation of nanoparticles, in which the spin waves are predicted[1] to be quantized with discrete, sharp energy levels, while showing a broadening with respect to the spin wave vector, q.

Few experimental studies have been performed on finite-sized systems in order to investigate spin wave quantization. Clear evidence for standing spin waves has been found by Brillouin light scattering in ferromagnetic NiFe wires of 1.8 μm width[2,3] and by pulsed-field techniques in square NiFe dots of 50 μm size.[4] In magnetic clusters, discrete energy levels have been observed by neutron scattering in Mn_{12} clusters,[5,6] and in Fe_8 clusters.[7] In both cluster studies, the reorientation of the total cluster spin was seen, corresponding to collective magnetic excitations, while in Mn_{12} transitions between different cluster spin values were also observed. This can be seen as a precursor to finite-size quantization of spin waves in nanoparticles, which has not yet been observed.

The magnetic dynamics of nanoparticles of the canted antiferromagnet hematite (α-Fe_2O_3) is particularly interesting due to a complicated magnetic structure, which gives rise to rich dynamics.[8–10] Further, an unexplained suppression of the Morin transition has been observed in hematite nanoparticles.[11,12] The Morin transition is related to the magnetic anisotropy, and thus studies of the suppression could yield important information on one of the key properties of magnetic nanoparticles.

Superparamagnetic relaxation and low-frequency collective magnetic excitations were directly observed by inelastic neutron scattering in a powder sample of diameter $d=16$ nm hematite particles.[9] The measurements were performed at a triple-axis spectrometer with a momentum transfer corresponding to the antiferromagnetic (003) reflection (hexagonal indexing), $\tau_{003}=1.37$ Å^{-1}, and a maximum energy transfer of 1.0 meV. The collective magnetic excitations (at $\varepsilon=\pm 0.26$ meV, $q=0$) were found to be strongly broadened,[9] to overlap at $\varepsilon=0$. The broadening could be caused by damping, distribution of anisotropy constants, or both. Later high-resolution neutron studies were focused on the study of superparamagnetic relaxation. These measurements were performed[13] with energy transfers up to 0.75 meV.

In this paper we present inelastic neutron scattering measurements on the same powder sample, as in Refs. 9 and 13, measured with momentum transfers corresponding to the antiferromagnetic (101) reflection, $\tau_{101}=1.51$ Å^{-1}. We show the existence of a second magnetic excitation mode with $q=0$ and with a resonance frequency of ~1.1 meV. The high-frequency mode is seen not only to be reasonably well defined in momentum (q), but also to be clearly localized in energy (ε). We argue that this implies a discrete spin wave spectrum with an anisotropy gap, in agreement with the theoretical predictions. The measurements allow an estimation of the temperature dependence of the anisotropy connected to the suppression of the Morin transition.

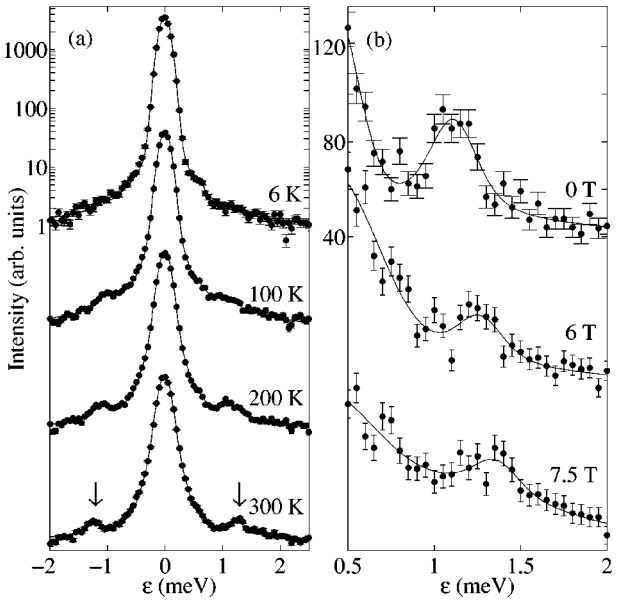

FIG. 1. Inelastic neutron scattering data measured at $\kappa = 1.50$ Å^{-1}, close to τ_{101}. (a) Logarithmic plot of the data at zero applied field at the indicated temperatures. The arrows indicate the position of the high-frequency collective magnetic excitation. (b) Linear plot of the data in applied fields at $T = 200$ K. The data are displaced by (a) a factor of 100 and (b) a constant. The solid lines represent fits as described in the text. The feature at 0.6 meV in (a) is a background signal as discussed in the text.

II. THE HEMATITE SAMPLE

Hematite has the corundum crystal structure, while the magnetic structure is essentially hexagonal with alternating planes of spins along the hexagonal *c* axis, i.e., along the [001] direction. In bulk hematite at high temperatures, the spins are lying in the basal (001) plane, but below the Morin temperature, $T_M = 263$ K, a spin flop transition takes place to leave the spins parallel to [001]. In nanoparticles below ≈20 nm, this Morin transition is suppressed, and only the high-temperature phase is found. In this phase, the spins have a small canting (in bulk ~0.1°) away from antiferromagnetic alignment, resulting in a small net magnetization within the plane. Hematite is the most stable form of iron oxide at ambient conditions and is found in vast quantities on Earth, and recently also on Mars.[14]

The powder sample of nanocrystalline hematite is the same as was used in the previous studies. It was prepared by thermal decomposition of $Fe(NO_3)_3 \cdot 9H_2O$, as described in Refs. 9 and 10. Mössbauer spectroscopy, electron microscopy, and x-ray diffraction have shown that the sample consists of nanocrystallites of hematite with a mean size of 16 nm and a small amount of impurities in the form of ferrihydrite, and that the Morin transition is suppressed in the nanoparticles.[9,10]

III. NEUTRON SCATTERING EXPERIMENTS

The neutron scattering experiments were performed at the RITA-2 and TASP spectrometers at SINQ, Paul Scherrer Institute, Switzerland. The RITA-2 spectrometer was run in the monochromatic point-to-point focusing[15] and in the monochromatic imaging[16] analyzer modes. The experiments at TASP were performed in standard triple-axis geometry. Some of the TASP experiments were performed with polarization analysis. Here, the small adjustable guide field at the sample position ensured that the neutron polarization would always point along the scattering vector, $\boldsymbol{\kappa}$. All experiments were performed with constant final neutron energy of 5.0 meV using relatively loose collimations.

A. Experiments with unpolarized neutrons

Figure 1 shows the normalized measured scattering intensity versus neutron energy transfer, $\varepsilon = \hbar\omega$, for scans performed at constant neutron momentum transfer $\kappa = 1.50$ Å^{-1} in zero applied field at the indicated temperatures and at 200 K in applied fields. In Fig. 1, a peak at ~1.1–1.3 meV is seen at both positive and negative energy transfers. The peak position increases with increasing temperature and increasing field. As we shall discuss later, we ascribe this signal to a high-energy mode of collective magnetic excitations.

The data have been fitted to an elastic signal from incoherent scattering and two damped harmonic oscillator models for the dynamics of the low-frequency and high-frequency precession states.[17] [Broadening of the elastic signal due to superparamagnetic relaxation can be neglected with the present energy resolution of approximately 100 μeV (HWHM); see Ref. 13.] Before correcting for experimental resolution and background, the model is given by

$$I(\varepsilon) = A_{\mathrm{inc}}\delta(\varepsilon) + \sum_{\pm} A^{\pm}\frac{D(\varepsilon)}{\pi}\frac{2\gamma^{\pm}\varepsilon_0^{\pm 2}}{(\varepsilon^2 - \varepsilon_0^{\pm 2})^2 + 4\gamma^{\pm 2}\varepsilon^2}, \quad (1)$$

where A_{inc} and $A^{\pm}$ are the integrated intensities (areas) of the incoherent elastic signal and the low-frequency (+) and high-frequency (−) inelastic components, respectively. $\gamma^{\pm}$ is the HWHM and $\varepsilon_0^{\pm}$ the positions of the inelastic peaks, respectively. $D(\varepsilon) = \varepsilon[n(\varepsilon) + 1]$ is the detailed balance factor, where $n(\varepsilon)$ is the Bose factor.

The inelastic background is modeled by a broad Lorentzian signal, found from measurements at other κ values. Further, a single Gaussian models an anomalous peak at ~0.6 meV, which is a subtle artifact of the open geometry of the RITA-2 spectrometer combined with a nonideal mosaic nature of the PG (002) analyzer crystal.[18] The energy resolution function used for the temperature series was measured on the hematite sample at $T = 6$ K. For the field series, it was measured in zero field at $T = 200$ K. The main component of the resolution function in the two data series is a Gaussian line with HWHM 107(2) μeV. Additionally, there is a much weaker Lorentzian component to the resolution function of HWHM 90(25) μeV. The parameters ε_0^{+} and γ^{+} of the inelastic component modeling the low-frequency collective magnetic excitations are fixed at the values obtained in the high-resolution experiment of Ref. 13. In Fig. 2 the position ε_0^{-} and the area A^{-} of the high-frequency peak as obtained from the fits are shown as a function of sample temperature and applied field.

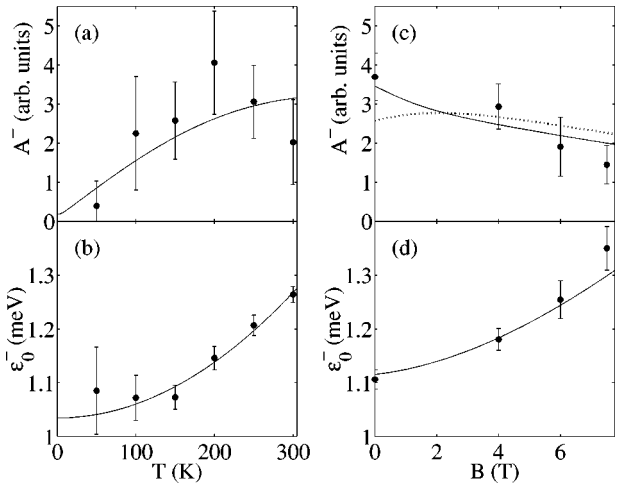

FIG. 2. (a) Area (A^-) and (b) position (ε_0^-) of the inelastic peak as a function of temperature in zero field. (c) Area (A^-) and (d) position (ε_0^-) of the inelastic peak as a function of applied field at 200 K. The lines show fits as described in the text.

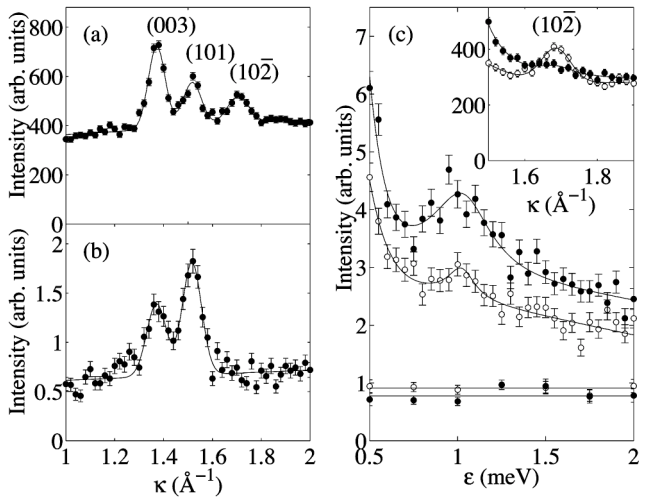

FIG. 3. (a) Diffraction data on hematite at 200 K. (b) Constant-ε-scan measured at $\varepsilon=1.1$ meV at 200 K. The solid lines are fits to the peaks multiplied with the Debye-Waller factor plus a sloping background. (c) Polarization data on hematite measured at 200 K in the non-spin-flip channel (○) and the spin-flip channel (●). The straight lines represent fits as described in the text. The main panel shows the inelastic intensity measured at the antiferromagnetic reflection at $\kappa=1.50$ Å^{-1}. The lower straight lines are the corresponding analyzer-turned background in the two channels. The inset shows diffraction data.

Figure 3(a) shows diffraction data measured at 200 K. The peaks at 1.372(2) Å^{-1} and 1.517(3) Å^{-1} are the antiferromagnetic (003) and (101) reflections from hematite, respectively. The peak at 1.704(5)Å^{-1} is the structural (10$\bar{2}$) reflection. In Fig. 3(b) a κ scan measured at constant neutron energy transfer $\varepsilon=1.1$ meV is shown. A peak at ~1.52 Å^{-1} is clearly seen. The peak at ~1.37 Å^{-1} is mostly due to a tail from the low-frequency excitation, as we will discuss below.

Figure 4 shows a (κ,ω) color map of the inelastic scattering around the magnetic scattering vectors $\boldsymbol{\tau}_{003}$ and $\boldsymbol{\tau}_{101}$ in zero field and $T=200$ K. The data were taken with the monochromatic imaging mode, yielding 7 data points per setting. The complete map was taken with 9 energy scans. The method, including data treatment procedure, is detailed in Ref. 18. The statistics of the data in the color map is inferior to the data of Figs. 1 and 3, but the overall tendencies can be more easily seen in a color map. The mode at $\varepsilon=1.1$ meV is clearly seen at $\kappa=\boldsymbol{\tau}_{101}$, and a faint signal at the same energy is seen at $\kappa=\boldsymbol{\tau}_{003}$. The (101) mode is clearly localized in (κ,ε) as a relatively sharp peak. This is in contrast to the low-frequency (003) mode, which is broad and has intensity even at $\varepsilon=0$.

B. Experiments with polarized neutrons

The purely structural reflection at $\kappa=1.70$ Å^{-1} has supposedly only non-spin-flip scattering. In the inset of Fig. 3(c), we show the polarization analysis of this reflection. From the small value of the measured spin-flip scattering, we determine the overall polarization of the experimental setup, which is comprised of initial polarization, depolarization in the setup, and polarization efficiency of the benders. The value was $P=0.69(9)$.

The main part of Fig. 3(c) shows the results of a polarization analysis of the inelastic peak measured at $\kappa=1.50$ Å^{-1}, close to $\boldsymbol{\tau}_{101}$. Since the neutron polarization is parallel to $\boldsymbol{\kappa}$, all magnetic scattering is ideally spin-flip scattering. With the present value (and uncertainty) of P, this gives that the ratio of the observed ratio of non-spin-flip scattering to spin-flip scattering is expected to be 1:5(2). Indeed, the largest part of the peak at ~1.1 meV is observed in the spin-flip channel. The non-spin-flip to spin-flip fraction is found to be 1:3.1(6). This does not contradict the hypothesis of a purely magnetic origin of the signal.

The background exceeding the analyzer-turned background originates from the sample. Since the intensity in the two channels is equal, except for a factor of 1.44(5), this

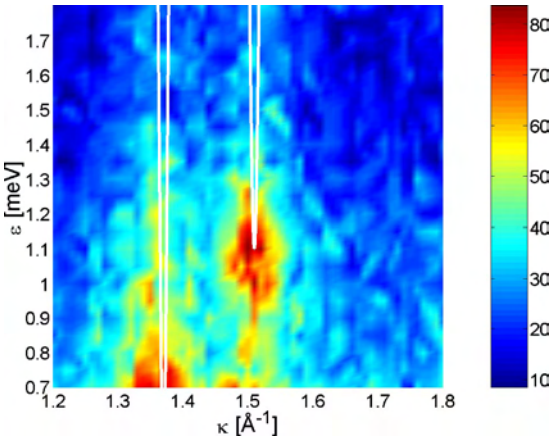

FIG. 4. (Color online) The scattered inelastic intensity at 200 K and zero field as a function of scattering vector, κ (horizontal) and energy transfer, $\hbar\omega$ (vertical). The bar to the right represents the color scale. The solid lines show the dispersion relation of bulk hematite with anisotropy gaps of 1.1 and 0.26 meV, as discussed in the text. The data have been normalized as described in Ref. 18.

signal probably comes from nuclear incoherent scattering, probably from ^{1}H. This ratio would be 1:2 for nuclear incoherent scattering with a totally polarized beam,[19] but with the present value of P, this would become 1:1.6(1), in agreement with measurements.

IV. DISCUSSION

A. Quantization of spin waves

The measured spin wave dispersion relation of bulk hematite is very steep,[20] with an energy given by $\varepsilon_q=\sqrt{c^2q^2+\varepsilon_0^{\pm 2}}$, where the effective spin wave velocity is $c=200$ meV Å. The first excited state with $q\neq 0$ of a spherical nanoparticle has a (standing) wavelength[1] of $\approx 1.42\,d$. For a $d=16$ nm particle (corresponding to $\sim 10^5$ spins) this gives the smallest nonzero q value of $q_{\min}\approx 0.028$ Å^{-1}, corresponding to a minimum energy of $\varepsilon_{\min}\approx 5.6$ meV for $\varepsilon_0^{\pm}\leqslant 1$ meV. The observed signals at ~ 0.26 meV and ~ 1.1 meV therefore cannot be caused by finite-size quantization. They must be assigned to uniform magnetic excitations ($q=0$ spin waves) and they determine the value of the small anisotropy gap, $\varepsilon_0^{\pm}$. This corresponds to the low-frequency and high-frequency modes of the weak ferromagnetic phase in bulk hematite.[8,20]

For spin waves in a bulk isotropic antiferromagnet, the scattering cross section for creation or annihilation of an excitation is proportional to[17,19,21]

$$I(\varepsilon,\boldsymbol{\kappa})\propto \mathcal{J}_0\langle S\rangle\sum_\beta [1-(\hat{\boldsymbol{\kappa}}\cdot\hat{\boldsymbol{M}}_\beta)^2]\frac{n(\varepsilon^{\pm}_{q,\boldsymbol{B}})+\frac{1}{2}\pm\frac{1}{2}}{\varepsilon^{\pm}_{q,\boldsymbol{B}}} \times\delta(\boldsymbol{\kappa}\mp\boldsymbol{q}-\boldsymbol{\tau})\delta(\varepsilon^{\pm}_{q,\boldsymbol{B}}\mp\varepsilon), \quad (2)$$

where β is a Cartesian coordinate, and $\hat{\boldsymbol{M}}_\beta$ and $\hat{\boldsymbol{\kappa}}$ are unit vectors pointing in one direction of the spin wave amplitude and the scattering vector, respectively. For isotropic spin waves, the sum is conventionally replaced by $1+(\hat{\boldsymbol{\kappa}}\cdot\hat{\boldsymbol{M}}_z)^2$, where z is the direction of the ordered moment.

In a powder sample like ours, the orientation of $\boldsymbol{\tau}_{101}$ (the relevant reciprocal lattice vector) is arbitrary. For a given length of the spin wave vector, q, the scattering vector, $\boldsymbol{\kappa}$, can thus fall in the interval $[\tau_{101}-q;\tau_{101}+q]$. This gives rise to a smearing of the signal in κ for a given energy transfer, ε.

The dispersion relation for the two modes in bulk hematite is shown in Fig. 4. It is seen that the steepness of the dispersions implies that the related smearing of the scattering vector at low energies is negligible in comparison with the finite-size broadening of the signal of $\delta\kappa\approx 2\pi/d \approx 0.04$ Å^{-1}. A bulk-like dispersion would thus have given rise to a signal at $\kappa\approx\tau_{101}$ with a large asymmetric tail towards the high energy side. Since we observe a symmetric peak with essentially no intensity above the two $q=0$ modes, we conclude that the bulk-like continuum is absent and that the spin wave spectrum is quantized, as expected.

B. Properties of the high-energy collective mode in zero field

The spin structure of bulk hematite is determined by Heisenberg and Dzyaloshinskii exchange interactions and a crystal field anisotropy

$$\mathcal{H}_{\rm an}=-\sum_i(\kappa_1 S_i^{x2}+\kappa_{\rm Bu}S_i^{z2}), \quad (3)$$

where the x direction is along [001] and the z direction is the easy axis within the (001) plane. The coefficients κ_1 and $\kappa_{\rm Bu}$ represent the anisotropy per atomic site and are related to the anisotropy constants $K_1<0$ of the [001] direction and $K_{\rm Bu}>0$ of the uniaxial basal plane anisotropy defined for hematite nanoparticles in Ref. 13 by $N\kappa_1 S^2=K_1V$ and $N\kappa_{\rm Bu}S^2=K_{\rm Bu}V$, where $S=\frac{5}{2}$ for Fe^{3+}, V is the particle volume, and N the number of spins. Simplifying the magnetic structure of hematite to a two-sublattice structure, and neglecting the small canting, the zero-field spin wave dispersion relation for wave vector $\boldsymbol{q}$ along the [001] direction is given by[21]

$$\varepsilon_q^{\pm}=2\frac{\langle S^z\rangle}{S}\sqrt{(\mathcal{A}+\mathcal{J}_0\pm\mathcal{J}_q)(\mathcal{B}+\mathcal{J}_0\mp\mathcal{J}_q)}, \quad (4)$$

where $\mathcal{A}=(-\kappa_1+\kappa_{\rm Bu})s'$ and $\mathcal{B}=\kappa_{\rm Bu}s'$ with $s'=S-\frac{1}{2}$.[28] Further, $\mathcal{J}_q=-S(J_1+3J_3+6J_4)\cos(cq)$, and $\mathcal{J}_0=\mathcal{J}_{q=0}$ with c being the lattice constant in the [001] direction. The nearest-neighbor out-of-plane exchange constants J_n ($J_1=6$ K, $J_3=-29.7$ K, $J_4=-23.2$ K, which are labeled according to increasing interionic distance) have been determined by spin wave measurements.[20] Since $J_0=556$ K is about 4 orders of magnitude larger than $\mathcal{A}$ and $\mathcal{B}$, the two energy gaps of the dispersion relation for $q\to 0$ are well approximated by

$$\varepsilon_0^+\approx\frac{2\langle S^z\rangle}{S}\sqrt{2\mathcal{J}_0\mathcal{B}} \quad\text{and}\quad \varepsilon_0^-\approx\frac{2\langle S^z\rangle}{S}\sqrt{2\mathcal{J}_0\mathcal{A}}. \quad (5)$$

The two branches ($\pm$) of the dispersion relation are the low-frequency and high-frequency modes described above. Hence, the two energy gaps (of the two modes at $q=0$) correspond to the low-frequency and high-frequency collective magnetic excitation, respectively. Using $\varepsilon_0^+=0.26$ meV and $\varepsilon_0^-=1.1$ meV, we find $\mathcal{A}=35$ mK and $\mathcal{B}=2.5$ mK.

In bulk hematite, both modes are of antiferromagnetic character, i.e., the two sublattices precess in antiphase. Due to the strong planar anisotropy, the spin precession is strongly elliptical and very different for the two modes. For the ε_0^+ mode the precession is almost exclusively in the (001) plane, whereas for the ε_0^- mode it is almost exclusively along the [001] direction. For extreme elliptical precession, the sum in (2) should be replaced by the factor $[1-(\hat{\boldsymbol{\kappa}}\cdot\hat{\boldsymbol{M}}_\beta)^2]$, where $\boldsymbol{M}_\beta$ is now along the long axis of the ellipse. This implies that the neutron scattering intensity of the ε_0^- mode is strongly suppressed when the scattering vector equals $\boldsymbol{\tau}_{003}$, while the ε_0^+ mode has maximum intensity for this scattering vector. In the nanoparticles, we observe exactly this: $I^-(003)/I^-(101)\approx 0.11$, proving that the high-energy mode is strongly elliptical and predominantly out-of-plane.

In zero applied field we assume that the variation of ε_0^- with temperature is solely due to changes in the anisotropy coefficient κ_1. We have no model for this temperature dependence, but as a starting point we fit ε_0^- to a second-order polynomium in T, as shown in Fig. 2(b). The intensity of the mode follows directly from Eq. (2); see the fit in Fig. 2(a). From the definitions of $\mathcal{A}$ and $\mathcal{B}$ we obtain $\mathcal{A}-\mathcal{B}=-\kappa_1 s'$. Further, Eq. (5) relates $\mathcal{A}$ and $\mathcal{B}$ to the energies ε_0^- and ε_0^+.

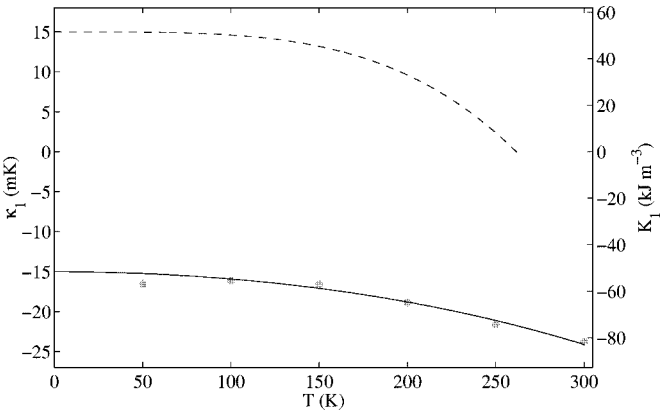

FIG. 5. Temperature dependence of κ_1 (K_1). The solid line represents our results for the hematite nanoparticles. The dashed line represents the value for bulk hematite (Ref. 8).

We have used ε_0^+ as determined in Ref. 13. The obtained value of $\kappa_1(K_1)$ is shown in Fig. 5. The value corresponds to $\kappa_1 = -16(1)$ mK at $T=0$ and $-23.7(1)$ mK at room temperature, and hence does not change sign with increasing temperature. This is in contrast to the bulk behavior, where κ_1 change sign at the Morin transition.[8] Thus, the measured temperature dependence of K_1 sheds new light on the suppression of the Morin transition in hematite nanoparticles. The overall temperature dependence of the anisotropy in nanoparticles is similar to that of the bulk, but shifted by a constant (positive) amount. In studies of the anisotropy of nanoparticles of α-Fe,[23] γ-Fe_2O_3 (maghemite),[22] and α-Fe_2O_3 (hematite, the in-plane anisotropy),[24] it has been found that the anisotropy constant increases with decreasing particle size. A main contribution to this is presumably surface anisotropy.[25] It is likely that the different values of K_1 in bulk and nanoparticles of α-Fe_2O_3 also can be explained by the influence of surface anisotropy in nanoparticles.

C. Effect of an applied field

The field dependence of the excitation energy is given by[8]

$$\varepsilon_{0,\boldsymbol{B}}^{\pm} = \sqrt{(\varepsilon_0^{\pm})^2 + (g\mu_B)^2[B^2\cos^2\xi + B_D(B\sin\xi + B_D)]}, \quad (6)$$

where B_D is the Dzyaloshinsky field and ξ the angle between the applied field $\boldsymbol{B}$ and the [001] direction. Note that due to the small canting, Eq. (6) differs in zero field from Eq. (4) by the term $(g\mu_B B_D)^2$, which equals $(0.24\ \text{meV})^2$. Here, we have used the values for bulk hematite[8] $B_D = 2.1$ T, and $g=2$.

In applied fields, $\varepsilon_{0,\boldsymbol{B}}^-$ depends on the angle ξ between $\boldsymbol{B}$, which is applied vertically, and the [001] direction. In order to contribute to the scattering, the particles of the powder sample have to be oriented so that their [101] direction coincides with the scattering vector, i.e., $\boldsymbol{\kappa} = \boldsymbol{\tau}_{101}$. Thus, the only degree of freedom is rotation of the (101) plane. Hence, for the different contributing particles the [003] direction will lie on a cone with symmetry axis equal to the [101] direction with varying ξ, as illustrated in Fig. 6. We assume that the contributing particles are randomly oriented and perform an average of the energy in Eq. (6). In Fig. 2(d) the result is shown for a fit with the bulk values[8] $B_D = 2.1$ T, and $g=2$. The only free parameter of the fit is the energy at $B=0$ T. We obtain $\varepsilon_0^- = 1.12(1)$ meV at $T=200$ K.

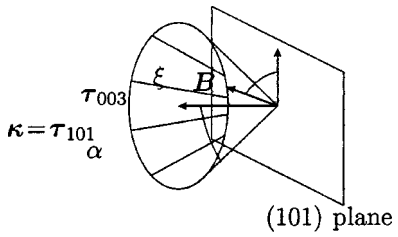

FIG. 6. Illustration of the scattering geometry for a powder sample when $\boldsymbol{\kappa} = \boldsymbol{\tau}_{(101)}$. The [001] direction makes an angle, $\alpha \sim 72°$, to the [101] direction.

The scattered intensity varies for the different contributing particles due to the factor $1-(\hat{\boldsymbol{\kappa}}\cdot\hat{\boldsymbol{M}})^2$ in Eq. (2). Again, we perform an average over the contributing particles. We use $\hat{\boldsymbol{M}} \propto (-[B\sin\xi + B_D], B\cos\xi, 0)$, where the x axis points in the [001] direction and the z axis is perpendicular to the applied field. Hence, we assume a zero-field spin direction given by the projection of the externally applied field onto the basal plane. In Fig. 2(c) the result of the described averaging over Eq. (2) is shown by the solid line. The dotted line models the scattered intensity if we assume approximately circular precessions (with $1-(\hat{\boldsymbol{\kappa}}\cdot\hat{\boldsymbol{M}})^2$ in Eq. (2) replaced[17,19] by $1+(\hat{\boldsymbol{\kappa}}\cdot\hat{\boldsymbol{M}})^2$), giving a clearly inferior fit. Hence, these data support the picture of the precession as strongly elliptical.[29] The strongest evidence for elliptical precession in the high-energy mode, however, comes from the strong suppression of its intensity at τ_{003}.

V. CONCLUSION

We have observed a second collective magnetic excitation, the high-frequency mode, in hematite nanoparticles by inelastic neutron scattering at momentum transfers equal to the antiferromagnetic (101) reflection. The precession is found to be strongly anisotropic with a large out-of-plane component. The mode has no dispersion, as seen from the sharpness in energy, giving evidence for quantization of spin waves in the system. A model including an analysis of the orientation of the contributing particles explains the temperature- and field dependence of peak position and scattered intensity. We find that the absolute value of the out-of-plane anisotropy constant κ_1 increases with temperature, without a change of sign as is seen in the bulk material. This is an important step towards explaining the suppression of the Morin transition in hematite nanoparticles.

ACKNOWLEDGMENTS

We thank F. Bødker for preparing the hematite nanoparticles. We are grateful to B. Lebech and N. B. Christensen for stimulating discussions. This work was supported by the

Danish Technical Research Council through the framework program on nanomagnetism, and the Danish Natural Science Research Council through the Danish Neutron Scattering Centre, DANSCATT. This work is based on experiments performed at the SINQ neutron source at the Paul Scherrer Institute, Villigen, Switzerland.

---

*Electronic address: stine.nyborg.klausen@risoe.dk
†Electronic address: kim.lefmann@risoe.dk

[1] P. V. Hendriksen, S. Linderoth, and P.-A. Lindgård, Phys. Rev. B **48**, 7259 (1993).
[2] C. Mathieu, J. Jorzick, A. Frank, S. O. Demokritov, A. N. Slavin, B. Hillebrands, B. Bartenlian, C. Chappert, D. Decanini, F. Rousseaux, and E. Cambril, Phys. Rev. Lett. **81**, 3968 (1998).
[3] J. Jorzick, S. O. Demokritov, C. Mathieu, B. Hillebrands, B. Bartenlian, C. Chappert, F. Rousseaux, and A. N. Slavin, Phys. Rev. B **60**, 15 194 (1999).
[4] T. M. Crawford, M. Covington, and G. J. Parker, Phys. Rev. B **67**, 024411 (2003).
[5] M. Hennion, L. Pardi, I. Mirebeau, E. Suard, R. Sessoli, and A. Caneschi, Phys. Rev. B **56**, 8819 (1997).
[6] I. Mirebeau, M. Hennion, H. Casalta, H. Andres, H. U. Güdel, A. V. Irodova, and A. Caneschi, Phys. Rev. Lett. **83**, 628 (1999).
[7] R. Caciuffo, G. Amoretti, A. Murani, R. Sessoli, A. Caneschi, and D. Gatteschi, Phys. Rev. Lett. **81**, 4744 (1998).
[8] A. H. Morrish, *Canted Antiferromagnetism: Hematite* (World Scientific, Singapore, 1994).
[9] M. F. Hansen, F. Bødker, S. Mørup, K. Lefmann, K. N. Clausen, and P.-A. Lindgård, Phys. Rev. Lett. **79**, 4910 (1997).
[10] F. Bødker, M. F. Hansen, C. B. Koch, K. Lefmann, and S. Mørup, Phys. Rev. B **61**, 6826 (2000).
[11] D. Schroeer and R. C. Nininger Phys. Rev. Lett. **19**, 632 (1967).
[12] W. Kündig, H. Bömmel, G. Constabaris, and R. H. Lindquist Phys. Rev. **142**, 327 (1966).
[13] S. N. Klausen, K. Lefmann, P.-A. Lindgård, K. N. Clausen, M. F. Hansen, F. Bødker, S. Mørup, and M. Telling, J. Magn. Magn. Mater. **266**, 68 (2003).
[14] P. R. Christensen, J. L. Bandfield, R. N. Clark, K. S. Edgett, V. E. Hamilton, T. Hoefen, H. H. Kieffer, P. O. Kuzmin, M. D. Lane, M. C. Malin, R. V. Morris, J. C. Pearl, R. Pearson, T. L. Roush, S. W. Ruff, and M. D. Smith, J. Geophys. Res., [Planets] **105**, 9623 (2000).
[15] K. Lefmann, D. F. McMorrow, H. M. Rønnow, K. Nielsen, K. N. Clausen, B. Lake, and G. Aeppli, Physica B **283**, 343 (2000).
[16] C. R. H. Bahl, P. Andersen, S. N. Klausen, and K. Lefmann, Nucl. Instrum. Methods Phys. Res. B (to be published in 2004).
[17] P.-A. Lindgård, in *Spin Waves and Magnetic Excitations*, edited by V. M. Agranovich and A. A. Maradudin, Modern Problems in Condensed Matter Sciences, Vol. 22.1 (North-Holland, Amsterdam, 1988).
[18] C. R. H. Bahl *et al.* (unpublished).
[19] S. W. Lovesey, *Theory of Neutron Scattering from Condensed Matter* (Oxford University Press, Oxford, 1984).
[20] E. J. Samuelsen and G. Shirane, Phys. Status Solidi **42**, 241 (1970).
[21] P.-A. Lindgård, A. Kowalska, and P. Laut, J. Phys. Chem. Solids **28**, 1357 (1967).
[22] E. Tronc, Nuovo Cimento D **18**, 163 (1996).
[23] F. Bødker, S. Mørup, and S. Linderoth, Phys. Rev. Lett. **72**, 282 (1994).
[24] F. Bødker and S. Mørup, Europhys. Lett. **52**, 217 (2000).
[25] L. Néel, J. Phys. Radium **15**, 225 (1954).
[26] M. Nielsen, H. Bjerrum-Møller, P.-A. Lindgård, and A. R. Mackintosh, Phys. Rev. Lett. **25**, 1451 (1970).
[27] S. N. Klausen, Magnetic Dynamics of Hematite Nanoparticles (Ph.D. thesis, Department of Physics, Technical University of Denmark, Denmark, 2004).
[28] Eq. (4) differs slightly from that given by Ref. 8, in which a hexagonal anisotropy is included. This cannot be present in a quantum-mechanical derivation for $S=\frac{5}{2}$. Further, the q dependence is ignored in Ref. 8. Magneto-elastic effects could be included in Eq. (4) via $\mathcal{A}$ and $\mathcal{B}$ directly from Ref. 26. They are effectively included in κ_B.
[29] The described analysis can be applied to all inelastic studies of powder samples; see Ref. 27. In our previous work on the low-frequency collective magnetic excitations of hematite we did not perform this detailed analysis (Refs. 9 and 13) since there is no angular dependence at τ_{003}; see Ref. 27.

Paper VI

Oriented attachment and exchange coupling of α-Fe_2O_3 nanoparticles

C. Frandsen,[1,2] C. R. H. Bahl,[1,3] B. Lebech,[3] K. Lefmann,[3] L. Theil Kuhn,[3] L. Keller,[4] N. H. Andersen,[3] M. v. Zimmermann,[5] E. Johnson,[3,6] S. N. Klausen,[3,7] and S. Mørup[1]

[1]*Department of Physics, Technical University of Denmark, DK-2800 Kgs. Lyngby, Denmark*

[2]*School of Conservation, DK-1263 Copenhagen K, Denmark*

[3]*Materials Research Department, Risø National Laboratory, DK-4000 Roskilde, Denmark*

[4]*Laboratory for Neutron Scattering, ETHZ & PSI, CH-5232 Villigen PSI, Switzerland*

[5]*Hamburger Synchrotronstrahlungslabor HASYLAB at Deutsches Elektronen-Synchrotron DESY, D-22603 Hamburg, Germany*

[6]*Nano Science Center, Niels Bohr Institute, University of Copenhagen, DK-2100 Copenhagen Ø, Denmark*

[7]*Materials Science Division, Argonne National Laboratory, Argonne, Illinois 60439, USA*

(Received 17 July 2004; published 6 December 2005)

We show that antiferromagnetic nanoparticles of α-Fe_2O_3 (hematite) under wet conditions can attach into chains along a common [001] axis. Electron microscopy shows that such chains typically consist of two to five particles. X-ray and neutron diffraction studies show that both structural and magnetic correlations exist across the interfaces along the [001] direction. This gives direct evidence for exchange coupling between particles. Exchange coupling between nanoparticles can suppress superparamagnetic relaxation and it may play a role for attachment along preferred directions. The relations between exchange coupling, magnetic properties, and oriented attachment are discussed.

DOI: 10.1103/PhysRevB.72.214406 PACS number(s): 75.50.Tt, 61.46.+w, 68.35.Ct, 75.25.+z

I. INTRODUCTION

The magnetic properties of nanoparticles can be strongly influenced by interparticle interactions. For ferro- and ferrimagnetic nanoparticles, strong dipole interactions may result in a divergence of the superparamagnetic relaxation time at a finite temperature, which depends on the strength of the interactions.[1,2] Below this critical temperature, such samples may have many similarities to spin glasses.[2–6] The superparamagnetic relaxation of antiferromagnetic nanoparticles can also be significantly suppressed by interparticle interactions. In this case, the dipole interactions are too weak to explain the observed effects, and therefore it has been concluded that exchange interactions between surface atoms of particles in close proximity are responsible for the effects.[7–9] It has been shown that exchange interactions between ferromagnetic nanoparticles and an antiferromagnetic environment can result in a greatly enhanced magnetic anisotropy, and this may be utilized to increase the information density in magnetic recording media.[10] The exchange interaction depends crucially on the atomic arrangement at the interface between neighboring particles, and studies of the magnetic properties of interacting antiferromagnetic nanoparticles may therefore give new information about the way they attach. Currently there is considerable interest in understanding and controlling the arrangement of nanoparticles because it is of importance for a number of interesting phenomena, including revealing the mechanisms behind crystal growth[11–14] and developing new technologies for building up nanostructured devices.[15] In order to control positioning of magnetic nanoparticles, their magnetic dipole moments have been utilized to guide them in applied fields or in stray fields from neighboring particles.[16–20] Another potential method of controlling the position and properties of magnetic nanoparticles is to utilize exchange interaction between particles. Although this kind of interaction is rather unexplored, it holds interesting prospects. Exchange coupling between particles can be orders of magnitude larger than the dipole coupling if the particles are in close proximity. However, it is considered a major challenge to establish strong exchange coupling between nanoparticles.[21]

To examine the exchange coupling between particles it is fruitful to study particles of antiferromagnetic materials, because they have insignificant magnetic dipole interactions. The most abundant antiferromagnetic material is probably α-Fe_2O_3 (hematite).[22] It is the most stable form of iron oxide and commonly found in rocks and sediments on Earth and recently also on Mars.[23] It has a pseudohexagonal unit cell with six puckered Fe-layers perpendicular to the [001] direction and the spins of adjacent Fe-layers are coupled antiparallel.[22,24] In α-Fe_2O_3 nanoparticles the spins are confined to lie in the low anisotropy (001) plane.[25,26] Within this plane, the sublattice magnetization directions can easily rotate while rotation out of the plane requires much more energy. Therefore, superparamagnetic relaxation mainly takes place within the (001) plane.[26,27] Mössbauer spectroscopy studies have shown that the superparamagnetic relaxation can be suppressed in samples in which α-Fe_2O_3 nanoparticles have agglomerated, suggesting that strong exchange interaction exists between the particles.[7,9] However, no direct observation of the coupling has been reported so far. In the following, we present studies of nanoparticles of α-Fe_2O_3 using high-resolution electron microscopy, high-energy synchrotron x-ray diffraction, neutron powder diffraction, and Mössbauer spectroscopy. We find that α-Fe_2O_3 nanoparticles arrange into chains along a common [001] axis, and we directly observe that also the magnetic order continues across the interfaces in this direction.

II. EXPERIMENTAL DETAILS

We prepared α-Fe_2O_3 nanoparticles by a gel-sol method similar to that described by Sugimoto *et al.*[28] After formation

of the particles in an aqueous solution, excess ions were washed out and the particles were freeze-dried. In the following, this dried sample is referred to as the as-prepared sample. In order to study how the interactions may be diminished due to mechanical treatments the agglomerated α-Fe_2O_3 particles were ground together with nonmagnetic nanoparticles of amorphous SiO_2 (weight ratio 1:3) in air in an agate ball mill. The mill rotated gently, 40 times per minute for 2 days. The weight ratio between balls and sample was 15:1. Mössbauer spectroscopy and x-ray diffraction showed that no chemical reaction (less than 5 wt %, if any) took place during grinding.

High-resolution electron microscopy (HREM) images were obtained by means of a JEOL 3000F FEG transmission electron microscope (TEM) using lacey carbon film on 200 μm mesh Cu grids as sample supports. Cryo-TEM imaging was made with a Philips CM200 FEG TEM using an Oxford Instruments CT3500 cryoholder at liquid nitrogen temperature.

High-energy synchrotron x-ray diffraction (HES-XRD) data were obtained using the three-crystal diffractometer at the BW5 beam-line at HASYLAB at DESY in Germany with incident photons with a wavelength of 0.12513 Å (approximately 100 keV). The monochromator and analyzer systems consist of Si(111)/Ge gradient crystals giving a full width at half maximum (FWHM) instrumental resolution $B_{i,XRD}$ (approximately independent of scattering vector Q) that is 0.0135 $Å^{-1}$ at $Q=3.1$ $Å^{-1}$.

Neutron powder diffraction (NPD) data were collected by means of the DMC diffractometer placed at the neutron spallation source SINQ at the Paul Scherrer Institute in Switzerland. A wavelength of 4.20 Å was used. The instrumental resolution $B_{i,NPD}$ is 0.017 $Å^{-1}$ at $Q=1.37$ $Å^{-1}$ increasing to 0.020 $Å^{-1}$ at $Q=2.32$ $Å^{-1}$.

^{57}Fe Mössbauer spectra were obtained by use of a conventional constant acceleration Mössbauer spectrometer with a 50 mCi source of ^{57}Co in a rhodium matrix. Low-temperature spectra were obtained using a temperature-controlled liquid nitrogen cryostat. The spectrometers were calibrated with a 12.5 μm α-Fe foil at room temperature.

III. RESULTS AND ANALYSIS

A. Electron microscopy

High-resolution electron microscopy images of agglomerates of the particles from the as-prepared sample, dried on a grid, are shown in Figs. 1(a) and 1(b). The individual particles are typically 5–10 nm in diameter and have rounded shapes without pronounced facets. Noticeably, the micrographs show that neighboring particles have a tendency to be aligned along their common [001] axis. Since no (00l) planes are seen due to extinction, the orientation of the [001] axis of the particles can only be established from other planes identified from their planar spacings and mutual angles. Typically, chains of two to five particles are observed. In most cases, where the particles share a common [001] axis, the arrangement of particles appears epitaxial, i.e., the lattice planes are continued from one particle into its neighbor [Fig. 1(a)]. In one case we found that the lattice planes other than

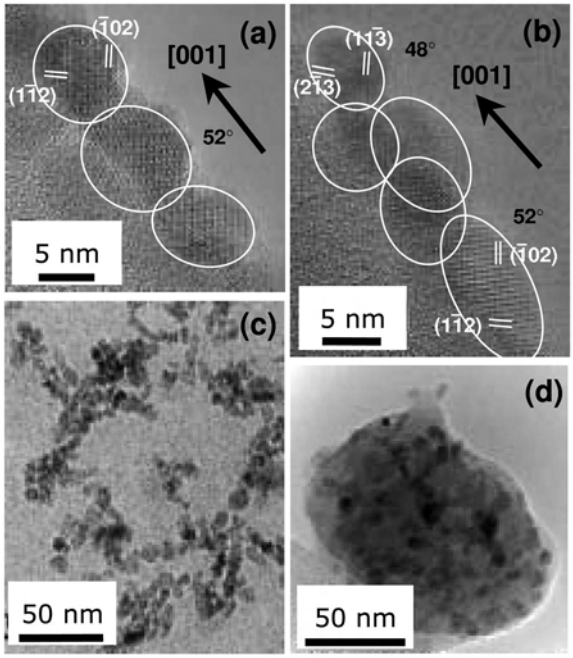

FIG. 1. Transmission electron microscopy images of α-Fe_2O_3 nanoparticles. (a), (b) HREM images showing that the particles are attached to one another along their common [001] axis. The arrows and angles indicate the direction of the [001] axis of the particles relative to the plane of the paper. The arrows point into the paper. (c) Cryo-TEM image of a frozen aqueous suspension of the particles. (d) Electron micrograph of the separated α-Fe_2O_3 particles (dark spots) after grinding with amorphous SiO_2 particles (the gray matrix of the composite).

(001) were not parallel for the first and the last particles in a chain [Fig. 1(b)], indicating that defects or polytypic stacking in principle could be incorporated by the attachment of the particles as suggested in Ref. 11. In general, polytypic stacking is difficult to observe by electron microscopy because the lattice planes of neighboring particles will only rarely be oriented parallel to the beam. Electron micrographs of a frozen aqueous suspension (cryo-TEM) show that the oriented particle arrangement is not induced by the substrate since the chain formation also is prevalent in suspension [Fig. 1(c)]. The TEM image, Fig. 1(d), shows that the α-Fe_2O_3 particles are rather well separated after grinding with amorphous silica.

B. X-ray diffraction

A quantitative measure of the correlation lengths associated with the attached particles can be obtained from diffraction data because the correlation lengths can be assumed to be inversely proportional to the broadening of the diffraction lines.[29] Figure 2(a) shows high-energy synchrotron x-ray diffraction data for the as-prepared sample. Most of the observed peaks correspond to the reflections expected for α-Fe_2O_3, but they are considerably broadened. Two narrow and resolution-limited peaks are the (200) aluminium reflection at 3.096 $Å^{-1}$ and a weak spurious peak of unidentified origin at 1.513 $Å^{-1}$. The observed Bragg peaks in the high-energy

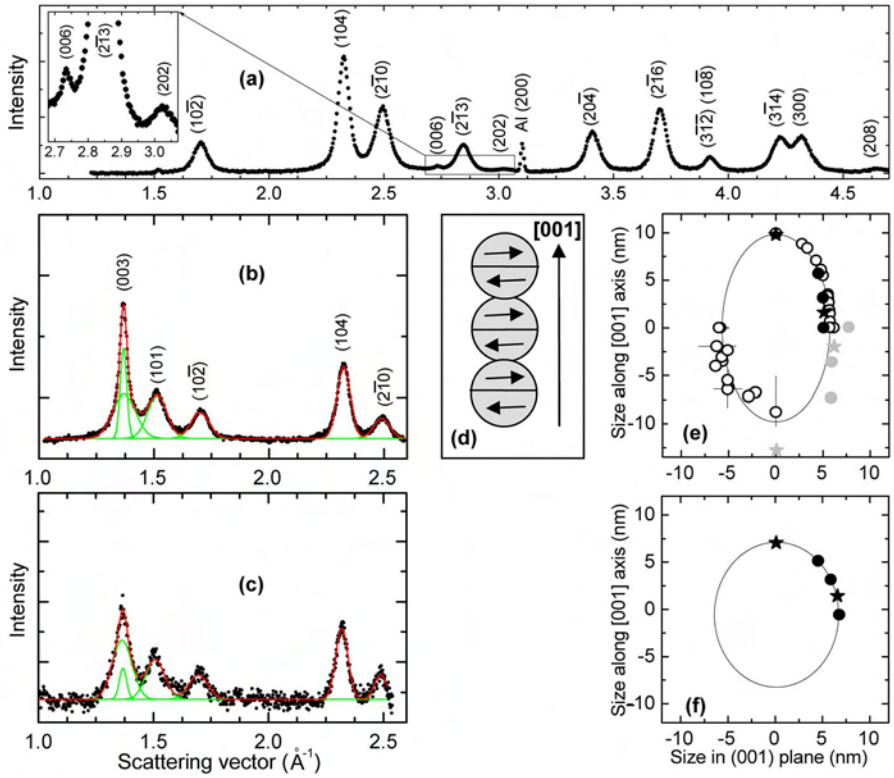

FIG. 2. (Color online) Diffraction data (background subtracted) of α-Fe_2O_3 particles obtained at room temperature. (a) HES-XRD data of the as-prepared nanoparticles. (b) NPD data of the same sample as in (a). (c) NPD data of the α-Fe_2O_3 sample after grinding. In (b) and (c), the solid lines represent the fits with Gaussian shaped peak profiles to the data (green denotes individual peaks, red the sum of peaks). (d) Schematic illustration of the antiferromagnetic correlation across the particle interfaces in the as-prepared sample. (e) Correlation lengths obtained for the as-prepared sample from HES-XRD (open dots) and NPD (filled dots) data by Fullprof fitting (first quadrant), and by fitting with pseudo-Voigt (third quadrant) and Gaussian (fourth quadrant, gray) peak profiles. Stars denote magnetic reflections. (f) Correlation lengths from Fullprof fitting for the ground sample, based on NPD data. The ellipses in (e) and (f) are guides to the eye obtained from the Fullprof fit.

synchrotron x-ray data were fitted to Gaussian shaped peak profiles. The crystalline correlation length, estimated from the FWHM of the α-Fe_2O_3 reflections as $2\pi/(\mathrm{FWHM}^2\text{-}B_{i,XRD}{}^2)^{1/2}$, was found to be typically about 7–8 nm. This correlation length is similar to the average particle size found by HREM. The (006) reflection is narrower and the correlation length was found to be longest along [001], indicating that the crystalline correlation exceeds the particle size in that direction. However, since the (006) peak is weak and partly overlapping with the much more intense $(2\bar{1}3)$ reflection, the estimated width of the (006) reflection depends on the choice of peak profile and the background estimate. Therefore, the correlation length in the [001] direction as determined from the (006) reflection is only indicative of extended particle alignment in the [001] direction.

C. Neutron diffraction

While x-ray diffraction provides information solely about the crystalline structure, neutron diffraction also reveals magnetic correlations. Figures 2(b) and 2(c) show neutron powder diffraction data for the as-prepared and the ground samples, respectively. These patterns also show broadened Bragg reflections when compared to the resolution-limited Gaussian diffraction peaks from a powder sample of α-Fe_2O_3 with grain size in the micrometer range.

The (003) and (101) reflections are purely magnetic; the remaining reflections are structural. In the spectrum of the as-prepared sample, most of the diffraction peaks have widths in accordance with the correlation length derived from the x-ray data. However, it is noticeable that the antiferromagnetic (003) reflection is considerably narrower than other reflections. This shows directly that the crystallographic alignment along [001] is accompanied by a similar magnetic correlation in that direction. The strong magnetic (003) reflection, which allows for a more detailed analysis than the weak structural (006) reflection, can be modeled by two Gaussian shaped contributions. After correction for the experimental resolution, one of these has a width corresponding to the average particle size, while the other, which covers ~36% of the total (003) reflection area, has a width corresponding to 22 nm. This suggests that on average about one-third of the particles have magnetic correlations extending over about three particle diameters along the [001] direction as illustrated schematically in Fig. 2(d).

The neutron diffraction data of the ground sample (after subtracting the contribution of the ground SiO_2 particles),

displayed in Fig. 2(c), show that after grinding, all reflections have widths almost corresponding to the size of the individual nanoparticles with nearly spherical shape. Thus the grinding has to a large extent destroyed the magnetic and structural correlation of neighboring particles without reducing the particle size. A double peak analysis of the ground sample results in a small narrow contribution to the (003) reflection, indicating that some of the particles may remain aligned after grinding.

A traditional way of analyzing powder diffraction data is by profile refinement. Therefore, in addition to modeling the data according to the description illustrated in Fig. 2(d), we have also analyzed the x-ray and neutron diffraction data by means of the refinement program FULLPROF,[30] which has the possibility to include anisotropic size broadening of the observed diffraction peaks. The analysis was based on the assumption that the chains of attached particles could be described as ellipsoidal-shaped particles. For the as-prepared sample this analysis showed average correlation lengths of ~10 nm and ~6 nm parallel and perpendicular to the [001] direction, respectively. The average correlation length in the [001] direction agrees within experimental accuracy with the average correlation length of ~13 nm estimated from the double peak analysis of the (003) reflection of the as-prepared sample. In contrast, the ground sample showed average correlation lengths of ~7 nm both parallel and perpendicular to the [001] direction. Hence, the FULLPROF analysis supports the conclusion of particle alignment along the [001] direction in the as-prepared sample.

FULLPROF fitting includes shape constraints as well as crystallographic constraints obtained for bulk materials, which determine the intensities, and which may not adapt to nanoparticles. Therefore, we have also fitted the diffraction peaks with pseudo-Voigt profiles without such constraints. This resulted in correlation lengths, which within the error bars are identical to those obtained from FULLPROF fitting.

Figures 2(e) and 2(f) show the correlations lengths for the different crystallographic directions obtained from the different types of fits of the as-prepared sample and the ground sample, respectively. For the as-prepared sample, all fits show that the correlation is longest along the [001] direction, while for the ground sample the correlation lengths are almost identical in all crystallographic directions. The directions closest to the [001] direction in the as-prepared sample have longer correlation lengths than those within the [001] plane. This supports the theory that the attachment of the particles is primarily epitaxial. In the case of polytypic particle arrangement along the [001] axis, only the [001] correlation length would be long and, e.g., the [104] correlation length would be similar to the in-plane correlation length, but this is not found. It is possible that during the epitaxial attachment of the particles the order of the six Fe-layers in the unit cell is not continued across the grain boundaries [this is equivalent to formation of stacking faults or twinning of (001) planes at the interfaces]. However, the data do not allow for a quantitative analysis of how prevalent such stacking might be.

Strain may, like nanocrystallinity, lead to broadening of the diffraction peaks. The diffraction data in Fig. 2 have only a couple of reflections belonging to the same directions in the crystal structure; therefore, we were not able to perform a full Williamson-Hall analysis of the strain in the various directions. However, the available data as well as previous studies of α-Fe_2O_3 nanoparticles prepared by the same technique[26,31] showed no significant influence of strain on the line broadening.

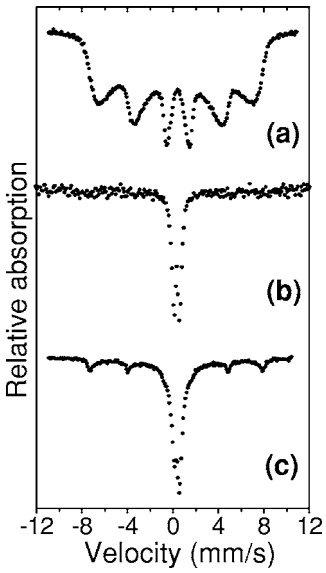

FIG. 3. Mössbauer spectra of α-Fe_2O_3 nanoparticles. (a) The as-prepared sample measured at ambient temperature. (b) The ground sample at ambient temperature. (c) The ground sample at 80 K.

The observation that both structural and magnetic correlations exceed the particle size in the [001] direction indicates that the distance between the (001) layers is the same across the interface as inside the particles. The constant separation of the (001) layers across the interface indicates that the surface layer of water or hydroxyl groups, which typically are adsorbed to nanoparticles, is expelled from the interface. The attachment of particles, with interfaces having more or less the same structure and chemical bonds as inside the crystals, is expected to result in relatively strong mechanical coupling between the particles.

The magnetic correlation along [001] shows that the alternating magnetization directions of the (001) layers of the particles are continued across the particle interfaces as illustrated in Fig. 2(d). The sublattice magnetization directions are arranged within the (001) planes such that the antiferromagnetic order is continued across the interface. The correlation implies that the exchange coupling exists across the interfaces and is similar to the exchange coupling between the Fe-layers within the particles. This is direct evidence of strong exchange coupling between particles.

D. Mössbauer spectroscopy

By use of Mössbauer spectroscopy we have studied the influence of sample treatments on interactions via studies of the superparamagnetic relaxation of the particles. The Mössbauer spectrum of the as-prepared sample, obtained at room temperature [Fig. 3(a)], consists of a sextet with broadened

lines, typical for samples of interacting nanoparticles.[7,9,32] There is no fast superparamagnetic relaxation in this sample, as indicated from the absence of a central doublet. After grinding the as-prepared sample, the room temperature spectrum, shown in Fig. 3(b), contains only a doublet. This indicates that all the particles now have fast superparamagnetic relaxation at this temperature. The doublet dominates down to at least 80 K [Fig. 3(c)]. The superparamagnetic blocking temperature was found to be about 50 K. This shows that the grinding has led to a significant reduction of the interactions such that the ground particles exhibit fast superparamagnetic relaxation in accordance with previous studies of the influence of grinding of interacting nanoparticles.[31]

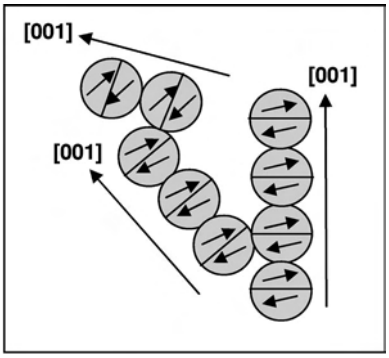

FIG. 4. Illustration of network of interacting α-Fe_2O_3 nanoparticles showing suppressed superparamagnetic relaxation at room temperature.

IV. DISCUSSION

Our results from electron microscopy and diffraction measurements show that on average a third of the particles in the as-prepared sample are attached into chains of three particles along a common [001] axis such that there is both structural and magnetic correlation in that direction. Gentle grinding can lead to separation of particles and reduce the correlation along [001]. Mössbauer studies show that superparamagnetic relaxation is suppressed even at room temperature in the as-prepared sample, but separation of particles by grinding leads to fast superparamagnetic relaxation.

Previous studies have shown that the only possible explanation for the strong suppression of superparamagnetic relaxation in the samples of agglomerated α-Fe_2O_3 nanoparticles is interparticle exchange interaction.[7,9] The magnetic correlation extending over several particles found in the present work is, however, a direct observation of exchange coupling existing between the particles.

In order to fully explain the suppression of superparamagnetic relaxation observed even at room temperature for all particles in the as-prepared sample, it is insufficient to consider solely interparticle exchange coupling for the fraction of the particles aligned into chains of about three particles. This would at maximum raise the blocking temperature by a factor of about 3 for about a third of the particles. Recent studies show that α-Fe_2O_3 nanoparticles may also agglomerate in a more random fashion during drying, i.e., with nonparallel [001] axes, but exchange coupling still exists across the interfaces [seen as a slight rotation of the sublattice magnetization out of the (001) plane],[33] although the coupling between particles with nonparallel [001] axes is likely to be weaker than between particles with parallel [001] axes.

The strong suppression of superparamagnetic relaxation in samples of agglomerated particles therefore seems to be due to the existence of larger networks of interacting particles with both parallel and nonparallel [001] axes. Figure 4 shows a schematic illustration of such a network. Here the particles are attached into small chains with parallel [001] axes, but the neighboring chains or particles have different orientations of their [001] axes. The picture of the magnetic structure and dynamics of particles as being governed by a network of exchange coupled, aligned and nonaligned particles is in good agreement with the model proposed in Ref. 7. In this model, it was assumed, in order to explain Mössbauer data of interacting 20 nm α-Fe_2O_3 particles, that the easy axes of the particles were parallel to the effective exchange field. This described most of the features well. Other features, which this model could not describe, were ascribed to interacting particles with nonparallel easy axes. Here we have obtained more direct observations of the arrangement and magnetic coupling of the particles assumed by the model.

It is interesting that oriented attachment is achieved between antiferromagnetic nanoparticles of α-Fe_2O_3 when prepared by wet chemistry or when dried from aqueous suspensions. Until recently, the general understanding was that crystals grow by addition of ions, but studies of TiO_2 and iron oxyhydroxides have lately revealed that crystals can also grow by oriented attachment of nanoparticles.[11–14] Particles in suspension may be brought together by Brownian motion, whereupon strong short-range forces cause the attachment. It has been suggested that reduction of surface energy of nanoparticles is the driving mechanism for this type of crystal growth.[11–14] The oriented attachment of the α-Fe_2O_3 nanoparticles with parallel [001] directions is surprising because the particles are nominally equidimensional[34] and the (001) planes of α-Fe_2O_3 are generally considered to be the planes of low surface energy. Calculations have shown that the (001) surface energy of α-Fe_2O_3 takes values between 0.75 and 1.65 J/m^2 depending on the environment.[35,36] Hydration as well as oxygen vs iron termination can significantly alter the surface energies.[35,36] Since α-Fe_2O_3 is magnetic and since we observe exchange coupling between agglomerated particles, it is worth considering if exchange interaction between particles can affect the attachment. As an example, we look at the interactions at the (001) interface. Magnetic coupling mechanisms would make it favorable for the particles to attach with parallel (001) planes: the superexchange coupling across the oxygen-layers is dominant compared to in-plane exchange interaction,[22] and the (001) plane is the plane where all spins are parallel so that coupling of two (001) planes will lead to least spin frustration. We find the exchange interaction between (001) planes to be 0.2 J/m^2 by using that the density of Fe-atoms in the (001) plane is one Fe per 11×10^{-20} m^2 and the exchange energy density is 2×10^{-20} J per Fe-atom (the energy density is calculated from the experimentally found ex-

change coupling constants, J_3 and J_4, of Ref. 37; an overview of the different types of exchange couplings within α-Fe_2O_3 is found in Ref. 22). Since the exchange energy is comparable in size, although smaller, to the surface energy, the contribution from the exchange energy may thus be considered an extra driving force for the oriented attachment. Exchange interactions between particles with non-parallel (001) planes may lead to magnetic frustration, which could result in repulsive forces.

V. CONCLUSIONS

The present study shows that α-Fe_2O_3 nanoparticles may show oriented attachment such that both the crystallographic and the magnetic correlations continue across the interfaces. The nanoscale coupling between particles is found to be sensitive to macroscopic handling such as gentle grinding. The observed alignment of α-Fe_2O_3 nanoparticles along a common [001] axis can in part explain the strong exchange coupling between agglomerated α-Fe_2O_3 particles, observed by Mössbauer spectroscopy as a suppression of the superparamagnetic relaxation. A complete description of the magnetic properties of the agglomerated particles can be obtained by also taking into account exchange coupling between particles with nonparallel [001] axes. It is possible that exchange coupling between nanoparticles plays a driving role for the arrangement of the particles. Studies of the mechanisms of exchange coupling and oriented attachment between nanoparticles are important for the understanding of crystal growth, and for the magnetic and the mechanical properties of, e.g., sediments formed under different conditions in nature, as well as for designing exchange coupled nanocrystalline magnetic materials and nanoscale devices.

ACKNOWLEDGMENTS

We thank Haldor Topsøe A/S, Kgs. Lyngby, Denmark, for the use of their cryo-TEM equipment. We acknowledge beam time allocation at Swiss Spallation Neutron Source, Paul Scherrer Institute SINQ, Villigen, Switzerland, and at Hamburger Synchrotronstrahlungslabor HASYLAB at Deutsches Elektronen-Synchrotron DESY, D-22603 Hamburg, Germany. The work was supported by the Danish Technical Research Council through the nanomagnetism framework programme and the Danish Natural Science Research Council through DANSCATT and Dansync.

[1] J. Zhang, C. Boyd, and W. Luo, Phys. Rev. Lett. **77**, 390 (1996).
[2] C. Djurberg, P. Svedlindh, P. Nordblad, M. F. Hansen, F. Bødker, and S. Mørup, Phys. Rev. Lett. **79**, 5154 (1997).
[3] H. Mamiya, I. Nakatani, and T. Furubayashi, Phys. Rev. Lett. **80**, 177 (1998).
[4] D. Fiorani, J. L. Dormann, R. Cherkaoui, E. Tronc, F. Lucari, F. D'Orazio, L. Spinu, M. Nogues, A. Garcia, and A. M. Testa, J. Magn. Magn. Mater. **196-197**, 143 (1999).
[5] T. Jonsson, P. Svedlindh, and M. F. Hansen, Phys. Rev. Lett. **81**, 3976 (1998).
[6] Y. Sun, M. B. Salamon, K. Garnier, and R. S. Averback, Phys. Rev. Lett. **91**, 167206 (2003).
[7] M. F. Hansen, C. B. Koch, and S. Mørup, Phys. Rev. B **62**, 1124 (2000).
[8] F. Bødker, M. F. Hansen, C. B. Koch, and S. Mørup, J. Magn. Magn. Mater. **221**, 32 (2000).
[9] C. Frandsen and S. Mørup, J. Magn. Magn. Mater. **266**, 36 (2003).
[10] V. Skumryev, S. Stoyanov, Y. Zhang, G. Hadjipanayis, D. Givord, and J. Noqués, Nature (London) **423**, 850 (2003).
[11] R. Lee Penn and J. F. Banfield, Science **281**, 969 (1998).
[12] R. Lee Penn and J. F. Banfield, Geochim. Cosmochim. Acta **63**, 1549 (1999).
[13] J. F. Banfield, S. A. Welch, H. Zhang, T. T. Ebert, and R. Lee Penn, Science **289**, 751 (2000).
[14] M. Nesterova, J. Moreau, and J. F. Banfield, Geochim. Cosmochim. Acta **67**, 1177 (2003).
[15] P. M. Mendes, Y. Chen, R. E. Palmer, K. Nikitin, D. Fitzmaurice, and J. A. Preece, J. Phys.: Condens. Matter **15**, S3047 (2003).
[16] K. Butter, P. H. H. Bomans, P. M. Frederik, G. J. Vroege, and A. P. Philipse, Nat. Mater. **2**, 88 (2003).
[17] Y. Lalatonne, J. Richardi, and M. P. Pileni, Nat. Mater. **3**, 121 (2004).
[18] A. Ghazali and J.-C. Lévy, Phys. Rev. B **67**, 064409 (2003).
[19] V. F. Puntes, K. M. Krishnan, and A. P. Alivisatos, Science **291**, 2115 (2001).
[20] V. F. Puntes, P. Gorostiza, D. M. Aruguete, N. G. Bastus, and A. P. Alivisatos, Nat. Mater. **3**, 263 (2004).
[21] H. Zeng, J. Li, Z. L. Wang, and S. Sun, Nature **420**, 395 (2002).
[22] A. H. Morrish, *Canted Antiferromagnetism: Hematite* (World Scientific, Singapore, 1994).
[23] P. R. Christensen, J. L. Bandfield, R. N. Clark, K. S. Edgett, V. E. Hamilton, T. Hoefen, H. H. Kieffer, R. O. Kuzmin, M. D. Lane, M. C. Malin, R. V. Morris, J. C. Pearl, R. Pearson, T. L. Roush, S. W. Ruff, and M. D. Smith, J. Geophys. Res., [Planets] **105**, 9623 (2000); R. V. Morris, G. Klingelhöfer, B. Bernhardt, C. Schröder, D. S. Rodionov, P. A. de Souza, A. Yen, R. Gellert, E. N. Evlanov, J. Foh, E. Kankeleit, P. Gütlich, D. W. Ming, F. Renz, T. Wdowiak, S. W. Squyres, and R. E. Arvidson, Science **305**, 833 (2004); G. Klingelhöfer, R. V. Morris, B. Bernhardt, C. Schröder, D. S. Rodionov, P. A. de Souza, A. Yen, R. Gellert, E. N. Evlanov, B. Zubkov, J. Foh, U. Bonnes, E. Kankeleit, P. Gütlich, D. W. Ming, F. Renz, T. Wdowiak, S. W. Squyres, and R. E. Arvidson, *ibid.* **306**, 1740 (2004).
[24] C. G. Shull, W. A. Stauser, and E. O. Wollan, Phys. Rev. **83**, 333 (1951).
[25] W. Kündig, H. Bömmel, G. Constabaris, and R. H. Lindquist, Phys. Rev. **142**, 327 (1966).
[26] F. Bødker and S. Mørup, Europhys. Lett. **52**, 217 (2000).
[27] F. Bødker, M. F. Hansen, C. B. Koch, K. Lefmann, and S. Mørup, Phys. Rev. B **61**, 6826 (2000).
[28] T. Sugimoto, Y. Wang, H. Itoh, and A. Muramatsu, Colloids Surf., A **134**, 265 (1998).
[29] B. E. Warren, *X-ray Diffraction* (Dover, New York, 1990).

[30] J. Rodriguez-Carvajal, Physica B **192**, 55 (1993).
[31] M. Xu, C. R. H. Bahl, C. Frandsen, and S. Mørup, J. Colloid Interface Sci. **279**, 132 (2004).
[32] S. Mørup, C. Frandsen, F. Bødker, S. N. Klausen, K. Lefmann, P.-A. Lindgård, and M. F. Hansen, Hyperfine Interact. **144/145**, 347 (2002).
[33] C. Frandsen and S. Mørup, Phys. Rev. Lett. **94**, 027202 (2005).
[34] R. Lee Penn, G. Oskam, T. J. Strathmann, P. C. Searson, A. T. Stone, and D. R. Veblen, J. Phys. Chem. B **105**, 2177 (2001).
[35] F. Jones, A. L. Rohl, J. B. Farrow, and W. van Bronswijk, Phys. Chem. Chem. Phys. **2**, 3209 (2000).
[36] X.-G. Wang, W. Weiss, S. K. Shaikhutdinov, M. Ritter, M. Petersen, F. Wagner, R. Schlögl, and M. Scheffler, Phys. Rev. Lett. **81**, 1038 (1998).
[37] E. J. Samuelsen and G. Shirane, Phys. Status Solidi **42**, 241 (1970).

Paper VII

Neutron study of magnetic excitations in 8-nm α-Fe_2O_3 nanoparticles

L. Theil Kuhn,* K. Lefmann, C. R. H. Bahl,[†,‡] S. Nyborg Ancona,[§] and P.-A. Lindgård
Materials Research Department, AFM-228, Risø National Laboratory, DK-4000 Roskilde, Denmark

C. Frandsen, D. E. Madsen, and S. Mørup
Department of Physics, Building 307, Technical University of Denmark, DK-2800 Kongens Lyngby, Denmark
(Received 9 June 2006; revised manuscript received 11 September 2006; published 3 November 2006)

By use of inelastic neutron scattering we have studied magnetic fluctuations in 8-nm particles of antiferromagnetic α-Fe_2O_3 (hematite) as a function of temperature and applied magnetic fields. The fluctuations are dominated by uniform excitations. Studies have been performed on both coated (noninteracting) and uncoated (interacting) particles. We have estimated the magnetic anisotropy energy and found that the data are in good agreement with the value obtained from Mössbauer spectroscopy. The energy ε_0 of the uniform excitations depends strongly on the uncompensated moment, which is caused by finite-size effects, and we have estimated the size of this moment from the experimental neutron data. The field dependence of ε_0 for the interacting nanoparticles differs strongly from that of the noninteracting nanoparticles, and this is a result of the influence of exchange interaction between the particles.

DOI: 10.1103/PhysRevB.74.184406 PACS number(s): 75.50.Tt, 75.30.Ds, 75.30.Gw, 25.40.Fq

I. INTRODUCTION

Materials composed of nanoscale magnetic grains are becoming important in technological applications, since they provide the possibility of designing materials with new magnetic properties. This is indeed true for magnetic nanoparticles used in, for example, ferrofluids, biomedicine, hard permanent magnets and magnetic recording media.[1,2] Understanding the fundamental properties of the grains and the influence of magnetic interactions is therefore of great importance.

The magnetic anisotropy of a single nanoparticle is in the first approximation assumed to be uniaxial with the anisotropy energy given by

$$E(\theta) = KV \sin^2 \theta, \tag{1}$$

where K is the magnetic anisotropy constant, V is the particle volume, and θ is the angle between the (sublattice) magnetization and an easy direction of magnetization. KV is the energy barrier that separates the two minima at $\theta=0$ and $\theta=\pi$. If the thermal energy is comparable to KV, superparamagnetic relaxation takes place, i.e., the magnetization vector fluctuates between the easy directions of magnetization.[3] At lower temperatures the magnetization vector fluctuates in directions close to one of the easy axes, i.e., performs collective magnetic excitations.[4,5] These magnetic fluctuations can be described as a uniform precession (a spin wave with wave vector $q=0$) of the magnetization vector around an easy direction of magnetization in combination with transitions between these precession states. Due to finite-size quantization there is a large energy gap in the spin wave spectrum to the spin waves with $q \neq 0$. The spin wave spectrum is discrete[6,7] and excitations of the uniform ($q=0$) mode are therefore predominant.[8]

Interactions between magnetic nanoparticles can have a strong influence on the magnetic properties. For ferromagnetic and ferrimagnetic nanoparticles, the interparticle dipole interaction can have a significant influence on the superparamagnetic relaxation time, see, e.g., Refs. 9–16. Nanoparticles of antiferromagnetic materials have recently attracted much attention because their properties in several ways differ from those of the bulk materials. They have a nonzero magnetic moment, which has been attributed to uncompensated spins,[17,18] but recently it was suggested that it also can have a contribution from so-called thermoinduced magnetization.[19] An anomalous temperature dependence of the magnetic moments, which has been observed in several studies[20–23] seems to support this, but may also be explained by shortcomings in the analysis of magnetization data for antiferromagnetic nanoparticles.[24] Macroscopic quantum tunneling of the magnetization, which is characterized by a temperature-independent relaxation, is expected to be more pronounced in antiferromagnetic nanoparticles than in ferromagnetic and ferrimagnetic nanoparticles.[25] Such a temperature-independent relaxation has been observed in low-temperature studies of, for example, ferritin[26,27] and α-Fe_2O_3 nanoparticles.[28] Other studies have shown that the magnetic structure of, for example NiO nanoparticles may differ from the bulk magnetic structure.[29] In α-Fe_2O_3 nanoparticles, the Morin transition is suppressed[30,31] and the spin-flop field decreases with decreasing particle size.[32] In samples of antiferromagnetic nanoparticles the interparticle dipole interactions are negligible, because the magnetic moments of the particles are small,[33] but the exchange coupling between surface atoms of nanoparticles in close contact may be a prominent source of interaction effects.[5,33–37]

In an atomic scale model for the interaction, we assume that the particles are magnetically coupled via exchange interaction between pairs of surface ions. The magnetic interaction energy of a particle p with surface spins $\mathbf{S}_i^p$ may be written

$$E_{\mathrm{ex}} = -\sum_i \mathbf{S}_i^p \cdot \sum_q \sum_j J_{ij}^q \mathbf{S}_j^q, \tag{2}$$

where $\mathbf{S}_j^q$ are the surface spins of the neighboring particles q and J_{ij}^q is the exchange coupling constant related to the inter-

action between the surface ions i of the particle p and the surface ions j of the neighboring particles q. Neglecting surface spin canting, we may write

$$\sum_j J_{ij}^q \mathbf{S}_j^q = A_q \mathbf{M}_q, \tag{3}$$

where $\mathbf{M}_q$ is the (sublattice) magnetization of the particle q and A_q is an effective interaction constant. Because $\Sigma_i \mathbf{S}_i^p$ is proportional to the (sublattice) magnetization $\mathbf{M}_p$ of the particle p, the total energy density may be written[5,33–36]

$$E_i = K_i \sin^2 \theta_i - \mathbf{M}_p \cdot \sum_q J_{pq} \mathbf{M}_q, \tag{4}$$

where J_{pq} is an effective exchange coupling constant.

If the first term in Eq. (4) is predominant, superparamagnetic relaxation of the individual nanoparticle may take place between the easy directions close to $\theta=0$ and $\theta=\pi$. However, if the interactions are significant, the energy at the two minima will differ and the populations will therefore differ. At finite temperatures, the (sublattice) magnetization may then mainly fluctuate around the direction corresponding to the lower energy minimum. The magnetic properties of interacting particles have been calculated by use of a simple mean field model in which the summation in the second term in Eq. (4) is replaced by an average value, which may be considered as an effective interaction field.[33–36]

Interaction effects in samples of magnetic nanoparticles have mainly been studied by ac and dc magnetization measurements and by Mössbauer spectroscopy, which together cover about 10 decades of relaxation times down to $\approx 10^{-10}$ s. It has been demonstrated that inelastic neutron scattering also is a very useful method for investigating spin dynamics in magnetic nanomaterials because the time scale of this technique expands the observable time range down to 10^{-14} s.[7,38–43] In the inelastic neutron scattering experiments the energy distribution of the neutrons, which are scattered at momentum transfer corresponding to an antiferromagnetic reflection, is measured. The neutrons can excite or de-excite a $q=0$ spin wave and thereby spin excitations can be probed.

In this paper we present the results of an inelastic neutron scattering study of coated and uncoated nanoparticles of α-Fe_2O_3 with a mean size of 8 nm. We assume that the coated nanoparticles can be treated as individual, noninteracting, particles, whereas the uncoated nanoparticles interact via exchange interactions within agglomerates. The study shows that interparticle exchange interactions between the α-Fe_2O_3 nanoparticles can have a strong effect on collective magnetic excitations. We compare the results with data obtained by Mössbauer spectroscopy on the same nanoparticle samples.

II. SPIN DYNAMICS IN HEMATITE NANOPARTICLES

α-Fe_2O_3 has the corundum crystal structure, and we describe the structure using the hexagonal unit cell. α-Fe_2O_3 nanoparticles smaller than about 20 nm in diameter are canted antiferromagnets with the spins in the (001) plane at least down to 5 K.[31] In bulk, the canting angle is approximately 0.07° and the out-of plane magnetocrystalline anisotropy is considerably larger than the in-plane anisotropy.[44] The Néel temperature of bulk α-Fe_2O_3 is $T_N=955$ K.[44] In nanoparticles, the in-plane anisotropy is larger than in bulk and may become comparable to the out-of-plane anisotropy.[7,31] Here, we will for simplicity assume that the magnetic anisotropy in α-Fe_2O_3 nanoparticles can be described as an effective uniaxial anisotropy [Eq. (1)] with anisotropy constant K_{eff}.

In noninteracting α-Fe_2O_3 nanoparticles, the amplitude of the uniform magnetic precession mode with lowest energy lies predominantly in the (001) plane,[39,43] while the second precession mode at higher excitation energy is predominantly perpendicular to the (001) plane.[7] Applied magnetic fields increase the excitation energy and hence suppress the amplitude of collective magnetic excitations. A quantum mechanical description of the details of the relaxation and precession modes can be found in Ref. 45.

In studies of magnetic nanoparticles using inelastic neutron scattering it has been found that superparamagnetic relaxation gives rise to an energy broadening of Lorentzian line shape of the magnetic Bragg reflections.[39,41,43] In the following, this will be termed the quasielastic signal. In inelastic scattering processes, the energy of the scattered neutrons can be changed by an amount ε_0 corresponding to the energy difference between two neighboring uniform precession states.[39–42] This gives rise to inelastic peaks at neutron energy transfers $\pm\varepsilon_0$. In 8-nm α-Fe_2O_3 nanoparticles, the lowest spin wave excitation with $q\neq 0$ has an energy larger than 10 meV and the antiphase $q=0$ excitation also has high energy.[6,7] Therefore, these transitions were not probed in the present measurements where only neutrons with energy transfer lower than 5 meV were detected.

The broadening of the quasielastic Lorentzian line shape due to superparamagnetic relaxation is given by[39]

$$I(\varepsilon) = D(\varepsilon) \frac{A_{\text{Bragg}}}{\pi} \frac{\Gamma}{\Gamma^2 + \varepsilon^2}, \tag{5}$$

where $D(\varepsilon)=\frac{\varepsilon}{k_b T}\left(\frac{1}{\exp(\varepsilon/k_B T)-1}+1\right)$ is the detailed balance factor, A_{Bragg} is the integrated intensity (area) of the quasielastic peak coming from the semistatic arrangement of spins, Γ is the half width at half maximum (HWHM) and is related to the lifetime of the superparamagnetic relaxation by $\Gamma=\hbar/\tau$.[41]

In previous inelastic neutron studies we have found that the damped harmonic oscillator model gives a good description of the collective magnetic excitations in both antiferromagnetic[7,39,40,43] and in ferrimagnetic nanoparticles.[42] Therefore, we will in this data analysis also apply the damped harmonic oscillator model given by[39,41,43]

$$I(\varepsilon) = D(\varepsilon) \frac{A_{\text{CME}}}{\pi} \frac{2\gamma\varepsilon_0^2}{(\varepsilon^2 - \varepsilon_0^2)^2 + 4\gamma^2\varepsilon^2}. \tag{6}$$

A_{CME} is the integrated intensity (area) of the peaks, γ is the width (HWHM) of the inelastic peaks and ε_0 is the energy difference between the precession modes. At low temperatures ($k_B T \ll K_{\text{eff}} V$) ε_0 can be approximated by[39]

$$\varepsilon_0 \approx g\mu_B\sqrt{2B_AB_E}. \quad (7)$$

$g=2$ is the g factor, μ_B is the Bohr-magneton, $B_E=900$ T is the exchange field, and B_A is the anisotropy field $B_A=K_{\text{eff}}/M_s$, where $M_s=9\times10^5$ A m^{-1} is the sublattice saturation magnetization of bulk α-Fe_2O_3.[44] The value of K_{eff} can be estimated from experimental neutron data.[7,39,41,43]

If the particles are exposed to a magnetic field, B_{appl}, which is large compared to the effective anisotropy field, the energy difference is given by[39]

$$\varepsilon_0 \approx g\mu_B B_{\text{appl}}. \quad (8)$$

In this work we analyze the data from interacting particles by use of the simple model outlined in Sec. I [Eq. (4)], where the influence of interactions is described by an effective interaction field.

The relative area of the inelastic peaks in neutron scattering experiments compared to the total magnetic scattering, also gives information on the magnetic fluctuations. For noninteracting particles with magnetic energy given by Eq. (1) the temperature dependence at low temperatures ($k_BT \ll K_{\text{eff}}V$) is given by[39,43]

$$\frac{A_{\text{CME}}}{A_{\text{Bragg}}+A_{\text{CME}}} = \langle \sin^2\theta \rangle \approx \frac{k_BT}{K_{\text{eff}}V}. \quad (9)$$

In Mössbauer spectroscopy, fast superparamagnetic relaxation results in a collapse of the magnetic hyperfine splitting, and at low temperatures ($k_BT \ll K_{\text{eff}}V$) collective magnetic excitations give rise to a reduction of the observed magnetic hyperfine field B_{obs} given by[4,5]

$$B_{\text{obs}} = B_0\langle \cos\theta \rangle \approx B_0\left(1-\frac{k_BT}{2K_{\text{eff}}V}\right), \quad (10)$$

where B_0 is the magnetic hyperfine field that would be measured in the absence of relaxation phenomena. For strongly interacting magnetic nanoparticles, Eq. (10) may be replaced by[5,33–35]

$$\langle B_{\text{obs}} \rangle \approx B_0\left(1-\frac{k_BT}{2K_{\text{eff}}V+E_{\text{int}}}\right), \quad (11)$$

where E_{int} is related to the strength of the interactions.

III. EXPERIMENTAL METHODS

The α-Fe_2O_3 nanoparticles were prepared by means of a gel-sol method similar to that developed by Sugimoto *et al.*[46] The particles resemble those described in Refs. 36, 37, 47, and 48. Part of the batch was treated with phosphate to produce a sample of particles coated with a layer of nonmagnetic material in order to minimize interparticle interactions.[42,50] For simplicity, the particles in this sample are in the following referred to as the noninteracting particles. Another part of the batch was uncoated and dried such that the particles in this sample were in direct contact. These are referred to as the interacting particles.

Transmission electron microscopy (TEM) images were obtained using a JEOL 3000F microscope, equipped with a Gatan MSC CCD-camera. TEM images are shown in Fig. 1. The particles of both samples are seen to be round with a good crystallinity. The phosphate coating is seen as an amorphous layer around the crystalline particles in Fig. 1(a). The average particle size is approximately 8 nm in accordance with x-ray and neutron powder diffraction data,[47] which also established that each particle consists of a single magnetic domain. In addition, neutron diffraction data confirmed the magnetic Bragg reflections at the scattering vectors $Q=1.37$ and 1.51 Å^{-1} corresponding to the purely antiferromagnetic (003) and (101) reflections, respectively. These data also showed that the nanoparticles are above the Morin transition in the entire measured temperature regime.

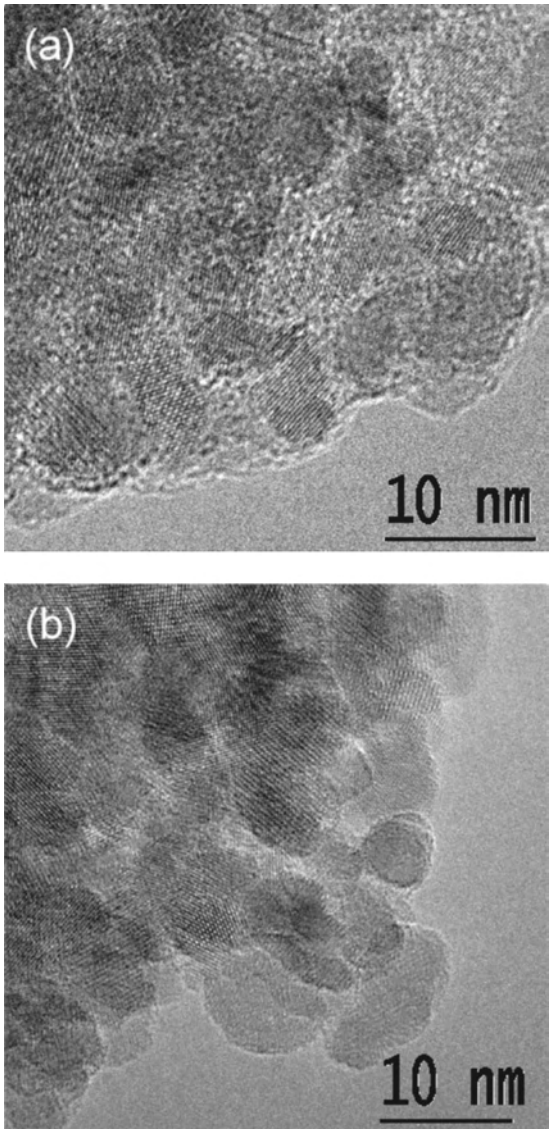

FIG. 1. TEM images of the 8-nm α-Fe_2O_3 nanoparticles. (a) The noninteracting (coated) particles and (b) the interacting (noncoated) particles. The coating is seen as an amorphous layer around the particles.

The Mössbauer spectra were obtained using constant-acceleration spectrometers with sources of ^{57}Co in rhodium. Spectra in the temperature range 18–300 K were obtained using a closed cycle helium refrigerator. Spectra at or below

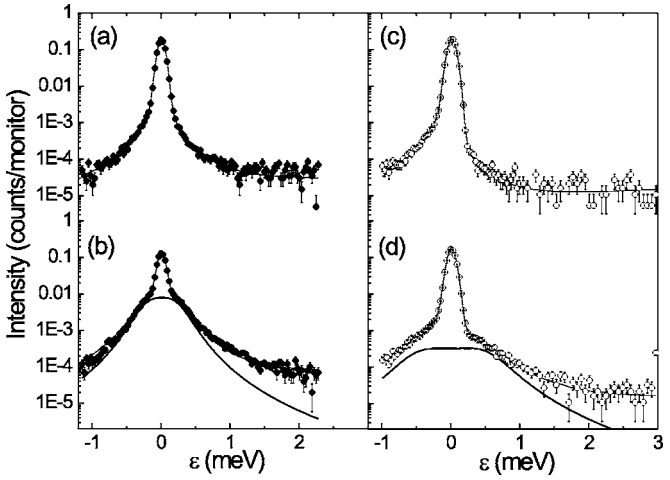

FIG. 2. Inelastic neutron data for 8-nm α-Fe_2O_3 nanoparticles. (a), (b) Energy scans with ε_f=3.7 meV at constant scattering vector τ_{003} at 10 and 150 K, respectively, for the noninteracting nanoparticles. Similar data for the interacting nanoparticles are shown in (c) and (d). The thin line represents the fit to the model as explained in the text and the bold line in (b) and (d) shows the contribution from just the collective magnetic excitations. The asymmetric tails is at $\varepsilon < 0.05$ meV are a part of the background, as explained in Sec. III. In each series of measurements, the spectra obtained at the lowest temperatures and zero applied field have been normalized to the same maximum intensity at ε_0=0 meV.

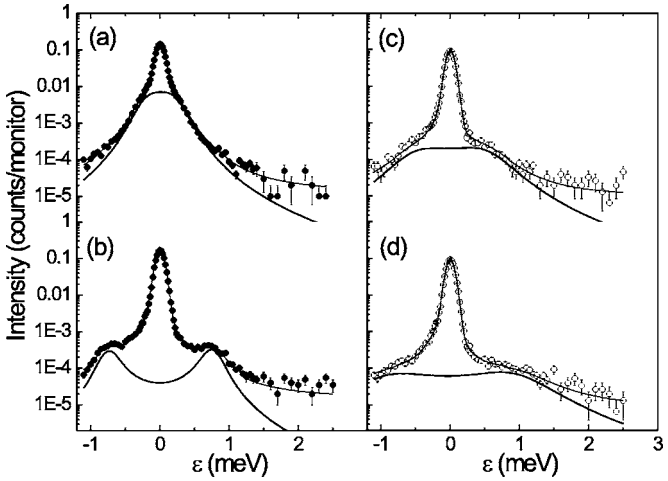

FIG. 3. Inelastic neutron data for the 8-nm α-Fe_2O_3 nanoparticles. (a), (b) Energy scans with ε_f=3.7 meV at constant scattering vector τ_{003} at 100 K at an applied magnetic field of 0 and 6 T, respectively, for the noninteracting nanoparticles. Similar data for the interacting nanoparticles are shown in (c) and (d). The thin line represents the fitted model as explained in the text, and the contribution from the just collective magnetic excitations is shown by the bold line.

18 K were obtained in a liquid helium cryostat. The spectrometers were calibrated with a 12.5-μm-thick $\alpha-$Fe foil at room temperature.

The inelastic neutron scattering experiments were performed at the cold-neutron triple-axis spectrometer RITA-2 at SINQ, Paul Scherrer Institute.[51] The experiments were performed with a 80 ′ collimator after a vertically focusing pyrolythic graphite (002) monochromator, and a radially collimating BeO filter after the sample. The final neutron energy was fixed at ε_f=3.7 meV giving an energy resolution of 80 μeV. Furthermore, spectra were also obtained for a final neutron energy of ε_f=2.9 meV. The spectrometer was run in the monochromatic point-to-point focusing analyzer mode with a position sensitive detector.[52] Following the same procedure as in Refs. 7, 39, and 43 the data were fitted using the models for superparamagnetic relaxation and collective magnetic excitations as described in Sec. II, Eqs. (5) and (6). First, the resolution function of the setup and the background function were determined from low temperature energy scans, where superparamagnetism and collective magnetic excitations are negligible, and from background energy scans performed at all temperatures at scattering vectors far from the Bragg reflections. The resolution function is composed of a strong Gaussian with FWHM=80 μeV (pure instrumental resolution) and a weak Lorentzian line with FWHM =2 meV centered at zero energy transfer (caused by incoherent scattering from water adsorbed at the nanoparticles and fluctuations of disordered surface spins[53]). Furthermore, an asymmetry is included for $\varepsilon < 0$ meV, caused by the BeO filter, which blocks elastically scattered (background-causing) neutrons at settings with $\varepsilon > 0.05$ meV. In the fitting procedure the obtained resolution function was convoluted with the expressions for the superparamagnetic relaxation and the collective magnetic excitations [Eqs. (5) and (6)], and a linear background with constant slope was added.

IV. EXPERIMENTAL RESULTS

A. Results from inelastic neutron scattering

Figures 2 and 3 show examples of the inelastic neutron scattering data obtained for a constant scattering vector at $Q=\tau_{003}=1.37$ Å^{-1}. In all figures the filled circles represent the data for the noninteracting nanoparticles and the open circles represent the interacting nanoparticles. The measurements were performed in the temperature range 5–300 K and in applied magnetic fields up to 10 T perpendicular to the incoming neutron beam and to the neutron scattering vector.

Figures 2(a) and 2(b) show the data for the noninteracting nanoparticles at T=10 and 150 K, respectively, including the fit to the model represented by the thin line. At the highest temperature the inelastic peaks have a large intensity indicating an increased population of the uniform magnetic excitations. The related part of the fit is shown by the bold line. Similar data for the interacting nanoparticles are shown in Figs. 2(c) and 2(d) for the temperatures T=5 and 150 K, respectively. The inelastic signal is less pronounced and appears considerably broadened as compared to the data for the noninteracting nanoparticles.

Figures 3(b) and 3(d) show the inelastic neutron scattering signal at T=100 K when a magnetic field of 6 T has been applied. Figures 3(a) and 3(c) show the corresponding zero field scans. It can be seen that application of a magnetic field increases the excitation energy in both samples. This is quali-

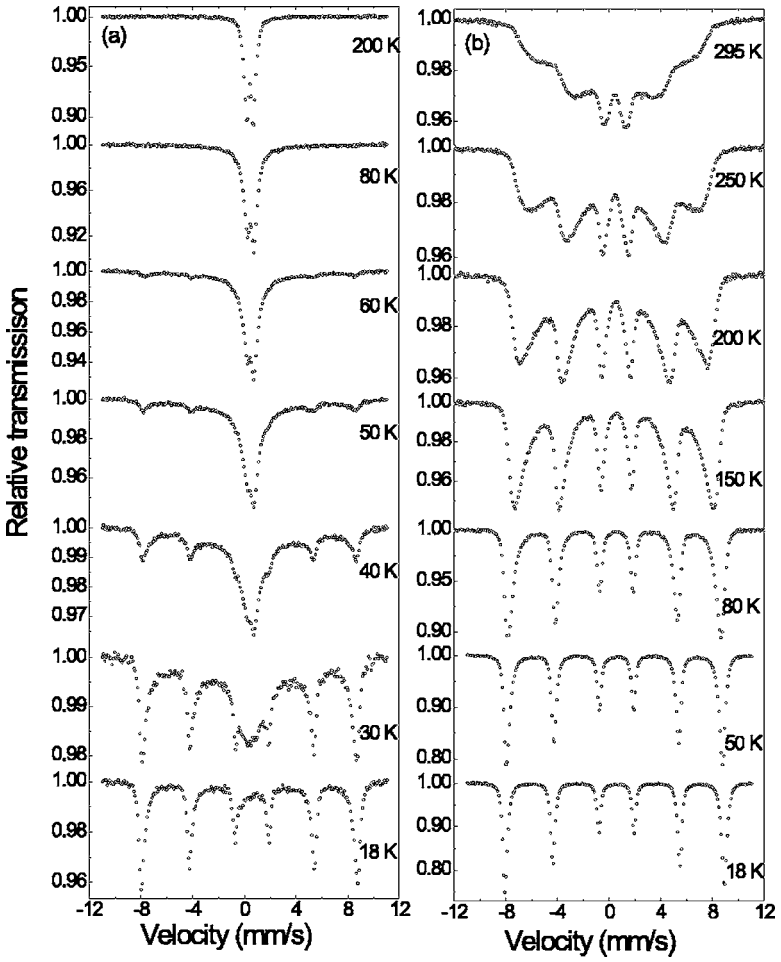

FIG. 4. Mössbauer spectra of the 8-nm α -Fe_2O_3 nanoparticles at various temperatures from 18 K to room temperature. (a) Data for the noninteracting particles and (b) data for the interacting particles.

tatively in accordance with Eq. (8). The broad inelastic components associated with the collective magnetic excitations are absent for data taken at nonmagnetic values of the scattering vector (data not shown).

B. Results from Mössbauer spectroscopy

Mössbauer spectra of the noninteracting and interacting particles, obtained at various temperatures, are shown in Fig. 4. The spectra of the coated nanoparticles [Fig. 4(a)] show a superparamagnetic behavior typical for noninteracting or weakly interacting nanoparticles.[33,35,36] At 18 K the spectrum consists of a sextet with narrow lines, indicating that at this temperature essentially all nanoparticles in the sample have relaxation times longer than the time scale of Mössbauer spectroscopy (i.e., $\geqslant 5\times 10^{-9}$ s). As the temperature is increased, a doublet appears in the spectra. This doublet is due to nanoparticles with a relaxation time shorter than the time scale of Mössbauer spectroscopy. The relative area of the doublet increases with increasing temperature, and at temperatures above 80 K the contribution from the sextet has disappeared. The spectra show a weak asymmetry of the sextet lines indicating that the coated nanoparticles may actually be weakly interacting.[33,35,36] The spectra of the interacting particles [Fig. 4(b)] show a completely different evolution with increasing temperature. Instead of the appearance of a doublet, the spectra show a substantial asymmetrical broadening of the lines of the sextet at temperatures up to room temperature. This is typical for Mössbauer spectra of interacting magnetic nanoparticles for which the energy is given by Eq. (4) and the relaxation may be described as fluctuations around a direction (mainly defined by the interaction field) rather than fluctuations between two equivalent minima at $\theta=0$ and $\theta=\pi$.[33–36]

V. DISCUSSION

We have applied the damped harmonic oscillator model to fit the inelastic neutron scattering spectra. Some of the parameters, obtained from the fits, are presented in Figs. 5, 7, and 8.

Around 200 K, the character of the relaxation changes. Well below this temperature, the dynamics can be described as a combination of uniform excitations with small amplitude (which give rise to the inelastic peaks) and superparamagnetic relaxation, i.e., reversal of the sublattice magnetization vectors (which gives rise to a broadening of the quasielastic peak). At temperatures of the order of 200 K, the thermal energy becomes comparable to the anisotropy energy, and then the two types of magnetic dynamics cannot be clearly separated because the sublattice magnetization vectors can fluctuate with similar probabilities in all directions. This isotropic relaxation regime[49] will be discussed

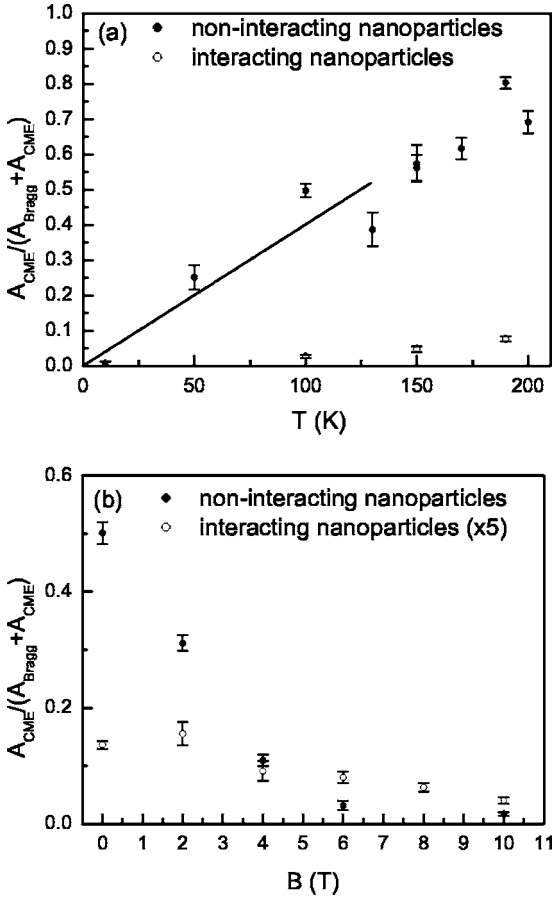

FIG. 5. The area fraction as a function of (a) temperature and (b) field at $T=100$ K. The fit to Eq. (9), which only applies at low temperatures, is shown by the solid line in (a). The data points for the interacting nanoparticles in (b) have been multiplied by 5 for clarity.

elsewhere.[48] Therefore, we will here only discuss the results obtained for $T<200$ K.

We have investigated the influence of a size distribution of the particles by weighting the inelastic neutron intensity with a log-normal size distribution (with standard deviation $\sigma=0.5$) and letting the anisotropy vary with size according to the findings of Ref. 31. For the nanoparticle sizes in this study it only introduces minor modifications, we therefore here present the analysis in which we have assumed monodisperse particles.

A. The magnetic anisotropy and interaction energies

The relative area of the inelastic peaks as compared to the total magnetic scattering, $A_{\mathrm{CME}}/(A_{\mathrm{Bragg}}+A_{\mathrm{CME}})$, as a function of temperature and applied field is shown in Figs. 5(a) and 5(b), respectively. For both samples, the relative area of the inelastic peaks increases with temperature, but the effect is strongest for the noninteracting particles. We have fitted the low-temperature data for the noninteracting particles with Eq. (9) yielding an estimate of the effective anisotropy of $K_{\mathrm{eff}}V/k_B=250(30)$ K $[K_{\mathrm{eff}}=1.3(2)\times10^4$ J/m$^3]$ for the noninteracting nanoparticles. The data for the interacting particles

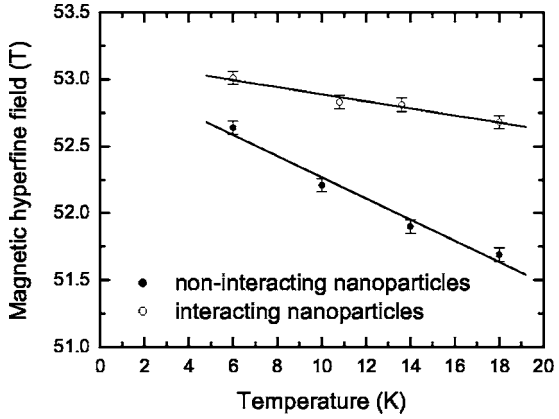

FIG. 6. The average observed hyperfine field $\langle B_{\mathrm{obs}}\rangle$ obtained from the Mössbauer data, as a function of temperature. The lines are linear fits to the data.

show a much smaller relative area of the inelastic peaks than for the noninteracting particles. Application of a magnetic field decreases the inelastic signal from the noninteracting nanoparticles, whereas only magnetic fields larger than about 3 T have a measurable effect on the interacting nanoparticles.

We have fitted the low-temperature Mössbauer spectra to estimate the average hyperfine field $\langle B_{\mathrm{obs}}\rangle$ at temperatures up to 18 K, i.e., in a range where the superparamagnetic relaxation of most particles are blocked, but the spectra are influenced by collective magnetic excitations. The temperature dependence of $\langle B_{\mathrm{obs}}\rangle$ is shown in Fig. 6. From the linear fits we find from Eq. (10) $K_{\mathrm{eff}}V/k_B=335(35)$ K $[K_{\mathrm{eff}}=1.7(2)\times10^4$ J/m$^3]$ for the noninteracting particles, which is in good agreement with the value found from the neutron data. For the interacting particles we find from Eq. (11) $(2K_{\mathrm{eff}}V+E_{\mathrm{int}})/k_B=1330(180)$ K. Assuming K_{eff}V to be the same for the two samples, we obtain $E_{\mathrm{int}}/k_B=660(200)$ K.

In α-Fe_2O_3 the different superexchange coupling constants are in the range 10–30 K,[44] For Fe^{3+} ions with spin $s=5/2$ this corresponds to an exchange energy per exchange bridge in the range 60–190 K. Therefore only a few (of the order of ten) exchange bridges between neighboring α-Fe_2O_3 nanoparticles are needed to account for the observed interaction effects. Similar values were estimated from Mössbauer data for interacting 20 nm α-Fe_2O_3 nanoparticles.[33]

B. The energy related to the uniform precession states

The measured dynamic behavior of the 8-nm hematite nanoparticles show several interesting effects, which were not observed in previous studies of larger particles.[7,39,43] First we discuss data for the noninteracting nanoparticles. The excitation energy ε_0 shows a weak linear increase with temperature [Fig. 7(a)]. Extrapolating ε_0 to $T=0$ K gives $\varepsilon_{0,T=0}=0.214(5)$ meV. The increase of ε_0 with increasing temperature is surprising since the damped harmonic oscillator model predicts a decreasing ε_0, which was also observed for larger 15-nm α-Fe_2O_3 nanoparticles.[39,43] Furthermore,

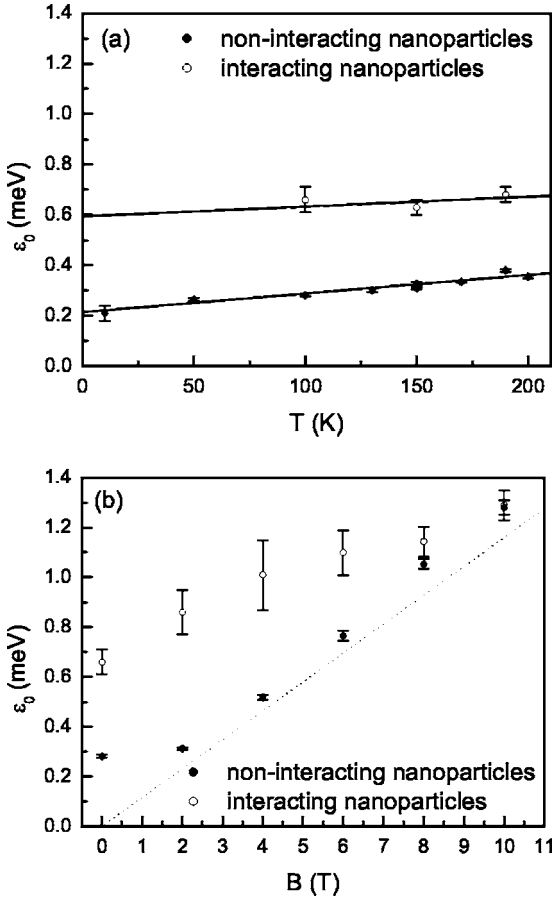

FIG. 7. Position of the inelastic peaks as a function of (a) temperature and (b) field at $T=100$ K. The solid lines in (a) show the linear extrapolation to $T=0$ K and in (b) the dotted line represents Eq. (8).

because the magnetic anisotropy constant of α-Fe_2O_3 nanoparticles increases with decreasing particle size[31] one would expect an increasing $\varepsilon_{0,T=0}$ with decreasing particle size, and this is also opposite to the present observation (for 15-nm α-Fe_2O_3 nanoparticles $\varepsilon_{0,T=0}=0.26$ meV).[39]

It is known[17,18] that antiferromagnetic nanoparticles usually have an uncompensated magnetic moment, with a relative size increasing with decreasing particle size. One can show that the equation of motion for the $q=0$ mode in a microscopic model for a particle with different number of spins in two sublattices is equivalent to that of two interacting macrospins.[54] Thus nanoparticles of antiferromagnetic materials should in principle be described as ferrimagnets with a very small difference ΔM between the sublattice magnetic moments. Even a small uncompensated moment can have a significant influence on the precession frequency of the uniform mode. Introducing the relative uncompensated moment $\zeta=\Delta M/M_s$ in one sublattice, Eq. (7) should be replaced by[55–58]

$$\varepsilon_0^{1,2}=\frac{1}{2}g\mu_B B_E[\sqrt{4\lambda^2+4\lambda(2+\zeta)+\zeta^2}\pm\zeta]. \qquad (12)$$

Here $\lambda=K_{\text{eff}}/(B_E M_s)$. We have assumed that the magnetic anisotropy is uniaxial and given by Eq. (1) and that the spin structure and the precession modes are not influenced by, for example, surface effects in the nanoparticles. In previous work on 15-nm α-Fe_2O_3 particles[7,39,43] the influence of an uncompensated moment on the precession frequency was not observed. However, in the 8-nm particles studied here, the relative uncompensated moment is expected to be larger and therefore to have a stronger influence on ε_0, and this may explain the small value of ε_0 and its anomalous temperature dependence. Inserting the measured value of $\varepsilon_{0,T=0}=0.214$ meV and using the estimated $K_{\text{eff}}=1.3\times10^4$ J/m^3 (obtained in Sec. V A) and assuming that the low-energy mode (ε_0^1) is predominant, we determine an uncompensated moment $\Delta M/M_{s,T=0}\approx1.1\%$. According to Eq. (12), the other mode with higher frequency (ε_0^2) then corresponds to $\varepsilon_{0,T=0}\approx1.7$ meV. We do not resolve the neutron intensity from this mode because it is significantly reduced in comparison to mode ε_0^1.

It should be emphasized that the use of the simple expression Eq. (1) for the magnetic anisotropy energy, which was also used in previous neutron studies of hematite nanoparticles,[39,43] is only a first order approximation. Both in bulk hematite and hematite nanoparticles, the sublattice magnetization is to a large extent confined to the (001) plane because of a large out-of-plane anisotropy with anisotropy constant K_1. The smaller in-plane anisotropy, K_{Bu} has been found to increase with decreasing particle size.[31] In neutron studies of the high-frequency and low-frequency modes in 15 nm particles the values $K_1=5\times10^4$ J/m^3 and $K_{\text{Bu}}=0.3\times10^4$ J/m^3 were estimated, but from the results above we estimate that K_{Bu} is larger in the present 8-nm particles. Unfortunately, the value of K_1 in 8-nm particles is not known, because we were unable to detect the high-frequency mode, and therefore we are not able to perform a more rigorous data analysis. However, it is likely that K_1 and K_{Bu} are of the same order of magnitude in the 8 nm particles, and therefore Eq. (1) may be a fair approximation to the magnetic anisotropy energy.

Néel[17,18] suggested some simple models for estimating the uncompensated moment. In one model, he assumed that the interior of the nanoparticle is essentially free of defects, but that the surface sites are randomly occupied such that the number of uncompensated spins is of the order of the square root of the number of surface spins. For the present particles this would give a fraction of uncompensated spins of about 0.8% in one sublattice, which is close to the value estimated from the experimental data $\approx1.1\%$.

Mössbauer spectroscopy with large magnetic fields applied to the sample can give information on the relative importance of the magnetic moments due to canting and to uncompensated spins. Such studies of 15-nm hematite particles showed that the moment due to uncompensated spins was small compared to the moment due to canting.[59] We have made similar measurements on the 8-nm particles and found that the two contributions in this case are of the same order of magnitude, i.e., the relative importance of the uncompensated spins is larger in this case.

The nanoparticles with an uncompensated moment may be considered as weak ferrimagnets. However, the dipole interaction energy, even between two particles in contact, is very weak ($\lesssim1$ K).[33] Thus, the interaction effects observed

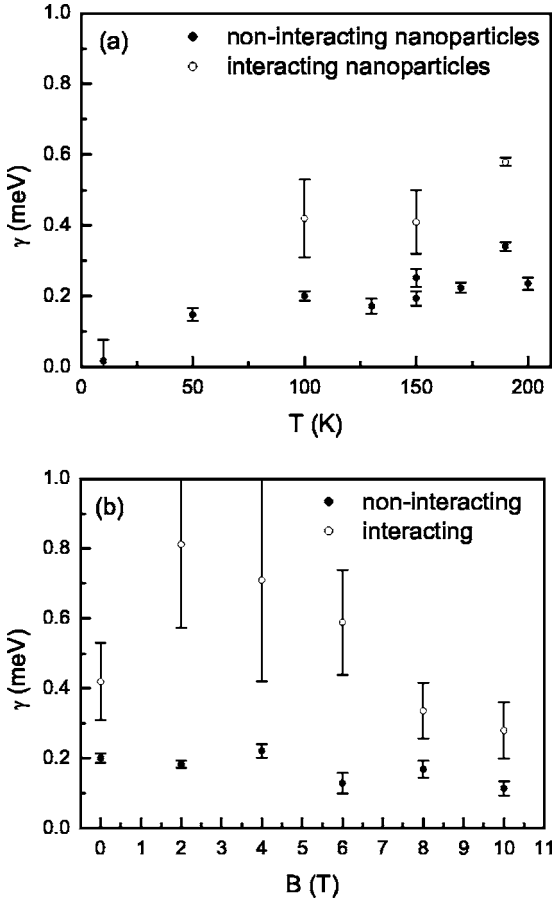

FIG. 8. Width of the inelastic peaks as a function of (a) temperature and (b) field at $T=100$ K.

in the interacting particles must be explained by exchange interactions.

When a magnetic field is applied [Fig. 5(b)] the amplitude of the inelastic peak decreases. This can be explained by the increase of the excitation energy of the precession modes, which results in a decrease of the thermal populations. ε_0 increases for the noninteracting nanoparticles at all fields up to 10 T. At large applied fields $\varepsilon_0(B)$ follows the behavior predicted by Eq. (8), which is shown by the dotted line in Fig. 7(b) (assuming[39] $g=2$).

The width γ of the inelastic peak increases with temperature [Fig. 8(a)]. Though the values are comparable, this increase with temperature is opposite to what was seen in previous experiments on 15-nm α-Fe_2O_3 nanoparticles.[39,43] Theoretically, it has been predicted that the width first decreases with temperature and then at a certain critical temperature starts to increase.[45] This is caused by the balance between the anisotropy energy barrier and the sublattice exchange interaction in α-Fe_2O_3. For the present experiments the anisotropy energy of the 8-nm α-Fe_2O_3 nanoparticles may be such that we have entered the regime where an increase in width is possible. For the interacting nanoparticles the width is a factor 2–3 larger indicating that there is a broad range of interaction energies.

Applying a magnetic field [Fig. 8(b)] reduces the width. The magnetic field narrows the range of frequencies and suppresses to some extent the amplitude of the excitations.

Now we discuss the corresponding measurements for the interacting particles. The temperature dependence of ε_0 is similar to that of the noninteracting particles. For the interacting nanoparticles, ε_0 [Fig. 7(b)] starts at a higher value for low magnetic fields $\varepsilon_0(B=0)\approx 0.65$ meV and reaches the value for the noninteracting nanoparticles at 10 T. The field dependence of ε_0 shows a significant deviation from Eq. (8) for fields up to 8 T. Thus the interaction energy is predominant and we estimate that the effective interaction field is of the order of 5 T. On the other hand, E_{int} can be considered as a product of this interaction field and an effective moment. For $E_{\text{int}}\approx 660$ K one can estimate an effective moment of 130 Bohr magnetons, which would correspond to about 50 iron atoms. The behavior of γ for the interacting nanoparticles starts to approach that of the weakly interacting nanoparticles at an applied field of 5 T, in accordance with the previous findings.

VI. CONCLUSION

Using inelastic neutron scattering we have studied the collective magnetic excitations in noninteracting and interacting 8-nm α-Fe_2O_3 nanoparticles. The data are well described by the damped harmonic oscillator model. The determined characteristic energy ε_0 suggests that the magnetic properties of the 8-nm α-Fe_2O_3 nanoparticles are strongly affected by an uncompensated moment in one sublattice of $\Delta M/M_{s,T=0}\approx 1.1\%$, which is present as a finite size effect in the antiferromagnetic nanoparticles. The collective magnetic excitations are strongly influenced by the interparticle exchange interactions, and from Mössbauer spectroscopy data we have estimated the interaction energy E_{int}/k_B to be approximately 660 K. This energy corresponds to in average a few exchange bridges between the α-Fe_2O_3 nanoparticles. This is supported by the neutron measurements. We conclude that inelastic neutron scattering besides probing spin dynamics in magnetic nanoparticles also can add important information on uncompensated moments and interparticle interactions.

ACKNOWLEDGMENTS

We thank F. Bødker for preparing the α-Fe_2O_3 nanoparticles. We have had many clarifying discussions with B. Lebech for which we are grateful. The work was supported by the Danish Technical Research Council through the framework program on nanomagnetism, and the Danish Natural Science Research Council through the Danish Neutron Scattering Centre, DANSCATT. The electron microscopy was carried out at the Danish TEM Centre, supported by the Danish Natural Science and Technical Research Councils. This work is based on experiments performed at the SINQ neutron source at the Paul Scherrer Institute, Villigen, Switzerland.

*Electronic address: luise.theil.kuhn@risoe.dk
†Author to whom correspondence should be addressed.
‡Electronic address: christian.bahl@risoe.dk
§Present address: Materials Science Div., Argonne National Laboratory, Argonne, IL 60439, USA.

[1] *Fifth International Conference on Fine Particle Magnetism*, edited by Q. Pankhurst, Journal of Physics: Conference Series 17, (2005).
[2] M. P. Morales, S. A. Walton, L. S. Prichard, C. J. Serna, D. P. E. Dickson, and K. O'Grady, J. Magn. Magn. Mater. **190**, 357 (1998).
[3] L. Néel, Ann. Geophys. (C.N.R.S.) **5**, 99 (1949).
[4] S. Mørup and H. Topsøe, Appl. Phys. **11**, 63 (1976).
[5] S. Mørup, J. Magn. Magn. Mater. **37**, 39 (1983).
[6] P. V. Hendriksen, S. Linderoth, and P.-A. Lindgård, Phys. Rev. B **48**, 7259 (1993).
[7] S. N. Klausen, K. Lefmann, P.-A. Lindgård, L. Theil Kuhn, C. R. H. Bahl, C. Frandsen, S. Mørup, B. Roessli, N. Cavadini, and C. Niedermayer, Phys. Rev. B **70**, 214411 (2004).
[8] S. Mørup and B. R. Hansen, Phys. Rev. B **72**, 024418 (2005).
[9] J. L. Dormann, L. Bessais, and D. Fiorani, J. Phys. C **21**, 2015 (1988).
[10] S. Mørup and E. Tronc, Phys. Rev. Lett. **72**, 3278 (1994).
[11] P. E. Jönsson and J. L. García-Palacios, Europhys. Lett. **55**, 418 (2001).
[12] Ò. Iglesias and A. Labarta, Phys. Rev. B **70**, 144401 (2004).
[13] J. Zhang, C. Boyd, and W. Luo, Phys. Rev. Lett. **77**, 390 (1996).
[14] C. Djurberg, P. Svedlindh, P. Nordblad, M. F. Hansen, F. Bødker, and S. Mørup, Phys. Rev. Lett. **79**, 5154 (1997).
[15] H. Mamiya, I. Nakatani, and T. Furubayashi, Phys. Rev. Lett. **80**, 177 (1998).
[16] D. Fiorani, J. L. Dormann, R. Cherkaoui, E. Tronc, F. Lucari, F. D'Orazio, L. Spinu, M. Nogues, A. Garcia, and A. M. Testa, J. Magn. Magn. Mater. **196–197**, 143 (1999).
[17] L. Néel, C. R. Hebd. Seances Acad. Sci. **252**, 4075 (1961).
[18] L. Néel, in *Low Temperature Physics*, edited by C. Dewitt, B. Dreyfus, and P. D. de Gennes (Gordon & Breach, New York, 1962), p. 420.
[19] S. Mørup and C. Frandsen, Phys. Rev. Lett. **92**, 217201 (2004).
[20] M. S. Seehra, V. S. Babu, A. Manivannan, and J. W. Lynn, Phys. Rev. B **61**, 3513 (2000).
[21] J. G. E. Harris, J. E. Grimaldi, D. D. Awschalom, A. Chiolero, and D. Loss, Phys. Rev. B **60**, 3453 (1999).
[22] S. H. Kilcoyne and R. Cywinski, J. Magn. Magn. Mater. **140–144**, 1466 (1995).
[23] S. A. Makhlouf, F. T. Parker, and A. E. Berkowitz, Phys. Rev. B **55**, R14717 (1997).
[24] N. J. O. Silva, V. S. Amaral, and L. D. Carlos, Phys. Rev. B **71**, 184408 (2005).
[25] B. Barbara and E. M. Chudnovsky, Phys. Lett. A **145**, 205 (1990).
[26] J. Tejada and X. X. Zhang, J. Phys.: Condens. Matter **6**, 263 (1994).
[27] M. Duran, E. del Barco, J. M. Hernandez, and J. Tejada Phys. Rev. B **65**, 172401 (2002).
[28] E. del Barco, M. Duran, J. M. Hernandez, J. Tejada, R. D. Zysler, M. Vasquez Mansilla, and D. Fiorani, Phys. Rev. B **65**, 052404 (2002).
[29] R. H. Kodama, S. A. Makhlouf, and A. E. Berkowitz, Phys. Rev. Lett. **79**, 1393 (1997).
[30] W. Kündig, K. J. Ando, G. Constabaris, and R. H. Lindquist, Phys. Rev. **142**, 327 (1966).
[31] F. Bødker and S. Mørup, Europhys. Lett. **52**, 217 (2000).
[32] R. D. Zysler, D. Fiorani, A. M. Testa, L. Suber, E. Agostinelli, and M. Godinho, Phys. Rev. B **68**, 212408 (2003).
[33] M. F. Hansen, C. B. Koch, and S. Mørup, Phys. Rev. B **62**, 1124 (2000).
[34] S. Mørup, M. B. Madsen, J. Franck, J. Villadsen, and C. J. W. Koch, J. Magn. Magn. Mater. **40**, 163 (1983).
[35] S. Mørup, C. Frandsen, F. Bødker, S. N. Klausen, K. Lefmann, P.-A. Lindgård, and M. F. Hansen, Hyperfine Interact. **144/145**, 347 (2002)
[36] C. Frandsen and S. Mørup, J. Magn. Magn. Mater. **266**, 36 (2003).
[37] C. Frandsen and S. Mørup, Phys. Rev. Lett. **94**, 027202 (2005).
[38] F. Gazeau, E. Dubois, M. Hennion, R. Perzynski, and Y. Raikher, Europhys. Lett. **40**, 575 (1997).
[39] M. F. Hansen, F. Bødker, S. Mørup, K. Lefmann, K. N. Clausen, and P.-A. Lindgård, Phys. Rev. Lett. **79**, 4910 (1997).
[40] K. Lefmann, F. Bødker, M. F. Hansen, H. Vázquez, N. B. Christensen, P.-A. Lindgård, K. N. Clausen, and S. Mørup, Eur. Phys. J. D **9**, 491 (1999).
[41] M. F. Hansen, F. Bødker, S. Mørup, K. Lefmann, K. N. Clausen, and P.-A. Lindgård, J. Magn. Magn. Mater. **221**, 10 (2000).
[42] K. Lefmann, F. Bødker, S. N. Klausen, M. F. Hansen, K. N. Clausen, P.-A. Lindgård, and S. Mørup, Europhys. Lett. **54**, 526 (2001).
[43] S. N. Klausen, K. Lefmann, P.-A. Lindgård, K. N. Clausen, M. F. Hansen, F. Bødker, S. Mørup, and M. Telling, J. Magn. Magn. Mater. **266**, 68 (2003).
[44] A. H. Morrish, *Canted Antiferromagnetism: Hematite* (World Scientific, Singapore, 1994).
[45] J. D. Lee, Phys. Rev. B **70**, 174450 (2004).
[46] T. Sugimoto, Y. Wang, H. Itoh, and A. Muramatsu, Colloids Surf., A **134**, 265 (1998).
[47] C. Frandsen, C. R. H. Bahl, B. Lebech, K. Lefmann, L. Theil Kuhn, L. Keller, N. H. Andersen, M. v. Zimmermann, E. Johnson, S. N. Klausen, and S. Mørup, Phys. Rev. B **72**, 214406 (2005).
[48] L. Theil Kuhn, K. Lefmann, C. R. H. Bahl, S. N. Klausen, A. Wischnewski, C. Frandsen, and S. Mørup (unpublished).
[49] A. Würger, Europhys. Lett. **44**, 103 (1998).
[50] E. Tronc and J. P. Jolivet, Hyperfine Interact. **28**, 525 (1986).
[51] S. N. Klausen, K. Lefmann, D. F. McMorrow, F. Altorfer, S. Janssen, and M. Luthy, Appl. Phys. A: Mater. Sci. Process. **74**, S1508 (2002); see also the home page http://sinq.web.psi.ch/sinq/instr/rita2
[52] K. Lefmann, D. F. McMorrow, H. M. Rønnow, K. Nielsen, K. N. Clausen, B. Lake, and G. Aeppli, Physica B **283**, 343 (2000).
[53] L. Theil Kuhn, K. Lefmann, S. N. Klausen, H. M. Rønnow, A. Murani, and R. Stewart, Physica B **350**, e217 (2004).
[54] C. R. H. Bahl, K. Lefmann, T. B. S. Jensen, P.-A. Lindgård, D. E. Madsen, and S. Mørup (unpublished)
[55] A. H. Morrish, *The Physical Principles of Magnetism* (Wiley, New York, 1965).
[56] C. Kittel, Phys. Rev. **82**, 565 (1951).
[57] F. Keffer and C. Kittel, Phys. Rev. **85**, 329 (1952).
[58] R. K. Wangsness, Phys. Rev. **86**, 146 (1952); **91**, 1085 (1953).
[59] F. Bødker, M. F. Hansen, C. B. Koch, K. Lefmann, and S. Mørup, Phys. Rev. B **61**, 6826 (2000).

Paper VIII

INSTITUTE OF PHYSICS PUBLISHING JOURNAL OF PHYSICS: CONDENSED MATTER

J. Phys.: Condens. Matter **18** (2006) 4161–4175 doi:10.1088/0953-8984/18/17/005

The magnetic moment of NiO nanoparticles determined by Mössbauer spectroscopy

C R H Bahl[1,2], M F Hansen[3], T Pedersen[1], S Saadi[1], K H Nielsen[1], B Lebech[2] and S Mørup[1]

[1] Department of Physics, Building 307, Technical University of Denmark, DK-2800 Kongens Lyngby, Denmark
[2] Materials Research Department, Building 227, Risø National Laboratory, DK-4000 Roskilde, Denmark
[3] MIC—Department of Micro and Nanotechnology, Building 345 East, Technical University of Denmark, DK-2800 Kongens Lyngby, Denmark

E-mail: morup@fysik.dtu.dk

Received 14 February 2006
Published 13 April 2006
Online at stacks.iop.org/JPhysCM/18/4161

Abstract

We have studied the magnetic properties of ^{57}Fe-doped NiO nanoparticles using Mössbauer spectroscopy and magnetization measurements. Two samples with different degrees of interparticle interaction were studied. In both samples the particles were characterized by high-resolution transmission electron microscopy and x-ray diffraction and found to be plate-shaped. Computer simulations showed that high-field Mössbauer data are very sensitive to the size of the uncompensated magnetic moment. From analyses of the Mössbauer spectra we have estimated that the size of the uncompensated magnetic moment is in accordance with a model based on random occupation of surface sites. The analyses of the magnetization data gave larger magnetic moments, but the difference can be explained by the different sensitivity of the two methods to a particle size distribution and by interactions between the particles, which may have a strong influence on the moments estimated from magnetization data.

(Some figures in this article are in colour only in the electronic version)

1. Introduction

NiO is an archetypal antiferromagnet and was one of the first materials in which antiferromagnetism was studied [1]. It has an fcc structure, with the spins arranged in alternating ferromagnetically ordered {111} planes, giving an antiferromagnetic ordering vector along the [111] direction, i.e. it is a so-called type II antiferromagnet. In bulk, the spins are confined to the [11$\bar{2}$] direction within the (111) plane [2]. Due to this spin structure, the exchange coupling to the nearest neighbours within the ferromagnetic planes is slightly larger than that to the nearest neighbours out of these planes. This exchange striction manifests itself

in NiO not being perfectly cubic but having a small contraction of the distance between the ferromagnetically ordered planes below the Néel temperature [3]. However, the difference in plane spacing is only about 0.1% at 300 K [3] and this deviation from cubic symmetry is in general ignored.

In a number of studies of nanoscale NiO it has been found that very small particles can have quite large magnetic moments [4–10]. Néel [11] suggested that this can be explained by the presence of uncompensated magnetic moments, and he considered three different situations for the number of uncompensated spins in small particles of an antiferromagnet. These general cases, also discussed in [6], give different numbers of uncompensated spins q depending on the model employed. If the uncompensated spins occur at random in a particle, a value of $q \approx n_s^{1/2}$ is found, where n_s is the number of spins. If the spins are arranged in ferromagnetically ordered layers stacked into a cube with an odd number of layers the value is $q \approx n_s^{2/3}$. Finally, if the structure is perfect except for spins missing at random on the surface, the value is $q \approx n_s^{1/3}$. From measurements of the relationship between the magnetic susceptibility and the particle size, Richardson *et al* [6] found a size dependence of the susceptibility with $q \propto n_s^{1/3}$, with a proportionality factor of about 4, but the shape of the particles was not mentioned. In the literature, it has often been assumed that the number of uncompensated spins is of the order of $n_s^{1/2}$. However, the model used to obtain this value, i.e. a random occupancy of the sites in the particle, would undoubtedly lead to severe crystallographic and magnetic disorder, but this is not observed in studies of, for example, nanoparticles of NiO [12] and α-Fe_2O_3 [13]. It therefore seems more realistic that the uncompensated moment has its main contribution from the surface. In the present work we have estimated the moments of plate-shaped NiO nanoparticles using high-field Mössbauer data and magnetization measurements.

2. Materials and methods

$Ni(OH)_2$ was chemically precipitated by mixing aqueous solutions of NaOH and $Ni(NO_3)_2{\cdot}6H_2O$. It was transformed to NiO by heating in atmospheric air at 300 °C for 3 h, as described in [14]. In order to enable Mössbauer spectroscopy, samples were made by the same procedure from $Ni(OH)_2$ doped with 0.5 at.% ^{57}Fe relative to Ni. The sample is from the same batch as the as-prepared sample of [14] displaying significant interparticle interaction. A second set of doped and undoped NiO samples displaying less interparticle interaction was prepared by grinding the as-prepared samples by hand in an agate mortar for 15 min. Earlier studies have shown that gentle grinding can significantly reduce interactions between nanoparticles [15].

^{57}Fe Mössbauer spectroscopy was performed on both the as-prepared and the ground sample using a source of ^{57}Co in a rhodium matrix. Spectra were recorded in a liquid helium cryostat at 6 K in zero applied field and in a magnetic field of 6 T applied parallel to the radiation direction. Temperature series from 80 to 295 K were recorded at zero applied field in a liquid nitrogen cryostat. The powder samples were diluted by mixing with boron nitride powder without grinding.

The samples were studied by high-resolution transmission electron microscopy (HRTEM) using a JEOL 3000 FEG microscope equipped with a Gatan 16 Mpix CCD camera. X-ray diffraction (XRD) was carried out at ambient conditions in a Philips PW 1820 diffractometer using the Kα radiation from a Cu anode. Magnetometry was performed using a LakeShore 7407 vibrating sample magnetometer (VSM), with a maximum field of 1.6 T. These measurements were carried out at temperatures from 80 to 300 K, using a liquid nitrogen cryostat. Samples of ~100 mg were measured in Teflon cups. The background signal from the empty cups was subtracted.

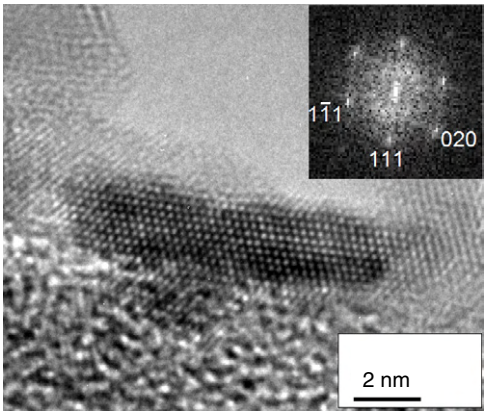

Figure 1. HRTEM image of a platelet-shaped NiO nanoparticle from the as-prepared sample, seen edge on. The inset is a Fourier transform of the image indicating how the (111) plane is parallel to the plate face. The plate face is seen to have an irregular surface.

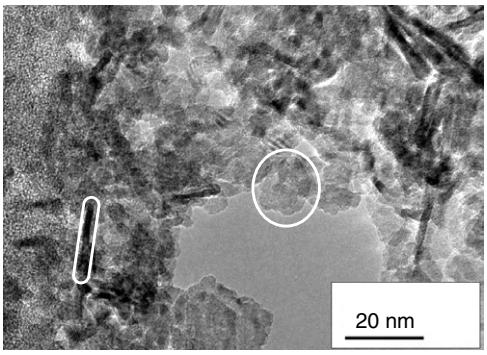

Figure 2. TEM image of the edge of an agglomerate of NiO nanoparticles in the as-prepared sample, showing how the platelet-shaped particles are found in random orientations. The two indicated platelets are oriented edge-on and face-on.

3. Results

3.1. Structure and morphology of the sample

Samples for HRTEM studies were prepared by suspending some of the powder in water and air drying a droplet on a grid. In both the ground and as-prepared samples the particles were found in 100–500 nm sized agglomerates. The particles are platelet-shaped particles, with {111} lattice planes as faces, as illustrated in figure 1 which shows a HRTEM image obtained from the as-prepared sample. Measuring the particle size in the as-prepared sample gave an average plate diameter of 13 $\pm$ 3 nm and an average thickness of 2.3 $\pm$ 0.4 nm. Here the uncertainties give the standard deviation of the size distributions. There is no obvious difference between images of the two samples. No interaction or orientation effects are observed in either sample, as the platelets are found with random orientations relative to each other throughout the agglomerates, as seen in figure 2.

XRD analysis showed that doping and grinding does not change the size or morphology of NiO samples [16]. Profile refinement using the FullProf software [17] was performed on the

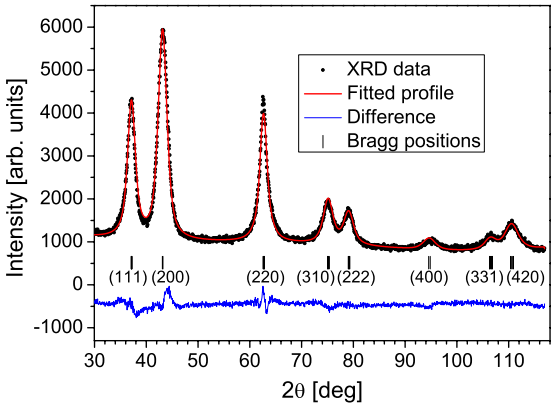

Figure 3. XRD spectrum from the as-prepared sample profile refined by the FullProf software, assuming a platelet particle shape. The refinement was done using a pseudo-hexagonal unit cell, as described in the text, but for clarity the conventional cubic indexing is used in the figure.

as-prepared undoped sample. The refinement showed that both samples consist of pure NiO with no visible trace of $Ni(OH)_2$ or other impurity phases. The refinement was done with the cubic unit cell and space group $Fm3m$, giving a lattice constant of $a = 4.194$ Å, which is slightly larger than the value of $a = 4.180$ Å found from the refinement of a spectrum recorded from a commercial bulk NiO powder but in accordance with the results of previous XRD studies of NiO nanoparticles [6, 18].

Assuming a spherical particle shape, the refined profile gave a particle diameter of 3.6 nm. From the knowledge gained from the TEM study, it seemed more realistic to fit the spectra assuming disc-shaped particles. In order for the software to distinguish between the four different ⟨111⟩ directions the cubic NiO unit cell was transformed to a pseudo-hexagonal one [19] with space group $R\bar{3}m$, the a and b axes in the (111) plane and the c axis along the [111] direction.

The fit of the spectrum of the as-prepared sample, assuming a platelet shape with the [111] direction perpendicular to the plate face, gave lattice parameters $a = 2.966$ Å and $c = 7.259$ Å compared to the values of $a = 2.955$ Å and $c = 7.246$ Å obtained in the bulk powder. The fit is shown in figure 3. It gave an estimated plate thickness of 2.3 nm and an estimated diameter of 7.9 nm. The diameter is smaller than that found by TEM, but the fit does not completely describe the narrow peak of the $(220)_{\text{cubic}} = (110)_{\text{hex}}$ reflection, which is in the disc plane. This will underestimate the diameter of the particles and is probably caused by the size distribution of the particles.

3.2. Mössbauer spectroscopy

Mössbauer spectra of the as-prepared and ground doped samples, recorded at temperatures from 6 to 295 K, are presented in figure 4. At low temperatures the spectra consist of magnetically split sextets. As the temperature increases the sextets gradually collapse into singlets, indicating fast superparamagnetic relaxation. At 295 K the spectra of both samples consist of a singlet with narrow line widths. The absence of quadrupole splitting shows that at least a large fraction of the ^{57}Fe atoms are in cubic environments as expected for a homogeneous substitution of ^{57}Fe in the Ni^{2+} sites in NiO in both samples. In the ground sample the sextet has almost collapsed at 105 K, whereas in the as-prepared sample the collapse is almost complete at

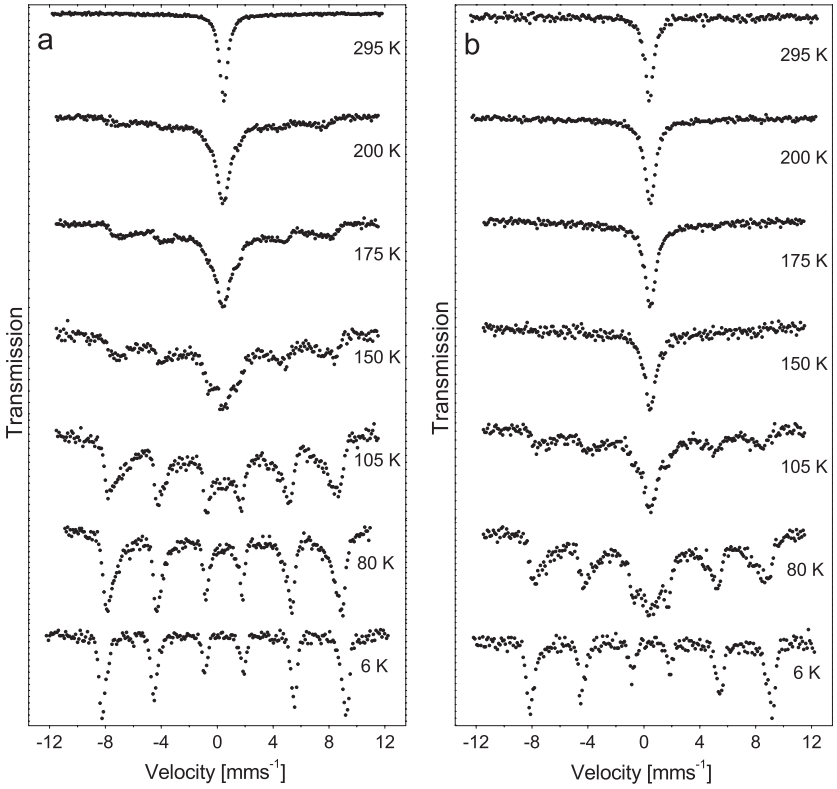

Figure 4. Mössbauer spectra of the ^{57}Fe-doped NiO nanoparticles recorded at temperatures in the range 6–295 K. (a) The as-prepared sample. (b) The ground sample.

around 175 K. Also, at $T \geqslant 80$ K the lines of the sextets are asymmetrically broadened due to hyperfine field distributions and relaxation effects. The asymmetric line broadening is typical for Mössbauer spectra of magnetic nanoparticles with some interparticle interaction due to exchange interaction between the particles [14, 20–22]. In [14] NiO particles from the same batch, but with significantly weaker interactions due to phosphate coating, were studied. In this sample, the blocking temperature, defined as the temperature where the singlet and sextet components have the same area, was about 50 K. In the present ground and as-prepared samples, the interaction raises the blocking temperatures to about 100 and 150 K, respectively.

Mössbauer spectra, obtained from both samples at 6 K in applied fields of 0 and 6 T, are shown in figures 5(a) and (b). The zero field spectra can be fitted with a single sextet. Line widths were constrained to be pair-wise identical. The Mössbauer parameters are given in table 1. The isomer shifts and magnetic hyperfine fields at low temperatures show that iron is present as Fe^{3+} in the high-spin state in both samples.

In ^{57}Fe Mössbauer spectroscopy, the areas of the lines in a magnetically split sextet (assuming a thin absorber) will scale as $3{:}p{:}1{:}1{:}p{:}3$, with

$$p = \frac{4\sin^2\theta}{2-\sin^2\theta}, \tag{1}$$

where θ is the angle between the total magnetic field at the nucleus and the incoming radiation. If the hyperfine fields of the particles in the sample are randomly oriented, the area ratio of

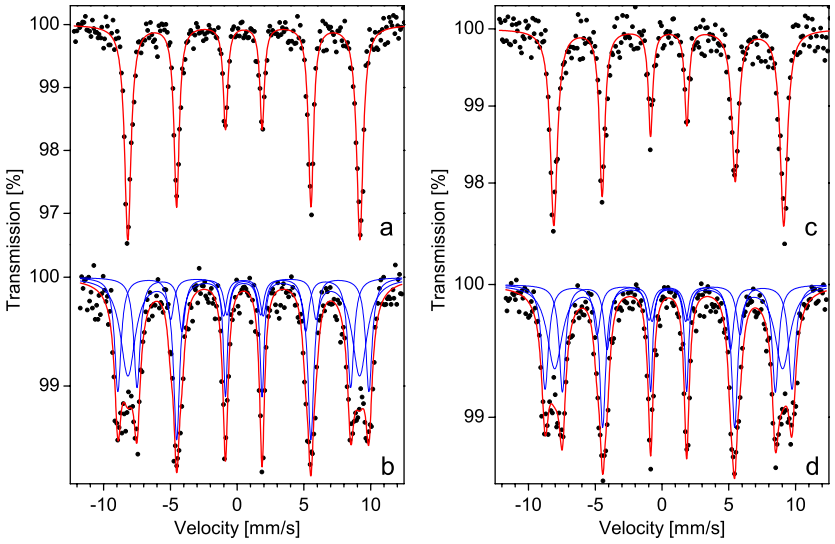

Figure 5. Mössbauer spectra of both samples of NiO nanoparticles doped with iron all recorded at 6 K. (a) The as-prepared sample recorded in zero applied field. (b) The as-prepared sample recorded in an applied field of 6 T. (c) The ground sample recorded in zero applied field. (d) The ground sample recorded in an applied field of 6 T. The small amount of iron in the samples is the reason for the poor statistics in the measured spectra. The thin lines (blue online) are the individual sextets, and the broader line (red online) is the sum of these.

Table 1. Parameters obtained from the fit to the 6 K Mössbauer spectra of NiO nanoparticles in zero applied field and an applied field of 6 T for both the as-prepared and the ground sample. The field is applied parallel to the propagation direction of the gamma rays. The line area parameters, p, for the sextets 2 and 3 in an applied field of 6 T were fixed according to the values of the total field at the nuclei as described in the text.

	B_{tot} (T)	Isomer shift (mm s^{-1})	Quadrupole shift (mm s^{-1})	Line area parameter p	Relative area of component (%)
As-prepared sample					
$B_{\mathrm{app}} = 0$ T					
Sextet 1	53.9(1)	0.50(2)	0.00(2)	2.1(2)	100
$B_{\mathrm{app}} = 6$ T					
Sextet 1	53.8(5)	0.50(3)	0.00	2.0(2)	53(3)
Sextet 2	49.6(4)	0.50(3)	0.00	1.44	24(3)
Sextet 3	58.3(4)	0.47(3)	0.00	1.09	23(3)
Ground sample					
$B_{\mathrm{app}} = 0$ T					
Sextet 1	53.4(1)	0.50(2)	0.00(2)	2.2(2)	100
$B_{\mathrm{app}} = 6$ T					
Sextet 1	53.0(5)	0.50(3)	0.00	1.7(2)	48(3)
Sextet 2	49.5(4)	0.51(3)	0.00	1.79	26(3)
Sextet 3	57.3(4)	0.49(3)	0.00	1.42	26(3)

the lines will be 3:2:1:1:2:3. Fitting the zero-field spectra obtained at 6 K with the area ratio 3:p:1:1:p:3 gave values of $p = 2.1(2)$ for the as-prepared sample and $p = 2.2(2)$ for the

ground sample, indicating that the particles in the samples are indeed close to being randomly oriented.

Application of a field of 6 T parallel to the propagation direction of the gamma rays results in a splitting of the spectra into more than one sextet (see figures 5(c) and (d)). The spectra were well fitted using three sextets, one with broad lines and an average hyperfine field close to that found in zero applied field, as expected for a powder of randomly oriented antiferromagnetic material. In the as-prepared sample, the other two have magnetic splittings about 4.3 T larger and smaller than found in zero applied field. In the ground sample, the two sextets have magnetic splittings about 3.9 T larger and smaller than found in zero applied field. The two sextets are similar to those found in high-field spectra of ferrimagnetic materials such as maghemite, in which atoms belonging to the two sublattices have hyperfine fields parallel and antiparallel to the applied field, respectively. Thus, the Mössbauer spectrum resembles that expected from a mixture of ferrimagnetic and antiferromagnetic material.

The fit of the spectrum of the as-prepared sample with the three sextets as described above reveals that the difference between the splittings of the 'ferrimagnetic' sextets (sextets 2 and 3) is (58.3(4)–49.6(4) T) = 8.7(6) T instead of 12 T as expected for a perfectly aligned ferrimagnetic material in an applied field of 6 T. The values of the total field at the nucleus, B_{tot}, the hyperfine field, B_{hf}, and the applied field, B_{app}, are related by the expression

$$B_{\mathrm{hf}}^2 = B_{\mathrm{tot}}^2 + B_{\mathrm{app}}^2 - 2B_{\mathrm{tot}}B_{\mathrm{app}}\cos\theta. \tag{2}$$

Thus, the magnitude of the magnetic splitting can be explained by imperfect alignment of the spins to the applied field and the angles θ can be calculated for each of the two sublattices. These angles also determine the area ratios of the lines according to equation (1). A model where all the spins in each sublattice are aligned at the same angle to the applied field is assumed. Iteratively fitting the spectrum with the three sextets keeping the area ratios in the two 'ferrimagnetic' sextets fixed to the values calculated from the splitting, and leaving it free in the 'antiferromagnetic' sextet, gives the parameters in table 1, and values of $\theta \approx 41°$ and $\theta \approx 133°$ for the two sublattices. The fit to the 'antiferromagnetic' part of the spectrum gave a line area parameter $p = 2.0(2)$. The line widths were constrained to be pair-wise identical. The FWHM of the lines in the the 'antiferromagnetic' component were found to increase from 0.4 to 1.3 mm s^{-1} towards the outer lines, yielding a FWHM of the field distribution for these corresponding to 4.0 T. The widths of the lines in the two 'ferrimagnetic' sextets were constrained to be identical and found to be around 0.6 mm s^{-1}. The quadrupole shifts were fixed to 0.00 mm s^{-1} in all the sextets in accordance with the result from the spectrum in zero applied field.

Similar results are found by fitting the ground sample in the same way, with a splitting of the ferrimagnetic sextets of 7.9(6) T. The widths of the lines were very close to those found in the as-prepared sample. The results of the fitting are also summarized in table 1.

3.3. Magnetometry

Hysteresis loops of the undoped as-prepared and ground samples were measured in the VSM in the temperature interval from 80 to 300 K. At 80 K there is a clear hysteresis, which diminishes as the temperature is increased and has completely disappeared at 200 K in both samples. The 80 and 200 K magnetization data are shown in figure 6, with the central parts of these hysteresis curves shown in the inset. Above the temperature where the hysteresis disappears and below the Néel temperature (≈460 K [12]) the particles are superparamagnetic. In this regime the specific magnetization of the ith particle may be described by a Langevin function in combination with

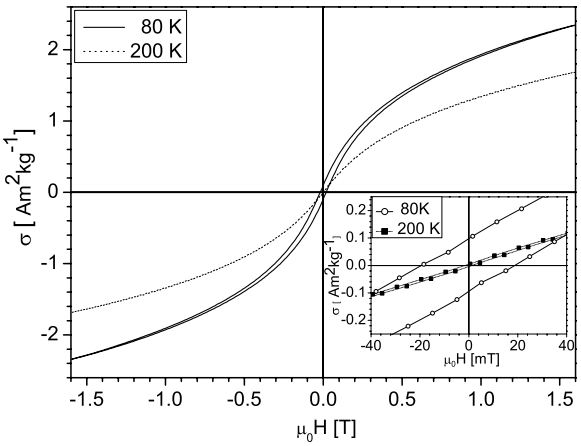

Figure 6. Hysteresis loops from the as-prepared sample at 80 and 200 K. The inset is a close up of the centre of the hystereses, showing the large remanence and coercivity of the particles at 80 K.

a linear term [6]:

$$\sigma_i = \frac{\mu_i}{m_i}\mathcal{L}\left(\frac{\mu_i B_{\text{app}}}{k_{\text{B}}T}\right) + \chi_{\text{A}}\frac{B_{\text{app}}}{\mu_0} \tag{3}$$

where $\mathcal{L}(x) = \coth(x) - \frac{1}{x}$ is the Langevin function, μ_i is the magnetic moment, m_i is the mass, χ_{A} is the antiferromagnetic mass susceptibility of the NiO, k_{B} is Boltzmann constant, μ_0 is the vacuum permeability and B_{app} is the applied field.

4. Discussion

4.1. Mössbauer data

When analysing the Mössbauer data, it must be realized that we do not directly observe the magnetic properties of the Ni^{2+} ions but obtain information on the substituted Fe^{3+} ions. It is reasonable to assume that the Fe^{3+} ions are randomly distributed among the two sublattices, such that the contribution to the net magnetization from the small number of Fe^{3+} ions is negligible. We also assume that the spins of the Fe^{3+} ions in otherwise defect-free environments are exchange coupled to the Ni^{2+} ions such that they are parallel (or antiparallel) to Ni^{2+} ions in the same layer. However, the requirement of charge balance presumably results in one cation vacancy for every two substituted Fe^{3+} ions. Therefore, some of the Fe^{3+} ions may have a vacancy in their near environments, and this may result in some local magnetic disorder. Also, the lack of neighbours creates non-cubic environments for Fe^{3+} ions at surface sites. However, the absence of quadrupole splitting in the superparamagnetic components indicates that a large fraction of the Fe^{3+} ions are in non-distorted cubic environments within the particles as expected for a homogeneous distribution of Fe^{3+} ions.

The fits of the 6 T Mössbauer spectra in both samples suggest that about half the Fe^{3+} spins are only weakly affected by the field, and the other half to some degree are aligned parallel or antiparallel with the field. Qualitatively, this may be explained by Néel's model for uncompensated spins in nanocrystals with even or odd numbers of layers with ferromagnetic order and alternating magnetization directions. In this model, particles with an even number of layers should behave as ideal antiferromagnets, whereas particles with an odd number of layers are expected to behave as ferrimagnets. Another possible explanation is that essentially

all particles have non-zero magnetic moments due to, for example, random occupation of sites in the surface layers. In such a model, the sublattice magnetization directions of all particles are expected to be strongly affected by the applied field. The 'antiferromagnetic' component in the 6 T spectrum may then be explained by Fe^{3+} ions, which are subject to strong localized spin-canting. Such a model with a ferrimagnetic component and a strongly canted component has been successfully used to explain Mössbauer data for MnZn ferrite [23] and for tin-doped maghemite and maghemite nanoparticles [24].

As the hyperfine field at a given site is antiparallel to the sublattice magnetization, application of a field to a ferrimagnetic material will lead to a predominance of hyperfine fields antiparallel to the applied field. Thus sextet 2 would be expected to have a larger area than sextet 3. However, within the uncertainty the areas of the two sextets do not differ. Therefore, the number of magnetic ions in the two sublattices differs only slightly. If the 'ferrimagnetic' component were due to particles with an odd number of defect-free layers, one should expect for the present particles with a thickness of ∼10 layers, that sextet 2 should have an area about 20% larger than sextet 3, assuming a small magnetic anisotropy, such that the spins align with the applied field. Since this is not the case, it is more likely that the second model, with more or less random occupation of surface sites and localized spin-canting, gives a better description of the sample. This is also in accordance with the HRTEM image (figure 1), which shows irregularities in the surface. Localized spin-canting may take place in environments with missing neighbour ions, i.e. around vacancies [25] and at some surface sites [26]. The canting angles depend primarily on the ratio between the exchange coupling constants to neighbouring ions [25].

If the applied magnetic field is too small to change the spin orientations of an antiferromagnetic material or strongly canted spins appreciably, it is simply added to the randomly oriented hyperfine fields and this results in a line broadening. Numerical integration of the vector sum of the applied field (6 T) and the hyperfine field at zero applied field for all orientations of a particle gives a broad distribution of hyperfine fields, that can be fitted with a broad Lorentzian centred around 53.6 T with a FWHM of 1.1 mm s^{-1}. This is close to the widths estimated from the fit of the 'antiferromagnetic' component in the 6 T spectra of 1.3 mm s^{-1} in both the as-prepared and ground samples.

In a classical mean-field model, the energy of an antiferromagnet with uniaxial anisotropy and an uncompensated magnetic moment may be written as (assuming low temperature, thus neglecting thermal effects) [27]

$$E = N_a S g \mu_B \big[B_E \xi \cos(\theta_a - \theta_b) - \tfrac{1}{2} B_A \cos^2(\theta_a - t) - \tfrac{1}{2} B_A \xi^2 \cos^2(\theta_b - t) - B_{app}(\cos\theta_a + \xi \cos\theta_b) \big]. \quad (4)$$

Here S is the spin of the individual ions and N_a and $N_b = \xi N_a$ ($\xi \leqslant 1$) are the numbers of spins in the two sublattices. B_E, B_A and B_{app} are the exchange, anisotropy and applied fields, respectively. In bulk NiO there are two magnetocrystalline contributions to the anisotropy: an out-of-plane anisotropy which keeps the spins in an easy plane, and a much weaker in-plane anisotropy keeping the spins in a direction within this plane [2]. As the out-of-plane anisotropy is much larger than the in-plane anisotropy our model will consider spins confined to the plane, i.e. with an infinite out-of-plane anisotropy. The in-plane anisotropy field is given by $B_A = \frac{K}{M} = \frac{2\kappa S}{g\mu_B}$, where K is the anisotropy energy density, M is the sublattice magnetization and κ is the single ion anisotropy energy. It is assumed that all three fields are constant everywhere within the particle. θ_a, θ_b are the angles between the two sublattice magnetization directions and the applied field, and t is the angle between the in-plane anisotropy field of the particle (the easy axis) and the applied field.

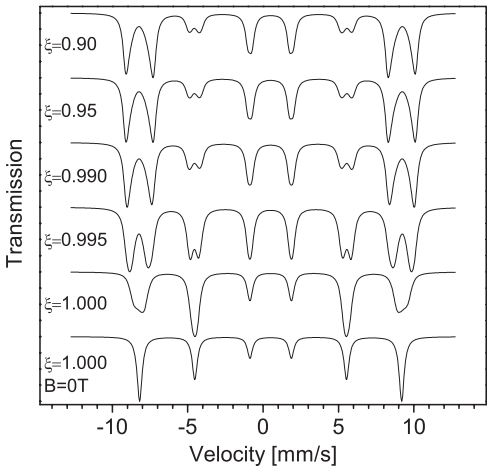

Figure 7. Simulated Mössbauer spectra of ideal antiferromagnetic particles with uncompensated spins. All spectra are normalized to the same maximum absorption. The spectra are simulated with exchange and anisotropy fields as described in the text, and an applied field of 6 T. The values of ξ are indicated. The bottom spectrum was simulated for zero applied field and $\xi = 1.000$.

We have simulated Mössbauer spectra using this model. We used the bulk value of the exchange field $B_E = 980$ T [2], and the applied field was set to $B_{app} = 6$ T as in the Mössbauer spectroscopy experiment. The in-plane anisotropy field $B_A = 0.014$ T was derived from the anisotropy constant found from the temperature dependence of the magnetic hyperfine splitting of very weakly interacting particles at low temperatures, as described in [22]. It is clear that regardless of the value of ξ, the exchange field will dominate, so the two sublattices will be very close to being antiparallel. In the perfect antiferromagnetic case, where $\xi = 1$, a moderate applied field cannot compete with the exchange field and the spin directions are mainly governed by the anisotropy field. However, only a small difference in the size of the total spins of the two sublattices can result in $B_{app}(1 - \xi) > B_A$, and then the applied field will dominate the alignment of the spins for all directions of the anisotropy field. In the regime where $B_A \approx B_{app}(1 - \xi)$, i.e. when $\xi \approx 0.990$, both the applied field and the anisotropy field will strongly influence the spin directions. For each orientation of the easy axis, the spin directions giving the lowest energy were used to generate a Mössbauer spectrum. These spectra were weighted by $\sin t$ and added to cover all orientations of the anisotropy field. Figure 7 shows Mössbauer spectra simulated by this procedure for values of ξ between 0.900 and 1.000 in an applied field of 6 T. A spectrum with zero applied field is also shown for comparison. As expected, the spectrum changes drastically above $\xi \approx 0.99$. Here the lines broaden, especially the pairs of lines in lines 1 and 6, and the separation between the two sextets changes.

Lorentzians have been fitted to the series of simulated spectra with varying ξ. The difference in the magnetic hyperfine splitting between the two sextets is plotted in figure 8(a) and the average areas of line pairs in lines 2 and 5 are plotted in figure 8(b). Using figure 8(a) the hyperfine field splittings measured in the experimental spectra give values of $\xi = 0.993(1)$ and 0.995(1) in the as-prepared and ground samples, respectively. The simulated spectra with $\xi = 0.993$ and 1.000 have been added. Overlaying this sum of spectra with the experimentally measured spectrum of the as-prepared sample gives a reasonably good agreement between the two, as illustrated in figure 9(a). The same is also true when adding simulated spectra with $\xi = 0.995$ and 1.000 and overlaying this with the spectrum from the ground sample (see figure 9(b)).

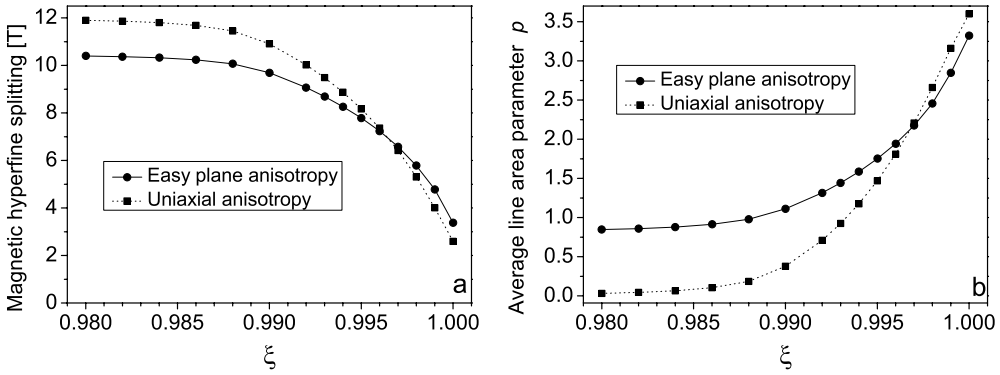

Figure 8. Parameters obtained by fitting Lorentzian line shapes to the simulated Mössbauer spectra as a function of the fraction of uncompensated moment. In both figures data are shown for the model in which the spins are confined to a plane with an easy direction (full line) as well as one assuming uniaxial anisotropy (dotted line). (a) The magnetic hyperfine field splitting between the two 'ferrimagnetic' sextets. (b) The average line area parameter, i.e. the area of lines 2 and 5.

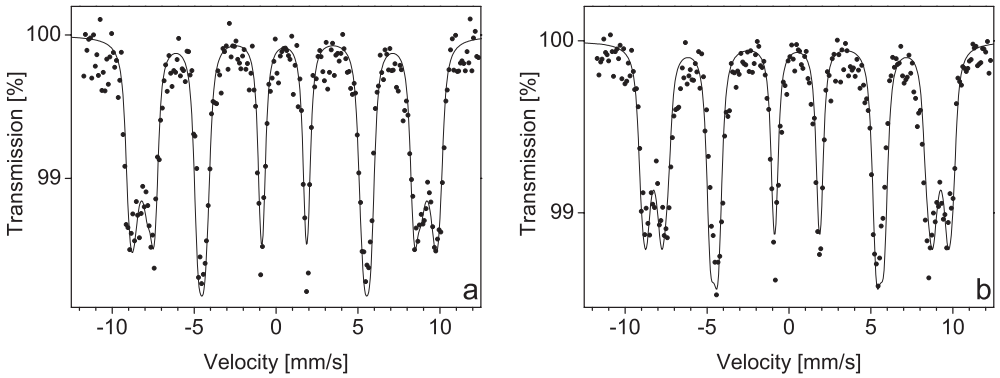

Figure 9. Overlay of the experimental data and the simulated spectra for both samples. (a) Simulated spectrum for the as-prepared sample consisting of the sum of a spectrum with $\xi = 1.000$ and one with $\xi = 0.993$. (b) Simulated spectrum for the ground sample consisting of the sum of a spectrum with $\xi = 1.000$ and one with $\xi = 0.995$.

Thus, the Mössbauer data can be explained by a model for an antiferromagnet with an easy plane anisotropy and uncompensated spins corresponding to about $(1 - \xi) = 0.005(1)$ and $(1 - \xi) = 0.007(1)$ for the as-prepared and ground samples, respectively, in addition to a number of ions with strong local spin-canting in both samples.

In nanoparticles the anisotropy is dominated by other contributions than in the bulk, such as, for example, surface anisotropy. In numerous studies of different magnetic nanoparticles it has been found that a simple uniaxial anisotropy (as in (4)) gives a good description of the magnetic properties. The simulated Mössbauer spectra have also been simulated using a model with uniaxial anisotropy, i.e. with zero out-of-plane anisotropy. The splittings of the sextets and average line area parameters obtained from this calculation are also presented in figures 8(a) and (b). It can be seen that at the relevant splittings the two models give similar values of the uncompensated moment.

4.2. Magnetization data

The VSM data, obtained above the blocking temperature, were first fitted assuming only one size of the magnetic moment, i.e. using (3) with $\sigma = N\sigma_i$, where N is the number of particles in the sample. However, the parameters obtained from these fits were apparently not reliable. For example, the value of χ_A was about seven times larger than the bulk value in both samples, although earlier experimental studies suggest that it is independent of particle size [6], and it was found to decrease with increasing temperature, which is opposite to the expected behaviour of an antiferromagnetic material. Further, the estimated average particle size in both samples was about seven to eight times larger than that found by electron microscopy, and the number of particles per gram apparently decreased with increasing temperature. It thus seemed likely that the contributions to the magnetization from the particles with the smallest moments could be well fitted with a straight line, and therefore the Langevin contributions from these particles were in practice indistinguishable from the linear term in (3). Silva *et al* [28] have recently pointed out that fitting magnetization data in this way can result in an apparent increase of the magnetic moment with temperature, because the size distribution is not correctly taken into account.

Another possible way of fitting the VSM data could be to fix the value of χ_A to the bulk value and fit the magnetization curves with a distribution of magnetic moments. However, unless the magnetic anisotropy is negligible compared to the Zeeman energy, it will give rise to deviations of the magnetization curves from Langevin functions [29, 30]. In nanoparticles with small magnetic moments, the deviations may be significant, and therefore the estimated moment distributions will not be reliable. To circumvent these complications, we have instead analysed the low-field data and estimated the initial susceptibility, which is independent of the anisotropy in samples with a random orientation of the easy axes [29–31]. For small applied fields, the magnetization of an assembly of nanoparticles can be approximated by

$$\sigma \approx \frac{1}{m}\sum_{i=1}^{N}\frac{\mu_i^2 B_{\mathrm{app}}}{3k_{\mathrm{B}}T} + \chi_{\mathrm{A}}\frac{B_{\mathrm{app}}}{\mu_0} = \frac{nB_{\mathrm{app}}}{3k_{\mathrm{B}}T}\langle\mu^2\rangle + \chi_{\mathrm{A}}\frac{B_{\mathrm{app}}}{\mu_0}. \tag{5}$$

Here m is the mass of the sample, and n is the number of particles per gram. The initial mass susceptibility is given by

$$\chi_{\mathrm{g}} = \frac{\mu_0\sigma}{B_{\mathrm{app}}} = \frac{n\mu_0}{3k_{\mathrm{B}}T}\langle\mu^2\rangle + \chi_{\mathrm{A}}. \tag{6}$$

We assumed that χ_A has a bulk value of 1.1×10^{-7} m^3 kg^{-1} in accordance with the results of an earlier study [6]. χ_A increases by about 10% from 160 to 300 K [32], but as χ_g was found to be $1.30(2)\times10^{-6}$ m^3 kg^{-1} $\gg \chi_A$ at 300 K in the as-prepared sample, the exact value of χ_A is not significant. Assuming the particle volume found by TEM ($\sim$300 nm^3), we arrive at an average of the squared moment of $\langle\mu^2\rangle \approx 2.74\times10^5\ \mu_B^2$ at 300 K in the as-prepared sample. For a lognormal distribution of the moments with a standard deviation between $\sigma_{\ln} = 0.4$ and 0.8 we have found that $\sqrt{\langle\mu^2\rangle}$ is between $1.1\langle\mu\rangle$ and $1.3\langle\mu\rangle$. Because the sublattice magnetization, and thus the measured moment of the NiO particles, decreases with increasing temperature [12], the low-temperature moment of the particles is about 25% larger than that measured at 300 K. Thus these two corrections counteract each other, depending on $\sigma_{\ln}$. Hence, we arrive at an average uncompensated moment of $\langle\mu\rangle \approx 520\ \mu_B$ corresponding to $\approx$260 Ni^{2+} ions each with an effective moment of $\mu_{\mathrm{eff}} = g\mu_B S = 2\ \mu_B$. Thus, the fraction of uncompensated spins $(1-\xi)$ corresponds to around 0.032 of the Ni^{2+} ions in one of the sublattices in the as-prepared sample. Note that whereas q denotes the fraction of uncompensated moment relative to the total number of ions, $(1-\xi)$ gives the fraction of uncompensated spins relative to the number of spins in one sublattice. In the ground sample a value of $\chi_g = 0.90(2)\times10^{-6}$ m^3 kg^{-1} was

found, yielding $\langle\mu^2\rangle \approx 1.83 \times 10^5\ \mu_B^2$ at 300 K. This gives a moment of $\langle\mu\rangle \approx 430\ \mu_B$ corresponding to a fraction of uncompensated spins, $(1 - \xi)$, of about 0.026.

There may be several reasons for the larger values of the uncompensated moments found by magnetometry compared to those obtained from the Mössbauer data. One reason may be that whereas the signal in Mössbauer spectroscopy is weighted by the volume of the particles, in magnetometry the signal is weighted by the moment. If there is a particle size distribution, and the moment of the small particles is larger than that of the large particles, a larger uncompensated moment will be observed by magnetometry than by Mössbauer spectroscopy. Another reason for this deviation may be magnetic interactions between the particles, especially in the as-prepared sample. Suppose the sample consists of clusters of strongly interacting particles, each containing N_c particles of moment μ_p. Then an analysis based on (5) according to the procedure described above and using as n the number of particles (not clusters) per gram will result in an estimate of the average of the squared moment of $\langle\mu^2\rangle \approx N_c\langle\mu_p^2\rangle$. Thus the calculated value of the uncompensated moment will be larger than the real value by a factor of $\sqrt{N_c}$. In fact, as mentioned above, the Mössbauer data in figure 4 show that there are indeed significant interactions between the particles in the as-prepared sample. In the ground sample the interparticle interactions are significantly less, but still present. As described above, a sample with negligible interaction has been prepared by coating separated particles with phosphate. However, the amount of phosphate compared to NiO and is not known. Further, the magnetic properties of the phosphate and a possible iron–phosphate interface layer are not known, so magnetization measurements on this sample would not be reliable. Mössbauer spectra from the sample contained a doublet component, presumably due to an iron–phosphate interface layer, that splits up into a sextet at low temperatures, making the sample unsuited for the high-field low-temperature experiments. As the effective fields from the interactions are weak compared to the applied field of 6 T, the value of the uncompensated moment, derived from the high-field Mössbauer spectrum, is only weakly affected by interactions between the particles. Thus, it is reasonable to assume that the uncompensated magnetic moments are of the order of 0.6% of the number of spins in one sublattice, as estimated from the Mössbauer data.

Thermoinduced magnetization has been proposed to explain the increase in the magnetic moment with temperature observed in nanoparticles of some antiferromagnetic materials [33, 34]. Applying the expression derived in [33] for this effect in a perfect antiferromagnet gives a moment of $\approx$100 μ_B at 300 K using the value of the in-plane anisotropy constant given below. Therefore, this contribution does not seem to be of major importance in the present NiO nanoparticles.

Using the particle size and shape obtained from TEM, we found that if the uncompensated magnetic moment were due to random occupation of surface sites, the number of uncompensated spins, $(1 - \xi)$, should be of the order of 0.003. This is in reasonable agreement with the values estimated from Mössbauer data. If the uncompensated moment were due to random occupation of sites throughout the particles one should expect a number of uncompensated spins, $(1 - \xi)$, of the order of 0.016, and if the particles consisted of even or odd numbers of defect-free planes, one would expect a number of uncompensated spins, $(1 - \xi)$, corresponding to about 20% of the number of spins in one sublattice. Thus, the data support the model with random occupation of surface sites. It is, however, likely that other effects, related to, for example, surface steps and localized spin-canting, also influence the size of the uncompensated moment. For spherical NiO nanoparticles simulations have shown that the magnetic structure may be more complex than the bulk magnetic structure [7, 35] and such phenomena may also be present in plate-shaped particles. However, neutron diffraction data from NiO nanoparticles prepared in the same way as the present samples were in accordance with a magnetic structure identical to that of bulk NiO [12].

Within the uncertainty, the two values of the uncompensated moment obtained from the Mössbauer data are the same, indicating that the interparticle interactions do not affect the uncompensated moment. Magnetization measurements gave two values that are clearly different, indicating varying degrees of clustering of the particles in the two samples as expected from the temperature series of Mössbauer data.

5. Conclusion

We have shown that high-field Mössbauer data are very sensitive to the magnitude of the uncompensated magnetic moment in nanoparticles of antiferromagnetic materials. This technique can be used to quantify the uncompensated magnetic moments in magnetic nanoparticles. Thus, we have found that the uncompensated magnetic moments in NiO nanoparticles correspond to about 0.7(1)% and 0.5(1)% of the number of Ni^{2+} ions in one sublattice in an as-prepared and a ground sample, respectively. The two samples display varying degrees of interparticle interaction. The measured moments are close to what is expected for a random occupation of surface sites in both samples, indicating that this is the main contribution to the uncompensated moment independent of interparticle interactions.

The analysis of the results of the magnetization measurements for the NiO particles showed that it is not straightforward to estimate the uncompensated moment from magnetization data. This is because of the broad distribution of magnetic moments, the influence of the magnetic anisotropy and the interparticle exchange interactions in both samples. An estimate, based on the initial susceptibility, which is independent of the magnetic anisotropy, gave uncompensated moments of about 3.2% and 2.6% in the as-prepared and ground samples, respectively. The larger values, compared to those obtained from Mössbauer data, can be explained by interparticle interactions in both samples as well as a difference in the sensitivity of magnetization measurements and Mössbauer spectroscopy to a particle size distribution.

Acknowledgments

The work was supported by the Danish Technical Research Council through the framework programme Nanomagnetism. The authors are grateful to H K Rasmussen for assistance with the low-temperature Mössbauer spectroscopy measurements and to F Bødker and L Lilleballe for preparation of the particles.

References

[1] Shull C G, Strauser W A and Wollan E O 1951 *Phys. Rev.* **83** 333
[2] Hutchings M T and Samuelsen E J 1972 *Phys. Rev.* B **6** 3447
[3] Bartel L C and Morosin B 1971 *Phys. Rev.* B **3** 1039
[4] Richardson J T and Milligan W O 1956 *Phys. Rev.* **102** 1289
[5] Schuele W J and Deetscreek V D 1962 *J. Appl. Phys.* **33** 1136
[6] Richardson J T, Yiagas D I, Turk B, Forster K and Twigg M V 1991 *J. Appl. Phys.* **70** 6977
[7] Kodama R H, Makhlouf S A and Berkowitz A E 1997 *Phys. Rev. Lett.* **79** 1393
[8] Makhlouf S A, Parker F T, Spada F E and Berkowitz A E 1997 *J. Appl. Phys.* **81** 5561
[9] Berkowitz A E, Kodama R H, Makhlouf S A, Parker F T, Spada F E, McNiff E J Jr and Foner S 1999 *J. Magn. Magn. Mater.* **196/197** 591
[10] Ichiyanagi Y, Wakabayashi N, Yamazaki J, Yamada S, Kimishima Y, Komatsu E and Tajima H 2003 *Physica* B **329–333** 862
[11] Néel L 1961 *Comp. Rend.* **252** 4075
[12] Klausen S N, Lindgård P-A, Bødker F and Mørup S 2002 *Phys. Status Solidi* a **189** 1039
[13] Bødker F, Hansen M F, Koch C B, Lefmann K and Mørup S 2000 *Phys. Rev.* B **61** 6826

[14] Bødker F, Hansen M F, Koch C B and Mørup S 2000 *J. Magn. Magn. Mater.* **221** 32
[15] Xu M, Bahl C R H, Frandsen C and Mørup S 2004 *J. Colloid Interface Sci.* **279** 132
[16] Bahl C R H and Mørup S 2006 *Nanotechnology* submitted
[17] http://www-llb.cea.fr/fullweb/
[18] Fiévet F, Germi P, de Bergevin F and Figlarz M 1979 *J. Appl. Crystallogr.* **12** 387
[19] Rodoc D, Spasojevic V, Kusigerski V, Tellgren R and Rundlof H 2000 *Phys. Status Solidi* b **218** 527
[20] Hansen M F, Koch C B and Mørup S 2000 *Phys. Rev.* B **62** 1124
[21] Frandsen C and Mørup S 2003 *J. Magn. Magn. Mater.* **266** 36
[22] Mørup S, Frandsen C, Bødker F, Klausen S N, Lefmann K, Lindgård P-A and Hansen M F 2002 *Hyperfine Interact.* **144/145** 347
[23] Anhøj T A, Bilenberg B, Thomsen B, Damsgaard C D, Rasmussen H K, Jacobsen C S, Mygind J and Mørup S 2003 *J. Magn. Magn. Mater.* **260** 115
[24] Helgason Ö, Rasmussen H K and Mørup S 2006 *J. Magn. Magn. Mater.* doi:10.1016/j.jmmm.2005.09.036
[25] Mørup S 2003 *J. Magn. Magn. Mater.* **266** 110
[26] Kodama R H, Berkowitz A E, McNiff E J Jr and Foner S 1996 *Phys. Rev. Lett.* **77** 394
[27] Pankhurst Q A 1991 *J. Magn. Magn. Mater.* **101** 291
[28] Silva N J O, Amaral V S and Carlos L D 2005 *Phys. Rev.* B **71** 184408
[29] Hanson M, Johansson C and Mørup S 1993 *J. Phys.: Condens. Matter* **5** 725
[30] Garcia-Palacios J L 2000 *Adv. Chem. Phys.* **112** 1
[31] Madsen D E, Mørup S and Hansen M F 2006 *J. Magn. Magn. Mater.* doi:10.1016/j.jmmm.2005.11.033
[32] Singer J R 1956 *Phys. Rev.* **104** 929
[33] Mørup S and Frandsen C 2004 *Phys. Rev. Lett.* **92** 217201
[34] Mørup S and Hansen B R 2005 *Phys. Rev.* B **72** 24418
[35] Lindgård P-A 2003 *J. Magn. Magn. Mater.* **266** 88

Paper IX

INSTITUTE OF PHYSICS PUBLISHING NANOTECHNOLOGY
Nanotechnology **17** (2006) 2835–2839 doi:10.1088/0957-4484/17/12/001

Varying the exchange interaction between NiO nanoparticles

Christian R H Bahl[1,2] **and Steen Mørup**[1]

[1] Department of Physics, Building 307, Technical University of Denmark, DK-2800 Kongens Lyngby, Denmark
[2] Materials Research Department, Risø National Laboratory, DK-4000 Roskilde, Denmark

Received 8 March 2006
Published 26 May 2006
Online at stacks.iop.org/Nano/17/2835

Abstract
We demonstrate that exchange interactions between antiferromagnetic nanoparticles of ^{57}Fe-doped NiO can be varied by simple macroscopic treatments. Mössbauer spectroscopy studies of the superparamagnetic relaxation behaviour show that grinding or suspension in water of nanoparticles of NiO can significantly reduce interparticle interactions. Slow drying of aqueous suspensions of NiO nanoparticles did not lead to enhanced interparticle interactions. This is opposite to the behaviour of α-Fe_2O_3 (hematite) nanoparticles.

1. Introduction

Numerous studies have shown that aggregation of nanoparticles can have a significant influence on their properties [1–9]. For example, it has been found that nanoparticles of TiO_2 [1, 2] as well as α-Fe_2O_3 [8] can have a tendency to attach in such a way that neighbouring particles have the same crystallographic orientation. In studies of 3 nm particles of ZnS it has been found that the internal structure becomes less disordered when the particles aggregate, and the phenomenon was found to be reversible [7]. It has also been found that the agglomeration of antiferromagnetic nanoparticles can have a significant influence on the magnetic properties [3–6, 8, 9].

NiO is an antiferromagnetic material that has a wide range of technological applications at the nanoscale. For example, nanoparticles of NiO have been found to be promising as an electrode material for lithium ion batteries [10]. Also, nanoscale NiO rings have been found to work as catalysts for CO oxidation [11]. Thin films of NiO have been applied to produce exchange bias in spin valves [12, 13]. NiO thin films have also been used in solar cells [14] and as an electrochromic material, where the application of a voltage is used to change its optical properties [15]. For technological applications, a detailed understanding of the size, morphology, magnetic properties and interparticle interactions of nanoscale NiO could be important [16].

Several studies have shown that the superparamagnetic relaxation is very sensitive to magnetic interactions between nanoparticles. In samples of ferro- and ferrimagnetic nanoparticles, dipole interactions can be important, but, in the case of antiferromagnetic nanoparticles, dipole interactions are too weak to have a significant influence on the relaxation. However, if the particles are in close proximity, exchange interaction between surface atoms belonging to neighbouring particles can result in strong suppression of superparamagnetic relaxation. This has been demonstrated in Mössbauer studies of nanoparticles of α-Fe_2O_3 [4–6, 8] and NiO [3] as well as in studies of mixtures of nanoparticles of different materials [6]. It has been found that the magnetic interaction between α-Fe_2O_3 nanoparticles can be varied by exposing samples to simple treatments like grinding [8, 17], ultrasonic treatments of suspensions [18] and subsequent drying [18]. In this paper we present a study of similar treatments of samples of NiO. Surprisingly, the influence of such treatments on NiO nanoparticles differs significantly from the behaviour of α-Fe_2O_3.

2. Methods

$Ni(OH)_2$ was chemically precipitated and subsequently freeze dried, as described elsewhere [3]. This results in a fine, bright-green powder. $Ni(OH)_2$ powder was subsequently heated in air at different temperatures for 3 h to produce NiO nanoparticles with different particle sizes. Particles obtained by heating at 300 °C were selected for studies of interparticle interactions. A $Ni(OH)_2$ sample doped with 0.5 at.% ^{57}Fe relative to Ni (referred to as sample A in the following) was prepared in the same way as the undoped sample in order to allow for Mössbauer spectroscopy studies. The sample obtained by heating sample A at 300 °C for 3 h is referred to as Ah. This sample was subsequently subjected to 15 min of grinding

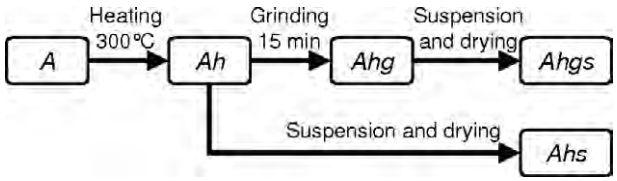

Figure 1. Flow chart for the sample preparation and naming of the samples.

by hand in an agate mortar, resulting in a sample referred to as Ahg. Finally, the sample was dispersed in 10 ml of demineralized water under mild ultra-sonic treatment, before being left to dry in atmospheric air in a small beaker glass covered by a perforated lid. The drying took around five days, resulting in the sample Ahgs. In addition to this, a part of the Ah was suspended in water, exposed to weak ultrasonic treatment, and dried as described above, without having been ground first. This sample is known as Ahs. For clarity, a flow chart of the sample preparation and naming of the samples is shown in figure 1.

The amount of material of the ^{57}Fe-doped samples was too small for detailed x-ray diffraction (XRD) studies. Therefore, samples were prepared from a larger amount of the undoped $Ni(OH)_2$, which was heated at 300 °C and subjected to treatments similar to those for the doped samples. In order to handle grinding of the larger amount of material, grinding was performed in a Retsch agate ball mill at low energy.

Mössbauer spectra of all the ^{57}Fe-doped samples at all stages of preparation were obtained at temperatures between 80 and 200 K in a liquid nitrogen cryostat by the use of conventional constant-acceleration spectrometers with sources of ^{57}Co in rhodium, calibrated at room temperature with a 12.5 μm thick α-Fe foil. A spectrum of the $Ni(OH)_2$ was recorded at 15 K in a closed-cycle helium refrigerator.

XRD patterns were recorded using a Philips PW 1820 diffractometer with a Cu anode. Transmission electron microscopy was performed using a JEOL 3000 FEG microscope equipped with a 16 Mpix CCD camera.

3. Results

The XRD patterns were profile refined using the FullProf software package [19]. As described elsewhere [20], a model that assumes plate-shaped particles was employed to fit both the $Ni(OH)_2$ and the NiO data.

The XRD pattern recorded from the $Ni(OH)_2$ sample was found not to contain any peaks due to impurities, showing that the $Ni(OH)_2$ was pure within the uncertainty of the measurement. The pattern contains narrow and broad lines, as shown in figure 2, and could be fitted well, assuming plate-shaped particles. $Ni(OH)_2$ has a hexagonal structure with the space group $P\bar{3}m1$ and the [001] direction was found to be perpendicular to the plate face. The estimated diameter was ∼7.4 nm and the estimated thickness was ∼1.5 nm.

After heating the $Ni(OH)_2$ at different temperatures $\geqslant$250 °C, the XRD patterns showed only diffraction peaks due to NiO, indicating that all the $Ni(OH)_2$ had been transformed; see figure 2. NiO has a cubic structure with the space group $Fm3m$. The plate-shape of the $Ni(OH)_2$ particles was

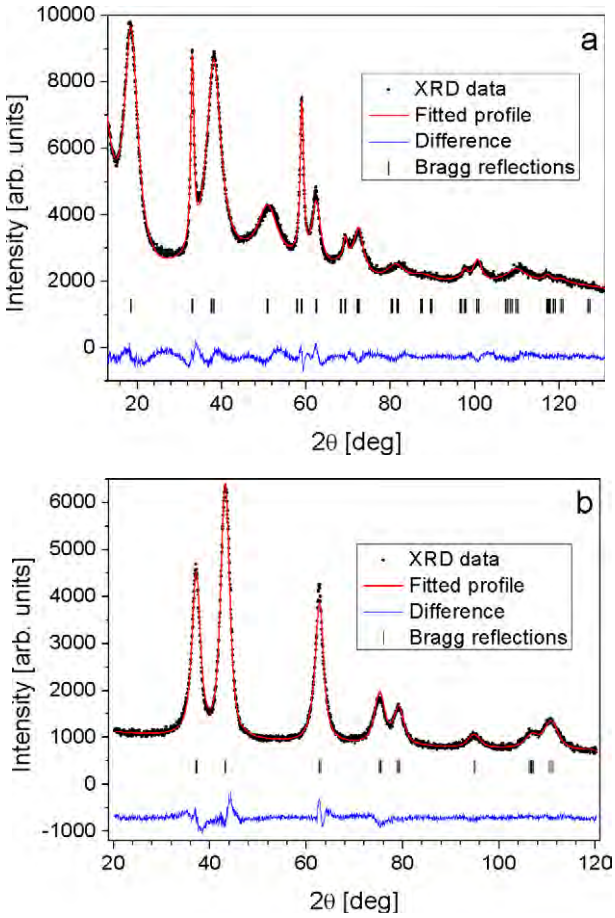

Figure 2. Refined XRD patterns of two of the samples: (a) the $Ni(OH)_2$ (sample A); (b) the unground NiO (sample Ah). The vertical lines indicate the calculated Bragg reflections.

(This figure is in colour only in the electronic version)

Table 1. Dimensions of NiO nanoparticles prepared by heating $Ni(OH)_2$ at different temperatures.

Heating temperature (°C)	Thickness (nm)	Diameter (nm)
250	1.6	7.2
300	2.3	7.9
350	3.7	11.0
600	12	38

inherited by the NiO particles after heating. However, the actual size of the NiO particles is dependent on the heating temperature. The particle sizes are summarized in table 1. At a heating temperature of 250 °C, which is the lowest temperature where full transformation to NiO occurred, the particle size is very similar to that of the $Ni(OH)_2$ particles. As the heating temperature increases, so does the particle size.

Grinding, suspending and drying, as described above, did not change the estimated sizes and shapes of the particles.

The plate-shaped nature of the $Ni(OH)_2$ and NiO particles produced by heating at 300 °C was confirmed by transmission electron microscopy (TEM) studies. The samples consist of loosely packed agglomerates of randomly oriented plates. The thickness of the NiO particles measured in TEM compare well with that found by XRD, but the plate diameter was found to

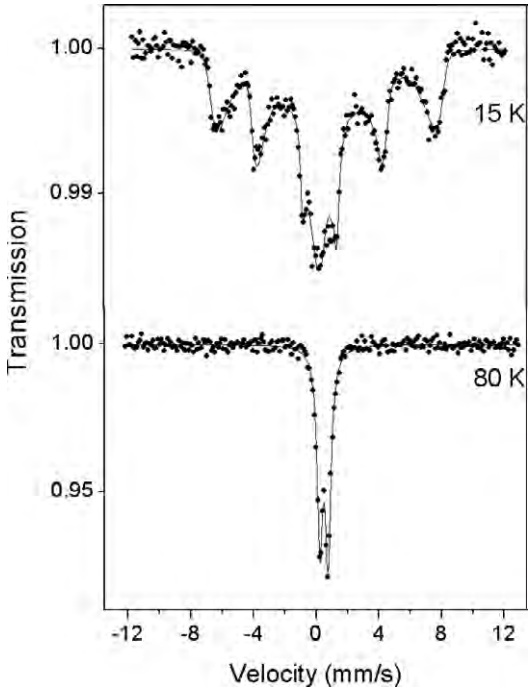

Figure 3. Mössbauer spectra of the $Ni(OH)_2$ sample. At 80 K, the line shows fits to the data consisting of a doublet. In the 15 K data, the line displays the fit to a hyperfine field distribution.

be larger (about 13 nm). However, as shown previously, the plate diameter is generally underestimated by XRD compared to TEM measurements, probably due to the size distribution of the particles making certain XRD reflections difficult to fit [20].

The Mössbauer spectrum of the sample of ^{57}Fe-doped $Ni(OH)_2$ (sample A) at 80 K consists of a paramagnetic doublet; see figure 3. The isomer shift is 0.49 mm s^{-1} and the quadrupole splitting is 0.52 mm s^{-1}. At 15 K, the spectrum shows the presence of a sextet displaying a broad distribution of hyperfine fields, with a maximum around 45 T, but still with a doublet component, as illustrated in figure 3. A temperature of 15 K is well below the Néel temperature of $T_N = 30$ K [21], so the doublet is presumably due to particles which exhibit fast superparamagnetic relaxation.

Mössbauer spectra of ^{57}Fe-doped NiO, prepared from sample A, are shown in figure 4. The spectra of the sample Ah display a magnetically split sextet at 80 K, which undergoes a gradual collapse to a singlet at 200 K due to fast superparamagnetic relaxation at this temperature. The isomer shifts and magnetic hyperfine fields at low temperatures show that iron is present as Fe^{3+} in the high-spin state. The requirement of charge balance will presumably result in some cation vacancies in the NiO. However, the absence of quadrupole splitting in the superparamagnetic component indicates that Fe^{3+} is present in cubic environments, as expected if it substitutes Ni^{2+} in NiO. This indicates a homogeneous substitution of Fe^{3+} predominantly in the interior of the NiO particles [20]. The lines of the sextets are asymmetrically broadened, and very broad features are observed at 150 K. The spectra of the sample after grinding (sample Ahg) and after subsequent suspension and drying (sample Ahgs) are very similar and show a superposition of a sextet and a singlet at 80 K. At 150 and 200 K, they only show the presence of a singlet. This shows that the superparamagnetic relaxation is much faster after these treatments. The Mössbauer spectra of the dried suspension of the sample Ahs show a more collapsed spectrum at 150 K than the sample Ah, but the spectrum has a broader line than those of samples Ahg and Ahgs at the same temperature.

We have re-measured the as-prepared NiO sample (with interacting nanoparticles) from [3] and found that storage in air for about six years had resulted in faster superparamagnetic relaxation.

4. Discussion

Mössbauer spectra of non-interacting and weakly interacting magnetic nanoparticles typically consist of a superposition of a sextet due to particles with superparamagnetic relaxation time longer than the timescale of Mössbauer spectroscopy and a doublet or singlet due to particles with shorter relaxation times. The relative area of the doublet or singlet increases with increasing temperature. However, in samples with strong interactions between the particles, the spectra typically consist of sextets in a broad range of temperatures, but with increasing temperature the lines become broadened and the average hyperfine splitting decreases [4–6]. Thus, the asymmetric broadening of the lines in the spectra of sample Ah, especially at 150 K, is typical for samples of nanoparticles with strong interparticle interactions. Grinding the sample Ah results in the appearance of a singlet at 150 K, indicating fast superparamagnetic relaxation. Since the XRD results did not show any indication of a decrease in the particle size, these results show that the interparticle interactions are strongly reduced after grinding. The subsequent suspension and drying only had little influence on the relaxation. The Mössbauer spectra of samples Ahg and Ahgs are typical for weakly interacting particles, and even at 80 K a large fraction of the particles are superparamagnetic.

When the as-prepared NiO sample (Ah) was suspended and subsequently dried, the interactions were reduced (sample Ahs), leaving essentially only a broad singlet in the Mössbauer spectrum at 150 K. The strength of interactions in this sample seems to be intermediate between those in samples Ah and Ahg. The mild ultrasonic treatment applied to the particles in sample Ahs might cause the reduction in exchange interactions. However, Mössbauer measurements from a sample that was prepared in exactly the same manner without this ultrasonic treatment gave very similar spectra. Thus the reduction in the exchange interaction between the particles is not caused by the ultrasonic treatment, but just by suspension.

When the NiO particles are formed at 250 °C, which is the minimum transformation temperature, the dimensions are almost the same at those of the $Ni(OH)_2$ precursor particles. The formation of larger particles at higher temperatures is presumably due to surface diffusion, during which atoms can also move to the interfaces and contribute to enhanced magnetic interaction. It is therefore not surprising that NiO nanoparticles, formed by heating a powder of $Ni(OH)_2$ nanoparticles at 300 °C, are significantly influenced by interparticle interactions. When grinding the NiO particles,

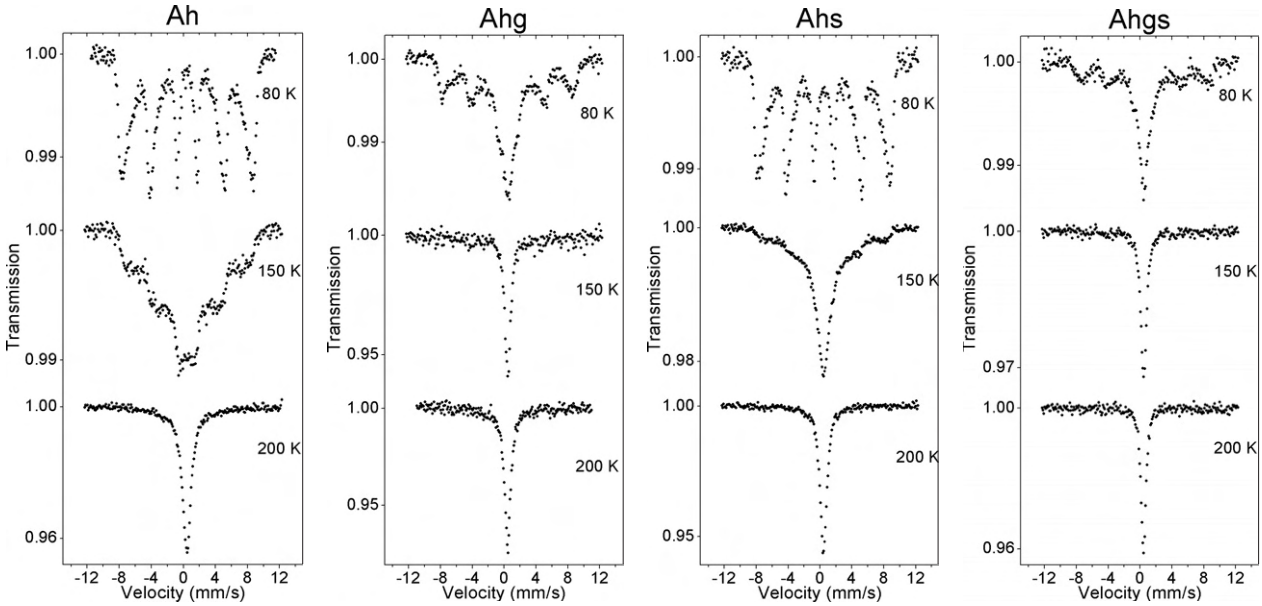

Figure 4. Mössbauer data recorded from the doped NiO sample before (Ah) and after (Ahg) the grinding treatment, after suspension and drying of the unground sample (Ahs) and after suspension and drying of the ground sample (Ahgs), as described in the text. The spectra were obtained at the indicated temperatures.

these are separated from each other, resulting in a significant reduction in the interparticle interactions.

It is interesting to compare the present results with those obtained for α-Fe_2O_3 nanoparticles treated in similar ways. α-Fe_2O_3 nanoparticles are often prepared in aqueous suspensions and, after drying, the magnetic properties can be significantly influenced by interparticle interactions in agglomerates. Gentle grinding by hand as well as strong ultrasonic treatments significantly reduce the interactions [8, 16, 18] as is also seen for NiO nanoparticles in the present study. However, when the suspended, ultrasonically separated α-Fe_2O_3 nanoparticles were dried, the interparticle interaction was re-established [18], but the present study shows that the strong interaction is not re-established during drying of aqueous suspensions of NiO nanoparticles. Also, contrary to NiO particles, α-Fe_2O_3 nanoparticles were not re-dispersed when they were suspended in water and exposed to mild ultrasonic treatments [18]. Thus α-Fe_2O_3 particles formed in water seem to form stronger interparticle bonds than NiO particles that are formed by thermal decomposition of $Ni(OH)_2$ nanoparticles in air. It has previously been observed in slow drying of suspended mixtures of α-Fe_2O_3 and NiO nanoparticles that the NiO nanoparticles impede the re-establishment of interparticle interactions of α-Fe_2O_3 nanoparticles [6].

The reason for the different behaviour of hematite and NiO is not clear. It is possible that the reconstruction of the NiO surface [22] can have an effect on coupling between the particles. NiO particles prepared from $Ni(OH)_2$ in the same way as the particles in the present study have been found to have a strong tendency to adsorb water [23], which may form hydroxyl species at the surface [24]. It is possible that such adsorbed water prevents the formation of bonds between the NiO particles. A strong affinity to water may also explain why suspension in water results in diminished interactions. The faster superparamagnetic relaxation after storage of a sample in air for more than six years also indicates diminished interparticle interaction. The observations suggest that water molecules can diffuse into the interfaces and thereby separate the particles. A layer of adsorbed water on NiO nanoparticles may also explain the lack of interparticle interactions in dried suspensions of mixtures of α-Fe_2O_3 and NiO nanoparticles. Water-covered NiO nanoparticles may act as buffers between the α-Fe_2O_3 nanoparticles, reducing exchange interactions between them.

α-Fe_2O_3 nanoparticles have been found to couple preferentially through the hexagonal (001) planes [8]. Simulations have shown that the surface energy of these planes is strongly increased by the adsorption of water in comparison to other crystallographic planes [25]. Thus it may seem that water will have larger affinity to other planes, and this may facilitate the coupling of (001) planes.

5. Conclusions

We have shown how simple macroscopic treatments can be used to vary the interparticle interactions of NiO nanoparticles. A significant reduction of the interactions in NiO could be obtained by hand grinding or suspension in water. Contrary to the result obtained from hematite nanoparticles, the interactions are not restored by suspension in water followed by very slow drying in air. Instead, this process was found to reduce the interactions in a sample of interacting particles. We suggest that the strong affinity of the surface atoms to water has an influence on the behaviour.

Acknowledgments

The work was supported by the Danish Technical Research Council through the framework programme Nanomagnetism.

The authors are grateful to Cathrine Frandsen for valuable comments.

References

[1] Penn R L and Banfield J F 1998 *Science* **281** 969
[2] Penn R L and Banfield J F 1999 *Geochim. Cosmochim. Acta* **63** 1549
[3] Bødker F, Hansen M F, Koch C B and Mørup S 2000 *J. Magn. Magn. Mater.* **221** 32
[4] Hansen M F, Koch C B and Mørup S 2000 *Phys. Rev.* B **62** 1124
[5] Mørup S, Frandsen C, Bødker F, Klausen S N, Lefmann K, Lindgård P A and Hansen M F 2002 *Hyperfine Interact.* **144/145** 347
[6] Frandsen C and Mørup S 2003 *J. Magn. Magn. Mater.* **266** 36
[7] Huang F, Gilbert B, Zhang H and Banfield J F 2004 *Phys. Rev. Lett.* **92** 155501
[8] Frandsen C *et al* 2005 *Phys. Rev.* B **72** 214406
[9] Frandsen C and Mørup S 2005 *Phys. Rev. Lett.* **94** 027202
[10] Wang X, Song J, Gao L, Jin J, Zheng H and Zhang Z 2005 *Nanotechnology* **16** 37
[11] Wang D, Xu R, Wang X and Li Y 2006 *Nanotechnology* **17** 979
[12] Oliveira N J, Li S X and Freitas P P 1999 *J. Appl. Phys.* **85** 5849
[13] Pinarbasi M, Metin S, Gill H, Parker M, Gurney B, Carey M and Tsang C 2000 *J. Appl. Phys.* **87** 5714
[14] Bandara J and Weerasinghe H 2005 *Sol. Energy Mater. Sol. Cells* **85** 385
[15] Granqvist C G, Avendaño E and Azens A 2003 *Thin Solid Films* **442** 201
[16] Polzot P, Laruelle S, Grugeon S, Dupont L and Tarascon J-M 2000 *Nature* **407** 496
[17] Xu M, Bahl C R H, Frandsen C and Mørup S 2004 *J. Colloid Interface Sci.* **279** 132
[18] Frandsen C and Mørup S 2006 *J. Phys.: Condens. Matter* at press
[19] http://www-llb.cea.fr/fullweb/
[20] Bahl C R H, Hansen M F, Pedersen T, Nielsen K H, Saadi S, Lebech B and Mørup S 2006 *J. Phys.: Condens. Matter* **18** 4161
[21] Szytula A, Murasik A and Balanda M 1971 *Phys. Status Solidi* b **43** 125
[22] Barbier A, Mocuta C, Kuhlenbeck H, Peters K F, Richter B and Renaud G 2000 *Phys. Rev. Lett.* **84** 2897
[23] Cronan C L, Micale F J, Zettlemoyer A C, Topic M and Leidenheiser H Jr 1980 *J. Colloid Interface Sci.* **75** 43
[24] Guo H and Zaera F 2003 *Catal. Lett.* **88** 95
[25] Jones F, Rohl A L, Farrow J B and van Bronswijk W 2000 *Phys. Chem. Chem. Phys.* **2** 3209

Paper X

Available online at www.sciencedirect.com
ScienceDirect
Physica B 385–386 (2006) 398–400
PHYSICA B
www.elsevier.com/locate/physb

Uniform magnetic excitations in NiO nanoparticles

C.R.H. Bahl[a,b,*,1], L. Theil Kuhn[a], K. Lefmann[a], P.-A. Lindgård[a], S. Mørup[b]

[a]*Materials Research Department, Risø National Laboratory, DK-4000 Roskilde, Denmark*
[b]*Department of Physics, Technical University of Denmark, DK-2800 Kgs. Lyngby, Denmark*

Abstract

A sample of isolated disc shaped NiO nanoparticles was studied at the RITA-II triple axis spectrometer at SINQ (PSI) using the newly implemented multi-analyser blade imaging mode. The particles were 13 nm in diameter and had a thickness of about 2.5 nm. A non-dispersive spin excitation was observed at the antiferromagnetic $(\frac{1}{2}\frac{1}{2}\frac{1}{2})$ reflection at a scattering vector of $\kappa = 1.30\,\text{Å}^{-1}$, at an energy of 0.51 ± 0.02 meV. This is shown to be due to uniform magnetic excitations in the nanoparticles.

PACS: 75.75.+a; 75.50.Ee; 78.70.Nx

Keywords: Nanomagnetism; Uniform magnetic excitations; Uncompensated spins

1. Introduction

Antiferromagnetism was first observed by neutron scattering in the antiferromagnets MnO and NiO [1]. In bulk NiO the spins were found to be stacked in alternating layers perpendicular to the (1 1 1) direction and an antiferromagnetic $(\frac{1}{2}\frac{1}{2}\frac{1}{2})$ reflection was observed at $\kappa = 1.30\,\text{Å}^{-1}$.

In antiferromagnetic nanoparticles the spin dynamics deviates from that observed in bulk. The spin wave spectrum will be quantised, due to the finite size of the particles. $q = 0$ spin waves are thermally activated, and are the dominant excitations in nanoparticles [2]. In the NiO nanoparticles presented here, there is a large gap (~20 meV) to the first $q \neq 0$ spin wave. Further thermal excitation may induce superparamagnetic relaxation, where the spins within the particle coherently reverse between the magnetic easy axes.

Early theoretical work on perfect uniaxial two-sublattice bulk antiferromagnets in zero applied field, with an exchange field, H_E, and an anisotropy field, H_A, predicted the presence of two degenerate resonance modes, i.e., $q = 0$ spin waves with precession energies given at low temperatures by Ref. [3]

$$\varepsilon = \hbar\omega = g\mu_B\sqrt{(2H_E + H_A)H_A}, \quad (1)$$

where g is the g-factor and μ_B is the Bohr magneton.

The anisotropy of bulk NiO is dominated by an "out of plane" term confining the spins to the (1 1 1) planes, and a significantly weaker "in plane" term aligning the spins to a certain direction within that plane. This anisotropy structure splits the two resonance modes into one low energy mode with an anisotropy field purely from the "in plane" anisotropy term, and one with a higher energy having an anisotropy field from both the "in plane" and "out of plane" anisotropy terms [4]. Hutchings and Samuelsen measured the spin wave gap of the low energy mode in bulk NiO at 78 K, finding a value of 1.0 ± 0.5 meV [5]. Using the quoted value of the exchange field, $H_E = 987$ T, this gives an anisotropy field of $H_A = 0.038^{+0.047}_{-0.029}$ T.

*Corresponding author. Risø National Laboratory, Frederiksborgvej 399, DK-4000 Roskilde, Denmark. Tel.: +45 4677 5491; fax: +45 4677 5758.
E-mail address: christian.bahl@risoe.dk (C.R.H. Bahl).

[1]This work was supported by the Danish Natural Sciences Council through the Danish Neutron Scattering Centre (DANSCATT). CRHB has been supported by the Danish Technical Research Council. The experimental work was performed at the SINQ neutron source at the Paul Scherrer Institut (PSI). We thank Lis Lilleballe for preparation of the sample.

0921-4526/$ - see front matter © 2006 Elsevier B.V. All rights reserved.
doi:10.1016/j.physb.2006.05.234

In nanoparticles the level splittings of the uniform excitations are given by Eq. (1) [6]. The anisotropy structure of nanoscale NiO has not previously been reported. However, in nanoscale hematite (α-Fe_2O_3), as in bulk, the anisotropy has a strong "out of plane" and a much weaker "in plane" component [7]. It would seem likely that this is also the case for NiO. Indeed, a high energy resonance mode has been observed in nanoparticles of NiO [8] by far infra-red absorption spectroscopy and we shall show evidence of a low energy resonance mode, measured by inelastic neutron scattering.

2. Results

Isolated NiO nanoparticles were prepared by heating chemically precipitated $Ni(OH)_2$ for 3 h at 300 °C. The sample was subsequently ball-milled, suspended in water and coated with phosphate, to avoid contact between the particles, before being freeze dried. The particles have been studied by transmission electron microscopy and X-ray diffraction. They were found to be disc shaped with a thickness of about 2.5 nm and a diameter of about 13 nm.

Inelastic neutron scattering was performed at the RITA-II triple axis spectrometer at SINQ (PSI). The sample was measured at 200 K, as the inelastic intensity was large at this temperature. Energy scans were measured centred around the antiferromagnetic $(\frac{1}{2}\frac{1}{2}\frac{1}{2})$ reflection at a scattering vector of $\kappa = 1.30\,\text{Å}^{-1}$. The final energy was 5.0 meV and a Be filter was placed between the sample and the analyser. To establish the instrumental resolution and asymmetry induced by the filter, two energy scans were measured at background values of $\kappa = 1.00$ and $1.60\,\text{Å}^{-1}$ and averaged to one background scan.

The RITA-II spectrometer was run in the newly implemented multi-blade analyser imaging mode as described in Ref. [9]. The seven analyser blades are situated at slightly different scattering angles (about 1° apart), each scattering neutrons into different channels of a collimator, situated in front of a position sensitive detector. Due to the small size of the particles the scattering reflections are very broad in κ. Thus an energy scan of the full antiferromagnetic reflection at $\kappa = 1.30\,\text{Å}^{-1}$ can be measured with good statistics by adding the data normalised to the scattering efficiency of the analyser blades in each of the seven channels. This is presented in Fig. 1 along with the background scan added in the same way. Alternatively the data in each channel can be plotted separately giving a (κ, ε) map. Five such scans adjacent to each other have been used to create the (κ, ε) map covering $\kappa = 0.92 - 1.68\,\text{Å}^{-1}$ shown in Fig. 2.

3. Discussion

It is seen in Fig. 2 that there is a localised inelastic signal at the antiferromagnetic reflection at $\kappa = 1.30\,\text{Å}^{-1}$. This is due to the uniform excitations and shows that the energy

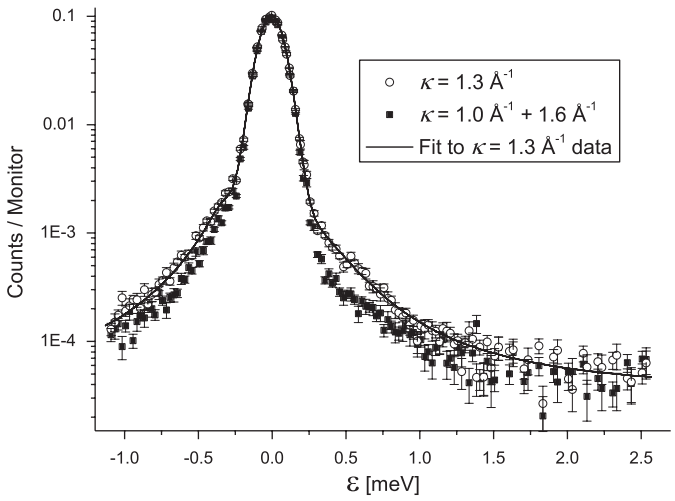

Fig. 1. Energy scans of the antiferromagnetic reflection at $\kappa = 1.30\,\text{Å}^{-1}$(○) and a background scan combined from scans at $\kappa = 1.00$ and $1.60\,\text{Å}^{-1}$(■). In all the scans the signals from each of the seven analyser blades have been added. The data was measured at 200 s/point, except in the range ±0.2 meV, where it was 50 s/point.

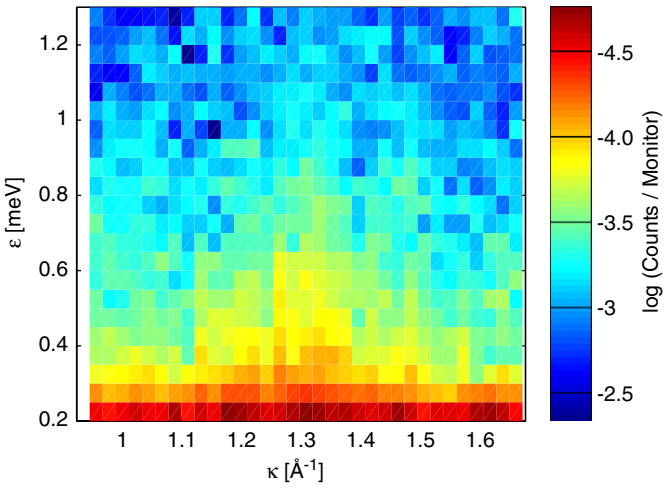

Fig. 2. Colour (κ, ε)-map showing the signal from uniform magnetic excitations at $\kappa = 1.30\,\text{Å}^{-1}$ and $\varepsilon_0 = 0.51$ meV. The map is constructed from five adjacent energy scans, each measuring with seven analyser blades.

spectrum of these, as expected, has no dispersion. The first $q \neq 0$ level is far beyond the energy range of the data.

The corresponding inelastic neutron signal from hematite nanoparticles has previously been successfully fitted with a damped harmonic oscillator model [6]. This model is a convolution of the resolution function, consisting of a Gaussian and a broad Lorentzian, and terms describing the Bragg peak, the incoherent elastic background, a quasielastic signal from superparamagnetic relaxation and finally the damped harmonic oscillator term describing the inelastic signal

$$I(\varepsilon) \propto D(\varepsilon)\frac{2\gamma\varepsilon_0^2}{(\varepsilon^2 - \varepsilon_0^2)^2 + 4\gamma^2\varepsilon^2}. \quad (2)$$

Here $D(\varepsilon)$ is the detailed balance factor, γ is the HWHM of the inelastic peaks and $\pm\varepsilon_0$ are the centre positions of these.

Applying this model to the data presented in Fig. 1, the parameters of the inelastic signal have been determined. We find values of $\varepsilon_0 = 0.51 \pm 0.02$ meV and $\gamma = 0.42 \pm 0.09$ meV. Although the measurement was performed at 200 K, this is still well below the reported Néel temperature of 460 K [10]. Assuming the bulk value of the exchange field, the anisotropy field is calculated from Eq. (1) yielding a value of $H_A = 0.0098 \pm 0.0008$ T.

However, due to the small size of nanoparticles, there will be a number of uncompensated spins on one of the sublattices and thus the particles may be considered as being weakly ferrimagnetic. This uncompensated moment in NiO nanoparticles has been observed in numerous papers, e.g., Ref. [11]. The surplus of spins on one sublattice will change the precession frequency of the resonance mode, splitting it into two modes. Assuming uniaxial anisotropy the energies of these are given by Ref. [3]

$$\hbar\omega_{\pm} = g\mu_B \left[\pm \frac{H_E}{2}\frac{\Delta S}{S} + \sqrt{\left(\frac{H_E}{2}\frac{\Delta S}{S}\right)^2 + H_E H_A \frac{\Delta S}{S} + (2H_E + H_A)H_A} \right]. \quad (3)$$

Here $\Delta S/S$ is the fraction of uncompensated spins relative to the number of spins in one sublattice. In a similar sample of NiO nanoparticles the uncompensated moment has been measured by high-field Mössbauer spectroscopy and magnetometry to be 0.6% [12]. Assuming that we are measuring the mode with the lowest energy, ω_-, Eq. (3) gives $H_A = 0.023$ T and thus a splitting between the two modes of $\Delta\omega = \omega_+ - \omega_- = 0.68$ meV. As we do not know the error on $\Delta S/S$ we cannot calculate the error on H_A. Due to the decrease of scattering cross-section with increasing energy transfer, it is likely that we observe the ω_- mode as the ω_+ mode is found at a higher energy, with much less intensity. Furthermore, the tails of the ω_- peak may obscure the signal from the ω_+ mode as γ is comparable to $\Delta\omega$.

Assuming the bulk value of the exchange field may be an overestimate as the many spins at the surface of a particle will have broken bonds. However, a reasonably smaller value of the exchange field would only give a slight increase of the anisotropy field.

4. Conclusion

The new seven blade analyser imaging mode of the RITA-II spectrometer has been used to study non-dispersive uniform magnetic excitations in disc-shaped NiO nanoparticles. An estimate of the "in plane" anisotropy field within the nanoparticles is given taking into account the uncompensated magnetic moment of the particles.

Although NiO has a similar anisotropy structure to hematite we do not observe the dramatic increase of anisotropy in nanoparticles compared to bulk which has previously been observed in hematite [13]. However, the "in plane" anisotropy of bulk hematite is extremely small giving $H_A \approx 0.001$ T compared to $H_A \approx 0.026$ T in hematite nanoparticles of a similar size as the present NiO particles. We observe comparable values of the "in plane" anisotropy in bulk and nanoscale NiO. This may be due to the bulk value being larger than in hematite.

References

[1] C.G. Shull, W.A. Strauser, E.O. Wollan, Phys. Rev. 83 (1951) 333.
[2] S. Mørup, B.R. Hansen, Phys. Rev. B 72 (2005) 24418.
[3] C. Kittel, Phys. Rev. 82 (1951) 565.
[4] P.-A. Lindgård, A. Kowalska, P. Laut, J. Phys. Chem. Solids 28 (1967) 1357.
[5] M.T. Hutchings, E.J. Samuelsen, Phys. Rev. B 6 (1972) 3447.
[6] M.F. Hansen, F. Bødker, S. Mørup, K. Lefmann, K.N. Clausen, P.-A. Lindgård, Phys. Rev. Lett. 79 (1997) 4910;
M.F. Hansen, F. Bødker, S. Mørup, K. Lefmann, K.N. Clausen, P.-A. Lindgård, J. Magn. Magn. Mater. 221 (2000) 10;
S.N. Klausen, K. Lefmann, P.-A. Lindgård, K.N. Clausen, M.F. Hansen, F. Bødker, S. Mørup, M. Telling, J. Magn. Magn. Mater. 266 (2003) 68.
[7] S.N. Klausen, K. Lefmann, P.-A. Lindgård, L. Theil Kuhn, C.R.H. Bahl, C. Frandsen, S. Mørup, B. Roessli, N. Cavadini, C. Niedermayer, Phys. Rev. B 70 (2004) 214411.
[8] V.V. Pishko, S.L. Gnatcheko, V.V. Tsapenko, R.H. Kodama, S.A. Makhlouf, J. Appl. Phys. 93 (2003) 7382.
[9] C.R.H. Bahl, P. Andersen, S.N. Klausen, K. Lefmann, Nucl. Instr. and Meth. B 226 (2004) 667;
C.R.H. Bahl, K. Lefmann, A.B. Abrahamsen, H.M. Rønnow, F. Saxild, T.B.S. Jensen, L. Udby, N.H. Andersen, N.B. Christensen, H.S. Jakobsen, T. Larsen, P.S. Häfliger, S. Streule, Ch. Niedermayer, Nucl. Instr. and Meth. B 246 (2006) 452.
[10] S.N. Klausen, P.-A. Lindgård, F. Bødker, S. Mørup, Phys. Stat. Sol. (A) 189 (2002) 1039.
[11] J.T. Richardson, D.I. Yiagas, B. Turk, K. Forster, M.V. Twigg, J. Appl. Phys. 70 (1991) 6977.
[12] C.R.H. Bahl, M.F. Hansen, T. Pedersen, S. Saadi, K.H. Nielsen, B. Lebech, S. Mørup J. Phys.: Condens. Matter. 18 (2006) 4161.
[13] F. Bødker, S. Mørup, Europhys. Lett. 52 (2000) 217.

Paper XI

INSTITUTE OF PHYSICS PUBLISHING JOURNAL OF PHYSICS: CONDENSED MATTER

J. Phys.: Condens. Matter **18** (2006) 11203–11216 doi:10.1088/0953-8984/18/49/013

Spin dynamics in weakly and strongly interacting NiO nanoparticles

C R H Bahl[1,2], K Lefmann[1], L Theil Kuhn[1], N B Christensen[1,3], H Vázquez[1,4] and S Mørup[2]

[1] Materials Research Department, Building 227, Risø National Laboratory, DK-4000 Roskilde, Denmark
[2] Department of Physics, Building 307, Technical University of Denmark, DK-2800 Kongens Lyngby, Denmark
[3] Laboratory for Neutron Scattering, Paul Scherrer Institute, CH-5232 Villigen, Switzerland

E-mail: christian.bahl@risoe.dk

Received 28 June 2006, in final form 3 October 2006
Published 22 November 2006
Online at stacks.iop.org/JPhysCM/18/11203

Abstract

The spin dynamics of plate-shaped nanoparticles of NiO has been studied by inelastic neutron scattering and Mössbauer spectroscopy. A value of the in-plane anisotropy energy constant significantly larger than the bulk value has been measured. The temperature and field dependence of the energy of the antiferromagnetic resonance mode associated with this in-plane anisotropy has been studied. Both Mössbauer spectroscopy and neutron scattering data show that the magnetic fluctuations are strongly affected by the strength of interparticle interactions.

(Some figures in this article are in colour only in the electronic version)

1. Introduction

The spin dynamics of antiferromagnetic nanoparticles differs from that of the corresponding bulk materials. Antiferromagnetic nanoparticles will exhibit superparamagnetism at finite temperatures. This is a thermally activated coherent flipping of the magnetization between the magnetically easy axes. Also, the spin wave spectrum will be quantized, due to the finite size of the particles. The lowest-energy excitation is a spin wave with zero wavevector ($\mathbf{q} = 0$), measured from an antiferromagnetic Bragg reflection. Such spin waves are coherent oscillations of the spins about the ordered moment direction, known as uniform magnetic excitations, and these are the predominant excitations in nanoparticles [1]. In the NiO nanoparticles presented here, there is a large gap, estimated to be ∼10–20 meV, to

[4] Present address: Departamento de Física Teórica de la Materia Condensada, Universidad Autónoma de Madrid, E-28049 Madrid, Spain.

the first $\mathbf{q} \neq 0$ spin wave [2]. Several studies of the spin dynamics in nanoparticles of the antiferromagnet hematite (α-Fe_2O_3) have been conducted [3–5]. Magnetic interactions between the particles have been found by Mössbauer spectroscopy [6, 7] and inelastic neutron scattering [8] to have a strong effect on the spin dynamics. In this paper we present inelastic neutron scattering and Mössbauer spectroscopy studies of weakly and strongly interacting plate-shaped NiO nanoparticles.

1.1. Nickel oxide

NiO has an fcc structure with a bulk unit cell parameter of $a = 4.177$ Å. Below the Néel temperature of 523 K in bulk NiO (460 K in the present nanoparticles [9]) there is a slight contraction of the cubic structure along the [111] direction, known as exchange striction [10]. Early neutron scattering work established that bulk NiO is antiferromagnetic with a $\mathbf{Q}_{\mathrm{AFM}} = \left(\frac{1}{2}\frac{1}{2}\frac{1}{2}\right)$ ordering vector and a confinement of the spins within the (111) plane [11], i.e. a type-II antiferromagnet. Later, an orientation of the spins in the $[11\bar{2}]$ direction within the (111) plane was established [12]. Bulk NiO has a magneto-crystalline anisotropy with a large out-of-plane anisotropy energy constant, K_1, and a much smaller in-plane anisotropy energy constant, K_2 [13]. The anisotropy part of the energy density can be stated macroscopically as in hematite [14]:

$$E = K_1 \cos^2\theta + K_2 \sin^2\theta \sin^2\phi. \tag{1}$$

Here K_i ($i = 1, 2$) are the anisotropy energy constants, θ is the angle between the spins and the [111] direction, and ϕ is the angle between the between the spins and the easy direction within the (111) plane. Anisotropy fields can be defined as $B_{\mathrm{A}i} = \frac{K_i}{M_{\mathrm{S}}}$, where M_{S} is the sublattice magnetization (5.5×10^5 J T^{-1} m^{-3}). As K_1 and K_2 are both positive and $K_1 \gg K_2$, the spins are confined near the (111) plane, making the spin structure essentially two dimensional.

An exchange field can be defined as $B_{\mathrm{E}} = \frac{\mathcal{J}_0 S}{g\,\mu_{\mathrm{B}}}$, where S is the spin of one ion ($S = 1$ in Ni^{2+}) and μ_{B} is the Bohr magneton. $\mathcal{J}_0 = \sum_l z_l J_l$ is the effective exchange constant, where z_l is the number of lth neighbours and J_l is the exchange constant to these. The g-factor is conventionally assumed to be 2, but values of $g = 2.227(2)$ [15] and $g = 2.34(8)$ [16] have been reported for bulk NiO. As will be shown in section 4.4, a value of $g = 2.19(6)$ has been measured in the present nanoparticle sample. In a type-II fcc antiferromagnet, the exchange contributions from the nearest neighbours cancel out [17]. There are six next nearest neighbours with an exchange constant of $J_2 = 221$ K [13] such that $\mathcal{J}_0 = 6J_2$, giving $B_E = 905$ T.

1.2. Uncompensated moments

Long before the advent of 'nanotechnology', Néel proposed that an antiferromagnetic nanoparticle will contain a number of uncompensated spins due the small size of the particle [18]. We define $\xi = \frac{n_2}{n_1}$ as the ratio between the number of spins in the two sublattices. An increase in the number of spins in one sublattice of an antiferromagnetic nanoparticle will change the magnetic properties [19–21] towards those of a ferrimagnet.

A value of $\xi \approx 0.994(1)$ has been obtained by high-field Mössbauer measurements on NiO nanoparticles similar to the particles presented here [22]. It has been suggested that the uncompensated moment may be explained by a random distribution of defects in the particles, by odd numbers of ferromagnetically ordered layers with opposite magnetization directions, or by random occupancy of surface sites [18, 19]. The latter model is in better agreement with the data obtained from Mössbauer spectroscopy than the two others [22]. Magnetization data also suggest that random occupation of surface sites is the main reason for the uncompensated

moment of NiO nanoparticles [19]. The value of $\xi \approx 0.994(1)$ will be assumed in the following, although it will be shown that the exact value is not important for the determined value of the in-plane anisotropy.

1.3. Antiferromagnetic resonance

In the ordered state of an ideal antiferromagnet with the anisotropy energies given by (1) there will be two non-degenerate spin wave branches. The resonance energies, i.e. spin wave energies at the wavevector $\mathbf{q} = 0$, can be approximated at low temperature by [5, 23, 24]

$$\hbar\omega_\alpha \approx g\mu_B\sqrt{2B_E B_{A2}} \tag{2}$$

$$\hbar\omega_\beta \approx g\mu_B\sqrt{2B_E(B_{A2}+B_{A1})} \approx g\mu_B\sqrt{2B_E B_{A1}}. \tag{3}$$

The equations assume $B_E \gg B_{Ai}$ and $B_{A1} \gg B_{A2}$, where $i = 1, 2$ refers to the two anisotropy energy constants.

From neutron scattering measurements on bulk NiO, Hutchings and Samuelsen [13] found a value of the out-of-plane anisotropy energy constant of $K_1 = 4.3(2) \times 10^5$ J m^{-3}, calculated from a resonance mode observed at $\hbar\omega_\beta = 4.5$ meV, in agreement with theoretical and experimental values obtained by others [25–27]. According to [13], the value of the in-plane anisotropy energy constant in bulk NiO is $K_2 = 2.3(1.9) \times 10^4$ J m^{-3}. However, care must be taken when measuring the in-plane anisotropy energy in bulk NiO, as lattice strain may lead to an overestimation of the value, and domain walls may lead to an underestimate of this [28]. Measurements from a strain and domain wall free sample of bulk NiO gave a value of $K_2 = 30$ J m^{-3} [28, 29], i.e. three orders of magnitude less than the value cited in [13].

Far infrared measurements involving two NiO nanoparticle samples with particle sizes of 43.5 and 5.7 nm were presented in [30]. A resonance energy, $\hbar\omega_\beta$, close to that of bulk NiO was found in both samples. Thus, the out-of-plane anisotropy energy constant, K_1, does not depend essentially on the particle size. Apart from preliminary neutron scattering results obtained at a single temperature in zero applied field [31, 32], no study of the in-plane anisotropy and associated resonance mode in nanoparticles of NiO has previously been reported.

This paper reports on a study of the spin dynamics in plate-shaped nanoparticles of NiO by inelastic neutron scattering and Mössbauer spectroscopy. The temperature and field dependence of the ω_α resonance frequency is measured. Nanoparticles of NiO will be shown to have a larger value of K_2 than bulk NiO.

2. Experimental details

Nickel oxide nanoparticles were prepared by heating chemically precipitated $Ni(OH)_2$ in air at 300 °C for 3 h, as described previously [22, 33]. This sample will be referred to as the as-prepared sample. A second sample with reduced interparticle interactions was prepared by separating the particles in the as-prepared sample by low-energy ball milling and subsequently suspending them in water and coating them with a layer of phosphate [33]. These treatments have been shown to result in a significant reduction of the interaction between NiO nanoparticles [33, 34]. This sample will be referred to as the coated sample. Each sample was prepared with a mass of about 5 g, sufficient to perform inelastic neutron scattering and x-ray diffraction.

Samples for Mössbauer spectroscopy were prepared by the same method, but starting with $Ni(OH)_2$ that was doped with about 0.5 at.% ^{57}Fe relative to Ni [22, 33, 34]. These samples were prepared at a smaller scale than the undoped samples, each sample having a mass of about 50 mg.

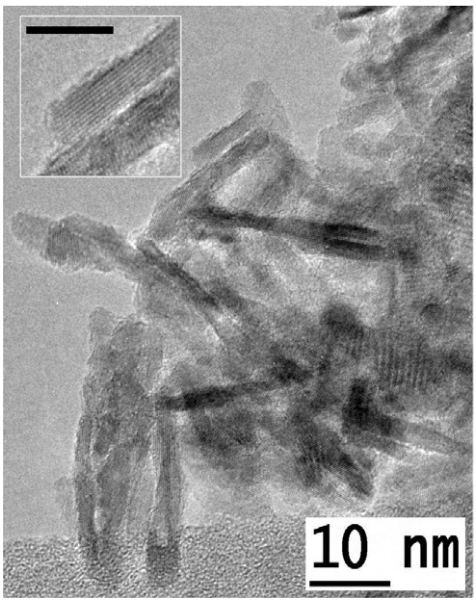

Figure 1. TEM image of an agglomerate of NiO particles in the as-prepared sample. The inset shows a magnified image of one of the plate-shaped particles viewed edge-on. The scale bar in the inset is 5 nm. The visible planes are the (111) planes, which are seen to be parallel to the plate face.

High-resolution transmission electron microscopy (TEM) was performed on the undoped samples using a JEM 3000F FEG microscope equipped with a 16 Mpix CCD camera. X-ray diffraction (XRD) on the undoped samples has been carried out using Cu Kα radiation in a Philips PW 1820 diffractometer.

Mössbauer spectra were obtained in the temperature range from 6 to 295 K using a source of ^{57}Co in a rhodium matrix. Above 80 K the samples were cooled in a temperature-controlled liquid nitrogen cryostat. At temperatures below 80 K the samples were cooled in a closed-cycle helium refrigerator, and below 20 K the samples were cooled in a liquid helium cryostat.

Inelastic neutron scattering was conducted at a range of temperatures on the as-prepared sample using the TAS7 triple-axis spectrometer at Risø National Laboratory and on the coated sample using the RITA-II triple-axis spectrometer at the Paul Scherrer Institute in Villigen, Switzerland. On TAS7 the signal was detected using a single analyser and detector at final neutron energies of $E_f = 5.0$ meV. The RITA-II spectrometer is equipped with a multiblade analyser and position-sensitive detector [35]. This multiblade analyser was used in the newly implemented imaging mode [35, 36] also at a final neutron energy of $E_f = 5.0$ meV. At both spectrometers, a Be filter was used to remove high-energy neutrons. Both temperature series were performed in the range 10–330 K using a closed-cycle helium refrigerator. At RITA-II, a field series on the coated sample in the range 0–13.5 T at 200 K was obtained using an Oxford 15 T magnet.

3. Results

3.1. Size and morphology

The size and morphology of the particles have been investigated by transmission electron microscopy (TEM); see figure 1. In both samples the particles were found in large, loosely

packed agglomerates. The interaction between nanoparticles is difficult to observe by TEM. A layer without visible lattice fringes, presumably due to adsorption of water and organic molecules from atmospheric air, is found to cover the surfaces of the particles in both samples. The phosphate coating of the coated sample may not be distinguished from the layer due to adsorption. The subtlety of the interaction between NiO nanoparticles is demonstrated in [34], where it is shown that long-term exposure to a humid atmosphere can significantly reduce the interparticle interaction.

The particles were observed to be disc shaped, with a thickness of 2.3 ± 0.4 nm in both samples and a diameter of 13 ± 3 nm in the as-prepared sample and 12 ± 2 nm in the coated sample. The listed uncertainties represent the standard deviation of the size distributions. In addition, it is observed in both samples that the faces of the discs are (111) planes. High-resolution TEM images show that the plate faces are not perfectly plane, but contain steps and kinks [22]. Except for the disc faces, no facets are observed.

The XRD patterns of the as-prepared and coated samples have been fitted using profile refinement in the software package FullProf [37]. Assuming a platelet shape, as described elsewhere [22], an estimated plate thickness of 2.3 nm and a diameter of $\sim$7.5 nm was obtained in both samples. The thicknesses are consistent with those found in TEM, but the diameters are underestimated compared to TEM. As discussed previously [22], this is probably due to particle size distributions giving difficulties in fitting the sharpest part of some of the reflections. Another possibility may be that each individual particle consists of more than one crystallite, but this has not been observed by high-resolution TEM.

Thus the particle size and morphology of the as-prepared and the coated samples are identical within experimental uncertainty. The ^{57}Fe-doped NiO nanoparticles have the same size and morphology as the undoped particles [38]. However, because the particles used for neutron scattering and Mössbauer spectroscopy were not taken from the same batch, there may be small differences, and a direct comparison between, for example anisotropy energies and interaction energies, should be taken with some reservation.

3.2. Mössbauer spectroscopy

Mössbauer spectra of the as-prepared and coated samples are shown in figure 2. The coated sample shows a behaviour typical for non-interacting or weakly interacting superparamagnetic particles [6, 8, 39]. The spectra consist of a superposition of a sextet due to particles with a relaxation time longer than the timescale of Mössbauer spectroscopy ($\sim$ a few nanoseconds) and a singlet due to particles with shorter relaxation time. The relative area of the singlet increases with increasing temperature, because of the temperature dependence of the relaxation time. At 295 K, almost all particles exhibit fast superparamagnetic relaxation. At 20 K a doublet with a small intensity is also visible; this is presumably due to iron atoms that have reacted with the phosphate layer, coating the nanoparticles. At elevated temperatures the area of the doublet is negligible compared to the singlet component, and therefore not observed. The spectra of the as-prepared sample show a quite different behaviour. Below 150 K the spectra consist of sextets and no singlet component is visible. Instead, the lines of the sextet become increasingly broadened with increasing temperature and the average hyperfine field decreases rapidly with increasing temperature. This behaviour is typical for samples of interacting nanoparticles for which the relaxation may be described as fluctuations of the sublattice magnetization around a direction mainly defined by an interaction field rather than fluctuations between two minima in opposite directions [6, 8, 39]. Similar results have been found in previous studies of weakly and strongly interacting nanoparticles of hematite [6, 8], NiO [22, 33, 34] and maghemite (γ-Fe_2O_3) [40].

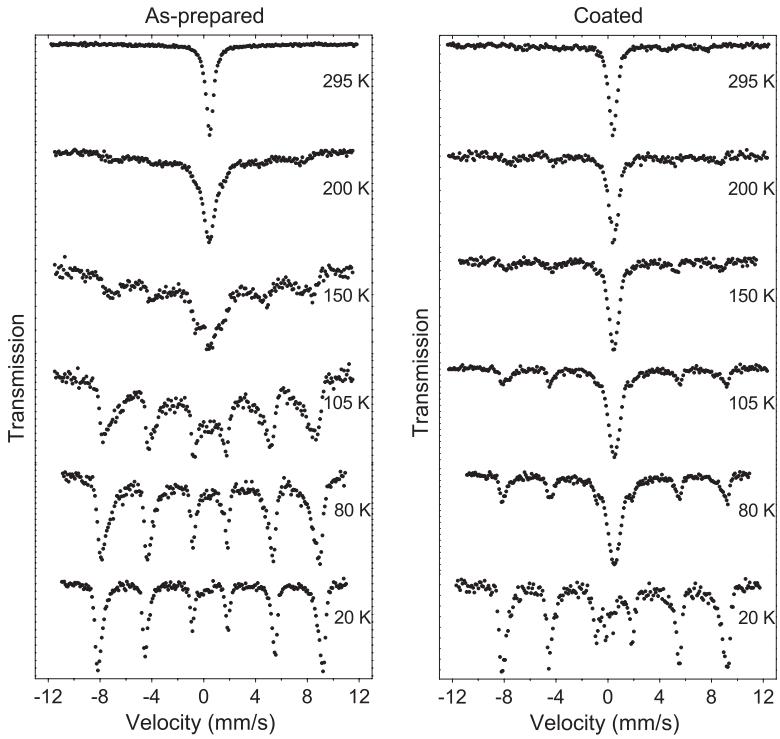

Figure 2. Mössbauer spectra of the ^{57}Fe-doped NiO nanoparticles in the as-prepared and coated samples recorded at temperatures in the range 20–295 K. The low-temperature data are fitted with a distribution of sextets, as discussed in section 4.1.

3.3. Inelastic neutron scattering

Inelastic neutron scattering was performed with the scattering vector, $\boldsymbol{\kappa}$, equal to the antiferromagnetic ordering vector $\mathbf{Q}_{\mathrm{AFM}} = \left(\frac{1}{2}\frac{1}{2}\frac{1}{2}\right)$. As the samples are powders, only the magnitude of the scattering vector is measured and $\kappa = Q_{\mathrm{AFM}} = 1.30$ Å^{-1}. Inelastic scans obtained at Q_{AFM} from the coated sample at 200 K in zero applied field and an applied field of 4 T are shown in figure 3. The inelastic scans reveal a quasielastic central peak and broad shoulders on both sides of this. This type of spectrum is well known from previous studies of hematite nanoparticles [3, 4]. The broad shoulders have been shown to be due to uniform magnetic excitations, and could be modelled with a damped harmonic oscillator model. The exponential relaxation rate of superparamagnetism results in an additional Lorentzian broadening of the quasielastic line shape. The dynamics can be described as [3, 4]

$$I(\varepsilon) = A_0\delta(\varepsilon) + W(\varepsilon)D(\varepsilon) + \frac{A_1}{\pi}D(\varepsilon)\frac{\Gamma}{\varepsilon^2+\Gamma^2} + \frac{A_2}{\pi}D(\varepsilon)\frac{2\gamma\varepsilon_0^2}{(\varepsilon^2-\varepsilon_0^2)^2+4\gamma^2\varepsilon^2} + C \qquad (4)$$

where A_1 is the area of the quasielastic peak and A_2 is the area of the inelastic components. A_0 is the area of the incoherent elastic background, $W(\varepsilon)$ is the contribution from adsorbed water, and C is the incoherent inelastic background. ε_0 is the position of the inelastic peaks on either side of zero, γ is the width of these peaks, and Γ is the width of the quasielastic peak. $D(\varepsilon)$ is the detailed balance factor, due to a difference in the population of the creation and annihilation

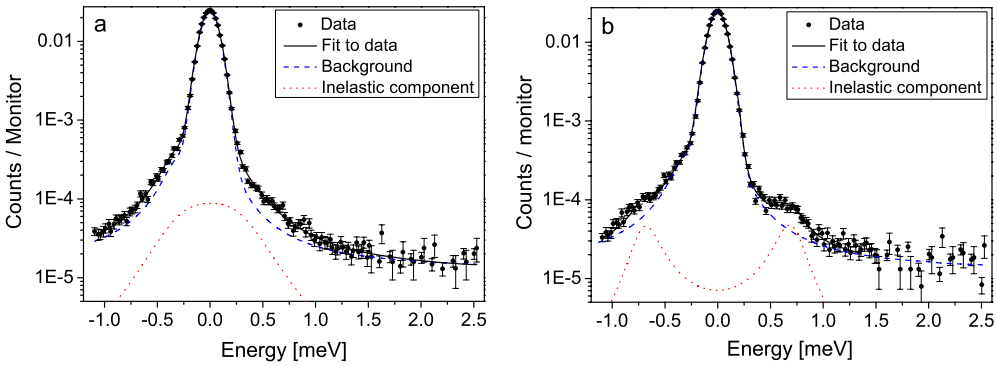

Figure 3. Inelastic neutron scattering data recorded from the coated sample at 200 K. The data points are obtained at the antiferromagnetic reflection and the solid line is a fit to this. The dashed line is a fit to the incoherent background data (not shown) and the dotted line is a plot of the inelastic component convoluted with the resolution function. (a) Data obtained at zero applied field showing a broad inelastic signal. (b) Data obtained with an applied field of 4 T.

states of uniform excitations, it is given at a temperature, T, by[5]

$$D(\varepsilon) = \frac{\varepsilon}{k_B T}\left(\frac{1}{\exp\left(\frac{\varepsilon}{k_B T}\right) - 1} + 1\right) \tag{5}$$

where k_B is Boltzmann's constant. Due to the extremely large surface area of the nanoparticles, water will inevitably be adsorbed during and after preparation. The water scatters neutrons incoherently with increasing mobility as the temperature is increased, resulting in a Lorentzian line shape, $W(\varepsilon)$, with increasing width as the temperature is increased. All the above-mentioned contributions must be convoluted with the resolution function of the spectrometer before fitting can be done. The resolution function has been determined to be the sum of a Gaussian and a much weaker Lorentzian, measured by fitting spectra recorded at low temperature. At each temperature, the background spectrum, including the contribution from adsorbed water, is fitted from scans at scattering vectors in the incoherent background on both sides of Q_{AFM}, i.e. $Q_{incoh} = 1.00$ and 1.60 Å^{-1}. Keeping these fixed, the remaining parameters in (4) are obtained from fits to the spectra at Q_{AFM}.

Parameters obtained from the fits to (4) are given in figures 4 and 5 and will be discussed in the following.

4. Discussion

According to the results of [30], discussed in section 1.3, the value of the out-of-plane anisotropy energy constant in NiO nanoparticles is similar to that found in bulk NiO. Using this value of the anisotropy energy constant and the volume obtained from TEM, an out-of-plane particle anisotropy of $K_1 V/k_B \approx 9000$ K may be estimated. From polarization arguments, the resonance mode associated with the out-of-plane anisotropy is not observable at $\kappa = 1.30$ Å^{-1}, but at the $\left(\frac{3}{2}\frac{1}{2}\frac{1}{2}\right)$ reflection at $\kappa = 2.50$ Å^{-1}. Due to the geometrical constraints of the cold neutron spectrometer employed and the sharp decrease in scattering intensity as the energy

[5] Note that this definition of the detailed balance factor differs from that stated in [3–5] due to a typing error there. The data in these publications were, however, fitted using the correct expression.

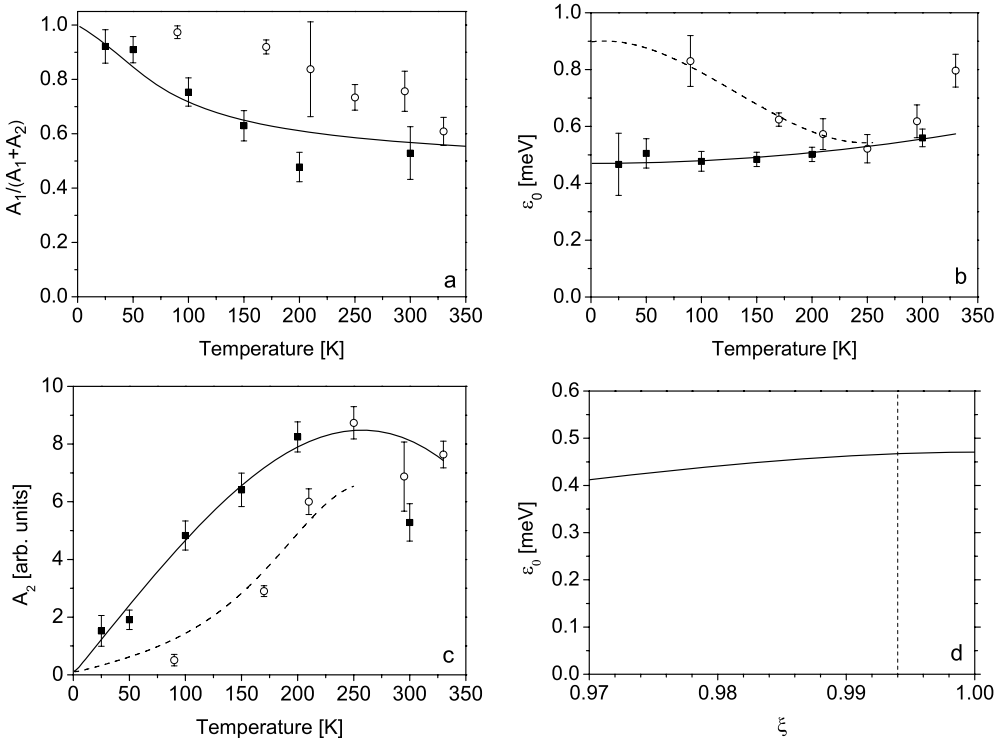

Figure 4. Fits to inelastic neutron scattering data obtained at a range of temperatures in zero applied field. ○ is data from the as-prepared sample and ■ is data from the coated sample. The lines are fits to the data discussed in the text. Full lines are fits to the data from the coated sample and the dashed lines are fits to the data from as-prepared sample. (a) The ratio of the inelastic signal to the total magnetic signal. (b) The position of the inelastic signals. (c) The intensity of the inelastic signal. (d) The resonance energy of the ω_α mode as a function of the ratio between the number of atoms in the two sublattices. The vertical line indicates the value of this ratio measured in [22].

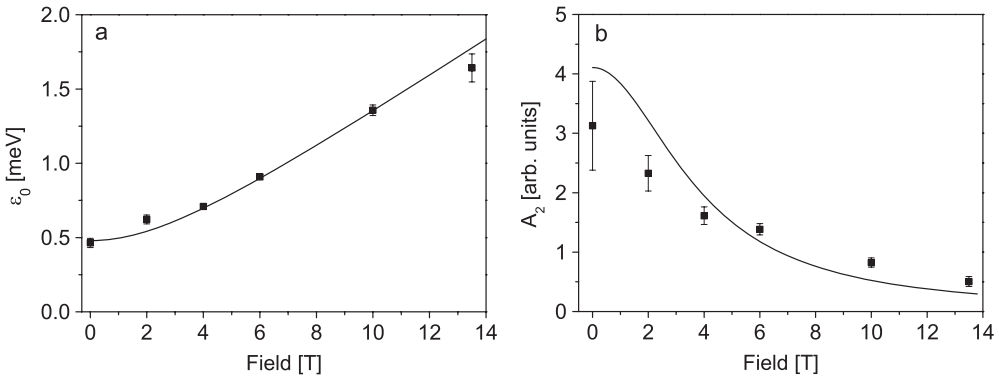

Figure 5. Parameters obtained from fits to inelastic neutron scattering data obtained from the coated sample at 200 K at a range of applied fields. The lines are fits to the data, as discussed in the text. (a) The field dependence of the position of the inelastic signal. (b) The intensity of the inelastic signals.

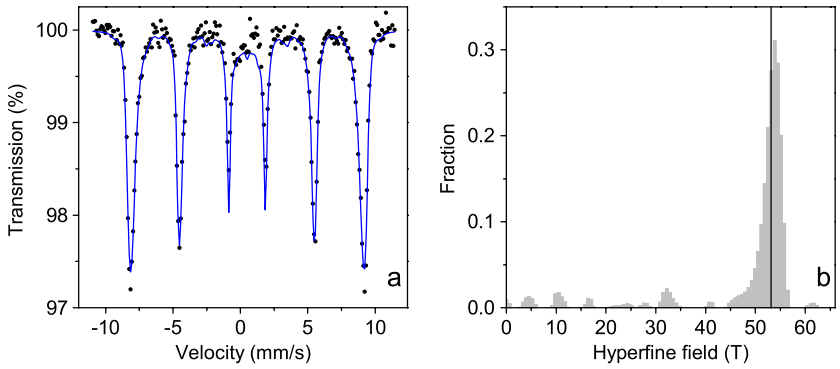

Figure 6. Mössbauer spectrum of the as-prepared sample at 20 K. (a) The spectrum is fitted with a distribution of sextets. The line indicates the sum of the sextets. (b) The distribution of hyperfine fields in the sextet component. The vertical line indicates the median hyperfine field.

transfer increases, measurement of the resonance mode ω_β was not feasible. Thus, in the following we shall assume the same value of K_1 as for bulk NiO.

4.1. Mössbauer spectroscopy data

At the lowest temperatures the Mössbauer spectra of both samples display a magnetically split sextet with a hyperfine field of about 54 T. As the temperature is increased the hyperfine field gradually diminishes. This reduction is due to the influence of collective magnetic excitations and can be described by [41]

$$B_{\mathrm{obs}}(T) \approx B_0(T)\left[1 - \frac{k_{\mathrm{B}}T}{2E_{\mathrm{a}}}\right] \tag{6}$$

where $B_0(T)$ is the hyperfine field in the absence of collective magnetic excitations in the sample at a temperature T, $B_{\mathrm{obs}}(T)$ is the measured hyperfine field and V is the particle volume. In order to take into account the particle size distribution the low-temperature spectra were fitted with a distribution of sextets [42]. Figure 6 shows such a fit and the distribution of hyperfine fields for the as-prepared sample at 20 K. The median of the hyperfine field distribution is indicated by a line. The temperature dependence of the median hyperfine fields, obtained in this way, were fitted with straight lines, as shown in figure 7. From the slopes, median values of E_{a} were calculated. As discussed above, iron that has reacted with phosphate contributes a small doublet component. This doublet component is fitted separately. At 15 K the doublet covers about 6% of the spectral area. The data from the coated sample at 6 K has been omitted as the doublet component due to the phosphate orders to a sextet, making fitting unreliable.

For the anisotropy configuration of NiO, E_{a} is related to the magneto-crystalline anisotropy by [6, 41]

$$\frac{1}{E_{\mathrm{a}}} = \frac{1}{2K_2V + E_{\mathrm{int}}} + \frac{1}{2K_1V + E_{\mathrm{int}}} \tag{7}$$

where E_{int} is related to the interaction energy of the interparticle interactions.

The linear fits to the low-temperature Mössbauer data in figure 7 yield values of $E_{\mathrm{a}}/k_{\mathrm{B}} = 310(30)$ K for the coated sample and $E_{\mathrm{a}}/k_{\mathrm{B}} = 650(50)$ K for the as-prepared sample. Assuming that the bulk value of $K_1V/k_{\mathrm{B}} = 9000$ K and that the coated sample has a

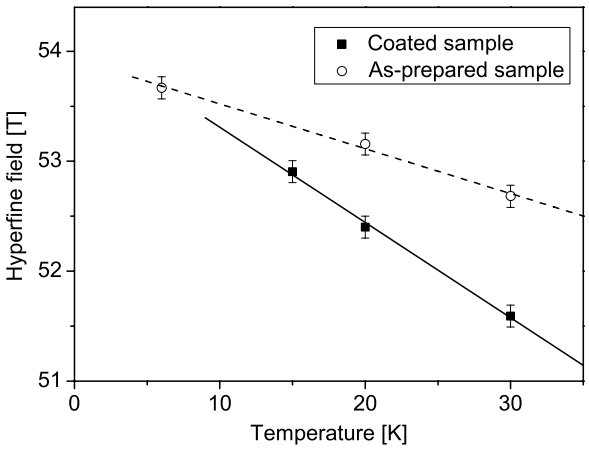

Figure 7. Linear fits to the average hyperfine field splittings measured at low temperatures in the as-prepared and coated samples.

negligible interaction energy, the in-plane anisotropy of the coated sample becomes $K_2V/k_B = 155(15)$ K, equivalent to $K_2 = 8.2(8) \times 10^3$ J m^{-3} or $B_{A2} = 15(2)$ mT. If the as-prepared sample is assumed to have the same in-plane anisotropy, K_2, the interaction energy is calculated from (7) to be $E_{int}/k_B = 360(60)$ K.

4.2. Inelastic neutron scattering data

Due to the nearly cubic nature of the crystal structure, there will be four almost equivalent sets of {111} planes. One of these is the (111) plane, in which the spins are confined uniquely, defined by the exchange striction. The other three are at an angle of ≈70.5° to this. However, the magnetic structure factors of the three $\{\frac{1}{2}\frac{1}{2}\frac{1}{2}\}$ reflections corresponding to the latter three planes are all zero, none of them contributing any scattering intensity.

The scattering intensity of the inelastic signal, $A_2D(\varepsilon)$ at Q_{AFM} with zero spin wavevector, i.e. infinite wavelength, is given by [43]

$$I(\varepsilon, Q_{AFM}) \propto \frac{\mathcal{J}_0\langle S\rangle^2}{\varepsilon_0}\sum_\alpha [1-\hat{\kappa}_\alpha^2]\Big[\big(n(\varepsilon)+1\big)\delta(\varepsilon-\varepsilon_0)+n(\varepsilon)\delta(\varepsilon+\varepsilon_0)\Big]. \tag{8}$$

Here $\langle S\rangle$ is the thermal average of the spin, $n(\varepsilon) = (\exp(\frac{\varepsilon}{k_BT}) - 1)^{-1}$ is the Bose factor, and δ is the Dirac delta function. α is a cartesian coordinate and $\hat{\kappa}_\alpha$ is the α component of the unit scattering vector along the spin fluctuation direction. Note that ε_0 is proportional to $\langle S\rangle$, giving the conventional linear dependence of the cross section on $\langle S\rangle$ [44]. Due to the large out-of-plane anisotropy energy, the precession will be strongly elliptical, with the long axis in the (111) plane. This has been confirmed experimentally for hematite, which has a similar anisotropy structure [5]. In this case the cartesian coordinate sum in (8) is approximately $[1-\hat{\kappa}_\beta^2]$, where β is in the direction of the long axis of the ellipse. As β is preferentially in the (111) plane and thus perpendicular to the scattering vector, this factor will give its maximum value, $\hat{\kappa}_\beta^2 \approx 0$.

In the case of superparamagnetism, the dynamics is longitudinal, with the spins flipping between the easy axes. The intensity of the resulting quasielastic signal will contain a cartesian coordinate sum equivalent to the one in (8). This sum simplifies to $[1-\hat{\kappa}_z^2]$, with $\hat{\kappa}_z$ the component of the unit scattering vector along z. Again, there is a maximum scattering intensity as Q_{AFM} is perpendicular to z, giving $\hat{\kappa}_z^2 = 0$.

4.3. Resonance parameters in zero field

4.3.1. Intensity ratio. Figure 4(a) shows the intensity ratio of the quasielastic signal over the total magnetic signal, $A_1/(A_1 + A_2)$, for both samples as a function of temperature. The anisotropy energies may be calculated from the low-temperature data using (8) in [4], which is derived from Boltzmann statistics. The intensity ratio depends only weakly on K_1V/k_B, so this is fixed to the bulk value of 9000 K. Fitting the data at temperatures below 175 K yields a value of $K_2V/k_B = 200(45)$ K, equivalent to $K_2 = 11(2) \times 10^3$ J m^{-3} or an anisotropy field of $B_{A2} = 20(5)$ mT, which is close to the result obtained from Mössbauer spectroscopy. No model for the intensity ratio in the complex situation of interacting particles is available.

4.3.2. Resonance energy. At low temperature the centre position of the inelastic signal in the coated sample is $\varepsilon_0(0) = 0.47(1)$ meV, as seen in figure 4(b). By (2), this gives an anisotropy field of 7.6(3) mT, equivalent to $K_2 = 4.2(2) \times 10^3$ J m^{-3}. This value is significantly less than the values of K_2 obtained by both low-temperature Mössbauer spectroscopy and the area method presented above. There may be several reasons for this underestimate of the in-plane anisotropy. Most likely it is due to an overestimate of the exchange field. As many of the ions are at surface sites with lower numbers of exchange bonds compared to the bulk value, a decrease in the exchange field of 10% may be justified. Also, the value of the exchange constant itself may be overestimated, as a value of $J_2 = 202$ K has been reported for bulk NiO [45]. Lastly, it is well known from previous work on similar nanoparticles that there is a significant amount of spin canting in the particles [22]. This may arise around defects in the structure and at surface sites [46]. The misalignment of the spins due to canting will also reduce the exchange field. Calculating the exchange field required to account for the measured resonance energy while assuming an anisotropy field of 15 mT gives a value of $B_E = 460$ T or about half the bulk value.

The dependence of the resonance energy of mode ω_α on the ratio between the number of spins on the two sublattices, ξ, has been calculated in [24] and plotted in figure 4(d). Here, the out-of-plane anisotropy field is set to 0.73 T, according to [30], and the in-plane anisotropy field is set to 15 mT, as determined by Mössbauer spectroscopy. Previously, the ratio of the number of spins on the two sublattices was measured to be $\xi = 0.994$ [22]. At this value the reduction of resonance energy is negligible, as illustrated in figure 4(d). Thus, no correction of the determined anisotropy energy due to the presence of uncompensated moment is necessary.

4.3.3. Temperature dependence of the resonance energy. As the temperature is increased, the centre position of the inelastic signal is almost constant, increasing slightly at high temperatures. This disagrees with the temperature dependence previously calculated by Boltzmann statistics [4], where the resonance energy was found to decrease with temperature when the system approaches the non-harmonic range of the energy landscape in (1). The observed temperature dependence of the precession energy is empirically approximated by a quadratic expression in temperature, shown as the solid line in figure 4(b).

The centre position of the inelastic signal in the as-prepared sample is found at a higher value than in the coated sample. As the temperature increases, the effect of the interparticle interactions decreases until the resonance energies in the two samples become the same at about 250 K. This temperature corresponds approximately to the interaction energy estimated from Mössbauer spectroscopy. The resonance energy of the as-prepared sample has also empirically been fitted with a polynomial expression.

In both samples the resonance energy seems to increase above 250 K. However, this is presumably because the model used to fit the data (equation (4)) is not valid at high

temperatures. Well below 250 K, the dynamics can be described as a combination of uniform excitations with small amplitude (which give rise to the inelastic peaks) and superparamagnetic relaxation, i.e. reversal of the sublattice magnetization vectors (which gives rise to a broadening of the quasielastic peak) as described by (4). At temperatures of the order of 250 K, the thermal energy becomes comparable to the anisotropy energy, K_2V. Then the two types of magnetic dynamics cannot be separated clearly, because the sublattice magnetization vectors can fluctuate with similar probabilities in all directions in or close to the (111) plane. The transition to this isotropic relaxation regime has been discussed by Würger [47]. For this reason, the data obtained above 250 K are not included in the fits.

4.3.4. Scattering intensity. Using the quadratic expression for the resonance energy determined above, the scattering intensity of the inelastic signal from the coated sample can be calculated by (8) within a proportionality factor. Normalizing this by the detailed balance factor, it may be fitted to the inelastic intensity, A_2, obtained by fitting the data with (4). The reduction in $\langle S \rangle$ with temperature is taken from the data in [9]. The intensity, plotted in figure 4(c), increases linearly up to 200 K, where it flattens out due to the increase in ε_0. For the as-prepared sample the increased energy required to excite the collective magnetic excitations (compared to the coated sample) will result in a reduction in the intensity from the inelastic signal. This suppression of the uniform magnetic excitations due to interactions was also observed in the low-temperature Mössbauer data. Using the empirical fit to the data in figure 4(b), the intensity is again calculated by (8), giving the dashed line plotted in figure 4(c), in qualitative agreement with the measured data.

4.4. Field dependence of resonance parameters

We only measure scattering from particles with the [111] direction along the scattering vector. Thus, all the particles that contribute have identically oriented (111) planes, as the field is applied perpendicular to the scattering vector. There is no component of the field out of the plane, and the strongly elliptical nature of the precessions is not expected to be affected by the field, so the value of the cartesian coordinate sum in (8) is independent of the field and will always be at its maximum value as $\hat{\kappa}_\beta \approx 0$.

At high applied fields the moment of a particle will align with the applied field. The spins will experience the sum of the applied field and the in-plane anisotropy field. Integrating this sum for all orientations of the anisotropy field gives an expression for the resonance energy of

$$\hbar\omega = \sqrt{\varepsilon_0^2 + (g\mu_B B_{\mathrm{appl}})^2}. \tag{9}$$

This expression is valid at zero applied field and at large applied fields. It is not valid in moderate applied fields, where the spin dynamics enters a complex regime in which the anisotropy field acting on all the spins and the applied field acting on the uncompensated spins become similar in size. The energy expression in (9) has been fitted to the field data obtained from the coated sample at 200 K. The fit was performed by omitting the data at 2 and 4 T as the expression is not presumed to be valid here. The fit is shown in figure 5(a). Except at 2 T, the expression fits the data well. The fit gives a value of $\varepsilon_0 = 0.48(3)$ meV and a value of the g-factor of $g = 2.19(6)$. This value of the g-factor is in accordance with the reported observations of non-quenched orbital momentum in NiO [15, 16].

Calculating the scattering intensity of the inelastic signal by (8) as a function of the applied field gives the line in figure 5(b). The calculated intensity is observed to be in qualitative agreement with the measured data except at the lowest applied fields.

5. Conclusion

Inelastic neutron scattering and Mössbauer spectroscopy have been employed to study the spin dynamics in a sample of interacting nanoparticles of NiO and one where the interactions have been removed by phosphate coating. Consistent values of the in-plane anisotropy energy constant in the weakly interacting nanoparticles have been measured by inelastic neutron scattering and Mössbauer spectroscopy, arriving at values more than two orders of magnitude larger than the bulk value. The temperature dependences of the resonance energies measured by neutron scattering could not be fully explained by the present model, so empirical models were employed. Interactions between the particles were observed to significantly increase the resonance energy, reducing the scattering intensity. A model assuming alignment of the particle moments in large applied fields, due to the presence of an uncompensated moment, was used to fit the field dependence of the resonance energy in the weakly interacting particles. The scattering intensities fit well using both the field model and the empirical temperature models for the resonance energy.

Acknowledgments

This project was supported by the Danish Technical Research Council through the Nanomagnetism programme. We thank P-A Lindgård for valuable discussions, L Lilleballe for help with the sample preparation, H K Rasmussen for help with Mössbauer measurements, and Ch Niedermayer and C Kägi for help with the neutron scattering measurements. We gratefully acknowledge the Danish Neutron Scattering Centre (DANSCATT) for financial support for the neutron scattering experiments. This work is based on experiments performed at the Swiss spallation neutron source SINQ and the Paul Scherrer Institute, Villigen, Switzerland. The 15 T magnet used at SINQ was funded by The Swiss National Science Foundation (through both NCCR/MaNEP, and R'EQUIP programs) as well as The Danish Natural Science Research Council and the Carlsberg Foundation. We also thank the EC-TMR-Access to the Large Scale Facilities programme for funding the neutron scattering at the Risø National Laboratory.

References

[1] Mørup S and Hansen B R 2005 *Phys. Rev.* B **72** 024418
[2] Hendriksen P V, Linderoth S and Lindgård P-A 1993 *Phys. Rev.* B **48** 7259
[3] Hansen M F, Bødker F, Mørup S, Lefmann K, Clausen K N and Lindgård P-A 1997 *Phys. Rev. Lett.* **79** 4910
[4] Klausen S N, Lefmann K, Lindgård P-A, Clausen K N, Hansen M F, Bødker F, Mørup S and Telling M 2003 *J. Magn. Magn. Mater.* **266** 68
[5] Klausen S N, Lefmann K, Lindgård P-A, Theil Kuhn L, Bahl C R H, Frandsen C, Mørup S, Roessli B, Cavadini N and Niedermayer C 2004 *Phys. Rev.* B **70** 214411
[6] Hansen M F, Koch C B and Mørup S 2000 *Phys. Rev.* B **62** 1124
[7] Frandsen C, Bahl C R H, Lebech B, Lefmann K, Theil Kuhn L, Keller L, Andersen N H, von Zimmermann M, Johnson E, Klausen S N and Mørup S 2005 *Phys. Rev.* B **72** 214406
[8] Theil Kuhn L, Lefmann K, Bahl C R H, Klausen S N, Lindgård P-A, Frandsen C, Madsen D E and Mørup S 2006 *Phys. Rev.* B **74** 184406
[9] Klausen S N, Lindgård P-A, Lefmann K, Bødker F and Mørup S 2002 *Phys. Status Solidi* a **189** 1039
[10] Bartel L C and Morosin B 1971 *Phys. Rev.* B **3** 1039
[11] Shull C G, Strauser W A and Wollan E O 1951 *Phys. Rev.* **83** 333
[12] Roth W 1958 *Phys. Rev.* **110** 1333
[13] Hutchings M T and Samuelsen E J 1972 *Phys. Rev.* B **6** 3447
[14] Bødker F, Hansen M F, Koch C B, Lefmann K and Mørup S 2000 *Phys. Rev.* B **61** 6826
[15] Low W 1958 *Phys. Rev.* **109** 247
[16] Fernandez V, Vettier C, de Bergevin F, Giles C and Neubeck W 1998 *Phys. Rev.* B **57** 7870

[17] Lefmann K and Rischel C 2001 *Eur. Phys. J.* B **21** 319
[18] Néel L 1961 *C. R. Hebd. Seances Acad. Sci.* **252** 4075
[19] Richardson J T, Yiagas D I, Turk B, Forster K and Twigg M V 1991 *J. Appl. Phys.* **70** 6977
[20] Zhang W S, Brück E, Zhang Z D, Tegus O, Li W F, Si P Z, Geng D Y and Buschow K H J 2005 *Physica* B **358** 332
[21] Makhlouf S A and Parker F T 1997 *Phys. Rev.* B **55** R14717
[22] Bahl C R H, Hansen M F, Pedersen T, Saadi S, Nielsen K H, Lebech B and Mørup S 2006 *J. Phys.: Condens. Matter* **18** 4161
[23] Lindgård P-A, Kowalska A and Laut P 1967 *J. Phys. Chem. Solids* **28** 1357
[24] Bahl C R H, Lefmann K, Jensen T B S, Lindgård P-A, Madsen D E and Mørup S 2006 unpublished
[25] Kondoh H 1960 *J. Phys. Soc. Japan* **15** 1970
[26] Sievers A J and Tinkham M 1963 *Phys. Rev.* **129** 1566
[27] Grimsditch M, McNeil L E and Lockwood D J 1998 *Phys. Rev.* B **58** 14462
[28] Kurosawa K, Miura M and Saito S 1980 *J. Phys. C: Solid State Phys.* **13** 1521
[29] Saito S, Miura M and Kurosawa K 1980 *J. Phys. C: Solid State Phys.* **13** 1513
[30] Pishko V V, Gnatcheko S L, Tsapenko V V, Kodama R H and Makhlouf S 2003 *J. Appl. Phys.* **93** 7382
[31] Lefmann K, Bødker F, Hansen M F, Vázquez H, Christensen N B, Lindgård P-A, Clausen K N and Mørup S 1999 *Eur. Phys. J.* D **9** 491
[32] Bahl C R H, Theil Kuhn L, Lefmann K, Lindgård P-A and Mørup S 2006 *Physica* B at press doi:10.1016/J.Physb.2006.05.234
[33] Bødker F, Hansen M F, Koch C B and Mørup S 2000 *J. Magn. Magn. Mater.* **221** 32
[34] Bahl C R H and Mørup S 2006 *Nanotechnology* **17** 2835
[35] Bahl C R H, Andersen P, Klausen S N and Lefmann K 2004 *Nucl. Instrum. Methods* B **226** 667
[36] Bahl C R H, Lefmann K, Abrahamsen A B, Rønnow H M, Saxild F, Jensen T B S, Udby L, Andersen N H, Christensen N B, Jakobsen H S, Larsen T, Häfliger P S, Streule S and Niedermayer C 2006 *Nucl. Instrum. Methods* B **246** 452
[37] The FullProf software can be found at http://www-llb.cea.fr/fullweb/
[38] Bahl C R H 2006 *PhD Thesis* Technical University of Denmark
[39] Mørup S, Frandsen C, Bødker F, Klausen S N, Lefmann K, Lindgård P-A and Hansen M F 2002 *Hyperfine Interact.* **144/145** 347
[40] Mørup S, Bødker F, Hendriksen P V and Linderoth S 1995 *Phys. Rev.* B **52** 287
[41] Mørup S 1983 *J. Magn. Magn. Mater.* **37** 39
[42] Wivel C and Mørup S 1981 *J. Phys. E: Sci. Instrum.* **14** 605
[43] Shirane G, Shapiro S M and Tranquada J M 2002 *Neutron Scattering with a Triple-Axis Spectrometer* (Cambridge: Cambridge University Press)
[44] Marshall W and Lovesey S W 1971 *Theory of Thermal Neutron Scattering* (Oxford: Oxford University Press)
[45] Srinivasan G and Seehra M S 1984 *Phys. Rev.* B **29** 6295
[46] Mørup S 2003 *J. Magn. Magn. Mater.* **266** 110
[47] Würger A 1998 *Europhys. Lett.* **44** 103

Paper XII

Uniform spin wave modes in antiferromagnetic nanoparticles with uncompensated magnetic moments

C. R. H. Bahl*,† K. Lefmann, T. B. S. Jensen, and P.-A. Lindgård
Materials Research Department, AFM-228, Risø National Laboratory, DK-4000 Roskilde, Denmark

D. E. Madsen and S. Mørup
Department of Physics, bldg. 307, Technical University of Denmark, DK-2800 Kongens Lyngby, Denmark

We have calculated the energy of uniform spin wave modes in antiferromagnetic nanoparticles as a function of the magnitude of the uncompensated magnetic moment. Such uniform spin waves with wave vector $\mathbf{q} = 0$ are predominant in nanoparticles. Two magnetic anisotropy terms are considered, an out-of-plane term confining the spins to the basal plane and an in-plane term determining an easy axis within this plane. Spin wave energies are calculated for various combinations of these two anisotropy terms ranging from the simple uniaxial case to the planar case with a strong out-of-plane anisotropy. In the uniaxial case even a small amount of uncompensated moment has a large influence on the excitation energy, but in the planar case the influence is much smaller. The calculations are important in order to explain previous and recent neutron scattering measurements on antiferromagnetic nanoparticles.

PACS numbers: 76.50.+g, 75.75.+a, 75.50.Ee, 75.30.Gw
Keywords: Spin waves, Antiferromagnetism, Uncompensated moment, Fine particle systems

I. INTRODUCTION

The magnetic properties of nanoparticles have been the subject of numerous studies because of the many technological applications of magnetic nanoparticles[1,2]. Several experimental and theoretical studies of spin waves in nanometer sized systems have been published[3–7]. In magnetic nanoparticles, it is characteristic that the magnetisation direction is not fixed as in bulk materials, but fluctuates due to thermal excitation of the uniform precession mode. In nanoparticles uniform precession around an easy direction of magnetisation in combination with transitions between precession states with different precession angles have been termed collective magnetic excitations[8,9]. As the temperature is increased such that the thermal energy is comparable to the magnetic anisotropy energy, the fluctuations become dominated by superparamagnetic relaxation, i.e. thermally induced magnetisation reversals.

The uniform precession states are predominant in nanoparticles compared to other spin wave excitations[10] and can be described as spin waves with the wave vector $\mathbf{q} = 0$. Uniform excitations in bulk antiferromagnetic materials are conventionally studied by antiferromagnetic resonance (AFMR) experiments, see, for example[11]. However, only few magnetic resonance studies have been performed on antiferromagnetic nanoparticles[12]. In Mössbauer spectroscopy, the uniform excitaions result in a reduction of the magnetic hyperfine splitting[8,9].

Inelastic neutron scattering is a useful tool for measuring the excitation energy of the uniform precession states[13]. The quantised nature of the $\mathbf{q} = 0$ spin waves and also the polarisation of these may be studied by inelastic neutron scattering[14].

Many previous calculations concerning antiferromagnetic spin waves assume a uniaxial anisotropy described by a single anisotropy term. However, often the anisotropy is better described by including more than one anisotropy term. In the present paper the $\mathbf{q} = 0$ spin wave energies in the presence of both an out-of-plane anisotropy energy, κ_1 and an in-plane anisotropy energy κ_2 are calculated. This description is applicable to hematite (α-Fe_2O_3) and NiO. In both bulk materials the value of κ_2 is very small compared to $|\kappa_1|$. In nanoparticles of these materials, the in-plane anisotropy energy has been found to be orders of magnitude larger than in bulk although still smaller than the out-of-plane anisotropy energy[15,16].

In practice, a nanoparticle of an antiferromagnetic material is not a perfect antiferromagnet, but has an uncompensated magnetic moment due to different numbers of spins in the two sublattices. This was proposed theoretically by Néel[17] and has been observed in nanoparticles of different antiferromagnetic materials such as ferritin[18,19] NiO[20–22], and Cr_2O_3[23].

In this paper, we derive expressions for the energy of the uniform excitations as a function of the magnitude of the uncompensated magnetic moment in the case of particles with a magnetic anisotropy similar to that of α-Fe_2O_3 and

* Corresponding author

NiO. We here neglect interparticle interactions.

We find that the effect of an uncompensated moment on the excitation energy depends strongly on the ratio between the two contributions to the anisotropy. The calculations assume localised spins, neglecting any non-collinear spin structures (spin-canting). In real nanoparticles, spin-canting may be present both at the surface and within the particles[24].

II. SPIN WAVES IN ANISOTROPIC ANTIFERROMAGNETS

We consider a nanoparticle of a two-sublattice antiferromagnet with sublattices labelled j and l. The number of lattice sites on sublattice j is N_j and on sublattice l it is N_l. The ratio between the number of spins on the sublattices is referred to as $\xi = \frac{N_l}{N_j}$.

The ground state of the system is assumed to be the Néel state having a complete antiparallel alignment of the spins with the spins on the sublattice j aligned along the positive z direction and those on sublattice l aligned along the negative z direction.

Considering only isotropic exchange interaction between the two sublattices and neglecting higher-order terms of the anisotropy energy the Hamiltonian of the system with ionic spins s_j and s_l can be written as

$$\mathcal{H} = \sum_{\langle jl \rangle} J_{jl} \hat{\mathbf{s}}_j \cdot \hat{\mathbf{s}}_l - \kappa_1 \left(\sum_j \left(\hat{s}_j^x\right)^2 + \sum_l \left(\hat{s}_l^x\right)^2 \right) - \kappa_2 \left(\sum_j \left(\hat{s}_j^z\right)^2 + \sum_l \left(\hat{s}_l^z\right)^2 \right) \tag{1}$$

where J_{jl} are the exchange constants, z is the easy axis of the spins within the easy plane and x is perpendicular to the easy plane. Thus, to maintain a ground state with the spin along z, κ_1 must be negative and κ_2 must be positive.

The exchange term summation $\sum_{jl} J_{jl}$ can be rewritten as

$$\sum_{\langle jl \rangle} J_{jl} = \sum_l \sum_{\boldsymbol{\delta}} J_{\boldsymbol{\delta}} \tag{2}$$

where $J_{\boldsymbol{\delta}} = J_{jl}$ with $\boldsymbol{\delta} = \mathbf{r}_l - \mathbf{r}_j$, with $\mathbf{r}_j$ the position of a spin in sublattice j.

The calculations follow the procedure outlined by Marshall and Lovesey[25]. The spin raising and lowering operators $\hat{s}^{\pm} = \hat{s}^x \pm \mathrm{i}\hat{s}^y$ satisfy the commutator relations

$$[\hat{s}_n^+, \hat{s}_m^-] = 2\hat{s}_n^z \delta_{n,m} \quad \text{and} \quad [\hat{s}_n^z, \hat{s}_m^{\pm}] = \pm \hat{s}_n^{\pm} \delta_{n,m}. \tag{3}$$

where m and n refer to spins on either of the sublattices. Rotating the l sublattice by π about the x axis gives the new operators, $\hat{t}$, where

$$\hat{s}_n^x = \hat{t}_n^x \qquad \hat{s}_n^y = -\hat{t}_n^y \qquad -\hat{s}_n^z = \hat{t}_n^z \qquad \hat{s}_n^+ = \hat{t}_n^- \qquad \hat{s}_n^- = \hat{t}_n^+. \tag{4}$$

At low temperature in the ordered state the spins will predominantly be along z in one sublattice and along $-z$ in the other sublattice, such that $\hat{s}_n^z \approx s$ and $\hat{t}_n^z \approx s$ are valid approximations.

Including only linear terms we reach four equations of motion:

$$\mathrm{i}\hbar \frac{d}{dt}\hat{s}_j^+ = [\hat{s}_j^+, \mathcal{H}] = s \sum_{\boldsymbol{\delta}} J_{\boldsymbol{\delta}}\, \xi \left(\hat{s}_j^+ + \hat{t}_l^-\right) + 2\kappa_2 s' \hat{s}_j^+ - \kappa_1 s' \left(\hat{s}_j^+ + \hat{s}_j^-\right) \tag{5}$$

$$\mathrm{i}\hbar \frac{d}{dt}\hat{t}_l^- = [\hat{t}_l^-, \mathcal{H}] = -s \sum_{\boldsymbol{\delta}} J_{\boldsymbol{\delta}}\, \left(\hat{t}_l^- + \hat{s}_j^+\right) - 2\kappa_2 s' \hat{t}_l^- + \kappa_1 s' \left(\hat{t}_l^- + \hat{t}_l^+\right) \tag{6}$$

$$\mathrm{i}\hbar \frac{d}{dt}\hat{s}_j^- = [\hat{s}_j^-, \mathcal{H}] = -s \sum_{\boldsymbol{\delta}} J_{\boldsymbol{\delta}}\, \xi \left(\hat{s}_j^- + \hat{t}_l^+\right) - 2\kappa_2 s' \hat{s}_j^- + \kappa_1 s' \left(\hat{s}_j^- + \hat{s}_j^+\right) \tag{7}$$

$$\mathrm{i}\hbar \frac{d}{dt}\hat{t}_l^+ = [\hat{t}_l^+, \mathcal{H}] = s \sum_{\boldsymbol{\delta}} J_{\boldsymbol{\delta}}\, \left(\hat{t}_l^+ + \hat{s}_j^-\right) + 2\kappa_2 s' \hat{t}_l^+ - \kappa_1 s' \left(\hat{t}_l^+ + \hat{t}_l^-\right) \tag{8}$$

To obtain the correct quantum mechanical form for the anisotropy terms we have used the Holstein-Primakoff transformation and well-ordered Bose operators[26]. This gives the factor $s' = s - \frac{1}{2}$, instead of the classical s. We have assumed periodic boundary conditions as is conventional for calculations of bulk materials. This assumption is valid also for the nanoparticle calculations in this paper, as only the uniform, $\mathbf{q} = 0$, spin wave mode will be considered.

Fourier transforms of the operators are defined by

$$\hat{S}^+_{\mathbf{q}} = \sum_j \mathrm{e}^{\mathrm{i}\mathbf{q}\cdot\mathbf{r}_j}\,\hat{s}^+_j \quad \text{and} \quad \hat{T}^-_{\mathbf{q}} = \sum_l \mathrm{e}^{\mathrm{i}\mathbf{q}\cdot\mathbf{r}_l}\,\hat{t}^-_l \tag{9}$$

and similar for $\hat{S}^-_{\mathbf{q}}$ and $\hat{T}^+_{\mathbf{q}}$. Due to the difference in the number of spins on sublattices j and l we get

$$\sum_l \sum_{\boldsymbol{\delta}} J_{\boldsymbol{\delta}} = \xi \sum_j \sum_{\boldsymbol{\delta}} J_{\boldsymbol{\delta}}. \tag{10}$$

Defining

$$\mathcal{J}(\mathbf{q}) = \sum_{\boldsymbol{\delta}} J_{\boldsymbol{\delta}}\,\mathrm{e}^{-\mathrm{i}\mathbf{q}\cdot\boldsymbol{\delta}}, \tag{11}$$

the equations of motion may be transformed as

$$\begin{aligned}
\mathrm{i}\hbar\frac{d}{dt}\hat{S}^+_{\mathbf{q}} &= \sum_j \mathrm{e}^{\mathrm{i}\mathbf{q}\cdot\mathbf{r}_j}\left[s\sum_{\boldsymbol{\delta}} J_{\boldsymbol{\delta}}\,\xi\left(\hat{s}^+_j + \hat{t}^-_l\right) + 2\kappa_2 s'\hat{s}^+_j - \kappa_1 s'\left(\hat{s}^+_j + \hat{s}^-_j\right)\right] \\
&= s\xi\mathcal{J}(0)\hat{S}^+_{\mathbf{q}} + s\mathcal{J}(\mathbf{q})\hat{T}^-_{\mathbf{q}} + 2s'\kappa_2\hat{S}^+_{\mathbf{q}} - s'\kappa_1(\hat{S}^+_{\mathbf{q}} + \hat{S}^-_{\mathbf{q}})
\end{aligned} \tag{12}$$

and

$$\begin{aligned}
\mathrm{i}\hbar\frac{d}{dt}\hat{T}^-_{\mathbf{q}} &= \sum_l \mathrm{e}^{\mathrm{i}\mathbf{q}\cdot\mathbf{r}_l}\left[-s\sum_{\boldsymbol{\delta}} J_{\boldsymbol{\delta}}\,\left(\hat{t}^-_l + \hat{s}^+_j\right) - 2\kappa_2 s'\hat{t}^-_l + \kappa_1 s'\left(\hat{t}^-_l + \hat{t}^+_l\right)\right] \\
&= -s\mathcal{J}(0)\hat{T}^-_{\mathbf{q}} - s\xi\mathcal{J}(\mathbf{q})\hat{S}^+_{\mathbf{q}} - 2s'\kappa_2\hat{T}^-_{\mathbf{q}} + s'\kappa_1(\hat{T}^-_{\mathbf{q}} + \hat{T}^+_{\mathbf{q}})
\end{aligned} \tag{13}$$

The transformed equations of motion in (12) and (13) can be written as the matrix $\underline{A}$.

$$\underline{A} = \begin{bmatrix}
\xi\mathcal{J}(0)s + a & \mathcal{J}(\mathbf{q})s & -b & 0 \\
-\xi\mathcal{J}(\mathbf{q})s & -\mathcal{J}(0)s - a & 0 & b \\
b & 0 & -\xi\mathcal{J}(0)s - a & -\mathcal{J}(\mathbf{q})s \\
0 & -b & \xi\mathcal{J}(\mathbf{q})s & \mathcal{J}(0)s + a
\end{bmatrix} \tag{14}$$

We have defined $a = (2\kappa_2 - \kappa_1)s'$ and $b = \kappa_1 s'$. Finding the eigenvalues by

$$|\underline{A} - \underline{I}\omega| = 0 \tag{15}$$

gives four spin wave solutions.

As discussed above the dominating excitation in nanoparticles is the uniform mode with $\mathbf{q} = 0$. Therefore only this case is considered in the further calculations, defining for simplicity $c = \mathcal{J}(0)s$.

We shall show that for the $\mathbf{q} = 0$ mode Equations (12) and (13) reduce to the equations of motions obtained when considering all the spins on a sublattice as a single super-spin, i.e. $\sum_j \hat{s}_j = N_j\hat{s}_j = \hat{S}$ and $\sum_l \hat{t}_l = N_l\hat{t}_l = \hat{T}$. These interact with the effective Hamiltonian

$$\mathcal{H} = J_{\mathrm{eff}}\hat{\mathbf{S}}\cdot\hat{\mathbf{T}} - K_1^S\left(\hat{S}^x\right)^2 - K_1^T\left(\hat{T}^x\right)^2 - K_2^S\left(\hat{S}^z\right)^2 - K_2^T\left(\hat{T}^z\right)^2 \tag{16}$$

Here K_1, K_2 and J_{eff} are the effective macroscopical constants, which are related to the microscopical constants in the following by considering the equations of motion with $\mathbf{q} = 0$. Equation (16) gives the equations of motion

$$\mathrm{i}\hbar\frac{d}{dt}\hat{S}^+ = TJ_{\mathrm{eff}}\hat{S}^+ + SJ_{\mathrm{eff}}\hat{T}^- + 2S'K_2^S\hat{S}^+ - S'K_1^S\left(\hat{S}^+ + \hat{S}^-\right) \tag{17}$$

and

$$\mathrm{i}\hbar\frac{d}{dt}\hat{T}^- = -SJ_{\mathrm{eff}}\hat{T}^- + TJ_{\mathrm{eff}}\hat{S}^+ - 2T'K_2^T\hat{T}^- + T'K_1^T\left(\hat{T}^- + \hat{T}^+\right) \tag{18}$$

where $S' = S - \frac{1}{2}$ and $T' = T - \frac{1}{2}$. When S and T are large one obviously obtains the classical approximation. With $\mathcal{J}(0) = N_jJ_{\mathrm{eff}}$, $\kappa_1 = N_jK_1^S = N_lK_1^T$ and $\kappa_2 = N_jK_2^S = N_lK_2^T$ Equations (17) and (18) become identical to Equations (12) and (13). This proves that for the $\mathbf{q} = 0$ mode the ferrimagnetic model is valid and needed, when the number of spins are different on the two sublattices.

Assuming only nearest neighbour interaction, Equation (11) gives $\mathcal{J}(0) = zJ$, where z is the number of nearest neighbours and J is the exchange constant. Due to the finite size of nanoparticles, a large fraction of the atoms will be at the surface of the particles. These will experience a reduced exchange of e.g. $\frac{z}{2}J$ as there are missing bonds. The $\mathbf{q} = 0$ mode measures the average value of $\mathcal{J}(0)$ in the particle, which is then reduced relative to the bulk value.

A. The uniform mode in antiferromagnetic nanoparticles

In a perfect antiferromagnetic nanoparticle the number of spins is the same on both sublattices such that $\xi = 1$. Solving Equation (15) gives the four solutions

$$\hbar\omega_\alpha = \pm 2\sqrt{\kappa_2 s' \left[(\kappa_2 - \kappa_1)s' + \mathcal{J}(0)s\right]} \tag{19}$$

$$\hbar\omega_\beta = \pm 2\sqrt{(\kappa_2 - \kappa_1)s' \left[\kappa_2 s' + \mathcal{J}(0)s\right]}. \tag{20}$$

The anisotropy and exchange fields are defined as

$$B_{\mathrm{A}i} = \frac{2|\kappa_i|s'}{g\mu_\mathrm{B}} \quad (i = 1, 2) \tag{21}$$

and

$$B_E = \frac{\mathcal{J}(0)s}{g\mu_\mathrm{B}} = \frac{c}{g\mu_\mathrm{B}}, \tag{22}$$

where g is the g-factor and μ_B is the Bohr magneton.

When $B_\mathrm{E} \gg B_{\mathrm{A}i}$ and $B_\mathrm{A1} \gg B_\mathrm{A2}$, the spin wave energies may be approximated by

$$\hbar\omega_\alpha \approx g\mu_\mathrm{B}\sqrt{2B_\mathrm{A2}B_\mathrm{E}} \tag{23}$$

$$\hbar\omega_\beta \approx g\mu_\mathrm{B}\sqrt{2(B_\mathrm{A2} + B_\mathrm{A1})B_\mathrm{E}} \approx g\mu_\mathrm{B}\sqrt{2B_\mathrm{A1}B_\mathrm{E}}. \tag{24}$$

The expressions are recognised as the conventional expressions for antiferromagnetic resonance[11] which is the same as $\mathbf{q} = 0$ spin waves.

B. The influence of uncompensated moments

As proposed by Néel[17] the small size of an antiferromagnetic nanoparticle will result in an excess number of spins on one sublattice compared to the other, i.e. $\xi \neq 1$. In this case the solutions to Equation (15) become more complex. Using the symbols defined above and defining

$$d = \sqrt{4a^2(\xi - 1)^2 + c^2(\xi - 1)^4 + 16b^2\xi + 4ac(\xi - 1)^2(\xi + 1)} \tag{25}$$

the spin wave energies are given by

$$\hbar\omega_\alpha = \sqrt{a^2 - b^2 + ac(\xi + 1) + \frac{1}{2}c^2(\xi - 1)^2 - d} \tag{26}$$

$$\hbar\omega_\beta = \sqrt{a^2 - b^2 + ac(\xi + 1) + \frac{1}{2}c^2(\xi - 1)^2 + d} \tag{27}$$

In the simple uniaxial case, where $\kappa_1 = 0\,(b = 0)$, the equations simplify to

$$\hbar\omega_{\alpha,\beta} = \frac{1}{2}\left[\pm c(\xi - 1) + \sqrt{c^2(1 - \xi)^2 + 4a^2 + 4ac(1 + \xi))}\right] \tag{28}$$

or stated in the anisotropy and exchange field terminology

$$\hbar\omega_{\alpha,\beta} = g\mu_\mathrm{B}\left[\pm\frac{B_\mathrm{E}}{2}(\xi - 1) + \sqrt{B_\mathrm{E}B_\mathrm{A2}(1 + \xi) + \left(\frac{B_\mathrm{E}}{2}(\xi - 1)\right)^2 + B_\mathrm{A2}^2}\right]. \tag{29}$$

This result is well known from previous classical calculations for a ferrimagnet assuming uniaxial anisotropy[27,28].

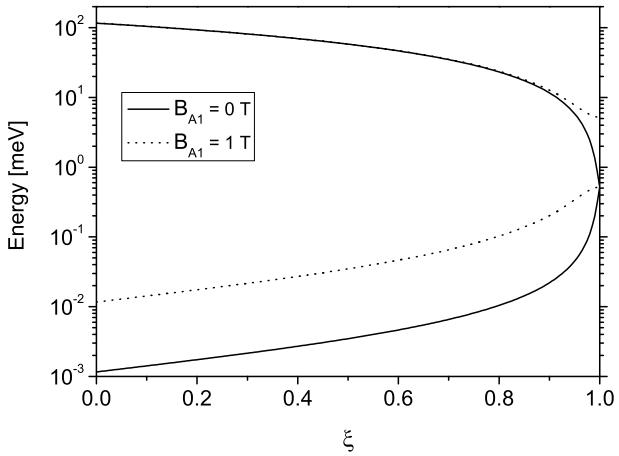

FIG. 1: Energies of the $\mathbf{q} = 0$ spin wave modes in a large range of values of the ratio between the number of spins on the two sublattices ξ. The upper mode is $\hbar\omega_\beta$ while the lower mode is $\hbar\omega_\alpha$. The energies are calculated with $B_{\mathrm{A2}} = 0.01$ T and $B_{\mathrm{E}} = 1000$ T. Two extreme values of B_{A1} are shown, the uniaxial where $B_{\mathrm{A1}} = 0$ and the planar where $B_{\mathrm{A1}} = 100\, B_{\mathrm{A2}}$. The spin wave energies are shown on a logarithmic scale as the presence of an uncompensated moment changes the energies by orders of magnitude.

III. CALCULATION OF RESONANCE ENERGIES

We have calculated the two resonance energies $\hbar\omega_\alpha$ and $\hbar\omega_\beta$ as a function of the magnitude of the uncompensated moment. The exchange field is often very large and is set to a typical value of $B_{\mathrm{E}} = 1000$ T in the calculations. The in-plane anisotropy field is set to $B_{\mathrm{A2}} = 0.01$ T, which is a realistic order of magnitude for nanoparticles[13–16,22]. Three different values of the out-of-plane anisotropy are considered, the uniaxial case where $B_{\mathrm{A1}} = 0$ T, the case where the anisotropy fields are equal in size, $B_{\mathrm{A1}} = 0.01$ T, and the strongly planar anisotropy case where $B_{\mathrm{A1}} = 1$ T.

Figure 1 shows the spin wave energies as a function of the ratio of the the number of spins on the two sublattices. Results for the two extremes of the anisotropy, the uniaxial case and the strongly planar case, are both plotted. In the case of uniaxial anisotropy ($B_{\mathrm{A1}} = 0$) the two spin wave branches are degenerate at zero uncompensated moment ($\xi = 1$). As the uncompensated moment increases, the modes split up with a strong dependence of the energies on the uncompensated moment. In the planar case ($B_{\mathrm{A1}} = 1$ T), however, the two modes are split at zero uncompensated moment.

At large values of the uncompensated moment, the energy of the high energy mode, $\hbar\omega_\beta$, is similar in the two cases. There is a large relative difference in the energy of the low energy mode, $\hbar\omega_\alpha$, in the two cases.

Figure 2 shows the resonance energies in the situation where the ratio between the number of spins in the two sublattices is close to unity. In the planar case ($B_{\mathrm{A1}} \gg B_{\mathrm{A2}}$) both the energies are only weakly dependent of the uncompensated moment. As the value of B_{A1} is reduced towards the uniaxial case ($B_{\mathrm{A1}} \ll B_{\mathrm{A2}}$) the dependence of $\hbar\omega_\alpha$ on ξ becomes ever stronger. When the two anisotropy fields become equal even an uncompensated moment as small as 1% results in a reduction of the energy by a factor of two, and in the uniaxial case ($B_{\mathrm{A1}} = 0$) this reduction is almost a factor of three.

A. Neutron studies of antiferromagnetic nanoparticles

The magnitude of the uncompensated magnetic moment of antiferromagnetic nanoparticles has in some cases been found to be roughly proportional to $N^{1/3}$, where N is the number of spins in a particle[21,22], corresponding to a situation where the uncompensated moment is due to a more or less random occupation of surface sites[17,21]. Thus, the importance of the uncompensated moment increases rapidly with decreasing particle size.

Inelastic neutron scattering studies of hematite nanoparticles have shown a size dependence of the energy of the uniform excitation mode that can be explained by the influence of the uncompensated magnetic moment. In a study of 16 nm α-Fe_2O_3 particles, it was found from magnetisation measurements that the fraction of uncompensated magnetic moment was $\xi \gtrsim 0.999$[29] in accordance with a $N^{1/3}$ dependence of the uncompensated moment. Inelastic neutron studies of this sample yielded the excitation energy $\hbar\omega_\alpha = 0.26$ meV at low temperatures[13]. For these particles, $B_{\mathrm{A1}} \approx 10\, B_{\mathrm{A2}}$[14], and the energy shift due to the uncompensated moment is, according to Equation (26), less than

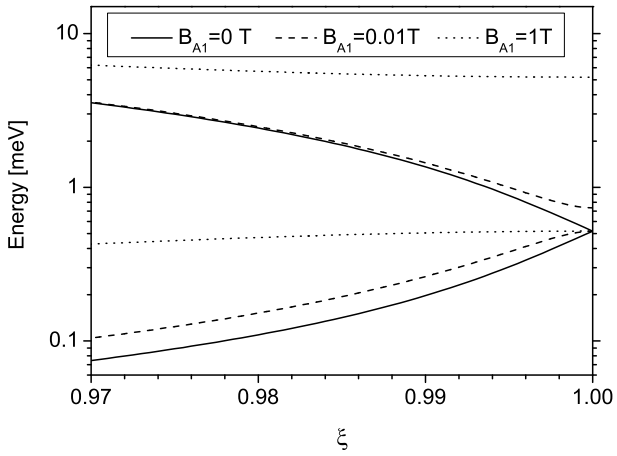

FIG. 2: Energies of the $\mathbf{q} = 0$ spin wave modes for small values of the ratio between the number of spins on the two sublattices ξ. The upper mode is $\hbar\omega_\beta$ while the lower mode is $\hbar\omega_\alpha$. The energies were calculated with $B_{\rm A2} = 0.01$ T and $B_{\rm E} = 1000$ T. The energies are plotted for $B_{\rm A1} = 0$, $B_{\rm A1} = B_{\rm A2}$ and $B_{\rm A1} = 100\, B_{\rm A2}$.

1%, i.e. negligible. In a recent study of 8 nm α-Fe_2O_3 particles, the energy was found to be $\hbar\omega_\alpha = 0.21$ meV at low temperature[15]. This lower value of the energy is not in accordance with Equation (23) as the magnetic anisotropy energy constant of α-Fe_2O_3 is known to increase with decreasing particle size[30], and this should lead to an increase of the energy. However, a reduction in the excitation energy can, at least qualitatively, be explained by the presence of an uncompensated moment. In the 8 nm α-Fe_2O_3 particles, $B_{\rm A1}$ and $B_{\rm A2}$ are of the same order of magnitude[15]. If one assumes that the uncompensated moment is the main reason for the reduction of the energy, one finds from Equation (26) that $\xi \approx 0.99$, which is reasonably well in accordance with an $N^{1/3}$ dependence of the uncompensated moment.

As reported in Ref.[16], the anisotropy energies in plate-shaped NiO nanoparticles resemble the planar case with $B_{\rm A1} \gg B_{\rm A2}$. In these particles, a value of $\xi = 0.994$ has been estimated from high-field Mössbauer spectroscopy[22]. It can be seen in Figure 2, that in this case the influence of the uncompensated moment on the excitation energy is small.

IV. CONCLUSION

The spin wave energy of $\mathbf{q} = 0$ spin waves (uniform precession) has been calculated as a function of the uncompensated moment of nanoparticles. Systems with double anisotropy, relevant for e.g. NiO and hematite, are considered. Different examples of such anisotropy ranging from uniaxial to planar anisotropy are presented. It is found that the resonance energy depends strongly on the magnitude of the uncompensated moment in the case of uniaxial anisotropy, but the dependence is weaker in the case of planar anisotropy. The results are important for the interpretaion of neutron scattering and AFMR experiments on nanoparticle systems.

† christian.bahl@risoe.dk

[1] J. L. Dormann, D. Fiorani, and E. Tronc, Adv. Chem. Phys. **98**, 283 (1997).
[2] Q. Pankhurst, ed., *Fifth International Conference on Fine Particle Magnetism* (Journal of Physics: Conference Series **17**, 2005).
[3] P. V. Hendriksen, S. Linderoth, and P.-A. Lindgård, Phys. Rev. B **48**, 7259 (1993).
[4] T. M. Nguyen, M. G. Cottam, H. Y. Liu, Z. K. Wang, S. C. Ng, M. H. Kuok, D. J. Lockwood, K. Nielsch, and U. G. sele, Phys. Rev. B **73**, 140402(R) (2006).
[5] M. Grimsditch, G. K. Leaf, H. G. Kaper, D. A. Karpeev, and R. E. Camley, Phys. Rev. B **69**, 174428 (2004).
[6] M. Grimsditch, L. Giovannini, F. Montoncello, F. Nizzoli, G. K. Leaf, and H. G. Kaper, Phys. Rev. B **70**, 054409 (2004).
[7] Z. K. Wang, H. S. Lim, H. Y. Liu, S. C. Ng, M. H. Kuok, L. L. Tay, D. J. Lockwood, M. G. Cottam, K. L. Hobbs, P. R. Larson, et al., Phys. Rev. Lett. **94**, 137208 (2005).
[8] S. Mørup and H. Topsøe, Appl. Phys. **11**, 63 (1976).
[9] S. Mørup, J. Magn. Magn. Mater. **37**, 39 (1983).

[10] S. Mørup and B. R. Hansen, Phys. Rev. B **72**, 024418 (2005).
[11] L. R. Maxwell and T. R. McGuire, Rev. Mod. Phys. **25**, 279 (1953).
[12] V. V. Pishko, S. L. Gnatcheko, V. V. Tsapenko, R. H. Kodama, and S. Makhlouf, J. Appl. Phys. **93**, 7382 (2003).
[13] M. F. Hansen, F. Bødker, S. Mørup, K. Lefmann, K. N. Clausen, and P.-A. Lindgård, Phys. Rev. Lett. **79**, 4910 (1997).
[14] S. N. Klausen, K. Lefmann, P.-A. Lindgård, L. Theil Kuhn, C. R. H. Bahl, C. Frandsen, S. Mørup, B. Roessli, N. Cavadini, and C. Niedermayer, Phys. Rev. B **70**, 214411 (2004).
[15] L. Theil Kuhn, K. Lefmann, C. R. H. Bahl, S. N. Klausen, P.-A. Lindgård, C. Frandsen, D. E. Madsen, and S. Mørup, Phys. Rev. B **74**, 184406 (2006).
[16] C. R. H. Bahl, K. Lefmann, L. Theil Kuhn, N. B. Christensen, H. Vázquez, and S. Mørup, J. Phys.: Condens. Matter. (in press) (2006).
[17] L. Néel, C. R. Hebd. Seances Acad. Sci. **252**, 4075 (1961).
[18] S. A. Makhlouf and F. T. Parker, Phys. Rev. B **55**, R14717 (1997).
[19] J. G. E. Harris, J. E. Grimaldi, D. D. Awschalom, A. Chiolero, and D. Loss, Phys. Rev. B **60**, 3453 (1999).
[20] W. J. Schuele and V. D. Deetscreek, J. Appl. Phys. **33**, 1136 (1962).
[21] J. T. Richardson, D. I. Yiagas, B. Turk, K. Forster, and M. V. Twigg, J. Appl. Phys. **70**, 6977 (1991).
[22] C. R. H. Bahl, M. F. Hansen, T. Pedersen, S. Saadi, K. H. Nielsen, B. Lebech, and S. Mørup, J. Phys.: Condens. Matter **18**, 4161 (2006).
[23] W. S. Zhang, E. Brück, Z. D. Zhang, O. Tegus, W. F. Li, P. Z. Si, D. Y. Geng, and K. H. J. Buschow, Physica B **358**, 332 (2005).
[24] S. Mørup, J. Magn. Magn. Mater. **266**, 110 (2003).
[25] W. Marshall and S. W. Lovesey, *Theory of Thermal Neutron Scattering* (Oxford University Press, 1971).
[26] T. Holstein and H. Primakoff, Phys. Rev. **58**, 1098 (1940).
[27] C. Kittel, Phys. Rev. **82**, 565 (1951).
[28] R. K. Wangsness, Phys. Rev. **91**, 1085 (1953).
[29] F. Bødker, M. F. Hansen, C. B. Koch, K. Lefmann, and S. Mørup, Phys. Rev. B **61**, 6826 (2000).
[30] F. Bødker and S. Mørup, Europhys. Lett. **52**, 217 (2000).

Risø's research is aimed at solving concrete problems in the society.

Research targets are set through continuous dialogue with business, the political system and researchers.

The effects of our research are sustainable energy supply and new technology for the health sector.